Interface Electronic Structure of Inverted Polymer Solar Cells

Rania Saleh Alqurashi

Department of Physics and Astronomy
University of Sheffield

Thesis submitted for the degree of
Doctor of Philosophy

July 2017

Acknowledgments

First of all, my deepest thankfulness goes to the Almighty ALLAH, whose blessings are abundant and favours are unlimited.

This work has not been completed without the academic and moral support of many wonderful people. I would like to express my indebtedness to the governor of Al-Baha University for providing me with this scholarship to fulfil my ambitions, and to the Royal Embassy of Saudi Arabia for all their financial and administration support.

I would also acknowledge my deep gratitude to my formal supervisor Alastair Buckley for providing me with this unique opportunity to discover the beauty of scientific research. Your guidance, encouragement, understanding and continued support have helped me throughout the last few years. To David Lidzey, thank you for all your valuable contributions and discussions. I could not ask for a better supervisory team.

The EPMM group and Ossila Ltd have continued to grow during my time in Sheffield, and it has been a pleasure working with you all. Thank you to Abdullah Alsulami for providing me with my initial training, and for being a friend and giving me someone to compete against. Thanks also to Jon Griffin for his help with metal oxides and continued support during my research, and to Martin Grill for the enlightening discussion we had at the UK Semiconductors Summer meeting. I would like to thank Daren Watters for his training and help with the UV-vis spectrometer, Edward Bovill for laboratory training at the Kroto Innovation Centre, and Lamiaa Alharbe for acquiring AFM images as well as being a great person. Special thanks to Deborah Hammond for XPS and UPS measurements and CasaXPS training, and to Lucy Lee for all her help and guidance through my most difficult times.

Outside academia, friendship with distinguished minds has provided endless laughter and great memories for many years, and so thank you to my close friends: Wala, Lamiaa, Latifah, Laila, Reem, and Khlood. Thanks also to all members of the Saudi Student Club in Sheffield for their voluntary contributions to support the Saudi community.

Without the unconditional love and support I have received from my amazing parents, this work would not have been possible. Their wise words, keen interest in my work and wellbeing, and steady encouragement have helped me to achieve my full potential. Their belief in me gave me the confidence to get where I am today.

Finally, I would like to give a big thank you to my husband Mashhour for his understanding, patience, valuable cooperation and willingness to present a shoulder to cry on whenever it needed. Another large thank you to my little man Abdulmalik; his laughter, enthusiasm, and true love have helped keep me on track during my PhD research. Thank you both.

Abstract

Most of the highly efficient polymer: fullerene bulk-heterojunction solar cells reported to date have been achieved by utilizing an inverted structure, where indium tin oxide (ITO) serves as a bottom cathode. Despite the advantages gained from applying such a structure, electron extraction at the ITO/organic layer is still one of the obstacles hindering effective charge collection. This is due to the unavoidable energetic mismatch existing between the ITO work function and fullerene LUMO energy level, which can limit commercial mass production using roll-to-roll processing.

This thesis describes the modification of the surface of ITO using many novel biomaterials that can be self-assembled into monolayers (SAM). These are non-toxic, water soluble, and hence providing a green alternative to standard modifying methods, with no need for aggressive chemical treatments. Using a combination of spectroscopic techniques and device characterization, it is shown that it is possible to achieve a large reduction of up to 1 eV in the ITO work function. The performance of modified inverted devices show significant sensitivities to the peptide backbone tail-group, post-deposition annealing temperature and donor polymers used within the active layer. Fabricated devices incorporating SAM exhibit improved efficiencies by 6 % compared to those of non-SAM.

Furthermore, after the successful fabrication of benchmark ITO-only inverted solar cells, the open circuit voltage is characterized in terms of the interface electronics of the cathode buffer layer. Two regimes are realized: a linear V_{oc} regime for work functions exceeding the fullerene LUMO energy level, and a constant V_{oc} regime for work functions lower than the LUMO level. It is necessary to overcome this threshold to realize high V_{oc}.

Publications

1) Rania Alqurashi, Jonathan Griffin, Abdullah Alsulami, Alastair Buckley. 'Open-circuit voltage in inverted polycarbazole: fullerene bulk heterojunction solar cells'. The IEEE Journal of Photovoltaics, 2016, 6, 918.

2) Abdullah Alsulami, Jonathan Griffin, Rania Alqurashi, Hunan Yi, Ahmad Iraqi, David Lidzey, and Alastair Buckley. 'Thermally stable solution processed vanadium oxide as a hole extraction layer in organic solar cells'. Materials, 2016, 9, 235.

Conference Contributions

Poster Presentations:

1) The Royal Society of Chemistry Annual Meeting, London, UK, January 2014
2) Hybrid and Organic Photovoltaics (HOPV15), Roma, Italy, May 2015
3) The 9th Saudi Students Conference, Birmingham, UK, February 2016

Oral Presentations:

1) UK Semiconductors Summer meeting 2015, Sheffield, UK, July 2015
2) EMN Meeting on Transparent Electrodes- Energy Materials and Nanotechnology, Orlando, Florida, USA, December 2016 - **Invited Speaker**

Table of Contents

Chapter 1

Introduction

1.1 Polymer Solar Cells

With increasing global awareness of the effects of carbon emissions on global warming, climate change, among other things, continuous efforts have been devoted to meeting the world’s demands for energy by shifting to lower carbon fuels using renewable sources. For last three successive years, the world energy consumption has been steady, growing by no more than 1 % [1], and in 2016, power gained from renewable sources (e.g. wind, solar, biofuel and waste, but excluding hydro) rose by 14.1 % (equivalent to 616.4 terawatt-hours) compared to 15.2 % (213 terawatt-hours) in 2015 [2]. The yield of renewable energy to global power production was 18 % in 2016 compared to 6.7 % in 2015 [1]. This increased yield has resulted from a significant reduction in coal consumption, by 1.7 %, as well as from advances in the technology of renewable energy. Among renewables sources, wind energy is still the leading source [1], whilst solar energy comes second accounting for only third of the total. It has been predicted, however, that renewable sources, including wind, wave and solar will be able to provide all global energy needs by 2030 [3].

Solar energy can be converted into electricity via a photovoltaic effect, where both voltage and electric current are created in a material upon exposure to sunlight. A photovoltaic cell (PV) is typically used to achieve this purpose. The simplest cell structure consists of a layer of optically absorbing material that is confined between two electrodes; one transparent and the other reflective. The sunlight enters the cell through the transparent electrode and is then absorbed by the confined layer, creating electron-hole pairs that are collected at the electrode interfaces when the cell is connected to an external load. Practically, numbers of these cells are connected together in arrays to form a photovoltaic panel that can be used in commercial and residential applications. This is done in order to magnify the output power, and hence increase the efficiency of the panel.

The efficiency of PV cells is restricted by the Shockley-Queisser limit [8]–[10]. This refers to the calculation of the maximum theoretical efficiency of a single p-n junction solar cell, which was first achieved by William Shockley and Hans Queisser [8]. By examining the amount of electrical energy that is extracted per incident photon, the maximum solar conversion efficiency is around 33.7%, assuming a single p-n junction with a band gap of 1.4 eV (using an AM 1.5 solar spectrum) [8]. Since the maximum efficiency is modelled as a function of the bandgap energy, there are a number of considerations. These include absorption restriction, recombination and solar spectrum losses. Light absorption is restricted by the bandgap of solar cell material, with only photons with energies equal to the bandgap being absorbed. This means that the whole solar spectrum cannot be harvested since photons with energies higher than the bandgap are converted into heat, reducing the output current. Recombination places an upper limit on the rate of electron-hole production and hence limits the output voltage.

There are various PV technologies available today in the market. PV cells based on inorganic semiconductors are the most efficient to date. A well-known and well-studied example of inorganic materials is silicon. The power conversion efficiency of single junction silicon solar cells has witnessed major improvements over the last 60 years, from 10 % in 1955 [4] to 24 % in 2014 [5]. The low band gap (1.1 eV) and high dielectric constant (~12) of silicon allow for efficient sunlight harvesting and excellent charge generation. Other existing inorganic materials are gallium arsenide (GaAs), indium phosphate (InP) and cadmium telluride (CdTe). PV panels based on these materials have achieved efficiencies of 29%, 22% and 21%, respectively [5]. Other combinations of III-V compounds, such as GaInP2/GaAs/Ge multi-junction cells, have shown maximum efficiencies of up to 32.3 % [6].

The efficiency is not the only feature by which PV panel manufacture is measured, however. Although, a breakthrough in the efficiency record of silicon solar cells was accomplished at a laboratory scale in 2016, with cells showing 35 % [7], the design of the developed cells rises some concerns in terms of scalability and production costs. This is because the cell design involves the incorporation of silicon solar cells with triple-junction solar cells. The complexity of this device architecture, and requirement for a thick absorbing layer are both necessary to overcome the Shockley-Queisser limit [8]–[10]. Other features, however, such as energy pay-back time, scarcity of materials, toxicity, cell thickness and weight should also be considered [11].

An alternative and promising technology is organic PV [12]. Unlike inorganic, organic materials are chemical compounds made of carbon atoms, facilitating solution processing onto various types of substrates such as glass, quartz and flexible substrates, and hence lowering the cost of fabrication [13]. This means that they are compatible for mass production using well-developed, inexpensive, and industrially available techniques like gravure printing, inkjet printing and spray coating [14], [15]. Unfortunately, the efficiency of organic PV currently lags far behind their inorganic competitors. Nonetheless, there is now extensive research towards developing new materials and novel device architectures.

Over the last two decades, significant and novel developments in respect to device structure have brightened the future of organic photovoltaics. The application of the bulk-heterojunction (BHJ) morphology of the absorbing layer, where n-type and p-type conducting organic materials are mixed together, introduces three different classes of BHJ solar cells dependent on the components of the active layer. These are polymer: polymer [16], polymer: fullerene [17] and small molecules [18] based BHJ solar cells. Among these, polymer: fullerene BHJ devices have an advantage in the form of the phenomenon of ultrafast photoinduced electron transfer [19] from the conducting polymer to fullerene molecules, increasing the rate of free charge generation. The efficiency of polymer: fullerene solar cells has reached a milestone by exceeding its theoretically predicted limit [20], due to the fruitful approach of inversing the device polarity [21], [22].

An inverted structure of BHJ solar cell applies the transparent indium tin oxide (ITO) electrode for electron collection rather than hole collection as would be the case for standard BHJ solar cells. This is beneficial in terms of increasing the lifetime of the device, enhancing air stability and durability [23], and ultimately improving cell outputs. A 10.31 % efficiency was realized for single-junction inverted polymer solar cells [22], with a lifetime of up to seven years reported in well-controlled laboratory conditions [24]. These achievements were seen at the laboratory scale, however, with several complicated chemical treatments and toxic materials applied within the device interlayer. Easier processing, and the use of environmentally friendly and efficient interface materials, is therefore the next target for cost effective roll-to-roll production.

1.2 Thesis Summary and Motivation

The aim of this thesis is to characterize the interface electronic structure of the ITO bottom electrodes used as electron extraction layers in inverted BHJ solar cells. The performance of solar cell devices with different ITO surfaces is correlated with the surface science determination of work function, surface dipole, Fermi levels, surface roughness and elemental composition using photoelectron spectroscopy. The surface electronic structure is varied by cleaning and pre-treatment techniques along with the addition of self-assembled monolayers. The goal is to further the understanding of BHJ performance and to find device architectures and materials systems that provide low cost, non-toxic and sustainable routes to solar cell mass production. A chapter-by-chapter summary of the work is given below:

Chapter 2 provides an overview of the background theory of conjugated polymers and the working principles of solar cells fabricated using these polymers.

Chapter 3 reviews the recent developments in cell architecture, the materials used within each device layer, and the methods to modify the interface of the bottom cathode electronic structure in inverted polymer solar cells.

Chapter 4 covers the procedures followed to fabricate inverted polymer solar cells, and discusses the performance measurements of these devices, along with the origins of the parameters affecting their performance.

Chapter 5 presents the analytical techniques used to characterize thin film surfaces and the theory related to each one. These include ultraviolet photoelectron spectroscopy, X-ray photoelectron spectroscopy, UV-vis absorption spectroscopy, and atomic force microscopy.

Chapter 6 is the first results chapter and forms the basis for the following chapters. It summarizes the optimal conditions for developing benchmark ITO-only inverted devices, as well as investigating the electronic structure of bare ITO cleaned with different methods. The results show that with careful control of the ITO surface chemistry, active layer processing and top anode layer thicknesses, it is possible to obtain efficient inverted devices without incorporating electron transporting layers.

Chapter 7 illustrates the relationship between the open circuit voltage and electronic structure of ITO cathodes studied for polycarbazole: fullerene based inverted devices. Comparisons against previously reported devices incorporating different electron transporting layers show the existence of a threshold work function, which is equal to the LUMO energy level of the fullerene material used. It is necessary to overcome this threshold in order to realize a high open circuit voltage. These results have been recently published in [25].

Chapter 8 provides detailed results in respect to both the device performance upon ITO modification with different peptide SAMs and the chemical structure of the modified surfaces. The results indicate that the intrinsic properties of the peptide materials can significantly affect the device parameters, as well as the ITO work function. The ultra-low work functions achieved with SAMs are seen to form non-Ohmic contacts at cathode interfaces, especially for polycarbazole-based devices, whereas significant improvements in device performance are seen for other BHJ donor polymer inverted devices. It should be noted that two of the examined peptide materials (Glut and Gly-Phe) are novel and have not yet been reported in the literature.

Chapter 9 concludes the current work and provides suggestions for further work. Overall, it has been discovered that biomaterial SAMs based on amino acid functional groups can be used successfully to modify the surface of ITO with no need for aggressive chemical pre-treatments. These materials provide environmentally friendly and low-cost alternatives for the existing SAM materials.

1.3 References

[1] British Petroleum, “BP Statistical Review of World Energy 2017,” *Nucl. Energy*, vol. June, 2017.

[2] B. Petroleum, “BP Statistical Review of World Energy 2016,” *BP Stat. Rev. World Energy*, no. June, pp. 1–48, 2016.

[3] M. Z. Jacobson and M. A. Delucchi, “Providing all global energy with wind, water, and solar power, Part I: Technologies, energy resources, quantities and areas of infrastructure, and materials,” *Energy Policy*, vol. 39, no. 3, pp. 1154–1169, 2011.

[4] B. P. Rand, J. Genoe, P. Heremans, and J. Poortmans, “Solar Cells Utilizing Small Molecular Weight Organic Semiconductors,” *Prog. Photovolt Res. Appl.*, vol. 15, no. February 2013, pp. 659–676, 2007.

[5] P. K. Nayak and D. Cahen, “Updated assessment of possibilities and limits for solar cells,” *Adv. Mater.*, vol. 26, no. 10, pp. 1622–1628, 2014.

[6] G. Ave, D. Friedman, T. Moriarty, and A. Duda, “32.3% efficient triple junction GaInP/sub 2//GaAs/Ge concentrator solar cells,” 2000.

[7] U. N. S. Wales, “Milestone in solar cell efficiency achieved: New record for unfocused sunlight edges closer to theoretic limits,” *Science Daily*, 2016. [Online].
Available: www.sciencedaily.com/releases/2016/05/160517121811.htm.

[8] W. Shockley and H. J. Queisser, “Detailed Balance Limit of Efficiency of p-n Junction Solar Cells,” *J. Appl. Phys.*, vol. 32, no. 3, p. 510, 1961.

[9] M. A. Green, “Third generation photovoltaics: Ultra-high conversion efficiency at low cost,” *Prog. Photovoltaics Res. Appl.*, vol. 9, no. 2, pp. 123–135, 2001.

[10] J. Nelson, *The Physics of Solar Cells*. London: Imperial College Press, 2003.

[11] J. Nelson, C. J. M. Emmott, P. T. R. S. A, J. Nelson, and C. J. M. Emmott, “Can solar power deliver ?,” *Philos. Trans. R. Soc. A*, vol. 371, p. 20120372, 2013.

[12] B. Kippelen and J.-L. Bredas, “Organic photovoltaics,” *Energy Environ. Sci.*, vol. 2, no. Copyright (C) 2011 American Chemical Society (ACS). All Rights

Reserved., pp. 251–261, 2009.

[13] C. J. M. Emmott, A. Urbina, and J. Nelson, “Environmental and economic assessment of ITO-free electrodes for organic solar cells,” *Sol. Energy Mater. Sol. Cells*, vol. 97, pp. 14–21, 2012.

[14] J. R. Sheats, “Manufacturing and commercialization issues in organic electronics,” *J. Mater. Res.*, vol. 19, no. 7, pp. 1974–1989, 2004.

[15] N. Espinosa, R. García-Valverde, A. Urbina, and F. C. Krebs, “A life cycle analysis of polymer solar cell modules prepared using roll-to-roll methods under ambient conditions,” *Sol. Energy Mater. Sol. Cells*, vol. 95, no. 5, pp. 1293–1302, 2011.

[16] D. Mori, H. Benten, I. Okada, H. Ohkita, and S. Ito, “Highly efficient charge-carrier generation and collection in polymer/polymer blend solar cells with a power conversion efficiency of 5.7%,” *Energy Environ. Sci.*, vol. 7, pp. 2–6, 2014.

[17] G. Dennler, M. C. Scharber, and C. J. Brabec, “Polymer-Fullerene Bulk-Heterojunction Solar Cells,” *Adv. Mater.*, vol. 21, no. 13, pp. 1323–1338, Apr. 2009.

[18] Y. Sun, G. C. Welch, W. L. Leong, C. J. Takacs, G. C. Bazan, and A. J. Heeger, “Solution-processed small-molecule solar cells with 6.7% efficiency,” *Nat. Mater.*, vol. 11, no. 1, pp. 44–48, 2011.

[19] C. J. Brabec, G. Zerza, G. Cerullo, S. De Silvestri, S. Luzzati, J. C. Hummelen, and S. Sariciftci, “Tracing photoinduced electron transfer process in conjugated polymer/fullerene bulk heterojunctions in real time,” *Chem. Phys. Lett.*, vol. 340, no. 3–4, pp. 232–236, Jun. 2001.

[20] M. C. Scharber, D. Mühlbacher, M. Koppe, P. Denk, C. Waldauf, a. J. Heeger, and C. J. Brabec, “Design Rules for Donors in Bulk-Heterojunction Solar Cells—Towards 10 % Energy-Conversion Efficiency,” *Adv. Mater.*, vol. 18, no. 6, pp. 789–794, Mar. 2006.

[21] S. Nam, J. Seo, S. Woo, W. H. Kim, H. Kim, D. D. C. Bradley, and Y. Kim, “Inverted polymer fullerene solar cells exceeding 10% efficiency with poly(2-ethyl-2-oxazoline) nanodots on electron-collecting buffer layers,” *Nat Commun*, vol. 6, pp. 1–9, 2015.

[22] S.-H. Liao, H.-J. Jhuo, P.-N. Yeh, Y.-S. Cheng, Y.-L. Li, Y.-H. Lee, S. Sharma, and S.-A. Chen, “Single Junction Inverted Polymer Solar Cell

Reaching Power Conversion Efficiency 10.31% by Employing Dual-Doped Zinc Oxide Nano-Film as Cathode Interlayer,” *Sci. Rep.*, vol. 4, p. 6813, Oct. 2014.

[23] P. Cheng and X. Zhan, “Stability of organic solar cells: challenges and strategies,” *Chem. Soc. Rev.*, vol. 45, pp. 2544–2582, 2016.

[24] C. H. Peters, I. T. Sachs-Quintana, J. P. Kastrop, S. Beaupré, M. Leclerc, and M. D. McGehee, “High efficiency polymer solar cells with long operating lifetimes,” *Adv. Energy Mater.*, vol. 1, no. 4, pp. 491–494, 2011.

[25] R. Alqurashi, J. Griffin, A. Alsulami, and A. Buckley, “Open-Circuit Voltage in Inverted Polycarbazole:Fullerene Bulk Heterojunction Solar Cells,” *IEEE J. Photovoltaics*, vol. 6, no. 4, pp. 918–923, 2016.

Chapter 2

Background Theory

2.1 Introduction

This chapter discusses the background theories of BHJ polymer solar cells. These include atomic and molecular orbital theory, orbital hybridization, conjugation and band formation. The optical and electronic characteristics of conjugated polymers are given. The photophysics of polymer solar cell devices, including exciton photogeneration, exciton dissociation, free charge transport and charge extraction are highlighted.

2.2 Atomic and Molecular Orbitals

Electrons present in an atom are said to be bound to the nucleus in orbitals, whose properties are determined by the uncertainty principle of quantum mechanics [1]. Unlike the classical orbits of physical bodies, therefore, the orbits of electrons are clouds of probable occupation, the shape and properties of which are determined by the values of four quantum numbers. These are: n, the principle quantum number, the potential energy of the electron; l, the magnitude of the angular momentum of the electron; m_l, the direction of the angular momentum; and m_s, the spin direction of the electron. The four quantum numbers that describe the orbits of electrons have integer values, except for m_s, the spin quantum number, which has a value of ±1/2. These numbers can be calculated using the set of inequalities outlined below.

$$n \geq 1$$ **Equation 2.1**

$$0 \leq l \leq n - 1$$ **Equation 2.2**

$$-l \leq m_l \leq l$$ **Equation 2.3**

$$-s \leq m_s \leq s$$ **Equation 2.4**

These inequalities can be used to calculate the values of the quantum numbers of any given orbital, and define its shape, as well as how many electrons it contains. An electron shell, however, is the set of allowed states that share the same principal quantum number, n (the number before the letter in the orbital label), that electrons may occupy. An atom's nth electron shell can accommodate $2n^2$ electrons, e.g. the first shell can accommodate 2 electrons, the second shell 8 electrons, and the third shell 18 electrons. The factor of two arises because the allowed states are doubled due to electron spin - each atomic orbital admits up to two otherwise identical electrons with opposite spin, one with a spin +1/2 (usually denoted by an up-arrow) and one with a spin −1/2 (with a down-arrow).

A subshell is the set of orbitals defined by a common azimuthal quantum number, l, within a shell. The values l = 0, 1, 2, 3 correspond to the s, p, d, and f labels, respectively. For example, the 3d subshell orbital has n = 3 and ℓ = 2. The maximum number of electrons that can be placed in a subshell orbital is given by 2(2ℓ+1). This gives two electrons in an s subshell, six electrons in a p subshell, ten electrons in a d subshell and fourteen electrons in an f subshell, following Pauli's Exclusion Principle [2].

Considering the 'particle-wave duality' property of electrons, there are two key features for an orbital, the spatial probability density of the electrons, known as the radial distribution because electrons are centred around the nucleus, and the shape of the orbital resulting from the angular distribution. The radial distribution is mostly dependent on the principle quantum number n, while the angular distribution depends on l and m_ℓ. **Table 2.1** shows the values of the four quantum numbers and total electrons in the first two atomic shells for simplicity. The first atomic shell ($n = 1$) contains only one subshell orbital, named the 1s orbital, which has two electrons corresponding to m_s values. S orbitals are wave functions with $l = 0$, hence having an angular distribution that is uniform at every angle. This means they are spheres [1], see **Figure 2.1 (a)**. Subsequent S orbitals, including 2s, 3s, 4s … etc., also have spherical symmetries with a maximum of two electrons.

The second atomic shell ($n = 2$) contains two subshell orbitals; 2s and 2p orbitals, with a total of eight electrons. The p orbitals are wave functions with $l = 1$ and a maximum of six electrons. They have an angular distribution that is not uniform at every angle with a shape that is best described as a 'dumbbell', as seen in **Figure 2.1 (b).** The dumbbell has one angular node (one angle at which the probability of an electron is always zero. Meanwhile, the radial probability distribution for a 2p (the probability of finding the electron at a particular radius) looks nearly identical to that for a 1s. The p orbital, however, is split into three sub-orbitals; $2\mathrm{p_x}, 2\mathrm{p_y},$ and $2\mathrm{p_z}$, one for each value of $m_l = -1, 0, +1$. Each sub-orbital is oriented into the direction of the orthogonal $x, y,$ and z-axes, respectively [1], and is occupied by two electrons (one for each value of m_s).

When $n = 3$, a new subshell orbital is introduced, making a total of three orbitals (s, p, and d) to satisfy the occupation of 18 electrons. This new orbital is known as the d orbital. The d orbitals have a value of $l = 2$ and are split into five sub-orbitals corresponding to their m_l values, allowing them to house a total of ten electrons. They have an even more complex angular distribution than the p orbitals, giving them their complex shapes. As n increases there are ever larger available ℓ numbers. These give even more complex angular distributions with more angular nodes. After the d orbitals l =2, come the f l =3, then g l =4, then h l =5.

Table 2.1: Values of the quantum numbers for the first two atomic shells, showing the names of subshell orbitals and the total number of electrons occupying each orbital.

Atomic Shell	**Quantum Numbers**				**Subshell Orbital**	**Total Electrons**
	n	l	m_l	m_s		
K	1	0	0	$+1/2$	1s	2
				$-1/2$		
L	2	0	0	$+1/2$	2s	2
				$-1/2$		
		1	-1	$+1/2$	$2p_x$	6
				$-1/2$		
			0	$+1/2$	$2p_y$	
				$-1/2$		
			1	$+1/2$	$2p_z$	
				$-1/2$		
				$-1/2$		

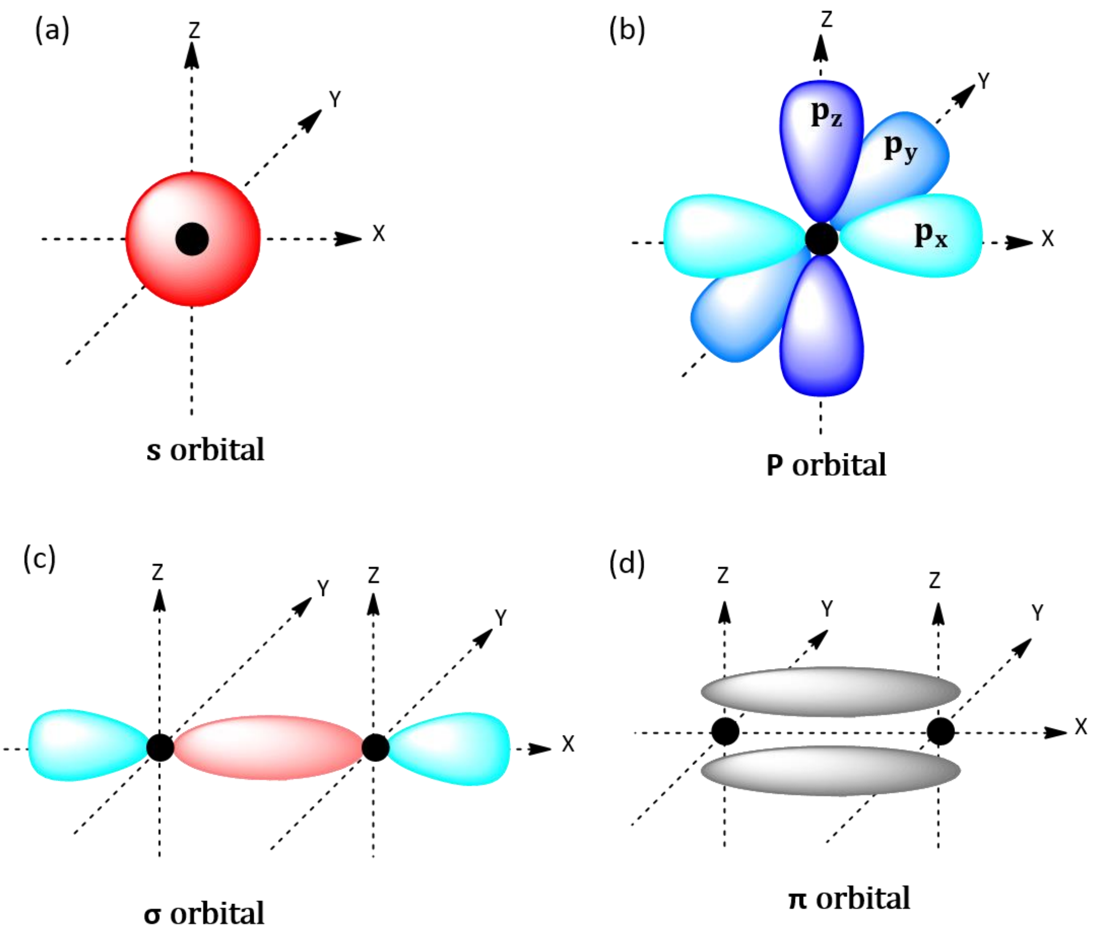

Figure 2.1 Schematic diagram of the shape and orientations of the atomic (a) 2s and (b) 2p orbitals, and the molecular (c) sigma (σ) and (d) pi (π) orbitals formed from the constructive overlap of two p_x orbitals and two p_z orbitals, respectively

A molecular orbital is formed when two atoms are brought together. This is similar to the idea of a chemical bond, where a pair of electrons are shared between two atoms. As the electrons are now equally likely to be found orbiting around atom number 1 as around atom number 2, the atomic orbitals of both atoms need to overlap, hence affecting the spatial distribution of the electrons. There are two types of molecular orbitals, depending on the spatial distribution of electrons; a sigma orbital (σ-orbital) and a pi orbital (π-orbital). The σ-orbital is formed if the spatial distribution of the electrons is centred around the axis joining the two atoms (**Figure 2.1 (c)**). The π-orbital is formed if the electrons are most likely to be found above and below the line connecting two atoms (**Figure 2.1 (d)**).

The overlap of atomic orbitals to form a molecular orbital is achieved by the overlap of electron wave functions. For example, a Hydrogen atom has a single electron orbiting around a proton with an electron configuration of $1s^1$. If two hydrogen atoms are brought close enough together, their atomic wave functions overlap and combine into molecular orbitals, creating a diatomic hydrogen molecule (H_2). Whenever a molecular orbital is created, the overlap of the original wave functions can be constructive or destructive, forming ‘bonding’ and ‘antibonding’ molecular orbitals, respectively, as seen in **Figure 2.2 (a)**. Bonding orbitals allow for an electron cloud to exist between the two nuclei, screening the repulsive force between them and hence producing a bound molecule [2]. The energy state of this orbital is therefore lower than that constituting unbound electrons due to the increased electron density between the nuclei: this can be considered as the equilibrated ground state. In contrast, the existence of electron density between the two nuclei is forbidden in antibonding orbitals, which reduces the shielding from the electron cloud. This leads to an unstable molecule that occupies a higher energy state than both the bonding orbital and the constituent atomic orbitals [2]. The corresponding energy levels of the bonding and anti-bonding molecular orbitals are showed in **Figure 2.2 (b)**. Note that a single σ bond is formed in the H_2, and hence its energy level diagram represents the σ-bonding and σ*-antibonding energy levels, as will be discussed later.

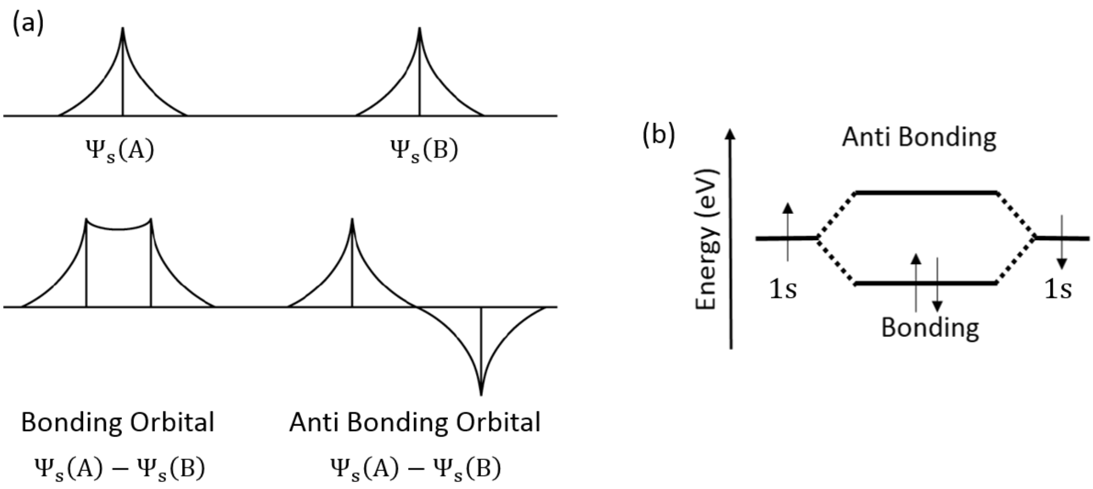

Figure 2.2 (a) Combination of two atomic wave functions to create bonding and anti-bonding molecular orbitals. (b) The energy levels of the molecular orbitals compared to unbounded atomic orbitals (representing σ-bonding and σ*-antibonding energy levels).

2.3 Orbital Hybridization

Orbital hybridization describes the mixture of atomic orbitals, allowing for an atom to combine with another atom with different electronic configuration. This is particularly important in organic materials whose backbone consists of carbon atoms bonded to hydrogen, oxygen and others. Carbon has six electrons adopting a configuration of $1s^2, 2s^2, 2p_x^1, 2p_y^1, 2p_z^0$. This configuration offers four valence electrons to form covalent bonds since the 1s orbital is not involved in any bonding. Note that the 2s orbital is fully occupied by two electrons that cannot principally form any bonds. To overcome this, orbital hybridization takes place in practice, allowing for the carbon atom to have four unpaired electrons. This involves the promotion of one of the 2s electrons to the empty $2p_z$ orbital, and then the formation of a new hybrid orbital (sp) as shown in **Figure 2.3**. The hybrid orbital has an energy state lying between the constituent 2s and 2p orbitals. The promoted carbon can hence bind to four hydrogen atoms, for example to form a methane molecule (CH_4).

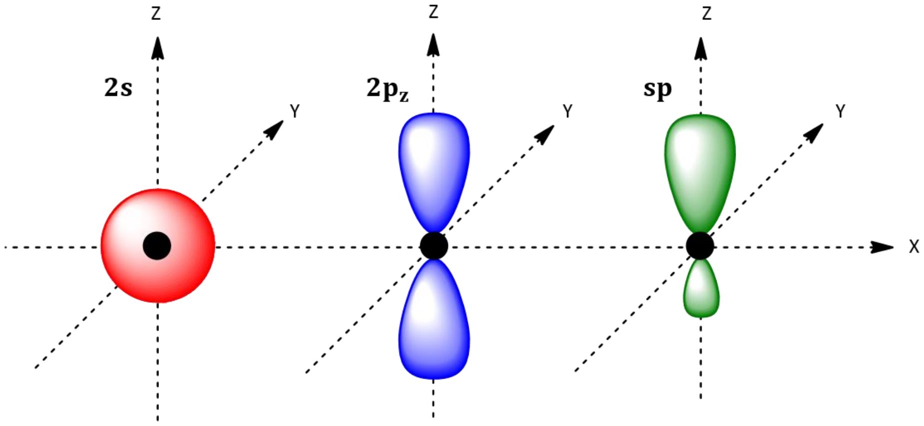

Figure 2.3 Hybridization of a 2s and a 2p orbital to form a hybrid sp orbital.

The characteristic of the hybrid sp orbital depends on the number of 2p orbitals undergoing the hybridization. There are therefore three possibilities of orbital hybridization: sp^1, sp^2, and sp^3. **Figure 2.4** shows these three possible hybridizations. In sp^1 hybridization, the 2s orbital is mixed with one of the three 2p orbitals, forming 2sp orbitals oriented perpendicularly with respect to the remaining two unhybridized 2p orbitals. For sp^2 hybridization, the mixture of the 2s orbital with two of the three 2p orbitals results in the formation of 3sp orbitals. The 3sp orbitals are arranged in a planar configuration with bond angles of 120° while the remaining unhybridized $2p_z$ orbital is perpendicular to this plane. Additionally, mixing the full three 2p orbitals with the 2s orbital is known as the sp^3 hybridization. This produces four non-overlapping sp orbitals directed to the corner of a tetrahedron.

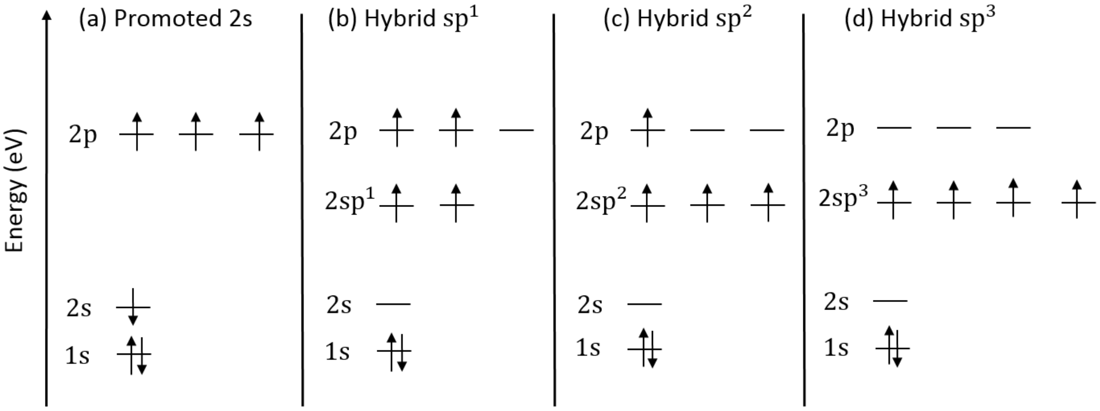

Figure 2.4 Orbital hybridization possibilities of a promoted carbon atom.

Bonding between two sp^2 hybridised carbon atoms can occur in one of two ways; sigma bonding (σ) occurs when two sp^2 orbitals form a covalent bond, and pi bonding (π) occurs when the remaining unhybridized 2pz orbitals overlap and form a much weaker bond that exists in a plane parallel to the σ bond. Carbon atoms that have only formed a σ bond are said to have formed a C-C single bond, and those that form π bonds in addition to the σ bond are said to have formed a C=C double bond.

To better understand how σ and π bonds are formed, consider the arrangement of electrons in molecular orbitals like those formed in ethene [3]. An ethene molecule is formed by bonding two sp^2 hybridised carbon atoms with four hydrogen atoms. Considering the carbon-carbon interaction, the energy level diagram is shown in **Figure 2.5**. The carbon 1s orbitals each contribute two electrons, giving a total of four electrons that accommodate in the σ-bonding and σ*-antibonding orbitals. The three $2sp^2$ hybrid orbitals on each carbon have three single electrons each. When these combine with the electron from the other carbon's $2sp^2$, the pair will fill the low-lying σ-bonding orbital, leaving the σ*-antibonding orbital empty at high energy. As a result, a strong net attractive interaction between the two nucleuses is obtained, allowing for σ-bonds to hold the molecule together. The remaining electron on each carbon's 2pz orbital accommodates the π orbital, leaving the π* orbital empty. In contrast to the σ orbital, meanwhile, the π orbital contributes very little to the net attractive attraction. Consequently, the spatial separation between π and π* orbitals is lower than those between σ and σ* orbitals. Thus, the potential energy of placing two electrons in the molecular π orbital is comparably lower than that needed if they were placed in the atomic pz orbital. It can see from **Figure 2.5**, however, that the highest occupied molecular orbital (HOMO) is the π orbital. The next highest orbital is π* orbital, which is empty, and is the lowest unoccupied molecular orbital (LUMO).

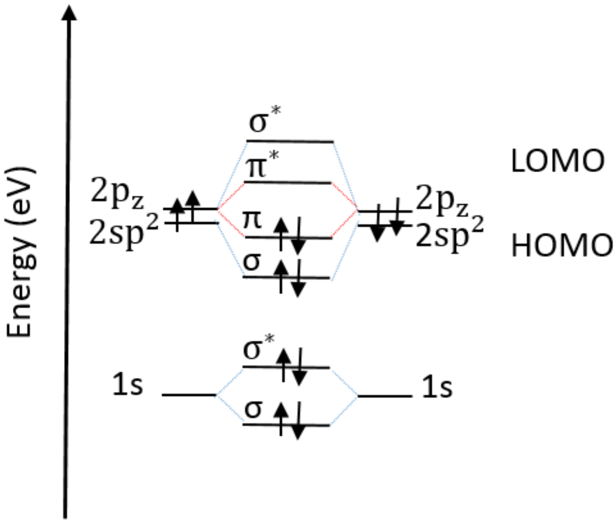

Figure 2.5 Simple energy level diagram showing the formation of σ and π bonds from atomic orbitals for ethene. Only orbitals involved in the carbon-carbon interaction are shown, with the ones involved in carbon-hydrogen interaction being omitted for simplicity. HOMO describes the highest occupied molecular orbital, that is the π orbital, while LUMO describes the lowest unoccupied molecular orbital, that is the π* orbital.

2.4 Conjugation and Band Formation

Carbon-carbon chains form the backbone of many polymers, and a polymer is said to be conjugated when there are alternating single and double bonds along a carbon chain. A common example of an alternating single-double carbon bond structure is benzene, shown in **Figure 2.6**. Benzene is a ring of six carbon atoms that are covalently bonded with sp2 hybridised orbitals and alternating single-double carbon bonds [1]. The positioning of the double bonds in benzene makes no difference to the material's properties and so benzene 1 and 2 are equivalent. The alternating single and double bonds result in the weakly bound electrons in the π bonds of the double bonded carbon atoms becoming delocalised over the benzene ring, leading to an equal probability of these electrons being found anywhere in the benzene ring.

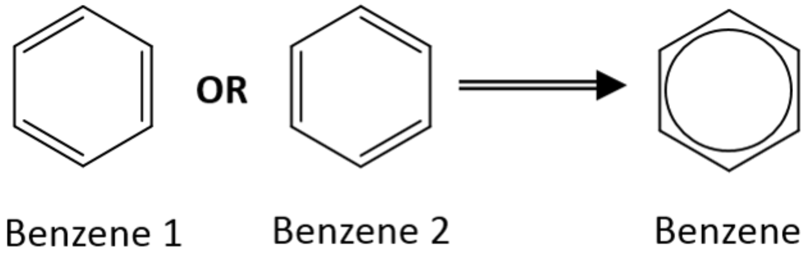

Figure 2.6 Benzene structures with alternating single-double bonds. A benzene ring is formed as an indication to the delocalization of π-electrons anywhere around the chain due to the equivalence of benzene 1 and benzene 2.

In the case of a conjugated polymer, a polymer segment (or molecule) is made of a number of sp^2 hybridised carbon atoms connected together to form a long chain. As the molecule will have alternating single and double carbon bonds, the delocalization of π-electrons along the polymer chain contributes to the formation of its energy bands, known as frontier orbitals. Frontier orbitals are formed from the block of filled orbitals ending with the HOMO and the sequence of unfilled ones starting with the LUMO, as seen in **Figure 2.7**. This is what gives conjugated polymers their semiconducting properties. Adding electrons to the empty LUMO, or removing electrons from the filled HOMO (corresponding to injection of holes) can change the electronic structure, as will be discussed in the following section. The HOMO and LUMO levels of semiconducting polymers can be compared to the valence and conduction bands in inorganic semiconductors, and the difference between the HOMO and LUMO energy levels is defined as the material's energy gap. These energy levels are not only affected by the individual atoms but also by the surrounding environment due to other electronic interactions [4]. Within tightly packed amorphous films, conjugated polymer energy levels are shifted due to a property known as energetic disorder [4], [5], although this effect is reduced in more ordered and crystalline materials.

Varying the components of a conjugated polymer chain can affect the HOMO and LUMO levels of the material, which can be utilised to tune the energy gap of the material and its charge transport properties. Polymers used for OPV applications tend to have an electron 'donor' component that is electron rich, and an electron 'accepting' component that is electron poor. Changing these components, or even just individual atoms, can affect these electron rich or poor areas, resulting in modified energy levels [6], [7].

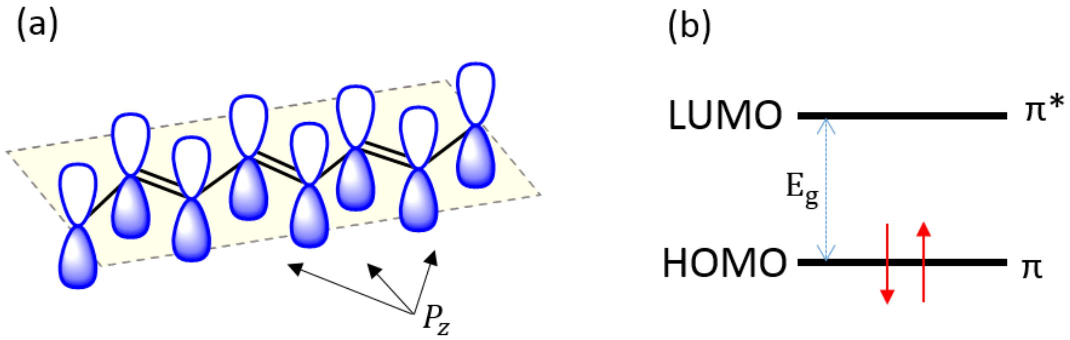

Figure 2.7 (a) a conjugated backbone with overlapping p_z orbitals that point out of the molecular plane. (b) Highest occupied and lowest unoccupied molecular orbitals (HOMO and LUMO), respectively. Arrows denote two electrons occupying the HOMO level with different spins. The energetic difference between the HOMO and LUMO level is equal to the band gap energy (Eg).

2.5 Photophysics of Polymer Solar Cells

Unlike in inorganic semiconductors, light absorption in organic semiconductors is not a straightforward process. Free charges are not photo-generated in one process, due to the relatively low dielectric constant of conjugated polymers, hence the electron-related interactions become significant. Five steps are required in order to deliver free charges in a polymer solar cells; exciton generation, exciton diffusion, exciton separation, free charge transport, and charge extraction at electrode interfaces, as will be discussed here in detail.

2.5.1 Exciton Photogeneration

Considering the picture of a molecule with one-electron orbitals, the configuration of frontier orbitals, as seen earlier in **Figure 2.7**, is said to describe its ground state. This is because the molecule has the lowest possible energy. The ground state is therefore known as the singlet energy state (S_0). Once light is absorbed by the molecule, an electron is promoted from the HOMO level to the LUMO level, leaving a “hole” in the HOMO level, forming a first singlet excited state (S_1). This "hole" can be considered as a particle having a charge equal and opposite to that of the electron. The electron-hole pair is coulombically bound with a neutral net charge and is referred to as a singlet exciton. This is because the configuration of singlet exciton involves having one electron in the HOMO and one in the LUMO with an anti-parallel spin. **Figure 2.8** shows the one-electron picture for singlet exciton formation.

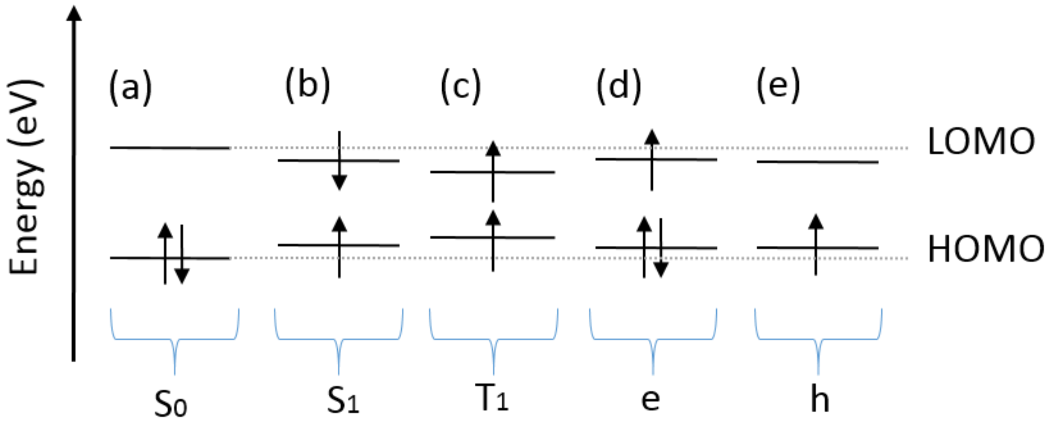

Figure 2.8 Electronic states of a conjugated polymer showing the one-electron orbital energies for the dominant configuration. (a) ground-state (S_0), (b) first excited singlet state (S_1), (c) first excited triplet state (T_1), (d) negative polaron (e), and (e) positive polaron (h). The arrows indicate the electron spin, the horizontal grey line is a guide to the eye.

A phonon is a quantised mode of vibrational energy created by oscillations in a lattice. Unlike in inorganic materials, electron-phonon interactions in organic semiconductors are comparable in strength to electronic interactions [4]. The electron interaction with a phonon can be considered as a quasi-particle called an electron-polaron. As seen in **Figure 2.8 (c and d)**, two charged states – negative or positive polarons – can be created by the addition of an electron to the LUMO or the subtraction of an electron from the HOMO, respectively. Polaron entities include the charge and reorganization energy of the surrounding molecular structure. When an electron in a conjugated polymer enters an excited state, the surrounding molecular structure undergoes a relaxation. This relaxation in the surrounding bonds acts to lower the energy of the system, and thus the LUMO level is reduced. The presence of a hole in the HOMO level also causes a deformation in the polymer chain, creating a hole-polaron and reducing the depth of the HOMO energy.

Triplet excitons (**Figure 2.8 (e)**) cannot be directly generated by the absorption of a photon in organic semiconductors due to symmetry considerations of p orbitals. Thus the assistance of spin–orbit coupling and/or electron–phonon interaction are required to enable transitions such as intersystem crossing, non-radiative transitions, and phosphorescence [11]. Organic semiconductors are composed of lightweight atoms such as carbon, hydrogen, oxygen, nitrogen and sulphur that do not show strong spin–orbit coupling. Consequently, the transitions between excitonic states of different spin multiplicities are normally not efficient in this class of materials. The lifetime of a triplet in organic semiconductors is therefore usually about six orders of magnitude longer than that of singlets. The energy that is carried by a triplet exciton is usually 0.7 eV below that of a singlet in a π system [12]. The work needed to separate the electron and the hole of an exciton is called the binding energy and is usually of the order of 0.3–0.5 eV for singlet excitons [13]–[15]. The binding energy of triplets is higher due to the attractive exchange interaction between electrons and holes with the same spin orientation [12].

The singlet ground and excited states are shown in **Figure 2.9**, based on the Frank-Condon principle. Singlet states are electronic states with a net spin of zero, while those with a net spin of one are called triplets. These singlet states contain several quantised vibrational modes (n) which form a ladder of states [8]. If the ground and excited state are labelled as S_0 and S_1 respectively, then these vibrational modes can be labelled as $S_{0,n}$ and $S_{1,n}$. A ground state electronic transition occurs when a photon with energy equal to or greater than the band gap energy is absorbed by the S_0 state, promoting the molecule to the S_1 state. Since this photoexcitation transition occurs on a shorter timescale than the motion of the nuclei, it can be considered to be stationary, and the transition is depicted by a vertical line in the energy level diagram (Born-Oppenheimer approximation).

Should the absorbed photon have a very high excess of energy compared to that of the energy gap, the electron is promoted to one of the S_1 high-vibrational modes (like $S_{1,2}$). The generated exciton then quickly relaxes via a non-radiative decay process to the lowest vibrational mode of the excited singlet state ($S_{1,0}$) (over timescales of ~ 0.1 ps [8]). Then, it will decay radiatively to one of the S_0 vibrational states in a process called fluorescence [9]. This decay occurs on the timescale of 100 to 1000 ps, a much longer period than that of the vibrational relaxation. This difference in timescales means that the decay to one of the S_0 states will occur from the $S_{1,0}$ state, regardless of the initial photon energy. Conversion between singlet states can occur if the wave functions of vibrational modes overlap. An example of this is shown using the $S_{1,0}$ and $S_{0,2}$ states in **Figure 2.9**. In this case, the higher the energy of the ground state vibrational mode ($S_{0,2}$), the lower the energy of the photon emitted during fluorescence (radiative decay).

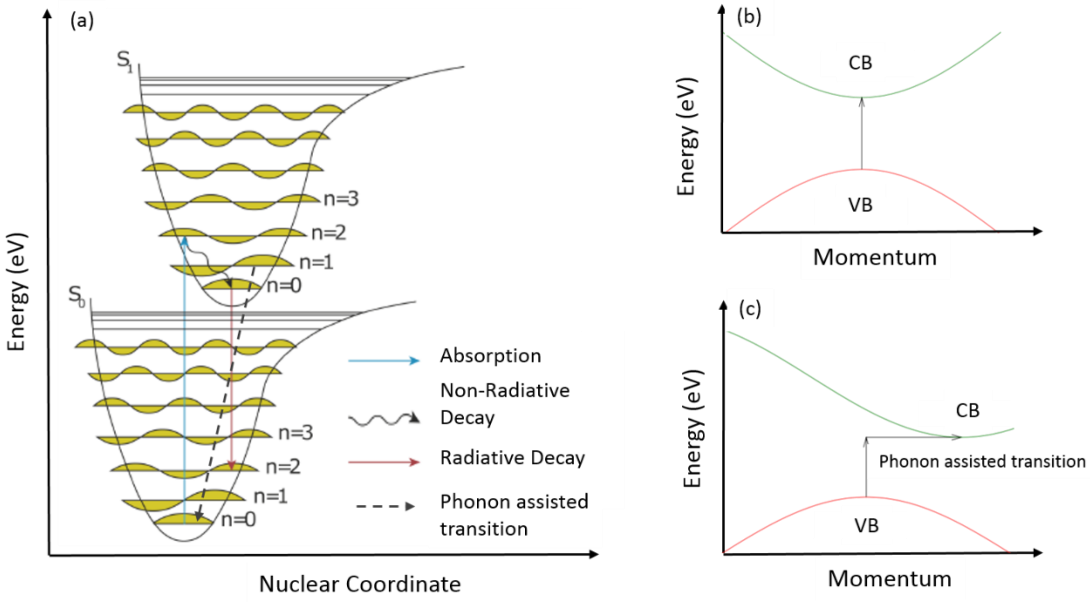

Figure 2.9 (a) Franck-Condon energy diagram for S_0 and S_1 energy states with absorption, non-radiative and radiative decays, and phonon assisted transition. (b) Energy diagram for a semiconductor with a direct band gap, showing that an electron can shift from the highest-energy state in the valence band (VB, red) to the lowest-energy state in the conduction band (CB, green) without a change in crystal momentum. A transition in which a photon excites an electron from the VB to the CB is depicted. (c) Energy diagram for a semiconductor with an indirect band gap, showing that an electron cannot shift from the highest-energy state in the VB to the lowest-energy state in the CB. Here, almost all of the energy comes from a photon (vertical arrow), while almost all of the momentum comes from a phonon (horizontal arrow). This is similar to the diagonal transition in (a).

2.5.2 *Exciton Dissociation*

The Coulombic attraction between the electron and hole is given by

$$V = \frac{q^2}{4\pi\varepsilon_r\varepsilon_0 r}$$ **Equation 2.5**

where q is the elementary charge of the electron, ε_r is the dielectric constant of the medium, ε_0 is the permittivity of free space, and r is the distance between charges. For a conjugated polymer, the dielectric constant is considered to be small ($\varepsilon_r \approx 3 - 4$) compared to that of a traditional silicon semiconductor ($\varepsilon_r \approx 12$) [13]. Having a low dielectric constant leads to an increase in the Columbic attraction within the pair itself, lowering the effectiveness of charge shielding, and so maintaining a binding energy higher than $\mathrm{k_B T}$. The exciton cannot, therefore, be dissociated by thermal means alone. This bound pair is known as a Frenkel exciton.

The Frenkel exciton requires a driving force to dissociate into free charges, which can be introduced by one of three different approaches; an interface of two materials of differing electron affinities, an electric field, or trap induced impurities. In a polymer solar cell, exciton dissociation at a donor-acceptor interface is considered to be an efficient approach and mainly depends on the morphology of the active layer. The photogenerated electron-hole pairs, however, must first diffuse to this energetically favourable interface before being dissociated. The distance that the exciton can travel is called the diffusion length (L_D) is calculated in **Equation 2.6** by the diffusion coefficient (D) and the photoluminescence decay lifetime (τ) [16], [17].

$$L_D = \sqrt{D\tau}$$ **Equation 2.6**

The typical diffusion length within conjugated polymers is found to be in the order of 10 nm, due to the short lifetime of Frenkel excitons [18]. The donor-acceptor interface should thus overcome this limit if exciton recombination is to be prevented. The details of the unique features of the donor-acceptor interfaces will be discussed later in **Chapter 3**, **Section 3.2.**

Dissociation is the process of separating the electron-hole pairs into free charges, which can happen at three sequential steps, as shown in **Figure 2.10**. The exciton diffuses firstly to the donor-acceptor interface that is energetically favourable (**Figure 2.10 (a)**) [14]. An appropriate interface requires the donor LUMO and HOMO levels to be at higher energies than the acceptor LUMO and HOMO levels, respectively. If the energy offset (ΔE) between the LUMO-LUMO levels overcomes the binding energy of the exciton (0.3 eV) [15], [19], the exciton can be transferred across the interface. The energetic driving force generated by ΔE dissociates the exciton into a geminate pair, wherein the electron hops from the donor to the acceptor LUMO levels via charge transfer states (CT) [20], and the hole remains at the donor HOMO level (**Figure 2.10 (b)**). Despite the spatial separation of the geminate pair, the electron and hole are still bound, and so recombination is likely to occur. A sufficient internal electric field is therefore required to overcome the Columbic attraction and further separate the pair into two free charges (**Figure 2.10 (c)**). The free charges are then transported through the donor-acceptor layer to their respective electrodes, wherein free electrons are transported via acceptor domains to a cathode electrode and holes are transported via donor domains to an anode electrode.

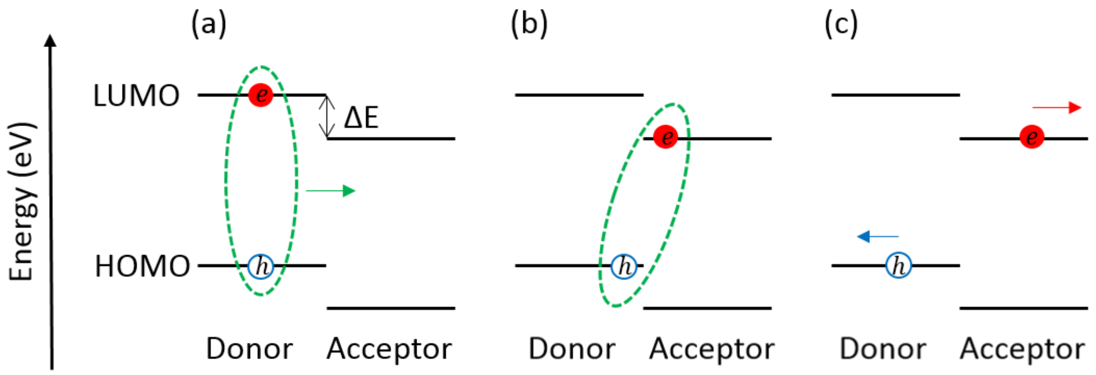

Figure 2.10 Illustration of the process of generating free charges; (a) Photoexcitation of an exciton that diffuses to the donor-acceptor interface, (b) Electron transfer to the acceptor LUMO level through Charge Transfer (CT) states, and (c) Full dissociation into two free charges driven by an internal electric field and transport to their prospective electrodes.

2.5.3 Charge Transport

Charge transport occurs ultimately once the exciton is fully dissociated into free charges. The free charges are then transported through the donor and acceptor domains to the electrodes for extraction. This process is assumed to be energetically driven with a dominant mechanism known as ‘hopping’ [21]: the charge carriers hop between the molecular states by tunnelling from one site to the next through a potential barrier separating the two sites. The differences in the energy and location of the two sites determine the barrier energy and the probability of tunnelling taking place. Meanwhile, the probability of hopping taking place is determined by the physical and energetic differences of the two adjacent states. Several parameters have significant influences on hopping transport, such as temperature, the energy differences of the hopping site and the distance between these sites [22], [23]. Importantly, energetic disorder plays a notable role in reducing charge transport. Energetic disorder refers to the variation in the energy of similar states that is introduced by structural disorder [20]. The hopping rate between these localized states is what determines the charge mobility in the conjugated polymers. To enhance the charge carrier mobility, therefore, the distance between hopping sites and the degree of energetic disorder should be reduced [24]–[26].

2.5.4 Charge Extraction

Upon exciton dissociation, separation and transport through the active layer, charge extraction may take place at the electrical contacts. The efficiency of this process is dependent on the work function (WF) of the contact materials matching the energy levels of the donor-acceptor materials, allowing for charge transport across the interface. In an ideal situation, the device electrodes should follow the rules below:

$$\phi_{Cathode} = (E_{LUMO})_{Acceptor}$$ **Equation 2.7**

$$\phi_{Anode} = (E_{HOMO})_{Donor}$$ **Equation 2.8**

Here, the WF of the anode is matched to the energy of the HOMO level of the donor for the extraction of holes, and the WF of the cathode is matched to the energy of the LUMO level of the acceptor for extraction of electrons. These interfaces, when matched in energy in such a way, are known as ohmic contacts.

The interfaces in OPVs are rarely so simple, however, due to the wide variety of materials used. Metal oxides have both valence and conduction bands, and a Fermi level in the energy gap. When initially comparing materials against one another the vacuum level is aligned, as shown in **Figure 2.11**, but this depiction of energy levels only holds true when the materials are not in electrical contact with one another. When materials are brought into electrical contact, Fermi level alignment can occur under certain conditions, where the Fermi levels of the two materials equalize [27]. It is this Fermi level alignment that allows for efficient charge transfer across such interfaces.

The simplest example of Fermi level alignment is the metal-metal interface, as shown in **Figure 2.11 (a)**. In this instance, electrons flow from the metal with the highest WF to the lower WF metal. For metal-organic contacts, the transfer of charges across the interface can be described by the integer charge-transfer model. This model assumes that metal/organic interfaces are passivated by oxides or residual hydrocarbons, which block the formation of interface dipoles. Electron transfer can still occur via tunnelling through this passivating layer, however, as long as the layer is thin enough [28]. The Fermi levels can align in one of two ways, however; if the WF of the metal is equal to or lower than the upper critical Fermi level (Φ_P) level of the organic material, LUMO alignment occurs, while if the WF of the metal is equal to or higher than the lower critical Fermi level (Φ_N) of the organic material, HOMO alignment occurs; shown in **Figure 2.11 (b), (c)** respectively. If the WF of the metal is between these two values then the Fermi levels will not align and the materials will remain vacuum level aligned [29].

Energy level alignment at interfaces is critical to device performance, as poor alignment can lead to charge transfer losses due to barriers forming that inhibit extraction [30]. Ohmic contacts form when there is no barrier to extraction due to well aligned energy levels, and Schottky-Mott contacts are formed when there is an energy barrier present [29]. Charge transfer can still occur in Schottky-Mott contacts, but at the cost of device efficiency resulting from an increase in device series resistance [10]. The dependence of the metal/organic contact on the electrode work function is seen in **Figure 2.12,** where an Ohmic contact is formed if the electrode WF is lower (higher) than Φ_P (Φ_N), and a Schottky-Mott contact is formed if $\Phi_P < WF < \Phi_N$.

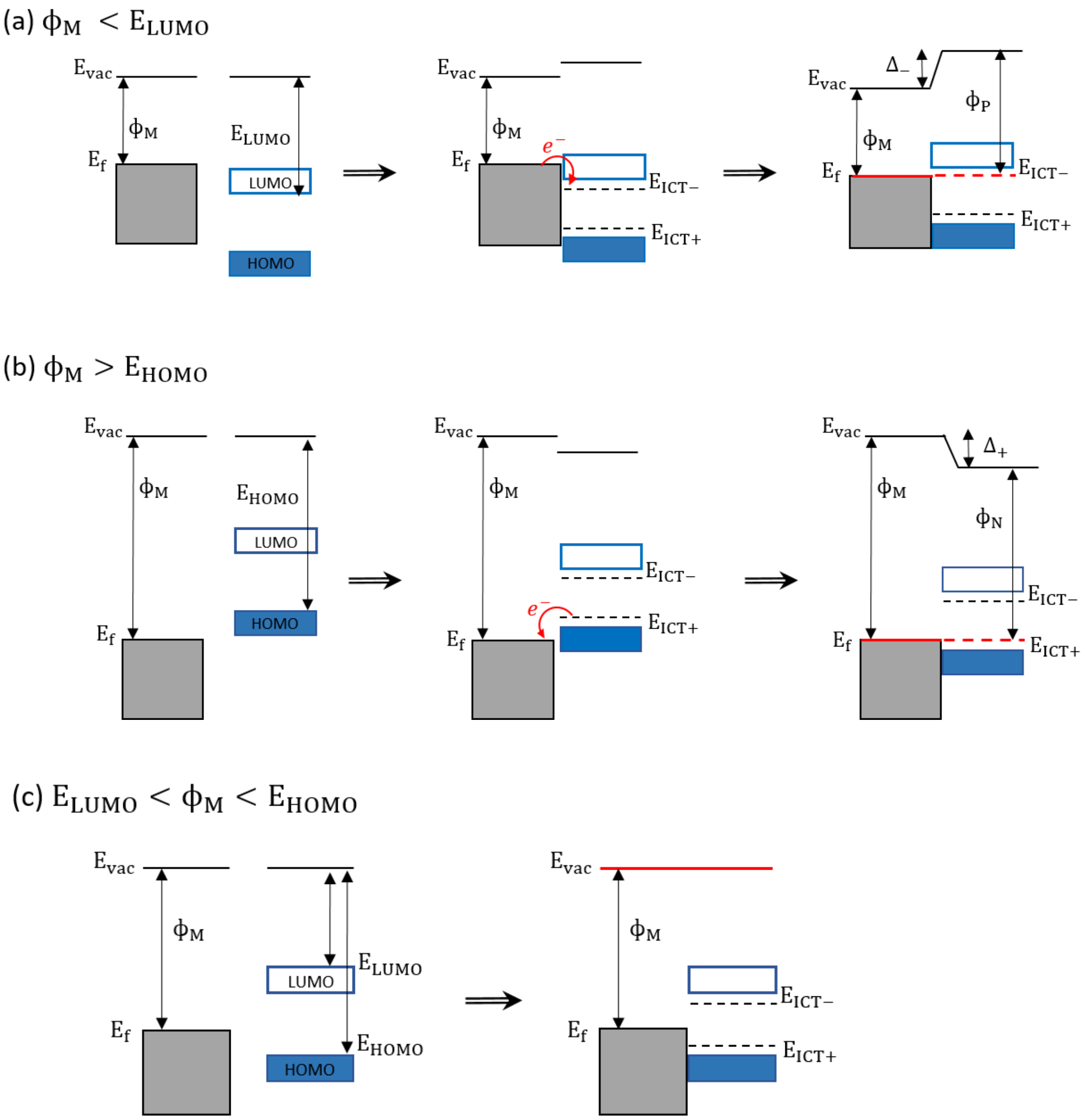

Figure 2.11 Energy level alignment at metal-organic interfaces before and after contact, and based on the integer charge transfer (ICT) model. (a) Fermi-LUMO alignment for electron extraction. (b) Fermi-HOMO alignment for hole extraction. (c) Vacuum level alignment with no charge transfer. ϕ_M is the work function of the metal electrode, ϕ_P is the upper critical Fermi level, ϕ_N is the lower critical Fermi level, and Δ is the potential energy of the interfacial dipole.

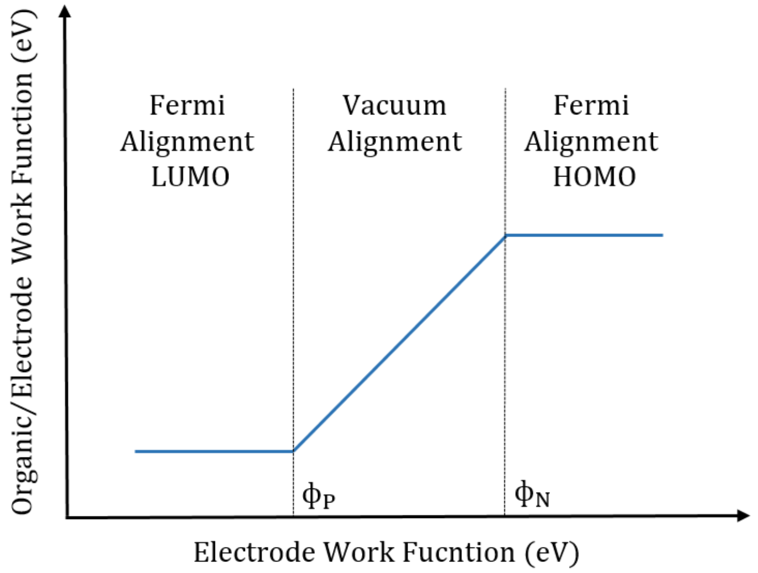

Figure 2.12 Relation of interfacial energy alignment to the electrode work function as a function of the organic/electrode work functions.

2.6 Open Circuit Voltage and Quasi Fermi Levels

The open circuit voltage (V_{oc}) is derived from the splitting of hole and electron quasi-Fermi levels, as seen in the Shockley-Queisser theory (**Chapter 1**). For perfect silicon p-n junction solar cells, the valence and conduction bands of p-type and n-type silicon are the same before they come into contact with each other. Although their Fermi levels are in different positions due to the different dopant types, the Fermi level of the p-type is close to the valence band for conducting holes, and that of the n-type is close to the conduction band for conducting electrons. Once both materials are brought together, redistribution of electrons and holes across the p-n junction produces a built-in potential. Under equilibrium, the two currents are equivalent and there is no net current flow inside the junction. The Fermi levels of the two silicon semiconductors are now the same. When the cell is illuminated, however, photogenerated excitons are immediately thermally dissociated into free electrons and holes. They then drift in opposite directions under the force of the built- in potential. The potential of the p side increases and the n side decreases, generating a so-called photo-voltage, which plays a role in cancelling out the built-in potential. Under open circuit conditions, their potentials eventually equal each other, and the system reaches a quasi-equilibrium state. The photo-voltage now is V_{oc} and approximately equal to the band gap, as in **Equation 2.9**, where q is the elementary charge, $E_{F,e}$ is the quasi Fermi level for electrons, and $E_{F,h}$ is the quasi Fermi level for holes.

$$qV_{oc} = E_{F,e} - E_{F,h}$$ **Equation 2.9**

A similar principle is applicable in the case of organic solar cells with respect to two considerations. First, V_{oc} has been found to be linearly related to the difference between the highest occupied molecular orbital (HOMO) level of the donor material and the lowest unoccupied molecular orbital (LUMO) level of the acceptor material. An empirical equation to express V_{oc} has been proposed by Scharber et al. [15], see **Equation 2.10** below. Where q is the elementary charge, $E_{D,HOMO}$ and $E_{A,LUMO}$ are the energies of the corresponding HOMO and LUMO energy levels of the donor and acceptor materials respectively, ΔV is usually an empirical term obtained by averaging over many materials. The second consideration is that disorder in organic materials plays a role in bringing the electron quasi-Fermi level down from the LUMO level of the acceptor, and lifting the hole quasi-Fermi level up from the HOMO level of the donor, and hence ultimately reducing V_{oc}.

$$qV_{oc} = (E_{D,HOMO} - E_{A,LUMO}) - \Delta V$$ **Equation 2.10**

While empirical predictions based on **Equation 2.10** have proven very useful and are relatively simple to make, it should be noted that such predictions typically deviate from measured V_{oc} values by over 100 mV [9]. A number of reasons have been suggested to figure out the source of this deviation. It could be related to the influence of dark current and field driven photocurrents [15] or the binding energy of the separated Frankel exciton [31], or the radiative and non-radiative temperature dependent losses [32]. Taking into account, however, that many models (e.g. the S-Q theory for perfect inorganics) make an assumption regarding how close the quasi Fermi levels can approach the band edges (or CT-state energies at donor/acceptor interfaces [33]), treating the difference (ΔV) as fixed, Durrant et al. [34], [35] argued that the ΔV depends on the materials system in question and varies according to the severity of recombination. Hence, blend optimization can be considered partly as a process of extending carrier lifetimes sufficiently that significant recombination losses are pushed to higher carrier densities and therefore higher cell voltages. [36], [37].

2.7 Properties of Indium Tin Oxide (ITO)

Currently, tin doped indium oxide (ITO) thin films are the primary transparent conducting oxide electrode utilized in organic thin-layer devices such as organic light emitting diodes (OLEDs) [38], organic photovoltaic devices (OPVs) [39], and others

[40]. Devices of this type generally require a large optical gap and operate at relatively high current densities, and consequently require high rates of charge injection to achieve satisfactory device performance. In this capacity, ITO surpasses other known TCO materials by providing a better combination of conductivity, optical transmission, and ease of processing through various techniques [38], [41]–[43].

ITO is a wide-gap, degenerate semiconductor where electrons are the major charge carriers. It composes a ternary composition of indium, tin and oxygen in varying proportions. A thin film of ITO is typically deposited from a mixture having 90% indium oxide (In2O3) and 10% tin oxide (SnO) in concentration. The basic crystal structure of most commercially available ITO is a cubic, C-type, rare-earth sesquioxide of In2O3 referred to as bixbyite [44]. The Sn atoms are considered to substitute for In, without ordering. The difference of valence between In^{3+} and Sn^{4+} results in the donation of a free electron to the lattice [45]. ITO thin films therefore exhibit high electrical conductivity (up to10^4 $\Omega^{-1}.cm^{-1}$).

The conductivity of ITO is special because while most conductive materials are opaque ITO is transparent. This is because the band gap of ITO is ~3.5 eV, and hence visible photon (energy of 1.8-3.0 eV) has not enough energy to excite electrons into higher energy state. Depending on the thickness, the transmission of ITO varies in the visible region between 80-90% throughout the band and exhibits a refractive index of approximately 2.0 throughout the visible range [46]. It also shows high infrared reflectivity for wavelengths higher than 1 μm [47].

2.8 Device Characterization

The principle metrics for device characteristics are achieved by analysing a current-voltage (J-V) curve. This is obtained by illuminating the device under simulated solar radiation, most often simulated AM1.5 solar spectrum (**Figure 2.13**), while applying a voltage sweep. Exciton generation, diffusion, disassociation and extraction will occur within a working device. The power conversion efficiency (PCE) of the device is an indication of the success of these processes. Here, device parameters including the power conversion efficiency, diode ideality factor, parasitic resistances, short circuit current, open circuit voltage, and fill factor will be highlighted.

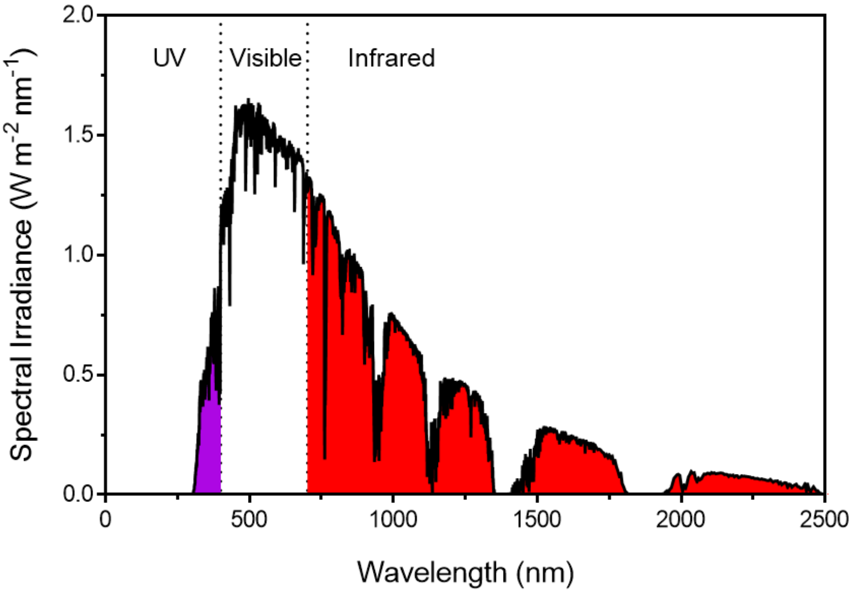

Figure 2.13 AM1.5 spectrum illustrating the ultraviolet, visible, and infrared regions of the solar cell spectrum. The spectrum is acquired from a Newport 92251A-1000 solar simulator with an output of 1000 $\mathrm{W.m^{-2}}$.

2.8.1 Power Conversion Efficiency

A typical J-V response for a polymer solar cell under illumination, is shown in **Figure 2.14**. The cell response is measured when two conditions are satisfied: an open-circuit condition at $J = 0\, mA.cm^{-2}$ and a short-circuit condition at ($V = 0\, V$). There are therefore four points that can be extracted from the J-V curve. These are the open-circuit voltage (V_{oc}), short-circuit current density (J_{sc}), the maximum power point current density (J_{mpp}) and voltage (V_{mpp}). Multiplying the J_{mpp} by the V_{mpp} defines the maximum power point (M_{pp}), which is used to calculate the maximum output power delivered by the cell (P_{out}). The ratio of the maximum output power delivered by the cell and the incident power of illumination (P_{in}) defines the measured device PCE. The ratio of the maximum output power and the product of the short-circuit current density and open-circuit voltage determines the fill factor (FF). PCE and FF can be calculated using **Equations 2.11** and **2.12** below.

$$PCE = \frac{P_{out}}{P_{in}} = \frac{J_{mpp}\, V_{mpp}}{P_{in}} = \frac{J_{sc}\, V_{oc}\, FF}{P_{in}} \qquad \textbf{Equation 2.11}$$

$$FF = \frac{J_{mpp}\, V_{mpp}}{J_{sc}\, V_{oc}} \qquad \textbf{Equation 2.12}$$

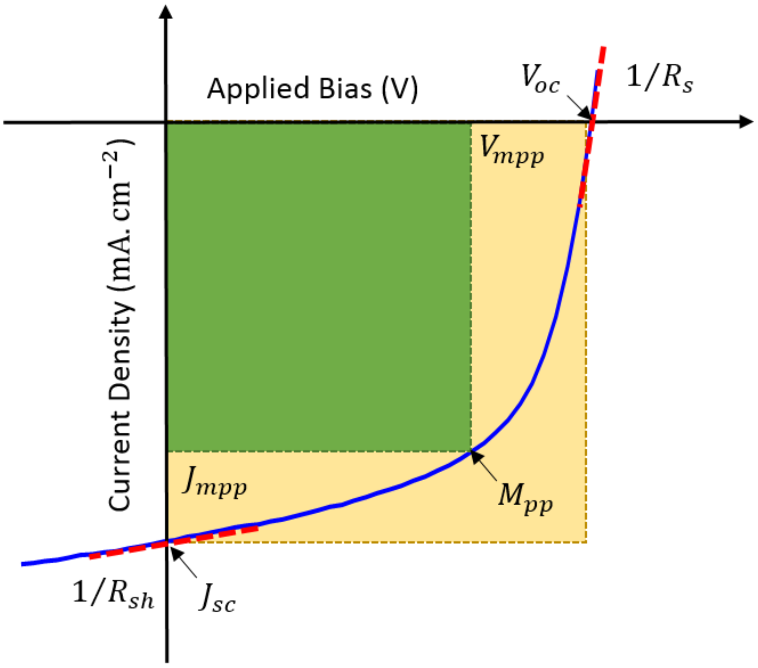

Figure 2.14 Typical current density-voltage (J-V) characteristic under illumination for a polymer solar cell, showing the measurable parameters, including V_{oc} ,J_{sc} ,V_{mpp} ,J_{mpp}.

To interpret the J-V characteristics, an equivalent circuit based on a diode model is used. For an ideal solar cell, the circuit consists of a current source, a diode and an external load. Under illumination, a solar cell works as a current source, providing a current density of J_{ph}. A proportion of this current counteracts the junction current of the diode, and the residual current flows to the load. According to Shockley's theory, the junction current density of the diode is presented by:

$$J_D = J_0\left[exp\left(\frac{qV}{kT}\right) - 1\right] \qquad \textbf{Equation 2.13}$$

Where T is the temperature, k is the Boltzmann constant, and J_0 is the reverse saturation current density. In a p–n junction solar cell, J_0 represents the current density of minority carriers in dark, which is a summation of the hole current in the n region (drift current) and the electron current in the p region (diffusion current). V is the output voltage (generally in a test, the potential drop on the load is stimulated with an externally applied voltage to counteract the output voltage of the cell). V is therefore also the voltage applied during the test.

For a practical solar cell, the model encounters the effect of parasitic resistances in dissipating the produced power, as seen in **Figure 2.15**. The power is dissipated through the resistance of the contacts and through leakage currents around the sides of the device. Thus, parasitic resistances are both series and parallel (shunt), and are known as R_s and R_{sh}, respectively. The total current recorded on the load as a function of the applied bias, $J(V)$, given in **Equation 2.14**, is therefore defined as the sum of the photogenerated current, J_{ph}, diode current, J_D, and shunt current, J_{sh}.

$$J(V) = J_{ph} - J_0\left[exp\left(\frac{q(V - JAR_s)}{nkT}\right) - 1\right] - \frac{V - JAR_s}{AR_{sh}} \qquad \textbf{Equation 2.14}$$

where J_0 is the dark saturation current, q is the elementary charge, V is the applied bias, A is the cell area, n is the diode ideality factor, k is Boltzmann's constant, T is the absolute temperature, R_s and R_{sh} are the series and shunt resistances. The second term in the equation represents the diode current, where J_0 and n attribute saturation current and ideality factor, respectively, while the third term represents the shunt current.

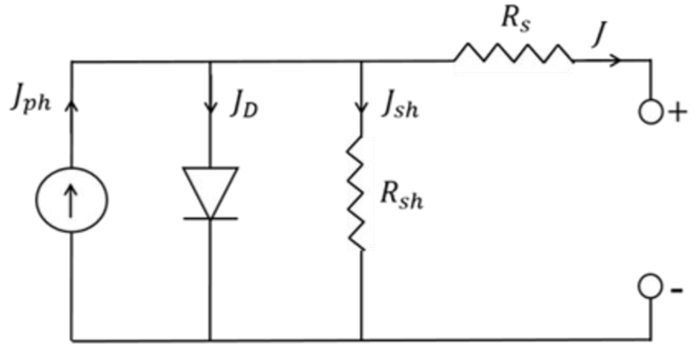

Figure 2.15 Equivalent circuit for a PSC accounting for the contribution of parasitic resistances, R_s and R_{sh}, to the generated current, J. J_{ph},J_D, and J_{sh} are the respective photocurrent, diode and shunt currents influencing the generated current, as described in **Equation 2.14.**

2.8.2 Diode Ideality Factor

The ideality factor describes the dominant recombination process in PSCs. For an ideal diode, the ideality factor is equal to 1 (**Equation 2.13**), corresponding to charge carrier recombination at contact surfaces. It has been found that the ideality factor for polymer solar cells takes values ranging between 1.35 and 2, depending on the materials used within the photoactive layer [48], [49]. This indicates the dominant recombination of deep states within the active layer rather than surface recombination [50]. There are two methods to determine the ideality factor experimentally. When the J-V characteristic is measured in the dark, the slope of the exponential regime of the J-V curve corresponds to the ideality factor. This method does not tell exactly whether the changes seen in the measured n are related to the recombination at contact, however. This is due to the contribution of both series and shunt resistances to the dark current. An alternative approach is the use of the light intensity dependence of V_{oc}. In an open circuit, the average generation and recombination rates have to be identical in order to maintain a zero net current flow. Because of the proportionality of generation rate to the light intensity (ϕ), the ideality number under illumination (n_i) is derived as seen in **Equation 2.15**. This method is only valid when the temperature is constant during the measurement, however, due to the dependence of voltage on temperature.

$$n_i = \frac{q}{kT}\frac{dV_{oc}}{d\ln(\phi)}$$ **Equation 2.15**

2.8.3 *Parasitic Resistances*

R_s and R_{sh} are known as parasitic resistances and can significantly influence the device performance. R_s arises from interfacial resistances between device layers and extraction barriers at contact interfaces, while R_{sh} originates from defects within device layers resulting in current leakage. For an ideal device, R_s (~ 0) is very small and R_{sh} $(\sim\infty)$ is very large. The non-ideal values in R_s and R_{sh} lead to a reduction in the fill factor by different mechanisms [51]. High series resistance lowers the J_{sc}. Low shunt resistance provides alternative paths for photogenerated charges to recombine and hence reduces V_{oc}. They can therefore be experimentally determined from the gradients of the J-V curve at open and short circuit conditions; R_s at open circuit ($J = 0$), and R_{sh} at short circuit ($V = 0$).

2.8.4 Short Circuit Current

At short circuit condition, $J(V = 0)$, the measured current density is defined as the maximum attainable current that can be drawn from a PSC under illumination and is annotated as J_{sc}. There are several factors influencing the J_{sc}: the amount of absorbed light that is controlled by the band gap of the donor polymer. A small band gap allows for photons with energy higher than the band gap to be absorbed, generating more excitons, and hence increasing J_{sc}, but a smaller band gap can cause a reduction in the V_{oc}. It is possible to encounter a reduction in the J_{sc} due to the recombination of charge carriers within donor/acceptor interfaces [52] or across device layers and the parasitic resistances.

2.8.5 Open Circuit Voltage

In open circuit conditions, $V(J = 0)$, the measured voltage defines the maximum attainable voltage that can be drawn from a PSC under illumination and is annotated as V_{oc}. Factors controlling the V_{oc} can be categorized into two groups depending on their origin. From the polymer point of view, ideally, to achieve the upper limit of $\mathrm{V_{oc}}$, the free charges should only recombined radiatively at the open circuit condition [53]. This is not the case in organic BHJ solar cells, however. Studies showed that $\mathrm{V_{oc}}$ in BHJ PSCs is influenced by the charge-carrier recombination rates, as well as the variation of charge carrier density due to dependence on light intensity [54], [55]. Charges can experience different types of recombination including monomolecular (geminate), bimolecular (non-geminate), and surface recombination at electrode interfaces, as a result of the severe luminescence quenching in conjugated polymers [49], [56], [57]. Since radiative recombination in PSCs is just a small proportion of the total recombination, the maximum obtainable $\mathrm{V_{oc}}$ is expected to reduce. Indeed, the voltage of most of the BHJ PSCs is in the order of 0.5 – 0.8 eV for polymers, with band gaps ranging from 1.6 eV to 2.0 eV [58]–[61]. V_{oc} is also found to be affected by other factors such as light intensity [55], temperature [62], processing conditions of the active layer [37], acceptor strength [63] and donor oxidation potential [64].

From the interface point of view, however, the type of contacts formed at electrode/active layer interfaces can significantly influence V_{oc}, as discussed earlier in **Section 2.5.4.** In the case of ohmic contacts, the Fermi level is pinned at either/both interfaces to polymer HOMO and/or fullerene LUMO levels, facilitating effective charge extraction and hence improved V_{oc}. This holds true when the electrode work function matches the HOMO and/or LUMO levels. For non-ohmic contacts, however, V_{oc} is regulated by the difference in the electrodes' work function for [65]. In addition, the presence of a dipole layer, which facilities charge transport by either reducing or increasing electrode work function, can influence V_{oc} as will be seen in **Chapter 8**.

2.8.6 Fill Factor

The FF describes how closely the behaviour of a PSC mimics an ideal diode. It is therefore affected by the parasitic resistances and diode ideality factor. A reduction in the FF can be realized for a large R_s, small R_{sh}, and $n > 1$. In order to overcome these effects and enhance the overall device performance, charge recombination and losses through interfacial resistance and device shorts should be reduced [66].

2.9 References

[1] J. Clayden, N. Greeves, and S. Warren, *Organic Chemistry*, 2nd ed. New York: Oxford University Press Inc, 2012.

[2] P. Atkins, *The Elements of Physical Chemistry*, 3rd ed. New York: Oxford University Press, 2001.

[3] A. Kohler and H. Bassler, *Electronic Processes in Organic Semiconductors: An Introduction*. Germany: Wiley-VCH Verlag GmbH & Co. KGaA, 2015.

[4] W. R. Salaneck, R. H. Friend, and J. L. Brédas, "Electronic structure of conjugated polymers: consequences of electron–lattice coupling," *Phys. Rep.*, vol. 319, no. 6, pp. 231–251, 1999.

[5] N. Tessler, Y. Preezant, N. Rappaport, and Y. Roichman, "Charge transport in disordered organic materials and its relevance to thin-film devices: A tutorial review," *Adv. Mater.*, vol. 21, no. 27, pp. 2741–2761, 2009.

[6] A. Bhuwalka, J. F. Mike, M. He, J. J. Intemann, T. Nelson, M. D. Ewan, R. A. Roggers, Z. Lin, and M. Jeffries-El, "Quaterthiophene-benzobisazole copolymers for photovoltaic cells: Effect of heteroatom placement and substitution on the optical and electronic properties," *Macromolecules*, vol. 44, no. 24, pp. 9611–9617, 2011.

[7] B. Kim, H. R. Yeom, M. H. Yun, J. Y. Kim, and C. Yang, "A Selenophene Analogue of PCDTBT: Selective Fine-Tuning of LUMO to Lower of the Bandgap for Efficient Polymer Solar Cells," *Macromolecules*, vol. 45, pp. 8658–8664, 2012.

[8] M. Pope and C. E. Swenberg, *Electronic Processes in Organic Crystals and Polymers*, 2nd ed. New York: Oxford University Press, 1999.

[9] T. M. Clarke and J. R. Durrant, "Charge photogeneration in organic solar cells," *Chem. Rev.*, vol. 110, no. 11, pp. 6736–6767, 2010.

[10] S. R. Cowan, A. Roy, and A. J. Heeger, "Recombination in polymer-fullerene bulk heterojunction solar cells," *Phys. Rev. B*, vol. 82, no. 24, p. 245207, 2010.

[11] O. V. Mikhnenko, P. W. M. Blom, and T.-Q. Nguyen, "Exciton diffusion in organic semiconductors," *Energy Environ. Sci.*, vol. 8, no. 7, pp. 1867–1888, 2015.

[12] A. Köhler and H. Bässler, "Triplet states in organic semiconductors," *Mater.*

Sci. Eng. R Reports, vol. 66, no. 4–6, pp. 71–109, 2009.

[13] J. L. Brédas, D. Beljonne, V. Coropceanu, and J. Cornil, "Charge-transfer and energy-transfer processes in π-conjugated oligomers and polymers: A molecular picture," *Chem. Rev.*, vol. 104, no. 11, pp. 4971–5003, 2004.

[14] B. C. Thompson and J. M. J. Fréchet, "Polymer-fullerene composite solar cells," *Angew. Chemie - Int. Ed.*, vol. 47, no. 1, pp. 58–77, 2008.

[15] M. C. Scharber, D. Mühlbacher, M. Koppe, P. Denk, C. Waldauf, a. J. Heeger, and C. J. Brabec, "Design Rules for Donors in Bulk-Heterojunction Solar Cells—Towards 10 % Energy-Conversion Efficiency," *Adv. Mater.*, vol. 18, no. 6, pp. 789–794, Mar. 2006.

[16] P. Peumans, A. Yakimov, and S. R. Forrest, "Small molecular weight organic thin-film photodetectors and solar cells," *J. Appl. Phys.*, vol. 93, no. 7, pp. 3693–3723, 2003.

[17] G. J. Hedley, A. Ruseckas, and I. D. W. Samuel, "Light Harvesting for Organic Photovoltaics," *Chem. Rev.*, vol. 117, no. 2, pp. 796–837, 2017.

[18] S. R. Scully and M. D. McGehee, "Effects of optical interference and energy transfer on exciton diffusion length measurements in organic semiconductors," *J. Appl. Phys.*, vol. 100, no. 3, 2006.

[19] X.-Y. Zhu, Q. Yang, and M. Muntwiler, "Charge-transfer excitons at organic semiconductor surfaces and interfaces.," *Acc. Chem. Res.*, vol. 42, no. 11, pp. 1779–1787, 2009.

[20] H. Bässler, "Charge Transport in Disordered Organic Photoconductors a Monte Carlo Simulation Study," *Phys. Status Solidi B*, vol. 175, no. 1, pp. 15–56, 1993.

[21] T. Dyson, H.- Fock, I. For, and S. Crati, "The Role of Driving Energy and Delocalized States for Charge Separation in Organic Semiconductors," *Science (80-.).*, vol. 335, pp. 1340–1344, 2012.

[22] V. Coropceanu, J. Cornil, D. Silva, D. A, Y. Olivier, R. Silbey, J. L. Bredas, D. A. da Silva Filho, J.-L. J.-L. Brédas, Y. Olivier, R. Silbey, and J.-L. J.-L. Brédas, "Charge transport in organic semiconductors.," *Chem. Rev.*, vol. 107, no. 4, pp. 926–52, 2007.

[23] Y. Kim, S. Cook, S. M. Tuladhar, S. A. Choulis, J. Nelson, J. R. Durrant, D. D. C. Bradley, M. Giles, I. McCulloch, C.-S. Ha, and M. Ree, "A strong regioregularity effect in self-organizing conjugated polymer films and high-efficiency polythiophene:fullerene solar cells," *Nat. Mater.*, vol. 5, no. 3, pp.

197–203, 2006.

[24] R. J. Kline, M. D. McGehee, E. N. Kadnikova, J. Liu, and J. M. J. Fréchet, “Controlling the field-effect mobility of regioregular polythiophene by changing the molecular weight,” *Adv. Mater.*, vol. 15, no. 18, pp. 1519–1522, 2003.

[25] H. Yan, Z. Chen, Y. Zheng, C. Newman, J. R. Quinn, F. Dötz, M. Kastler, and A. Facchetti, “A high-mobility electron-transporting polymer for printed transistors.,” *Nature*, vol. 457, no. 7230, pp. 679–686, 2009.

[26] W. Ma, C. Yang, X. Gong, K. Lee, and A. J. Heeger, “Thermally stable, efficient polymer solar cells with nanoscale control of the interpenetrating network morphology,” *Adv. Funct. Mater.*, vol. 15, no. 10, pp. 1617–1622, 2005.

[27] C. Tengstedt, W. Osikowicz, W. R. Salaneck, I. D. Parker, C.-H. Hsu, and M. Fahlman, “Fermi-level pinning at conjugated polymer interfaces,” *Appl. Phys. Lett.*, vol. 88, no. 5, p. 53502, Feb. 2006.

[28] I. Lange, J. C. Blakesley, J. Frisch, A. Vollmer, N. Koch, and D. Neher, “Band bending in conjugated polymer layers,” *Phys. Rev. Lett.*, vol. 106, no. 21, pp. 1–4, 2011.

[29] S. Braun, W. R. Salaneck, and M. Fahlman, “Energy-Level Alignment at Organic/Metal and Organic/Organic Interfaces,” *Adv. Mater.*, vol. 21, no. 14–15, pp. 1450–1472, Apr. 2009.

[30] C. V Hoven, R. Yang, A. Garcia, V. Crockett, A. J. Heeger, G. C. Bazan, and T.-Q. Nguyen, “Electron injection into organic semiconductor devices from high work function cathodes.,” *Proc. Natl. Acad. Sci. U. S. A.*, vol. 105, no. 35, pp. 12730–5, Sep. 2008.

[31] B. P. Rand, D. P. Burk, and S. R. Forrest, “Offset energies at organic semiconductor heterojunctions and their influence on the open-circuit voltage of thin-film solar cells,” *Phys. Rev. B*, vol. 75, no. 11, p. 115327, Mar. 2007.

[32] K. Vandewal, K. Tvingstedt, A. Gadisa, O. Inganäs, and J. V Manca, “Relating the open-circuit voltage to interface molecular properties of donor:acceptor bulk heterojunction solar cells,” *Phys. Rev. B*, vol. 81, p. 2452041, 2010.

[33] K. Vandewal, K. Tvingstedt, A. Gadisa, O. Inganäs, and J. V Manca, “On the origin of the open-circuit voltage of polymer-fullerene solar cells.,” *Nat. Mater.*, vol. 8, no. 11, pp. 904–909, 2009.

[34] D. Credgington, R. Hamilton, P. Atienzar, J. Nelson, and J. R. Durrant, “Non-

geminate recombination as the primary determinant of open-circuit voltage in polythiophene:fullerene blend solar cells: An analysis of the influence of device processing conditions," *Adv. Funct. Mater.*, vol. 21, no. 14, pp. 2744–2753, 2011.

[35] D. Credgington and J. R. Durrant, "Insights from transient optoelectronic analyses on the open-circuit voltage of organic solar cells," *J. Phys. Chem. Lett.*, vol. 3, no. 11, pp. 1465–1478, 2012.

[36] G. Namkoong, J. Kong, M. Samson, I.-W. Hwang, and K. Lee, "Active layer thickness effect on the recombination process of PCDTBT:PC71BM organic solar cells," *Org. Electron.*, vol. 14, no. 1, pp. 74–79, Jan. 2013.

[37] L. Zhao, S. Zhao, Z. Xu, W. Gong, Q. Yang, X. Fan, and X. Xu, "Influence of morphology of PCDTBT:PC71BM on the performance of solar cells," *Appl. Phys. A*, vol. 114, no. 4, pp. 1361–1368, Sep. 2013.

[38] H. Kim, J. S. Horwitz, G. P. Kushto, Z. H. Kafafi, and D. B. Chrisey, "Indium tin oxide thin films grown on flexible plastic substrates by pulsed-laser deposition for organic light-emitting diodes," *Appl. Phys. Lett.*, vol. 79, no. 3, pp. 284–286, 2001.

[39] B. G. Lewis and D. C. Paine, "Applications and Processing of Transparent Conducting Oxides," *MRS Bull.*, vol. 25, pp. 22–27, 2000.

[40] N. G. Patel, P. D. Patel, and V. S. Vaishnav, "Indium tin oxide (ITO) thin film gas sensor for detection of methanol at room temperature," *Sonsors Actuators B Chem.*, vol. 96, pp. 180–189, 2003.

[41] C. Su, T. K. Sheu, Y. T. Chang, M. A. Wan, M. C. Feng, and W. C. Hung, "Preparation of ITO thin films by sol-gel process and their characterizations," *Synth. Met.*, vol. 153, no. 1–3, pp. 9–12, 2005.

[42] T. Maruyama and K. Fukui, "Indium tin oxide thin films prepared by chemical vapour deposition," *Thin Solid Films*, vol. 203, no. 2, pp. 297–302, 1991.

[43] C. A. Pan and T. P. Ma, "High-quality transparent conductive indium oxide films prepared by thermal evaporation," *Appl. Phys. Lett.*, vol. 37, no. 2, pp. 163–165, 1980.

[44] L. Voisin, M. Ohtsuka, S. Petrovska, R. Sergiienko, and T. Nakamura, "Structural, optical and electrical properties of DC sputtered indium saving indium-tin oxide (ITO) thin films," *Opt. - Int. J. Light Electron Opt.*, no. 2010, 2017.

[45] H. Kim, C. M. Gilmore, A. Piqué, J. S. Horwitz, H. Mattoussi, H. Murata, Z.

H. Kafafi, and D. B. Chrisey, “Electrical , optical , and structural properties of indium – tin – oxide thin films for organic light-emitting devices Electrical , optical , and structural properties of indium – tin – oxide thin films for organic light-emitting devices,” vol. 6451, no. 1999, 2000.

[46] M. T. Bhatti, A. M. Rana, and A. F. Khan, “Characterization of rf-sputtered indium tin oxide thin films,” *Mater. Chem. Phys.*, vol. 84, no. 1, pp. 126–130, Mar. 2004.

[47] N. Nadaud, N. Lequeux, M. Nanot, J. Jovenstitut, and T. Roisnel, “Structural Studies of Tin-Doped Indium Oxide (ITO) and In 4 Sn 3 O 12,” *J. Solid State Chem.*, vol. 135, no. 135, pp. 140–148, 1998.

[48] B. Kippelen, J.-L. Brédas, and J.-L. Br Edas, “Organic photovoltaics,” *Energy Environ. Sci.*, vol. 2, no. 3, p. 251, 2009.

[49] S. A. Hawks, G. Li, Y. Yang, and R. A. Street, “Band tail recombination in polymer:fullerene organic solar cells,” *J. Appl. Phys.*, vol. 116, no. 86, pp. 113301–243502, 2014.

[50] T. Kirchartz and J. Nelson, “Meaning of reaction orders in polymer:fullerene solar cells,” *Phys. Rev. B - Condens. Matter Mater. Phys.*, vol. 86, no. 16, pp. 1–12, 2012.

[51] R. A. Street, K. W. Song, and S. Cowan, “Influence of series resistance on the photocurrent analysis of organic solar cells,” *Org. Electron.*, vol. 12, no. 2, pp. 244–248, Feb. 2011.

[52] R. A. Street, M. Schoendorf, A. Roy, and J. H. Lee, “Interface state recombination in organic solar cells,” *Phys. Rev. B*, vol. 81, no. 20, p. 205307, May 2010.

[53] W. Shockley and H. J. Queisser, “Detailed Balance Limit of Efficiency of p-n Junction Solar Cells,” *J. Appl. Phys.*, vol. 32, no. 3, p. 510, 1961.

[54] C. G. Shuttle, B. O’Regan, A. M. Ballantyne, J. Nelson, D. D. C. Bradley, and J. R. Durrant, “Bimolecular recombination losses in polythiophene: Fullerene solar cells,” *Phys. Rev. B - Condens. Matter Mater. Phys.*, vol. 78, no. 11, pp. 1–4, 2008.

[55] L. J. a Koster, V. D. Mihailetchi, R. Ramaker, and P. W. M. Blom, “Light intensity dependence of open-circuit voltage of polymer:fullerene solar cells,” *Appl. Phys. Lett.*, vol. 86, no. 12, pp. 1–3, 2005.

[56] J.-L. Brédas, J. E. Norton, J. Cornil, and V. Coropceanu, “Molecular understanding of organic solar cells: the challenges.,” *Acc. Chem. Res.*, vol. 42,

no. 11, pp. 1691–1699, 2009.

[57] A. Foertig, J. Kniepert, M. Gluecker, T. Brenner, V. Dyakonov, D. Neher, and C. Deibel, "Nongeminate and geminate recombination in PTB7:PCBM Solar Cells," *Adv. Funct. Mater.*, vol. 24, no. 9, pp. 1306–1311, 2014.

[58] G. Li, C.-W. Chu, V. Shrotriya, J. Huang, and Y. Yang, "Efficient inverted polymer solar cells," *Appl. Phys. Lett.*, vol. 88, no. 25, p. 253503, Jun. 2006.

[59] Y. Sun, J. H. Seo, C. J. Takacs, J. Seifter, and A. J. Heeger, "Inverted polymer solar cells integrated with a low-temperature-annealed sol-gel-derived ZnO Film as an electron transport layer.," *Adv. Mater.*, vol. 23, no. 14, pp. 1679–83, Apr. 2011.

[60] Y.-M. Chang and C.-Y. Leu, "Conjugated polyelectrolyte and zinc oxide stacked structure as an interlayer in highly efficient and stable organic photovoltaic cells," *J. Mater. Chem. A*, vol. 1, no. 21, p. 6446, May 2013.

[61] C.-Z. Li, C.-Y. Chang, Y. Zang, H.-X. Ju, C.-C. Chueh, P.-W. Liang, N. Cho, D. S. Ginger, and A. K.-Y. Jen, "Suppressed Charge Recombination in Inverted Organic Photovoltaics via Enhanced Charge Extraction by Using a Conductive Fullerene Electron Transport Layer," *Adv. Mater.*, vol. 26, no. 36, pp. 6262–6267, Sep. 2014.

[62] A. K. Thakur, G. Wantz, G. Garcia-Belmonte, J. Bisquert, and L. Hirsch, "Temperature dependence of open-circuit voltage and recombination processes in polymer-fullerene based solar cells," *Sol. Energy Mater. Sol. Cells*, vol. 95, no. 8, pp. 2131–2135, 2011.

[63] C. J. Brabec, A. Cravino, D. Meissner, N. S. Sariciftci, T. Fromherz, M. T. Rispens, L. Sanchez, and J. C. Hummelen, "Origin of the Open Circuit Voltage of Plastic Solar Cells," *Adv. Funct. Mater.*, vol. 11, no. 5, pp. 374–380, Oct. 2001.

[64] A. Gadisa, M. Svensson, M. R. Andersson, and O. Inganäs, "Correlation between oxidation potential and open-circuit voltage of composite solar cells based on blends of polythiophenes/ fullerene derivative," *Appl. Phys. Lett.*, vol. 84, no. 9, p. 1609, Feb. 2004.

[65] V. D. Mihailetchi, P. W. M. Blom, J. C. Hummelen, and M. T. Rispens, "Cathode dependence of the open-circuit voltage of polymer:fullerene bulk heterojunction solar cells," *J. Appl. Phys.*, vol. 94, no. 10, p. 6849, Oct. 2003.

[66] G. F. a. Dibb, F. C. Jamieson, A. Maurano, J. Nelson, and J. R. Durrant, "Limits on the Fill Factor in Organic Photovoltaics: Distinguishing Nongeminate and Geminate Recombination Mechanisms," *J. Phys. Chem. Lett.*, vol. 4, no. 5, pp. 803–808, Mar. 2013.

Chapter 3

Literature Review on the Materials used in Polymer: Fullerene Solar Cells

3.1 Introduction

The historical evolution of organic solar cells is reviewed, with an illustration of the structural differences between standard and inverted cell architectures. Reviews are provided on recent developments in respect to BHJ donor polymers, BHJ acceptor fullerene, and indium tin oxide (ITO) as a transparent electrode. The progress in interfacial engineering for electron extraction layers using metal oxides, polyelectrolytes, and others, is evaluated. Moreover, the contributions of small organic molecules as cathode modifiers forming self-assembled monolayers are highlighted.

3.2 Device Architecture

The architecture of an organic photovoltaic cell has developed over the years, starting from single p-n junction to heterojunction designed devices. Many of these developments were adapted from the conception of silicon solar cells. The initial organic single junction cell dated back to 1973, when Ghosh et al. fabricated devices out of a photoactive layer of tetracene that was confined between aluminium and gold electrodes [1]. The photocurrent was extracted by the assistance of a built-in potential that was derived from dissimilar electrode work functions. Unfortunately, the efficiencies of these devices were very limited, achieving only 10^{-4} %. Although the replacement of tetracene with a merocyanine dye enhanced device performance slightly, still, efficiencies of only up to 0.7 % were obtained due to the poor fill factor (~ 30 %)

[2]. The performance of such cells was most likely restricted by the fact that organic materials unlike silicon, do not generate free charges upon photoexcitation. The electric field due to the built-in potential is not enough to effectively separate the strongly bound Frenkel excitons and hence another driving force (i.e. local internal field) has to be introduced into the cell design.

In 1986, Tang et al. proposed the first organic planar heterojunction (PHJ) cell, where two layers with different organic materials topped on each one were confined between two electrodes [3]. The materials used were copper phthalocyanine (CuPc), serving as an electron donor, and a perylene tetracarboxylic derivative (PV), serving as an electron acceptor. An indium tin oxide (ITO) transparent electrode was implemented as an anode contact for the first time, due to its unique optical transparency and electrical conductivity, and this material has since been used commonly. The CuPc/PV interface has the advantage of creating an internal electric field that overcomes the binding energy of the Frenkel excitons. This led to the efficiency of the cell increasing to 1 % with a better fill factor (65 %) compared to the previous single junction device.

A drawback of the bilayer design of the active layer is the long distance that excitons must travel for dissociation if they were generated further away from the donor-acceptor interface. As mentioned previously in **Chapter 2**, **Section 5.2**, 10 nm is a typical length for exciton diffusion towards an interface before geminate recombination occurs. Reducing the bilayer thickness to be of the order of this 10 nm would therefore significantly reduce the absorption of light. Some losses in the photocurrent are unavoidable, however, because excitons who are generated near to the donor-acceptor interface are only able to be separated and collected at the electrodes.

A modification to the planar heterojunction design was introduced in 1995, as shown in **Figure 3.1**. In this approach, the donor and acceptor materials were intimately mixed together to form a single layer known as ‘Bulk heterojunction’ (BHJ) [4], [5]. The BHJ morphology benefits fromthe discovery of the ultrafast process of charge transfer (~45 fs) that takes place from the donor polymer to buckminsterfullerene (C_{60}) [6], [7] The first semiconducting donor polymer to be tested in BHJ devices was MEH-PPV. Yu et al. blended MEH-PPV with C_{60} into the same solution at an appropriate ratio to fabricate devices, achieving efficiencies as high as 2.5 % [5], which was twice the efficiency obtained for devices with pure MEH-PPV. This enhancement in device performance can be attributed to the morphology of the BHJ layer, which increases the external quantum efficiency.

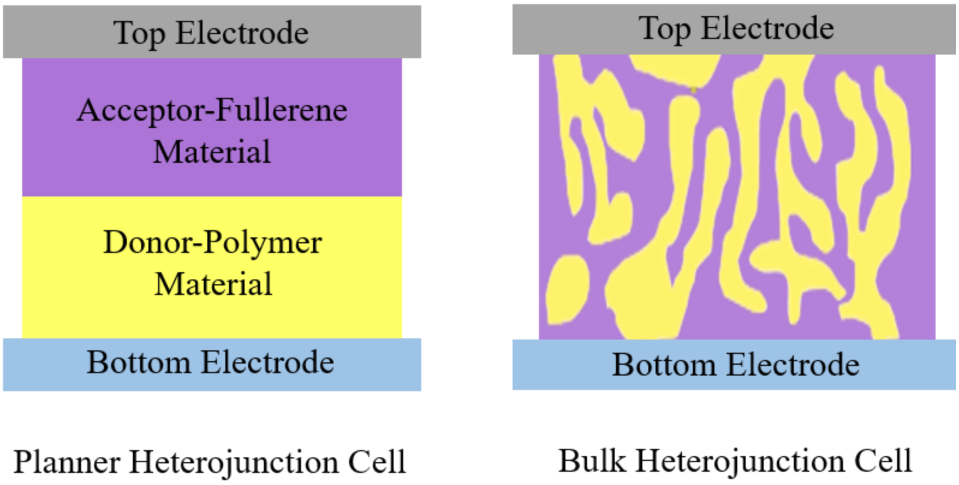

Figure 3.1 Cell configurations comparing between the planar and bulk heterojunction active layers.

In the BHJ layer, fullerene molecules are distributed around the polymer chains **to** form bicontinuous interpenetrating networks of both materials throughout the blend layer. Indeed, an ideal morphology should provide short distances (≤ 10 nm) for an exciton to diffuse from wherever it has been created to reach the dissociating interface, and continuous pathways through both material enrichments for charge transport, while maintaining the appropriate thickness of the blend layer for efficient light absorption. Thereby, every absorbed photon results in a separated pair of charge carriers and the whole photocurrent can be efficiently extracted at the electrodes, giving rise to an internal quantum efficiency of ~ 100 % [8]. Since this layer is often deposited from a blend solution, however, the resultant morphology may be thermodynamically unstable and depend fundamentally on several factors: for example, the intrinsic properties of both materials, including the molecular weight, the nature of the side chain, and the configuration of the backbone [9], [10]. The processing conditions, such as solvent selection, can influence the length-scale of phase separation (the de-mixing domains of the two materials in the layer) by tuning the solvent-evaporation rate [11]–[13]. In addition, thermal annealing of the dried BHJ layer can improve the morphology by inducing controlled phase separation as a result of removing trapped solvent molecules [14]. The direction of electrode polarity within the device architecture can also tune the vertical phase segregation of the BHJ layer [15]–[17], where the polymer enrichment is organized at the free surface and fullerene enrichment at the electrode-organic interfaces.

The BHJ cell architecture is similar to any solar cell, wherein the BHJ layer is confined between a transparent bottom electrode for cell illumination and a reflective top electrode. The bottom electrode is an ITO coated glass substrate whereas the top one is a thin layer of reflective metallic, most likely either aluminium (Al) or sliver (Ag). In a silicon based cell, however, the polarity of the bottom electrode is defined by whether a p-type or n-type doped silicon layer is deposited first onto ITO surface. In contrast, the polarity of the bottom electrode in a BHJ cell can be manipulated by inserting an intermediate layer at the ITO/BHJ interface, called a ‘buffer layer’ [18], [19]. The buffer layer is a thin film made out of functional material to serve various roles in the device, as will be seen in **Section 3.6**. There are therefore only two basic structures for BHJ cells; standard (conventional) and inverted, as shown in **Figure 3.2.**

The standard structure (**Figure 3.2 (a)**) has an ITO bottom electrode to serve as an anode, where positive charges (holes) are extracted. A buffer layer made from a p-type material (e. g. PEDOT:PSS) is typically inserted at ITO/BHJ layer interface. This p-type layer adjusts the energy level alignment between the donor HOMO level and the ITO work function, as shown in **Figure 3.2 (c)**, facilitating the transport of holes by reducing the energy barrier. Meanwhile, its shallow conduction band creates an energetic barrier for negative charges (electrons), and hence effectively blocks the electron current from passing through, leading to this often being referred to as the ‘Hole Transporting Layer’ (HTL). When an n-type material (e. g. ZnO) is used to form a thin layer on the ITO surface, however, then an inverted BHJ structure is made (**Figure 3.2 (b)**). Here, ITO can serve as a cathode electrode, where negative charges (electron) current are extracted. In this case, the n-type layer adjusts the energy level alignment between the acceptor LUMO level and the ITO work function, providing an energetic barrier blocking the hole current, as can be seen in **Figure 3.2 (d)**. This is known as an ‘Electron Transporting Layer’ or (ETL). It should be noted that HTL or ETL can be also be inserted at the top metallic electrode and BHJ layer interface, depending on the cell structure employed, in order to maximize the efficiency of charge extraction at both electrode interfaces.

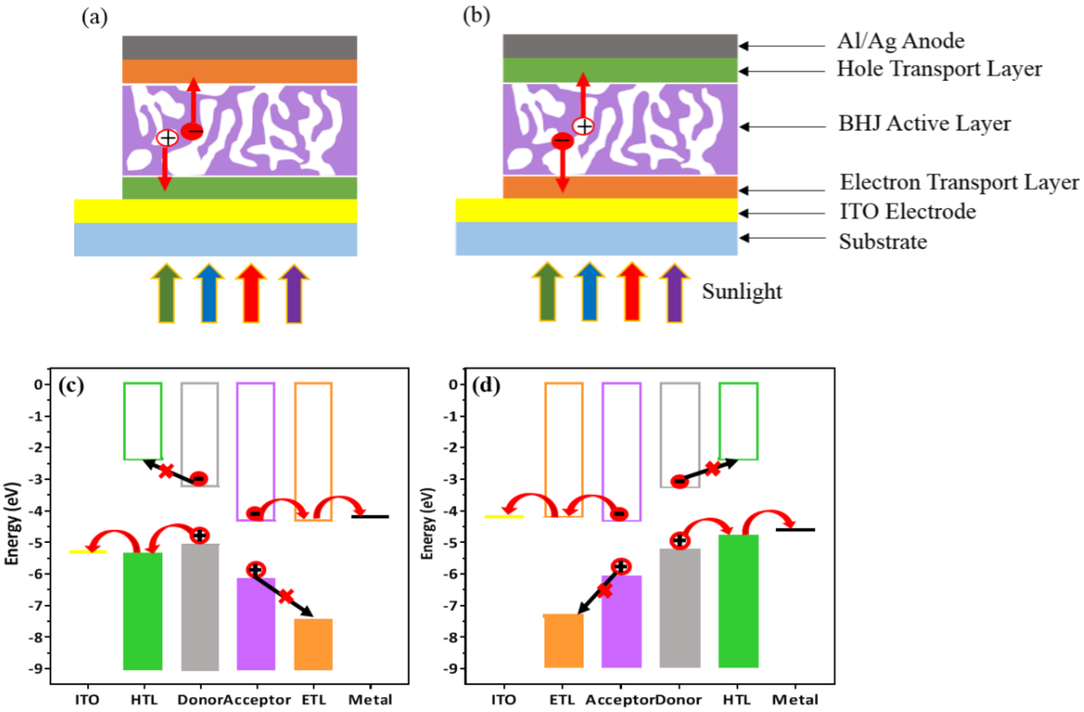

Figure 3.2 Basic structures of bulk heterojunction solar cells showing the flow directions of free charges across the cell upon photoexcitation for (a) standard and (b) inverted structures. Indicative energy diagrams for (c) standard and (d) inverted structures.

The inverted structure was first proposed in 2006 [20], and since then has shown a number of advantages compared to the standard structure. In particular, it allows a wide range of materials to be used as ETLs, such as metal oxides, conjugated polyelectrolytes, and surface organic modifiers, hence enhancing the durability and lifetime of the cell [21], [22]. A literature review on these materials will be provided in **Section 6.3**. Placing ETLs directly onto ITO allows those ETLs to be processed in an ambient rather than inert atmosphere, and obviates the need for high vacuum processing, thus reducing production costs and making the study of ambient stability easier [23], [24]. It also means that the use of water soluble PEDOT: PSS on ITO can be eliminated, which benefits device stability, since it has been found silver diffusion into the organic BHJ layer causes layer degradation [25]. Device stability also gets better when a low work function metallic like Ca and LiF, as used in the standard structure, is substituted by a metal oxide in the inverted structure. These metallic materials need to be deposited in an inert high vacuum atmosphere, however, to avoid reaction with ambient gasses, which can provides paths for current leakage [23].

3.3 Donor Polymers

Donor polymers are p-type conducting organic macromolecules whose energy band structures play important roles in light absorption and hence the generation of mobile charges. We have seen earlier in **Chapter 2** that the absorption of a particular photon energy (wavelength) is restricted by the band gap energy, since a photon that has an energy below the band gap does not have enough energy to create electron-hole pairs, and therefore is not absorbed. To determine how far light of a particular wavelength can penetrate before it is absorbed, an absorption coefficient (α) can be calculated using the Tauc relation seen in **Equation 3.1** or **Equation 3.2**.

$$\mathrm{\alpha hv = A(hv - E_g)^{1/2}}$$ **Equation 3.1**

$$\mathrm{\alpha = \frac{4\pi k}{\lambda}}$$ **Equation 3.2**

Where *hv* is photon energy, *A* is a constant depending on optical transition probability, *Eg* is the optical band gap energy, *k* is the extinction coefficient of the polymer, and λ is the wavelength.

It can see that the absorption coefficient is a function of the photon energy and band gap energy. At a particular wavelength, a large absorption coefficient means a high probability of absorbing that light, while a small coefficient means that the polymer is relatively transparent to that light. Since a conjugated polymer normally has a direct band gap as seen earlier in **Chapter 2**, **Section 2.5.1**, its absorption coefficient ($\sim 10^5 cm^{-1}$) is typically higher than that of silicon ($10^2 cm^{-1}$) [26]. This is because the optical transition taking place in direct band gap material does not require the reaction of a phonon in order to create an electron-hole pair. Its absorption bandwidth is usually narrow, however, only covering the visible range of solar spectrum. The sunlight harvest efficiency of most organic materials is therefore less than 40%, which is one of the main reasons why the efficiency of organic solar cells is generally less than that of inorganic solar cells [26]. Moreover, the low carrier mobility of organic materials limits the thickness of organic photovoltaic devices to 10-100 nm, which decreases the light absorption ability further. Hence, improving the molar absorption coefficient, reducing the band gap and broadening the absorption of the active material are effective methods to enhance solar energy absorption.

Over the years, intensive research has been conducted towards the synthesis of new donor polymers. Examples of the most studied donor polymers are given in **Figure 3.3**. Poly (3-hexylthiophene) (P3HT) (**Figure 3.3(a)**) is one of the promising conjugated polymers that has been extensively studied for several years. It has been discovered that the post-deposition thermal treatment of P3HT:PCBM devices can result in efficiencies of 3.5 % [27]. Further increases to 5 % have been achieved, resulting from improved polymer regioregularity [28] and molecular weight, optimized annealing temperature [29] and reduced interface losses. The relatively low bandgap of P3HT (1.95 – 2.0 eV) showed better light harnessing compared to MHV-DD, giving a fill factor of 70 % [30], although it does not absorb sunlight at longer wavelengths. Besides, the energetic incompatibility between P3HT and PC60BM energy levels restricts the open circuit voltage (Voc) with the highest value of 0.66 eV reported [31].

The next generation of donor polymers has therefore been synthesised with the aims of widening the range of wavelengths absorbed by the active layer and increasing the cell lifetime by preventing oxidation. This has been achieved by developing a group of polymer families that have relatively smaller band gap energies as well as deep-lying HOMO levels. A popular example are carbazole co-polymers such as poly [[9-(1-octylnonyl)-9H-carbazole-2,7-diyl]-2,5-thiophenediyl-2,1,3-benzothiadiazole-4,7-diyl-2,5-thiophenediyl] (PCDTBT) [32], see **Figure 3.3(b)**. PCDTBT has tuneable band gap energies varying between 1.80 and 1.90 eV depending on the electron donating and withdrawing functional groups added to the polymer backbone [33], [34]. The energy levels of PCDTBT sit well with PC70BM, providing 100 % internal quantum efficiency according to Heeger's research group [8]. This means that every absorbed photon is successfully converted into free charges. The operating efficiency of these devices was 6.1 %. Controlling the morphology of the PCDTBT: PCBM blend by the addition of solvent additives has led to maximum enhancements in device performance, with 7 % efficiency reported [35]. Other studies have optimized the device structure, such as by employing an inverted design [36], modifying the metal electrode [37], applying thermal treatments [38], and altering the structure of the cathode interlayer [39]. Furthermore, the device stability and degradation pathways have also been characterized, with lifetimes up to ten years being reported [40], [41].

Another successful family are polymers with thieno[3,4-b]thiophene and benzodithiophene units (PTB) [40]. The introduction of fluorine into the thieno[3,4-b]thiophene side of the polymer chain shifts the HOMO level further downwards compared to that of PCDTBT, as seen in PTB7 (poly({4,8-bis[(2-ethylhexyl)oxy]benzo[1,2-b:4,5-b′]dithiophene-2,6-diyl}{3-fluoro-2-[(2-ethylhexyl)carbonyl]thieno[3,4-b]thiophenediyl})) (**Figure 3.3(c)**) [42]–[44]. This has a band gap energy of 1.70 – 1.74 eV, with excellent absorption, in the range of 700 nm, enabling more photocurrent to be produced. For the first time, devices with 7.4 % efficiency have been reported for PTB7: PC71BM solar cells [43]. The performance of PTB7 devices has been found to be greatly affected by the molecular weight and molar mass distribution of the PTB7, however [45].

To overcome these issues with PTB7, a new polymer family has been synthesized by combining two different polymers together, one has a benzodithiophene (BDT) unit while the other has a thieno[3,4-b]thiophene (TT) unit, known as PBDTTs. PBDTT polymers offer dual benefits: they have the lowest band gap energy (1.6 eV), and it is possible to modify either/both units, resulting in high photocurrent and voltage, as seen in PBDTTT-C [46], PBDTTT-CF [47], PBDTTT-C-T [48], PBDTT-FTTE (known as PTB7-Th, **Figure 3.3(d)**) [49]. In 2006 it was proposed that the limit for the efficiency of single junction polymer solar cells was 10 % [50], but in 2014 a PBDTT-FTTE: PC71BM device was able to achieve an efficiency of 10.31 % [51], and, in 2017, the efficiency was increased even further to over 13 % [52].

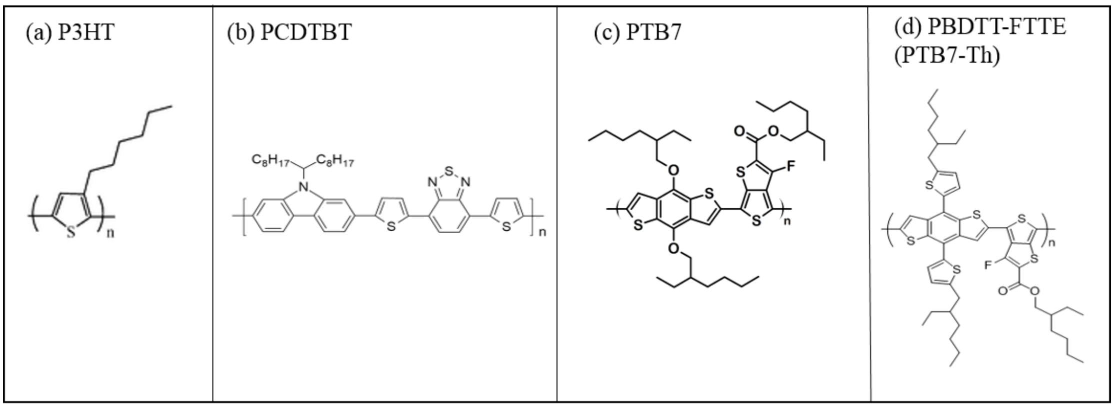
(a) P3HT
(b) PCDTBT
(c) PTB7
(d) PBDTT-FTTE (PTB7-Th)

Figure 3.3 Chemical structures of the most studied donor polymers over the years

3.4 Acceptors

In BHJ based solar cells, typical acceptors are small molecules, mostly popular fullerenes. Fullerenes are n-type conducting organic molecules. They consist of 60 carbon atoms bonded together via sp^2 hybridization to form a spherical geometry known as buckminsterfullerene (C60) [53], see **Figure 3.4(a)**. Due to their high mobilities [54], ultrafast photoinduced electron transfer occurs at the bicontinuous network interfaces when they were blended with a conducting polymer as described previously at **Section 3.2**. C60 molecules have shown a tendency to aggregate as a consequence of their low solubility in many organic solvents, however [54]. To solve this limitation, a methyl ester group has been attached to the C60 buckyball, forming the well-known fullerene derivative PC60BM [54], as seen in **Figure 3.4(b)**. PC60BM has a LUMO energy level of – 4.3 eV, which makes it a suitable candidate for several donor polymers. Another popular fullerene derivative utilizes 70 carbon atoms, instead of C60, and is known as PC70BM (**Figure 3.4(c)**). A comparison between PC60BM and PC70BM shows the latter has a better absorption coefficient within the visible range of the solar spectrum due to the lack of the spherical geometry [55]. This increases the rate of electron transfer, significantly improving the Jsc. Non-fullerene acceptors (like acceptor polymers and small molecules) have also been synthesised, however, and have already been applied in devices. Further information can be found in [52], [56].

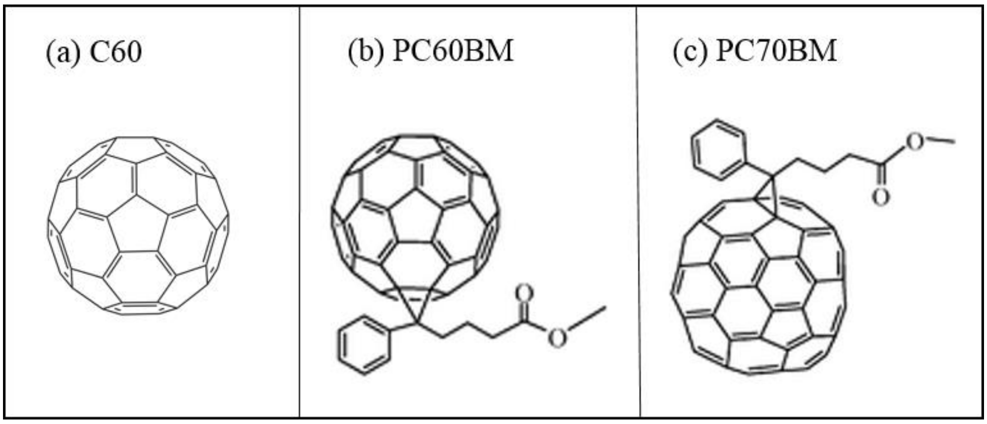

Figure 3.4 Chemical structures of well-known acceptor fullerenes

3.5 Indium Tin Oxide (ITO)

Indium tin oxide (ITO) is a well-known n-type transparent conducting transition metal oxide material, formed by the doping of indium oxide with tin at an optimum ratio of 90:10. Due to its high optical transmittance, electrical conductivity and wide band gap (>3.5 eV), it has been widely used in many optoelectronic devices, including photovoltaics [57], organic light emitting diodes [58] and gas sensors [59], among others. For polymer solar cells, ITO has been applied mostly as a transparent substrate, where a thin film of ITO is deposited onto a glass substrate. Despite the continued efforts to replace the ITO substrate with Fluorine doped tin oxide (FTO) [60], [61] or other materials [62], [63], due to the former's scarcity and toxicity, and the high cost of the Indium source, ITO substrate is still leading material in the current market. To fabricate well-performing ITO thin film, various deposition techniques have been employed such as sol-gel [64], chemical vapour [65], thermal evaporation [66], pulsed laser deposition [58], radio frequency and magnetron sputtering [67]–[71].

Over years of developments, ITO thin-film substrate has become commercially available with attractive low sheet resistance and surface roughness. The fabricating process or packaging and delivery processing has severely affected the electronic structure of ITO, however, due to accumulated contaminations. This results in a high work function in practice, in the order of $4.7 - 5.0$ eV, along with high surface roughness, with a typical RMS of $2.5 - 3.5$ nm [72], [73], which can significantly limit device performance [74]. The high work function does not suit ITO serving as an electron collection electrode. The significant energetic mismatch between ITO's work function and the LUMO energy level of fullerene can cause current leakage across the interface [75]. In addition, the rigid ITO surface can affect the homogenous coverage of the organic layer and hence provide trapping sites for the mobile charges [76]. It is therefore essential to modify the surface of the ITO substrate before the deposition of the sequent layer.

3.6 Electron Extraction Materials

Despite the continuous efforts to find the ideal polymer, the realization of highly efficient devices is significantly affected by device interfacial engineering. This is due to the low mobility of the charge carriers within the organic layer, which requires the introduction of energetic driving forces for efficient extraction at electrode interfaces. The insertion of interlayer at the electrode/organic layer can therefore play multiple roles. The energy level alignment at the interface can be tuned depending on the electronic structure of the interlayer [77], [78]. An interlayer with a suited work function can reduce the energetic mismatch between the BHJ layer and the ITO work function, allowing for the Fermi level to pin perfectly to the LUMO level of the fullerene molecules [79], [80], and hence preventing holes to pass through the contact, as discussed earlier in **Section 3.1**. Consequently, the possibility of bimolecular (non-geminate) recombination is reduced [81], [82]. In addition, the electrical properties of the interlayer can also contribute to the total current extracted [83]. This is controlled by the layer thickness. At optimal thicknesses, the resistivity of the layer is reduced, resulting in enhanced charge mobility [84]. The interlayer surface energy and composition can also influence current extraction via smoothing the ITO surface and thereby reducing charger recombination rate at the contact interface. Furthermore, the interlayer optical transparency influences the efficiency of the light absorption by the BHJ layer [85], [86]. This is achieved by the redistribution of the electromagnetic field across the device layer, since the ETL can be used as an optical spacer. Considering all these effects for contact design, careful choices of the interlayer materials are highly important for the realization of efficient cells.

A non-comprehensive survey of the timeline of the evolution of power conversion efficiency for inverted BHJ solar cells is shown in **Figure 3.5**. The survey accounts for the progress in exemplary materials used for electron extraction interfaces as well as the band gaps of exemplary polymers. The reviewed polymers are P3HT (2.0 eV), PCDTBT (1.90 eV), PTB7 (1.74 eV), and PTB7-Th (1.60 eV). Details of the metrics of the reviewed devices are listed in **Table 3.1**. Since the first application of an inverted structure within P3HT-based solar cells, incorporating caesium carbonate (Cs_2CO_3) layer and achieving and efficiency of 2.25 % in 2006 [87], a gradual increase in the efficiency has been seen over the years along with a lowering of the polymer band gap energy and persistent advances in the ETL. In 2014, a breakthrough in device performance was finally realized upon the use of dual doped zinc oxide (ZnO) within PTB7-Th inverted devices [51], with a 10.31 % efficiency that exceeds the predicted limit suggested by Scharber and co-workers in 2006 [50]. This progress in efficiency has continued, with 13 % being the best reported to date [52].

The major advance in efficiency was achieved using state-of-art ZnO-based inverted devices. Starting from an intrinsic ZnO layer to a dually doped one, the efficiency increased from 4 % [88] to 10.31 % [51]. The dually doped layer (InZnO-BisC60) was employed in PTB7-Th BHJ inverted devices, and incorporated both indium and bis-functional hydroxylated fullerene derivative as dopants. Opposite gradient dopant concentration profiles were obtained, one being rich in fullerene derivative at the InZnO-BisC60/BHJ interface and the other rich in indium at the ITO/InZnO-BisC60 interface. Such doping in ZnO not only gave improved surface conductivity by a factor of 270 (from 0.015 to 4.06 S cm^{-1}) but also provided enhanced electron mobility by a factor of 132 (from $8.25x10^{25}$ to $1.09x10^{22}$ cm^2 V^{-1} s^{-1}). This reduces the opportunities for electron/hole recombination at the interface by cutting off the chance for direct contact of polymer with either the ZnO or the InZnO, thus facilitating a more effective collection of electrons from the bulk ZnO. The InZnO-BisC60 precursor has to be prepared in an Argon-filled glovebox, however, along with the layer deposition, meaning that this technique cannot be used for mass production. Efforts to prepare ZnO layer using spray-coating and brush coating techniques have therefore recently been reported [89]. Although both techniques were shown to produce a good ZnO layer that benefits device stability, the efficiency of PTB7-Th BHJ devices was relatively lower than the one reported for InZnO-BisC60 (6.7 % for spray coated ZnO and 7.63 % for brush coated ZnO, compared to 10.31 %).

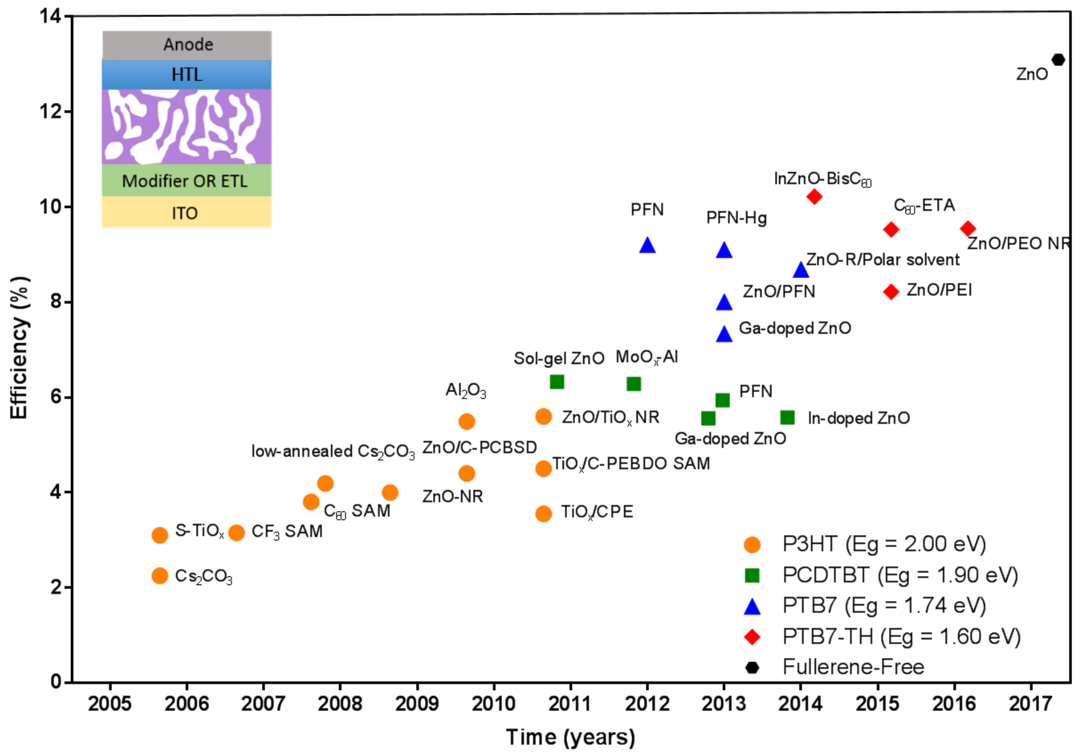

Figure 3.5 Evolution of the efficiency of inverted polymer: fullerene solar cells with various materials used to modify the surface of ITO electrodes. Data taken from [20], [49], [52], [84]-[103]. Inset shows the structure of the reported devices.

Table 3.1 Summary of the parameters reported in the literature for inverted devices

ITO Modifier	**Donor Polymer**	**V_{OC} (V)**	**J_{SH} (mA.cm^{-2})**	**FF (%)**	**PCE (%)**	**Year**	**Ref**
Cs2CO3	P3HT: PC60BM	0.56	8.42	62.1	2.25	2006	[20]
Soluble TiO2		0.56	9	62.0	3.1	2006	[84]
CF3 SAM		0.60	13.87	38	3.15	2007	[85]
C60-SAM		0.62	10.6	57.2	3.8	2008	[86]
Low annealing Cs2Co3		0.59	11.3	64.0	4.19	2008	[87]
ZnO nanorigid		0.6	10.76	62	4.0	2009	[88]
Al2O3		0.63	10.4	58	5.49	2010	[89]
ZnO/C-PCBSD		0.60	12.8	58	4.4	2010	[90]
ZnO/TiOx nanorods		0.79	11.3	63	5.6	2011	[91]
TiOx/C-PEBOD SAM		0.61	12.25	61.26	4.50	2011	[92]
TiO2/CPE		0.58	8.85	70	3.55	2011	[93]
Sol-gel ZnO	PCDTBT: PC70BM	0.88	10.41	68.8	6.33	2011	[34]
MoO3-Al		0.89	10.7	66	6.28	2012	[37]
PFN		0.91	11.71	57	5.94	2013	[94]
Ga-doped ZnO		0.90	10.46	59.03	5.56	2013	[95]
In doped ZnO		0.878	12.28	51.72	5.58	2014	[96]
PFN	PTB7: PC71BM	0.754	17.46	69.99	9.214	2012	[97]
Ga-doped ZnO		0.75	14.96	64.95	7.34	2013	[95]
ZnO/PFN		0.75	15.5	68.9	8.01	2013	[98]
PFN-Hg		0.74	17.37	71.2	9.11	2013	[99]
ZnO-R/Polar solvent		0.71	16.76	73	8.69	2014	[100]
InZnO-BisC60	PTB7-Th: PC71BM	0.8	17.24	74.1	10.22	2014	[49]
ZnO/PEO nanodots		0.798	18.10	67.95	9.53	2015	[101]
ZnO/PEI		0.78	16.25	64	8.22	2015	[102]
C60-ETA		0.78	17.43	68.5	9.55	2016	[103]

3.6.1 Metal Oxides

Metal oxides offer superior properties for use as electron and hole extraction layers, such as excellent stability, low cost and desirable electronic properties like high charge carrier mobilities [90]. Besides ITO, applied as a transparent electrode, titanium oxide (TiO_2) and zinc oxide (ZnO) are the most common metal oxides applied as ETLs in inverted polymer solar cells. The relatively wide band gap and low conductivity of TiO_2 has triggered several attempts to modify its properties with the aim of ultimately improving device performance [61], [91]–[93]. Doping TiO_2 with tin (Sn) enhanced the efficiency of PTB7:PCBM inverted devices from 6.70 % (undoped TiO_2) to 7.59 % (Sn-doped TiO_2) [92], as a consequence of reduced interfacial charge recombination. ZnO, however, has shown more progress than TiO_2 since it was first proposed in 2003 [94]. The use of ZnO nanoparticles within MDMO:PPV devices was firstly reported by Beek et al. [95]. Similar to TiO_2, chemical doping of ZnO enhances the surface conductivity and charge mobility, and provides favourable distribution of dopants at ZnO/ITO and ZnO/organic interfaces [51], [84], [96]. Treating the surface of a pristine ZnO film with ionic surface modifiers like PEIE [97] and PEI [98] has be shown to enhance device performance effectively. Although these treatments can be effective for devices at a laboratory scale, however, they are not suitable for mass production, where low cost, and easy processing materials with high yields suitable for large area and flexible roll-to-roll production are required.

3.6.2 *Conjugated Polyelectrolyte*

Organic conjugated polyelectrolytes (CPE) are alternatives to metal oxide materials. CPEs are n-type conducting materials, soluble in alcohol based solvents, solution processed, compatible with the top organic layer, and applicable for spray-coating. A thin layer of CPE, in the order of 5 – 10 nm, is sufficient to tune the electronic structure of ITO via the formation of a dipole layer. The most popular example is poly[(9,9- dioctyl-2,7-fluorene)- alt -(9,9-bis(3 ′ -(N , N -dimethylamino)propyl)- 2,7-fluorene)] (PFN) [99]–[101]. Direct deposition of PFN onto the ITO surface for PCDTBT: PCBM based inverted devices has improved their efficiencies from 1.82 % (without PFN) to 5.90 %, compared to 5.65 % for standard devices. This is due to the improved V_{oc} from 0.57 eV (without PFN) to 0.9 eV for both device structures [100]. In addition, PFN has been used to modify the ZnO surface, with a 17 % increase in PTB7:PCBM devices reported [102]. PFN does not only enhance electron extraction at ZnO/PTB7 BHJ interface, but also increases device reliability by smoothing the ZnO surface.

Furthermore, much of the benefit of conjugated polyelectrolytes is simply from using a polar solvent with little to do with the polymer itself [103], [104]. Zhou et al. [103] reported a significant enhancement of efficiency in PTB7-based inverted devices by methanol treatment. The effects of methanol treatment were shown in an improvement in the built-in voltage, a decrease in series resistance, an enhanced charge-transport property, an accelerated and enlarged charge extraction, and a reduced charge recombination, which induce a simultaneous enhancement in V_{oc}, Jsc, and FF. Other types of ionic organic materials have been also reported, however, such as non-conjugated PE [105], zwitterions [106], and self-assembled monolayers [107].

3.6.3 *Organic Surface Modifiers*

Organic surface modifiers refer to small organic molecules that are able to form an ultra-thin layer of ordered self-assembling monolayers (SAMs). The formation of a SAM does not require a huge amount of materials, and is therefore considered to be cost effective. The unique features of these modifiers allow them to adhere strongly to inorganic surfaces (e. g. ITO) via their terminal functional groups, enabling them to tune the surface work function, surface homogeneity and surface energy [107]. Well-studied SAM materials are based on phosphoric acid [108], trimethoxysilane [109], carboxylic acid [110], benzoic acid [111] among others. Changes in the ITO work function of up to 1.0 eV have already been reported using these materials. The resultant work functions were varied from 4.4 eV to 5.5 eV. These materials are usually processed from toxic-organic solvents and require a pre-treatment of the ITO surface with a strong acid solution. Alternatively, a recently emerging new kind of surface modifier are naturally occurring peptide molecules, which are water soluble, non-toxic and easy-to-process [112]–[114]. These result in a significant reduction in the ITO work function to be in order of 3.5 eV – 3.85 eV.

3.7 References

[1] A. K. Ghosh and T. Feng, "Rectification, space-charge-limited current, photovoltaic and photoconductive properties of Al/tetracene/Au sandwich cell," *J. Appl. Phys.*, vol. 44, no. 6, pp. 2781–2788, 1973.

[2] A. K. Ghosh and T. Feng, "Merocynanine organic solar cells," *J. Appl. Phys.*, vol. 49, no. 12, pp. 5982–5989, 1978.

[3] C. W. Tang, "Two-layer organic photovoltaic cell," *Appl. Phys. Lett.*, vol. 48, no. 2, p. 183, Jan. 1986.

[4] J. J. M. Halls, C. A. Walsh, N. C. Greenham, E. A. Marseglia, R. H. Friend, S. C. Moratti, and A. B. Holmes, "Efficient photodiodes from interpenetrating polymer networks," *Nature*, vol. 376, no. 6540, pp. 498–500, Aug. 1995.

[5] G. Yu, J. Gao, J. C. Hummelen, F. Wudl, and a. J. Heeger, "Polymer Photovoltaic Cells: Enhanced Efficiencies via a Network of Internal Donor-Acceptor Heterojunctions," *Science (80-.).*, vol. 270, pp. 1789–1791, 1995.

[6] N. S. Sariciftci, L. Smilowitz, A. J. Heeger, and F. Wudl, "Photoinduced electron transfer from a conducting polymer to buckminsterfullerene.," *Science*, vol. 258, no. 5087, pp. 1474–6, Nov. 1992.

[7] C. J. Brabec, G. Zerza, G. Cerullo, S. De Silvestri, S. Luzzati, J. C. Hummelen, and S. Sariciftci, "Tracing photoinduced electron transfer process in conjugated polymer/fullerene bulk heterojunctions in real time," *Chem. Phys. Lett.*, vol. 340, no. 3–4, pp. 232–236, Jun. 2001.

[8] S. Park, A. Roy, S. Beaupré, S. Cho, N. Coates, J. Moon, D. Moses, M. Leclerc, and K. Lee, "Bulk heterojunction solar cells with internal quantum efficiency approaching 100%," *Nat. Photonics*, vol. 3, pp. 297–302, 2009.

[9] C. J. Brabec, M. Heeney, I. McCulloch, and J. Nelson, "Influence of blend microstructure on bulk heterojunction organic photovoltaic performance," *Chem Soc Rev*, vol. 40, no. 3, pp. 1185–1199, 2011.

[10] J. W. Kingsley, P. P. Marchisio, H. Yi, A. Iraqi, C. J. Kinane, S. Langridge, R. L. Thompson, A. J. Cadby, A. J. Pearson, D. G. Lidzey, R. A. L. Jones, and A. J. Parnell, "Molecular weight dependent vertical composition profiles of PCDTBT:PC 71 BM blends for organic photovoltaics," *Sci. Rep.*, vol. 4, p. 5286, 2014.

[11] A. J. Moulé and K. Meerholz, “Morphology control in solution-processed bulk-heterojunction solar cell mixtures,” *Adv. Funct. Mater.*, vol. 19, no. 19, pp. 3028–3036, 2009.

[12] S. Alem, T.-Y. Chu, S. C. Tse, S. Wakim, J. Lu, R. Movileanu, Y. Tao, F. Bélanger, D. Désilets, S. Beaupré, M. Leclerc, S. Rodman, D. Waller, and R. Gaudiana, “Effect of mixed solvents on PCDTBT:PC70BM based solar cells,” *Org. Electron.*, vol. 12, no. 11, pp. 1788–1793, Nov. 2011.

[13] X. Liu, S. Huettner, Z. Rong, M. Sommer, and R. H. Friend, “Solvent additive control of morphology and crystallization in semiconducting polymer blends.,” *Adv. Mater.*, vol. 24, no. 5, pp. 669–74, Feb. 2012.

[14] E. Verploegen, R. Mondal, C. J. Bettinger, S. Sok, M. F. Toney, and Z. Bao, “Effects of Thermal Annealing Upon the Morphology of Polymer-Fullerene Blends,” *Adv. Funct. Mater.*, vol. 20, no. 20, pp. 3519–3529, Oct. 2010.

[15] M. Campoy-Quiles, T. Ferenczi, T. Agostinelli, P. G. Etchegoin, Y. Kim, T. D. Anthopoulos, P. N. Stavrinou, D. D. C. Bradley, and J. Nelson, “Morphology evolution via self-organization and lateral and vertical diffusion in polymer:fullerene solar cell blends,” *Nat. Mater.*, vol. 7, no. 2, pp. 158–164, Jan. 2008.

[16] Z. Xu, L. M. Chen, G. Yang, C. H. Huang, J. Hou, Y. Wu, G. Li, C. S. Hsu, and Y. Yang, “Vertical phase separation in poly(3-hexylthiophene): Fullerene derivative blends and its advantage for inverted structure solar cells,” *Adv. Funct. Mater.*, 2009.

[17] L. M. Chen, Z. Hong, G. Li, and Y. Yang, “Recent progress in polymer solar cells: Manipulation of polymer: Fullerene morphology and the formation of efficient inverted polymer solar cells,” *Advanced Materials*. 2009.

[18] F. L. Zhang, A. Gadisa, O. Inganäs, M. Svensson, and M. R. Andersson, “Influence of buffer layers on the performance of polymer solar cells,” *Appl. Phys. Lett.*, vol. 84, no. 19, pp. 3906–3908, 2004.

[19] R. Po, C. Carbonera, A. Bernardi, and N. Camaioni, “The role of buffer layers in polymer solar cells,” *Energy Environ. Sci.*, vol. 4, no. 2, p. 285, 2011.

[20] G. Li, C.-W. Chu, V. Shrotriya, J. Huang, and Y. Yang, “Efficient inverted polymer solar cells,” *Appl. Phys. Lett.*, vol. 88, no. 25, p. 253503, Jun. 2006.

[21] B. Zimmermann, U. Würfel, and M. Niggemann, “Longterm stability of efficient inverted P3HT:PCBM solar cells,” *Sol. Energy Mater. Sol. Cells*, vol. 93, no. 4,

pp. 491–496, 2009.

[22] A. R. bin Mohd Yusoff, H. P. Kim, and J. Jang, “Inverted organic solar cells with TiOx cathode and graphene oxide anode buffer layers,” *Sol. Energy Mater. Sol. Cells*, vol. 109, pp. 63–69, Feb. 2013.

[23] P. Cheng and X. Zhan, “Stability of organic solar cells: challenges and strategies,” *Chem. Soc. Rev.*, vol. 45, pp. 2544–2582, 2016.

[24] J. Jung, D. L. Kim, S. H. Oh, and H. J. Kim, “Stability enhancement of organic solar cells with solution-processed nickel oxide thin films as hole transport layers,” *Sol. Energy Mater. Sol. Cells*, vol. 102, pp. 103–108, Jul. 2012.

[25] M. Girtan and M. Rusu, “Role of ITO and PEDOT:PSS in stability/degradation of polymer:fullerene bulk heterojunctions solar cells,” *Sol. Energy Mater. Sol. Cells*, vol. 94, no. 3, pp. 446–450, Mar. 2010.

[26] M. S. Vezie, S. Few, I. Meager, G. Pieridou, B. Dörling, R. S. Ashraf, A. R. Goñi, H. Bronstein, I. McCulloch, S. C. Hayes, M. Campoy-Quiles, and J. Nelson, “Exploring the origin of high optical absorption in conjugated polymers,” *Nat. Mater.*, vol. 15, no. 7, pp. 746–753, 2016.

[27] F. Padinger, R. S. Rittberger, N. S. Sariciftci, F. Padinger, R. S. Rittberger, R. S. Rittberger, N. S. Sariciftci, and N. S. Sariciftci, “Effects of postproduction treatment om plastic solar cells,” *Adv. Funct. Mater.*, vol. 13, no. 1, p. 85, 2003.

[28] Y. Kim, S. Cook, S. M. Tuladhar, S. A. Choulis, J. Nelson, J. R. Durrant, D. D. C. Bradley, M. Giles, I. McCulloch, C.-S. Ha, and M. Ree, “A strong regioregularity effect in self-organizing conjugated polymer films and high-efficiency polythiophene:fullerene solar cells,” *Nat. Mater.*, vol. 5, no. 3, pp. 197–203, 2006.

[29] W. Ma, C. Yang, X. Gong, K. Lee, and A. J. Heeger, “Thermally stable, efficient polymer solar cells with nanoscale control of the interpenetrating network morphology,” *Adv. Funct. Mater.*, vol. 15, no. 10, pp. 1617–1622, 2005.

[30] M. D. Irwin, D. B. Buchholz, A. W. Hains, R. P. H. Chang, and T. J. Marks, “p-Type semiconducting nickel oxide as an efficiency-enhancing anode interfacial layer in polymer bulk-heterojunction solar cells,” *Proc. Natl. Acad. Sci.*, vol. 105, no. 8, pp. 2783–2787, 2008.

[31] A. J. Moulé and K. Meerholz, “Controlling morphology in polymer-fullerene mixtures,” *Adv. Mater.*, vol. 20, no. 2, pp. 240–245, 2008.

[32] N. Blouin, a. Michaud, and M. Leclerc, “A Low-Bandgap Poly(2,7-Carbazole) Derivative for Use in High-Performance Solar Cells,” *Adv. Mater.*, vol. 19, no. 17, pp. 2295–2300, Sep. 2007.

[33] H. Yi, S. Al-Faifi, A. Iraqi, D. C. Watters, J. Kingsley, and D. G. Lidzey, “Carbazole and thienyl benzo[1,2,5]thiadiazole based polymers with improved open circuit voltages and processability for application in solar cells,” *J. Mater. Chem.*, vol. 21, no. 35, p. 13649, 2011.

[34] D. C. Watters, H. Yi, A. J. Pearson, J. Kingsley, A. Iraqi, and D. Lidzey, “Fluorene-based co-polymer with high hole mobility and device performance in bulk heterojunction organic solar cells.,” *Macromol. Rapid Commun.*, vol. 34, no. 14, pp. 1157–62, Jul. 2013.

[35] T.-Y. Chu, S. Alem, S.-W. Tsang, S.-C. Tse, S. Wakim, J. Lu, G. Dennler, D. Waller, R. Gaudiana, and Y. Tao, “Morphology control in polycarbazole based bulk heterojunction solar cells and its impact on device performance,” *Appl. Phys. Lett.*, vol. 98, no. 25, p. 253301, 2011.

[36] Y. Sun, J. H. Seo, C. J. Takacs, J. Seifter, and A. J. Heeger, “Inverted polymer solar cells integrated with a low-temperature-annealed sol-gel-derived ZnO Film as an electron transport layer.,” *Adv. Mater.*, vol. 23, no. 14, pp. 1679–83, Apr. 2011.

[37] D. C. Watters, J. Kingsley, H. Yi, T. Wang, A. Iraqi, and D. Lidzey, “Optimising the efficiency of carbazole co-polymer solar-cells by control over the metal cathode electrode,” *Org. Electron.*, vol. 13, no. 8, pp. 1401–1408, Aug. 2012.

[38] T. Wang, A. J. Pearson, A. D. F. Dunbar, P. a. Staniec, D. C. Watters, H. Yi, A. J. Ryan, R. a. L. Jones, A. Iraqi, and D. G. Lidzey, “Correlating Structure with Function in Thermally Annealed PCDTBT:PC70BM Photovoltaic Blends,” *Adv. Funct. Mater.*, vol. 22, no. 7, pp. 1399–1408, Apr. 2012.

[39] J. Liu, S. Shao, G. Fang, B. Meng, Z. Xie, and L. Wang, “High-Efficiency Inverted Polymer Solar Cells with Transparent and Work-Function Tunable MoO3-Al Composite Film as Cathode Buffer Layer,” *Adv. Mater.*, vol. 24, no. 20, pp. 2774–2779, May 2012.

[40] C. H. Peters, I. T. Sachs-Quintana, J. P. Kastrop, S. Beaupré, M. Leclerc, and M. D. McGehee, “High efficiency polymer solar cells with long operating lifetimes,” *Adv. Energy Mater.*, vol. 1, no. 4, pp. 491–494, 2011.

[41] C. H. Peters, I. T. Sachs-Quintana, W. R. Mateker, T. Heumueller, J. Rivnay, R. Noriega, Z. M. Beiley, E. T. Hoke, A. Salleo, and M. D. McGehee, “The

mechanism of burn-in loss in a high efficiency polymer solar cell," *Adv. Mater.*, vol. 24, no. 5, pp. 663–668, 2012.

[42] Y. Liang, Y. Wu, D. Feng, S.-T. Tsai, H.-J. Son, G. Li, and L. Yu, "Development of New Semiconducting Polymers for High Performance Solar Cells," *J. Am. Chem. Soc.*, vol. 131, no. 1, pp. 56–57, 2008.

[43] Y. Liang, Z. Xu, J. Xia, S.-T. Tsai, Y. Wu, G. Li, C. Ray, and L. Yu, "For the bright future-bulk heterojunction polymer solar cells with power conversion efficiency of 7.4%.," *Adv. Mater.*, vol. 22, no. 20, pp. E135-8, May 2010.

[44] Y. Liang, D. Feng, Y. Wu, S. T. Tsai, G. Li, C. Ray, and L. Yu, "Highly efficient solar cell polymers developed via fine-tuning of structural and electronic properties," *J. Am. Chem. Soc.*, vol. 131, no. 22, pp. 7792–7799, 2009.

[45] C. H. To, A. Ng, Q. Dong, A. B. Djurišić, J. A. Zapien, W. K. Chan, and C. Surya, "Effect of PTB7 Properties on the Performance of PTB7:PC $_{71}$ BM Solar Cells," *ACS Appl. Mater. Interfaces*, vol. 7, no. 24, pp. 13198–13207, 2015.

[46] H.-Y. Chen, S.-H. Lin, J.-Y. Sun, C.-H. Hsu, S. Lan, and C.-F. Lin, "Morphologic improvement of the PBDTTT-C and PC71BM blend film with mixed solvent for high-performance inverted polymer solar cells.," *Nanotechnology*, vol. 24, no. 48, p. 484009, 2013.

[47] C. H. Chen, J. Hou, S. Zhang, Y. Liang, G. Yang, Y. Yang, L. Yu, Y. Wu, and G. Li, "Polymer solar cells with enhanced open-circuit voltage and efficiency," *Nat. Photonics*, vol. 3, p. 649653, 2009.

[48] P. Adhikary, S. Venkatesan, N. Adhikari, P. P. Maharjan, O. Adebanjo, J. Chen, and Q. Qiao, "Enhanced charge transport and photovoltaic performance of PBDTTT-C-T/PC70BM solar cells via UV-ozone treatment.," *Nanoscale*, vol. 5, no. 20, pp. 10007–10013, 2013.

[49] S. H. Liao, H. J. Jhuo, Y. S. Cheng, and S. A. Chen, "Fullerene derivative-doped zinc oxide nanofilm as the cathode of inverted polymer solar cells with low-bandgap polymer (PTB7-Th) for high performance," *Adv. Mater.*, vol. 25, no. 34, pp. 4766–4771, 2013.

[50] M. C. Scharber, D. Mühlbacher, M. Koppe, P. Denk, C. Waldauf, a. J. Heeger, and C. J. Brabec, "Design Rules for Donors in Bulk-Heterojunction Solar Cells—Towards 10 % Energy-Conversion Efficiency," *Adv. Mater.*, vol. 18, no. 6, pp. 789–794, Mar. 2006.

[51] S.-H. Liao, H.-J. Jhuo, P.-N. Yeh, Y.-S. Cheng, Y.-L. Li, Y.-H. Lee, S. Sharma,

and S.-A. Chen, “Single Junction Inverted Polymer Solar Cell Reaching Power Conversion Efficiency 10.31% by Employing Dual-Doped Zinc Oxide Nano-Film as Cathode Interlayer,” *Sci. Rep.*, vol. 4, p. 6813, Oct. 2014.

[52] W. Zhao, S. Li, H. Yao, S. Zhang, Y. Zhang, B. Yang, and J. Hou, “Molecular Optimization Enables over 13% Efficiency in Organic Solar Cells,” *J. Am. Chem. Soc.*, vol. 139, no. 21, pp. 7148–7151, 2017.

[53] M. M. Wienk, J. M. Kroon, W. J. H. Verhees, J. Knol, J. C. Hummelen, P. A. van Hal, and R. A. J. Janssen, “Efficient Methano[70]fullerene/MDMO-PPV Bulk Heterojunction Photovoltaic Cells,” *Angew. Chemie Int. Ed.*, vol. 42, no. 29, pp. 3371–3375, 2003.

[54] T. B. Singh, N. Marjanović, G. J. Matt, S. Günes, N. S. Sariciftci, A. Montaigne Ramil, A. Andreev, H. Sitter, R. Schwödiauer, and S. Bauer, “High-mobility n-channel organic field-effect transistors based on epitaxially grown C60 films,” *Org. Electron.*, vol. 6, no. 3, pp. 105–110, 2005.

[55] J. W. Arbogast and C. S. Foote, “Photophysical properties of C70,” *J. Am. Chem. Soc.*, vol. 113, no. 23, pp. 8886–8889, 1991.

[56] H. Lin and Q. Wang, “Non-fullerene small molecule electron acceptors for high-performance organic solar cells,” *J. Energy Chem.*, 2017.

[57] B. G. Lewis and D. C. Paine, “Applications and Processing of Transparent Conducting Oxides,” *MRS Bull.*, vol. 25, pp. 22–27, 2000.

[58] H. Kim, J. S. Horwitz, G. P. Kushto, Z. H. Kafafi, and D. B. Chrisey, “Indium tin oxide thin films grown on flexible plastic substrates by pulsed-laser deposition for organic light-emitting diodes,” *Appl. Phys. Lett.*, vol. 79, no. 3, pp. 284–286, 2001.

[59] N. G. Patel, P. D. Patel, and V. S. Vaishnav, “Indium tin oxide (ITO) thin film gas sensor for detection of methanol at room temperature,” *Sonsors Actuators B Chem.*, vol. 96, pp. 180–189, 2003.

[60] S. Optik, F. Nipis, T. Oksida, and T. Florin, “Structural , Optical and Electrical Properties of Fluorine Doped Tin Oxide Thin Films Deposited Using Inkjet Printing Technique,” *Sains Malaysiana*, vol. 40, no. FTO, pp. 251–257, 2011.

[61] F. Li, C. Chen, F. Tan, C. Li, G. Yue, L. Shen, and W. Zhang, “Semitransparent inverted polymer solar cells employing a sol-gel-derived TiO2 electron-selective layer on FTO and MoO3/Ag/MoO3 transparent electrode,” *Nanoscale Res. Lett.*, vol. 9, no. 1, p. 579, 2014.

[62] J. Van De Lagemaat, T. M. Barnes, G. Rumbles, S. E. Shaheen, T. J. Coutts, C. Weeks, I. Levitsky, J. Peltola, and P. Glatkowski, “Organic solar cells with carbon nanotubes replacing In2 O3: Sn as the transparent electrode,” *Appl. Phys. Lett.*, vol. 88, no. 23, pp. 1–4, 2006.

[63] S.-I. Na, S.-S. Kim, J. Jo, and D.-Y. Kim, “Efficient and Flexible ITO-Free Organic Solar Cells Using Highly Conductive Polymer Anodes,” *Adv. Mater.*, vol. 20, no. 21, pp. 4061–4067, 2008.

[64] C. Su, T. K. Sheu, Y. T. Chang, M. A. Wan, M. C. Feng, and W. C. Hung, “Preparation of ITO thin films by sol-gel process and their characterizations,” *Synth. Met.*, vol. 153, no. 1–3, pp. 9–12, 2005.

[65] T. Maruyama and K. Fukui, “Indium tin oxide thin films prepared by chemical vapour deposition,” *Thin Solid Films*, vol. 203, no. 2, pp. 297–302, 1991.

[66] C. A. Pan and T. P. Ma, “High-quality transparent conductive indium oxide films prepared by thermal evaporation,” *Appl. Phys. Lett.*, vol. 37, no. 2, pp. 163–165, 1980.

[67] M. Chuang, “ITO Films Prepared by Long-throw Magnetron Sputtering without Oxygen Partial Pressure,” *J. Mater. Sci. Technol.*, vol. 26, no. 7, pp. 577–583, 2010.

[68] M. Huang, Z. Hameiri, A. G. Aberle, and T. Mueller, “Comparative study of amorphous indium tin oxide prepared by pulsed-DC and unbalanced RF magnetron sputtering at low power and low temperature conditions for heterojunction silicon wafer solar cell applications,” *Vacuum*, vol. 119, pp. 68–76, 2015.

[69] S. Ishibashi, Y. Higuchi, Y. Ota, and K. Nakamura, “Low resistivity indium–tin oxide transparent conductive films. II. Effect of sputtering voltage on electrical property of films,” *J. Vac. Sci. Technol. A Vacuum, Surfaces, Film.*, vol. 8, no. 3, pp. 1403–1406, 1990.

[70] T. Karasawa and Y. Miyata, “Electrical and optical properties of indium tin oxide thin films deposited on unheated substrates by d . c . reactive sputtering,” *Technology*, vol. 223, pp. 135–139, 1993.

[71] L. Meng and M. . dos Santos, “Properties of indium tin oxide films prepared by rf reactive magnetron sputtering at different substrate temperature,” *Thin Solid Films*, vol. 322, no. 1–2, pp. 56–62, 1998.

[72] K. Sugiyama, H. Ishii, Y. O. Seki, K. Sugiyama, H. Ishii, and Y. Ouchi,

"Dependence of indium – tin – oxide work function on surface cleaning method as studied by ultraviolet and x-ray photoemission spectroscopies," vol. 87, no. 1, pp. 295–298, 2000.

[73] A. Sharma, S. E. Watkins, D. A. Lewis, and G. Andersson, "Effect of indium and tin contamination on the efficiency and electronic properties of organic bulk hetero-junction solar cells," *Sol. Energy Mater. Sol. Cells*, vol. 95, pp. 3251–3255, 2011.

[74] Y. T. Cheng, J. J. Ho, C. K. Wang, W. Lee, C. C. Lu, B. S. Yau, J. L. Nain, S. H. Chang, C. C. Chang, and K. L. Wang, "Improvement of organic solar cells by flexible substrate and ITO surface treatments," *Appl. Surf. Sci.*, vol. 256, no. 24, pp. 7606–7611, 2010.

[75] F. Marchesi, P. P. Boix, S. Ruiz-raga, T. Ripolles-sanchis, and A. Guerrero, "How the Charge-Neutrality Level of Interface States Controls Energy Level Alignment in Cathode Contacts of Organic Bulk-Heterojunction Solar Cells," no. 4, pp. 3453–3460, 2012.

[76] V. Coropceanu, J. Cornil, D. Silva, D. A, Y. Olivier, R. Silbey, J. L. Bredas, D. A. da Silva Filho, J.-L. J.-L. Brédas, Y. Olivier, R. Silbey, and J.-L. J.-L. Brédas, "Charge transport in organic semiconductors.," *Chem. Rev.*, vol. 107, no. 4, pp. 926–52, 2007.

[77] Y. Q. Li, Q. K. Wang, Q. D. Ou, and J. X. Tang, "Interface energetics and engineering of organic heterostructures in organic photovoltaic cells," *Sci. China Chem.*, vol. 59, no. 4, pp. 422–435, 2016.

[78] Q. D. Yang, H. W. Li, Y. Cheng, Z. Guan, T. Liu, T. W. Ng, C. S. Lee, and S. W. Tsang, "Probing the Energy Level Alignment and the Correlation with Open-Circuit Voltage in Solution-Processed Polymeric Bulk Heterojunction Photovoltaic Devices," *ACS Appl. Mater. Interfaces*, vol. 8, no. 11, pp. 7283–7290, 2016.

[79] C. Tengstedt, W. Osikowicz, W. R. Salaneck, I. D. Parker, C.-H. Hsu, and M. Fahlman, "Fermi-level pinning at conjugated polymer interfaces," *Appl. Phys. Lett.*, vol. 88, no. 5, p. 53502, Feb. 2006.

[80] I. Lange, J. C. Blakesley, J. Frisch, A. Vollmer, N. Koch, and D. Neher, "Band bending in conjugated polymer layers," *Phys. Rev. Lett.*, vol. 106, no. 21, pp. 1–4, 2011.

[81] T. M. Clarke, J. Peet, A. Nattestad, N. Drolet, G. Dennler, C. Lungenschmied, M. Leclerc, and A. J. Mozer, "Charge carrier mobility, bimolecular

recombination and trapping in polycarbazole copolymer:fullerene (PCDTBT:PCBM) bulk heterojunction solar cells," *Org. Electron.*, vol. 13, no. 11, pp. 2639–2646, Nov. 2012.

[82] Z. He, C. Zhong, X. Huang, W.-Y. Wong, H. Wu, L. Chen, S. Su, and Y. Cao, "Simultaneous enhancement of open-circuit voltage, short-circuit current density, and fill factor in polymer solar cells.," *Adv. Mater.*, vol. 23, no. 40, pp. 4636–43, Oct. 2011.

[83] C. Z. Li, C. C. Chueh, F. Ding, H. L. Yip, P. W. Liang, X. Li, and A. K. Y. Jen, "Doping of fullerenes via anion-induced electron transfer and its implication for surfactant facilitated high performance polymer solar cells," *Adv. Mater.*, vol. 25, no. 32, pp. 4425–4430, 2013.

[84] X. Liu, X. Li, Y. Li, C. Song, L. Zhu, W. Zhang, H. Q. Wang, and J. Fang, "High-Performance Polymer Solar Cells with PCE of 10.42% via Al-Doped ZnO Cathode Interlayer," *Adv. Mater.*, pp. 7405–7412, 2016.

[85] J. Y. Kim, S. H. Kim, H.-H. Lee, K. Lee, W. Ma, X. Gong, and a. J. Heeger, "New Architecture for High-Efficiency Polymer Photovoltaic Cells Using Solution-Based Titanium Oxide as an Optical Spacer," *Adv. Mater.*, vol. 18, no. 5, pp. 572–576, Mar. 2006.

[86] A. Roy, S. H. Park, S. Cowan, M. H. Tong, S. Cho, K. Lee, and A. J. Heeger, "Titanium suboxide as an optical spacer in polymer solar cells," *Appl. Phys. Lett.*, vol. 95, no. 1, pp. 1–4, 2009.

[87] G. Li, C. W. Chu, V. Shrotriya, J. Huang, and Y. Yang, "Efficient inverted polymer solar cells," *Appl. Phys. Lett.*, vol. 88, no. 25, pp. 3–6, 2006.

[88] N. Sekine, C.-H. Chou, W. L. Kwan, and Y. Yang, "ZnO nano-ridge structure and its application in inverted polymer solar cell," *Org. Electron.*, vol. 10, no. 8, pp. 1473–1477, Dec. 2009.

[89] J.-W. Lee, J.-S. Yeo, and S.-S. Kim, "Inverted polymer solar cells with brush-painted ZnO electron transport layer," *J. Ind. Eng. Chem.*, 2017.

[90] S. Chen, J. R. Manders, S.-W. Tsang, and F. So, "Metal oxides for interface engineering in polymer solar cells," *Journal of Materials Chemistry*. p. 24202, 2012.

[91] J. You, C.-C. Chen, L. Dou, S. Murase, H.-S. Duan, S. A. Hawks, T. Xu, H. J. Son, L. Yu, G. Li, and Y. Yang, "Metal oxide nanoparticles as an electron-transport layer in high-performance and stable inverted polymer solar cells.,"

Adv. Mater., vol. 24, no. 38, pp. 5267–72, Oct. 2012.

[92] M. Thambidurai, J. Y. Kim, H. Song, Y. Ko, N. Muthukumarasamy, D. Velauthapillai, V. W. Bergmann, S. a. L. Weber, and C. Lee, "Enhanced power conversion efficiency of inverted organic solar cells by using solution processed Sn-doped TiO2 as an electron transport layer," *J. Mater. Chem. A*, vol. 2, no. 29, p. 11426, 2014.

[93] Y. Bai, F. D. Angelis, J. Bisquert, and P. Wang, "Titanium dioxide nanomaterials for photocatalytic applications," *Chem. Rev.*, pp. 10131–10176, 2014.

[94] T. Umeda, T. Shirakawa, A. Fujii, and K. Yoshino, "Improvement of characteristics of organic photovoltaic devices composed of conducting polymer-fullerene systems by introduction of ZnO layer," *Japanese J. Appl. Physics, Part 2 Lett.*, vol. 42, no. 12 A, pp. 8–11, 2003.

[95] W. J. E. Beek, M. M. Wienk, and R. A. J. Janssen, "Efficient hybrid solar cells from zinc oxide nanoparticles and a conjugated polymer," *Adv. Mater.*, vol. 16, no. 12, pp. 1009–1013, 2004.

[96] M. Thambidurai, J. Y. Kim, C. Kang, N. Muthukumarasamy, H.-J. Song, J. Song, Y. Ko, D. Velauthapillai, and C. Lee, "Enhanced photovoltaic performance of inverted organic solar cells with In-doped ZnO as an electron extraction layer," *Renew. Energy*, vol. 66, pp. 433–442, Jun. 2014.

[97] L. Nian, W. Zhang, S. Wu, L. Qin, L. Liu, Z. Xie, H. Wu, and Y. Ma, "Perylene Bisimide as a Promising Zinc Oxide Surface Modifier: Enhanced Interfacial Combination for Highly Efficient Inverted Polymer Solar Cells," *ACS Appl. Mater. Interfaces*, vol. 7, no. 46, pp. 25821–25827, 2015.

[98] X. Jia, N. Wu, J. Wei, L. Zhang, Q. Luo, Z. Bao, Y. Q. Li, Y. Yang, X. Liu, and C. Q. Ma, "A low-cost and low-temperature processable zinc oxide-polyethylenimine (ZnO:PEI) nano-composite as cathode buffer layer for organic and perovskite solar cells," *Org. Electron. physics, Mater. Appl.*, vol. 38, pp. 150–157, 2016.

[99] Z. He, C. Zhang, X. Xu, L. Zhang, L. Huang, J. Chen, H. Wu, and Y. Cao, "Largely enhanced efficiency with a PFN/Al bilayer cathode in high efficiency bulk heterojunction photovoltaic cells with a low bandgap polycarbazole donor.," *Adv. Mater.*, vol. 23, no. 27, pp. 3086–9, Jul. 2011.

[100] R. Xia, D.-S. Leem, T. Kirchartz, S. Spencer, C. Murphy, Z. He, H. Wu, S. Su, Y. Cao, J. S. Kim, J. C. DeMello, D. D. C. Bradley, and J. Nelson, "Investigation of a Conjugated Polyelectrolyte Interlayer for Inverted Polymer:Fullerene Solar

Cells," *Adv. Energy Mater.*, vol. 3, no. 6, pp. 718–723, Jun. 2013.

[101] M. V. Srinivasan, M. Ito, P. Kumar, K. Abhirami, N. Tsuda, J. Yamada, P.-K. Shin, and S. Ochiai, "Performance Evaluation of an Organic Thin-Film Solar Cell of PTB7:PC 71 BM with an Alcohol-Soluble Polyelectrolyte Interlayer Prepared Using the Spray-Coating Method," *Ind. Eng. Chem. Res.*, vol. 54, no. 1, pp. 181–187, Jan. 2015.

[102] Y.-M. Chang and C.-Y. Leu, "Conjugated polyelectrolyte and zinc oxide stacked structure as an interlayer in highly efficient and stable organic photovoltaic cells," *J. Mater. Chem. A*, vol. 1, no. 21, p. 6446, May 2013.

[103] H. Zhou, Y. Zhang, J. Seifter, S. D. Collins, C. Luo, G. C. Bazan, T.-Q. Nguyen, and A. J. Heeger, "High-efficiency polymer solar cells enhanced by solvent treatment.," *Adv. Mater.*, vol. 25, no. 11, pp. 1646–52, Mar. 2013.

[104] Y. Zheng, S. Li, D. Zheng, and J. Yu, "Effects of different polar solvents for solvent vapor annealing treatment on the performance of polymer solar cells," *Org. Electron.*, vol. 15, no. 11, pp. 2647–2653, 2014.

[105] H. Kang, S. Hong, J. Lee, and K. Lee, "Electrostatically self-assembled nonconjugated polyelectrolytes as an ideal interfacial layer for inverted polymer solar cells.," *Adv. Mater.*, vol. 24, no. 22, pp. 3005–9, 2938, Jun. 2012.

[106] I. Etxebarria, J. Ajuria, and R. Pacios, "Solution-processable polymeric solar cells: A review on materials, strategies and cell architectures to overcome 10%," *Org. Electron.*, vol. 19, pp. 34–60, Jan. 2015.

[107] F. Rissner, G. M. Rangger, O. T. Hofmann, A. M. Track, G. Heimel, and E. Zojer, "Understanding the electronic structure of metal/SAM/organic-semiconductor heterojunctions," *ACS Nano*, vol. 3, no. 11, pp. 3513–3520, 2009.

[108] P. J. Hotchkiss, S. C. Jones, S. A. Paniagua, A. Sharma, B. Kippelen, N. R. Armstrong, and S. R. Marder, "The modification of indium tin oxide with phosphonic acids: Mechanism of binding, tuning of surface properties, and potential for use in organic electronic applications," *Acc. Chem. Res.*, 2012.

[109] C. G. Allen, D. J. Baker, J. M. Albin, H. E. Oertli, D. T. Gillaspie, D. C. Olson, T. E. Furtak, and R. T. Collins, "Surface modification of zno using triethoxysilane-based molecules," *Langmuir*, vol. 24, no. 23, pp. 13393–13398, 2008.

[110] S. a. Jadhav, "Self-assembled monolayers (SAMs) of carboxylic acids: an overview," *Cent. Eur. J. Chem.*, vol. 9, no. 3, pp. 369–378, 2011.

[111] S. K. Hau, H.-L. Yip, O. Acton, N. S. Baek, H. Ma, and A. K.-Y. Jen, "Interfacial modification to improve inverted polymer solar cells," *J. Mater. Chem.*, vol. 18, no. 42, p. 5113, Oct. 2008.

[112] A. L. and X. D. Riming Nie, "Environmentally friendly biomaterials as an interfacial layer for highly efficient and air-stable inverted organic solar cells," *J. Mater. Chem. A*, vol. 2, pp. 6734–6739, 2014.

[113] X. Deng, R. Nie, A. Li, H. Wei, S. Zheng, W. Huang, Y. Mo, Y. Su, Q. Wang, Y. Li, J. Tang, J. Xu, and K. Wong, "Ultra-Low Work Function Transparent Electrodes Achieved by Naturally Occurring Biomaterials for Organic Optoelectronic Devices," *Adv. Mater. Interfaces*, vol. 1, no. 7, pp. 1400215–1400221, Oct. 2014.

[114] A. Li, R. Nie, X. Deng, H. Wei, S. Zheng, Y. Li, J. Tang, and K. Y. Wong, "Highly efficient inverted organic solar cells using amino acid modified indium tin oxide as cathode," *Appl. Phys. Lett.*, vol. 104, no. 12, 2014.

Chapter 4

Device Fabrication

4.1 Introduction

This chapter reports on the process followed to fabricate inverted polymer solar cells used in this study. These include substrate treatment, solution preparation, thin film deposition, thermal evaporation, and encapsulation, respectively.

4.2 Substrate Treatment

The substrate used to fabricate inverted PSC devices was a 20 mm x 15 mm pre-patterned glass with a 100 nm thick layer of fully oxide ITO supplied by Ossila Ltd. The sheet resistance of the ITO layer is 20 Ω/□ with a route mean square (RMS) of 1.8 nm. **Figure 4.1** shows the detailed dimensional design of the ITO substrate (a) and device's six pixels (b). Note that the overlap between the top metallic contact and ITO fingers defines the six pixels as having a size of 2 mm x 2 mm (4 mm^2) for each pixel per substrate.

The surface treatment of ITO substrates included two sequential procedures that take place under a laminar fume hood in the clean room. First, a rigorous cleaning of any dirt and dust that may be present ono the ITO surface was undertaken, since these contribute to the formation of shorts and other defects affecting the quality of charge transport. This was done by sonicating the substrates in a hot water ultrasonic bath (60 °C) with Hellmanex III for 10 min. They were then 'dump-rinsed' in de-ionized water (DI) twice before a final sonication in isopropanol alcohol (IPA) for a further 10 min. With no further rinses required, the substrates were dried with a nitrogen flow. The second procedure was the modification of the cleaned ITO surface to fit the purpose of this thesis. These modifications form the basis of the following **Chapter 6**, **Chapter 7** and **Chapter 8**.

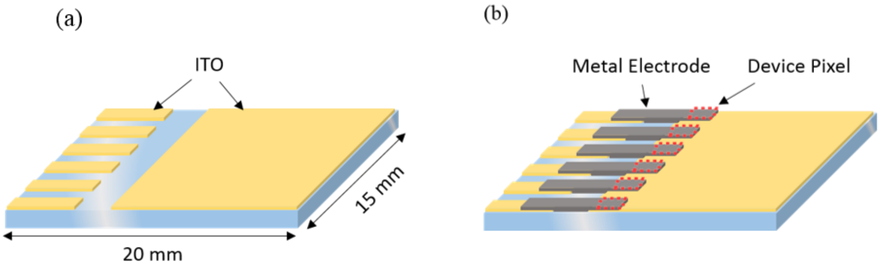

Figure 4.1 (a) ITO substrate design. (b) Device pixels defined by the overlap of ITO patterns and the metal electrode.

The ITO substrates used to fabricate the devices discussed in **Chapter 6** were modified by changing the organic detergent applied at the final ultrasonic bath. In addition to IPA, deionized water, methanol and acetone were tested. Some cleaned substrates were also subjected to UV ozone plasma and Argon sputtering for comparison. In **Chapter 7**, the cleaned substrates were thermally annealed at different temperatures ranging from 100 °C to 400 °C for 15 min before being transferred to a nitrogen filled glovebox.

For the purpose of **Chapter 8**, the ITO surface was modified with self-assembled monolayers (SAM) to introduce and control the direction of the surface dipole that was formed.

Table 4.1 lists the SAM materials used throughout this work, showing their chemical structure, molecular weight and the type of side chain charge. All SAM materials were sourced from Sigma & Aldrich and used as received. Before the treatment with the SAMs, however, the cleaned substrates were further subjected to UV ozone for 60 min. This step was critical to enhance the chemical adhesion of the SAM molecules onto the ITO surface. The substrates were then loaded into glassware containing a 10 mM aqueous solution of SAM (depending on the molecular weight for each material) and placed onto a hotplate heated at 90 °C to initiate the chemical reaction. The glassware was covered with aluminium foil to stop it absorbing ambient gasses during the treatment. The substrates were left there for 120 min before being rinsed in an excess of clean DI water so as to wash off any physisorbed molecules, followed by nitrogen flow drying. A summary of the steps involved in the SAM treatment is shown in **Figure 4.2**.

Table 4.1 List of self-assembled monolayer (SAM) materials used to modify the ITO surface for fabricating inverted polymer solar cells.

Full Name	**abbreviation**	**Chemical Structure**	**Molecular Weight (g/mol)**	**Side-chain Polarity**
Lysine	Lys	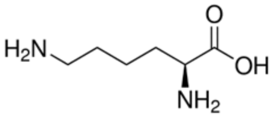	146.19	Positive
Glutamic Acid	Glut	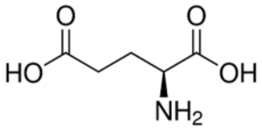	147.13	Negative
Serine	Ser	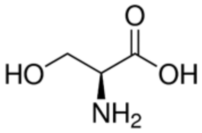	105.09	Neutral
Glycyl-glycine	Gly-Gly	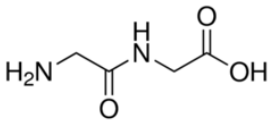	132.12	Non-polar
Glycyl-L-phenylalanine	Gly-Phe	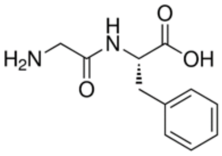	222.24	Non-polar

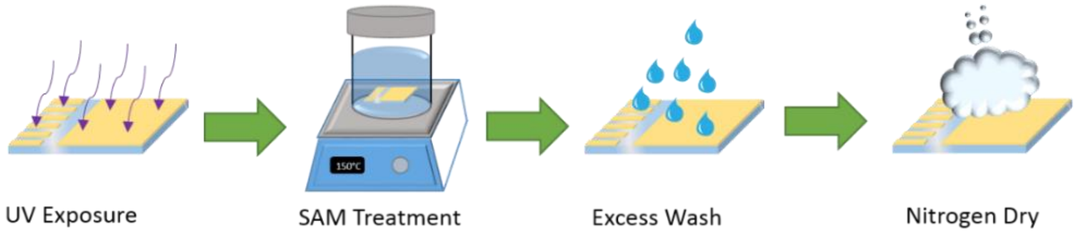

Figure 4.2 Chart flow showing the sequential process followed to treat ITO substrates with self-assembled monolayers.

Another way to modify the cleaned ITO surface was the use of buffer layers, as proposed in **Chapter 6**. These layer were made out of a solution-processable conjugated polyelectrolyte called poly [(9,9-bis(3'-(N,N-dimethylamino)propyl)-2,7-fluorene)-alt-2,7-(9,9–dioctylfluorene)] (PFN) and zinc oxide nanoparticles (ZnO-NP). Details of the ZnO-NP and PFN solution recipes and deposition conditions will be discussed in the following **Sections 4.2.2** and **4.2.3**, respectively. Note that, prior to the deposition of the metal oxide layer, the substrates were further cleaned in UV ozone for 60 min to enhance the wettability of the ITO. After finishing the surface treatment of the ITO substrates, they were transferred to a nitrogen filled glove box so that the active layers could be deposited.

4.3 Solution Preparation

All materials and solvents were used as received. The donor polymers and fullerene derivatives were supplied by either Ossila Ltd or Solarmer. Solvents and additives were provided by Sigma and Aldrich. The structure of the organic semiconductors used to fabricate inverted PSCs is shown in **Figure 4.3**. The optical and electronic properties of PCDTBT, PBDTT-FTTE, PTB7 PC70BM, and PC71BM, as provided by suppliers, are listed in **Table 4.2**.

(a) PCDTBT Poly(N-9’-heptadecanyl-2–7-carbazolealt-5,5-(4’,7’-di-2-thienyl-2’-1’-3’-benzothiadiazole) 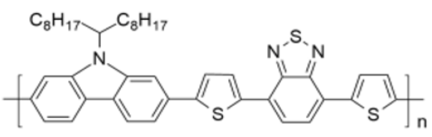 	(b) PBDTT-FTTE (PTB7-Th) Poly[4,8-bis(5-(2-ethylhexyl)thiophen-2-yl)benzo[1,2-b;4,5-b’]dithiophene-2,6-diyl-alt-(4-(2-ethylhexyl)-3-fluorothieno[3,4-b]thiophene-)-2-carboxylate-2-6-diyl)] 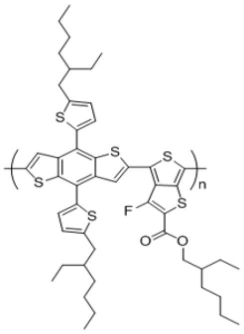
(c) PTB7 Poly[[4,8-bis[(2-ethylhexyl)oxy]benzo[1,2-b:4,5-b']dithiophene-2,6-diyl][3-fluoro-2-[(2-ethylhexyl)carbonyl]thieno[3,4-b]thiophenediyl]] 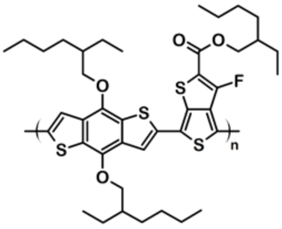 	(d) PC70BM [6,6]-Phenyl-C71-butyric acid methyl ester 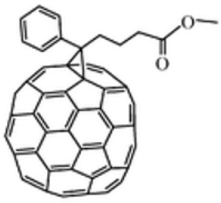

Figure 4.3 Chemical structures with full names of the donor polymers and fullerene derivative used to fabricate inverted PCS.

Table 4.2 Optical and electronic properties of the organic semiconductors studied. Data for PCDTBT and PC70BM were provided by the supplier, Ossila Ltd, while Solarmer supplied the data regarding PTB7-Th and PTB7. *The HOMO levels of PCDTBT and PC70BM were measured by UPS showing the average values of three samples with standard deviation errors calculated.

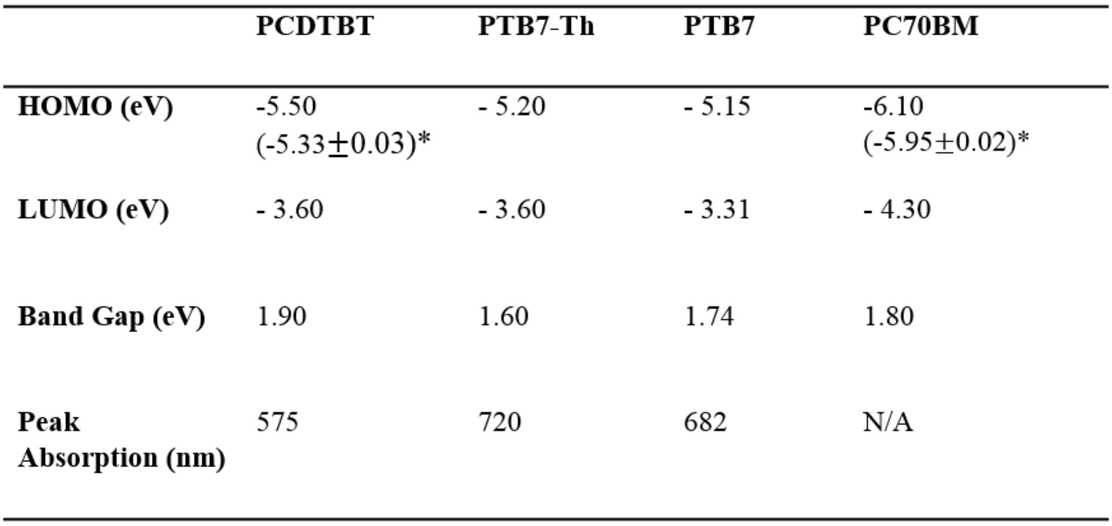

	PCDTBT	**PTB7-Th**	**PTB7**	**PC70BM**
HOMO (eV)	-5.50 (-5.33±0.03)*	- 5.20	- 5.15	-6.10 (-5.95±0.02)*
LUMO (eV)	- 3.60	- 3.60	- 3.31	- 4.30
Band Gap (eV)	1.90	1.60	1.74	1.80
Peak Absorption (nm)	575	720	682	N/A

The preparation of the polymer: fullerene solution blend was performed within a clean room environment and by six sequential steps. First, four 4 ml amber glass vials (V1, V2, V3, V4) were cleaned as follows; nitrogen blow-dried to remove large dust particles from both the vials and their screw cap and then cleaned using isopropanol and acetone, respectively, finishing off with a further nitrogen dry. The second step involved the weighing of each material in one of the clean vials using a chemical electronic balance. The dry polymer was weighed out at the desired concentration (5 – 14 mg/ml) into a clean vial (V1), while the dry fullerene was weighed out into V2. In the third step, all four vials were transferred into a nitrogen filled glovebox in order to make the solutions. The polymer solution was prepared by dissolving the dry polymer into either chlorobenzene (CB) or di-chlorobenzene (DCB). Then, the V1 was placed onto a hotplate with a fixed temperature (70 ˚C). Stir bars and frequent shaking were used to ensure full dissolving. The heating duration was varied from 2 - 12 hours depending on the solubility of the donor polymer. In the fourth step, the V1 was allowed to cool down for 10 min before the polymer solution was filtered into the clean V3 vial, using a 0.45 μm polytetrafluoroethylene (PTFE) filter. In the fifth step, the required blend ratio was achieved by dispensing the correct volume of the polymer solution into the V2 vial containing the dry fullerene. The polymer solution left over was either disposed of or saved for re-use on the same day in a further experiment with vial caps wrapped off with a Parafilm to prevent solvent evaporation. The polymer: fullerene solution (V4 vial) was retained back onto the hotplate. The heating temperature and duration were kept constant and similar to that used initially for preparing the donor polymer ink. Finally, the blend solution was cooled down for 10 mins before filtering through the 0.45 μm polytetrafluoroethylene (PTFE) filter into the clean V3 vial to remove large aggregates of fullerene. In some cases, a 2.5 % additive such as 1, 8-diiodooctane (DIO) was added to the blend ink (V4 vial) prior to the deposition in order to enhance the morphology of the active layer. Details of the blend ratio, solvent, additive, heating temperature, time, and total concentration can be found in **Table 4.3** for each polymer: fullerene system.

The preparation of ZnO-NP and PFN precursor solutions were carried out under a fume hood. 164 mg of zinc acetate hydrate (Sigma & Aldrich) was dissolved in 1 ml 2-methoxyethanol (99.99%) with the aid of 5% v/v ethanolamine in order to enhance the solubility. The solution was then heated at 60 ˚C for 30 min stirring at 600 rpm to ensure full solvation. No filtration was conducted in order to preserve the nanoparticle dispersion. The solution was cooled down for 10 min before being spin coated onto the ITO surface. In addition, 2 mg/ml of PFN (Ossila) was dissolved in methanol with the aid of 2 µl/ml acetic acid. The solution was stirred with a magnetic stirrer at room temperature for 30 min to ensure that it was fully dissolved and then filtered through a 0.45 µm PVDF filter.

Table 4.3 Details of the active layer inks used to fabricate inverted polymer solar cells based on PCDTBT, PTB7-Th, and PTB7 bulk heterojunction, showing the blend ratio, the solvent and additive used, if applicable, the total concentration of the ink, and the annealing conditions of the inks, including temperature and time duration

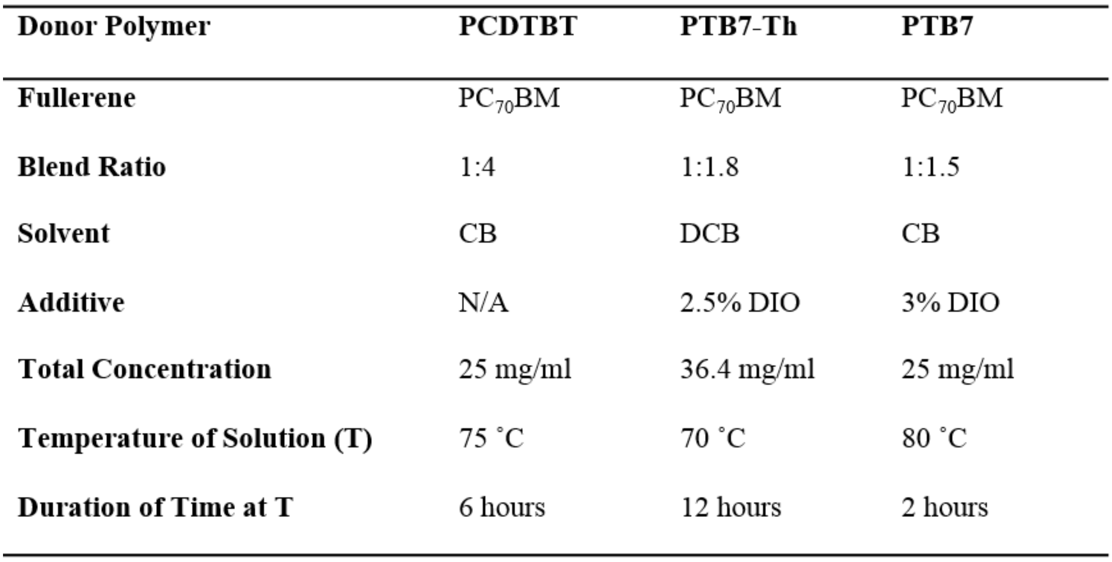

Donor Polymer	**PCDTBT**	**PTB7-Th**	**PTB7**
Fullerene	$PC_{70}BM$	$PC_{70}BM$	$PC_{70}BM$
Blend Ratio	1:4	1:1.8	1:1.5
Solvent	CB	DCB	CB
Additive	N/A	2.5% DIO	3% DIO
Total Concentration	25 mg/ml	36.4 mg/ml	25 mg/ml
Temperature of Solution (T)	75 ˚C	70 ˚C	80 ˚C
Duration of Time at T	6 hours	12 hours	2 hours

4.4 Thin Film Deposition

The thin films were deposited using the spin coating technique. This involved dispensing a small amount of material solution onto the centre of a secured rotating substrate. Centrifugal force contributed to an even spread of the solution over all the substrate, whilst the excess solution was ejected off the edges. As a result, a uniform film was created via the evaporation of the solvent in a process that is dependent on both spin speed and time. The time scale over which the solvent fully evaporates is determined by its boiling point; 131 ˚C for CB and 181 ˚C for DCB. For a CB-based solution, 40 s was enough to create a fully dried film at high spin speeds. At low spin speeds (< 1000 rpm), an additional spin regime with a very high speed (3000 rpm) but a short duration (10 s) was applied in order to dry the film corners. In the case of a DCB-based solution, a longer time of 60-90 s was needed, followed by slow drying under a vacuum for 20 – 30 min.

The thickness of the films was measured using a Dektak surface profiler. The active layer was initially spun onto cleaned artificial quartz-coated glass slides that served as reference samples. A step was then scraped onto the surface using a very sharp tweezer, and the depth profile was constructed, as illustrated in **Figure 4.4**. Fine-tuning of the film thickness can be attained by altering the spin speed through the following equation:

$$\omega_2 = \omega_1 \left(\frac{d_1}{d_2}\right)^2 \qquad \textbf{Equation 4.1}$$

where d_1 is the thickness of reference samples achieved by spin speed ω_1, and d_2 is the desired thickness achieved by spin speed ω_2. To ensure the validity of **Equation 4.1**, it is important to keep the solution concentration and solvent viscosity (dependent on solution concentration) constant, as governed by **Equation 4.2**; where c and η(c) are the solution concentration and solvent viscosity, respectively.

$$d = \frac{c\eta(c)}{\sqrt{\omega}} \qquad \textbf{Equation 4.2}$$

For the deposition of the electron extracting layers, a 40 µl solution of zinc oxide nanoparticle precursor was spun onto the cleaned ITO substrate at 2000 rpm for 40 s. The ITO cathode strips were cleaned by wet cotton pads immersed in IPA before the coated substrate was annealed at 275 ˚C for 15 min. The annealing step was necessary in order to convert the precursor solution into a thin film of dispersed nanoparticles. The film was measured to be 30 – 40 nm thick. The coated substrates were then transferred to the glove box to deposit the active layers with no further annealing requirement.

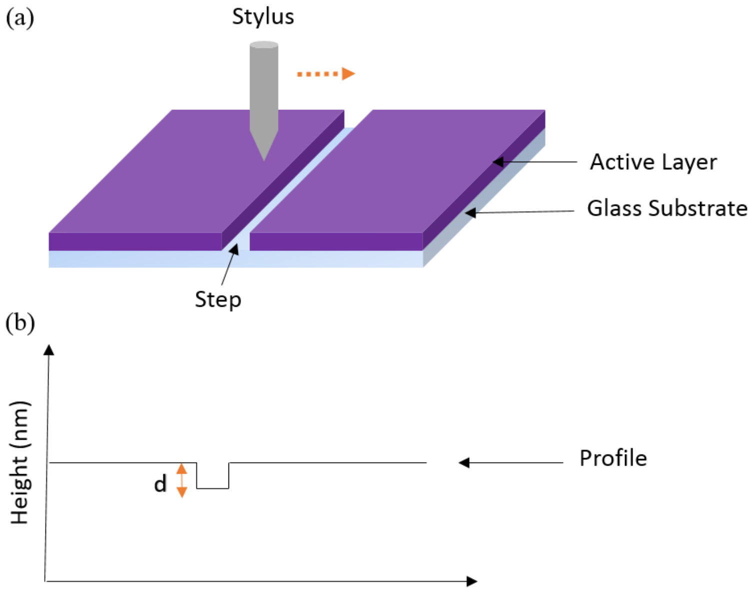

Figure 4.4 (a) Schematic showing how the Dektak stylus moves across the surface of the active layer. (b) Dektak depth profile of the active layer surface.

4.5 Thermal Evaporation

Thermal evaporation is a common vacuum deposition technique used to deposit metallic thin films that cannot be solution processed. The basic features of thermal evaporation include the evaporation of a hot material source and its condensation onto the substrate. This takes place under a high vacuum so as to provide a ballistic pathway for the evaporated particles to travel directly towards the substrate without colliding with ambient molecules. Examples of materials that can be thermally evaporated are Calcium (Ca), molybdenum oxide (MoO_3), and metals like Aluminium (Al) and Silver (Ag).

The vacuum chamber used to perform thermal evaporation was housed within nitrogen filled glove box allowing for in-house encapsulation and storage. **Figure 4.5** illustrates a simple schematic of the components of the vacuum chamber. It has multiple sources that are useful for subsequent evaporations with no need to break the high vacuum ($10^{-7} - 10^{-6}\ mbar$). The sources consist of crucibles wrapped with a resistive tungsten coil allowing for a current to be passed through. The thickness of the resultant film is monitored during the evaporation by a quartz crystal microbalance calibrated for each of the different source geometries. A rotating substrate holder is used in order to ensure a consistent coverage across the substrate surface. A shutter is placed directly under the rotating holder to protect the substrate from excess deposition.

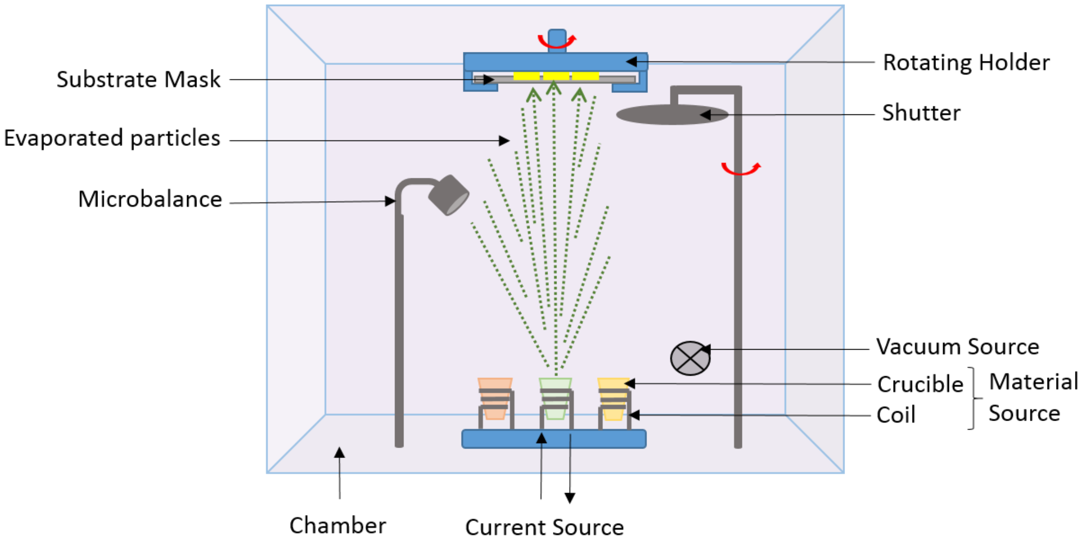

Figure 4.5 Simple schematic of the vacuum chamber used for thermal evaporation of the top contacts in polymer solar cells.

For the deposition of the metallic top contacts, the substrates were loaded into a stainless steel evaporation mask that defined the desired area for metal deposition onto the substrate. The mask was then transferred to the vacuum chamber and secured to the rotating holder. The chamber was next pumped down to a typical base pressure of $10^{-7} - 10^{-6}$ mbar in order to eliminate oxygen and nitrogen gas that might react with the metal evaporant. The material source was gradually heated and allowed to evaporate metal particles for 5-10 min before opening the shutter. This was done to clean any contaminants from the surface of the source material. Once the optimum conditions were met, the shutter was opened and the actual metal deposition was carried out. Finally, the whole system was allowed to cool down for 10 min before venting the chamber to atmospheric pressure and removing the substrates.

For all the inverted PSCs that were fabricated, the top anode contacts were sequential double layers of Molybdenum Oxide (MoO_x) and Aluminium (Al). The deposition rate and layer thickness were kept constant for all devices; (0.3˚A/s, 20 nm) for MoO_x, and (1.2˚A/s, 100 nm) for Al.

4.6 Encapsulation

The final step in fabricating the inverted PSCs is an encapsulation. This is important to sustain the lifetime of the devices due by preventing water and ambient gas molecules from penetrating into the polymer: fullerene layer. After the deposition of the top metallic contacts, a glass slip was stacked up using epoxy glue that was cured by exposure to an ultraviolet light for 30 min. **Figure 4.6** summarises the process of fabricating the inverted polymer solar cells.

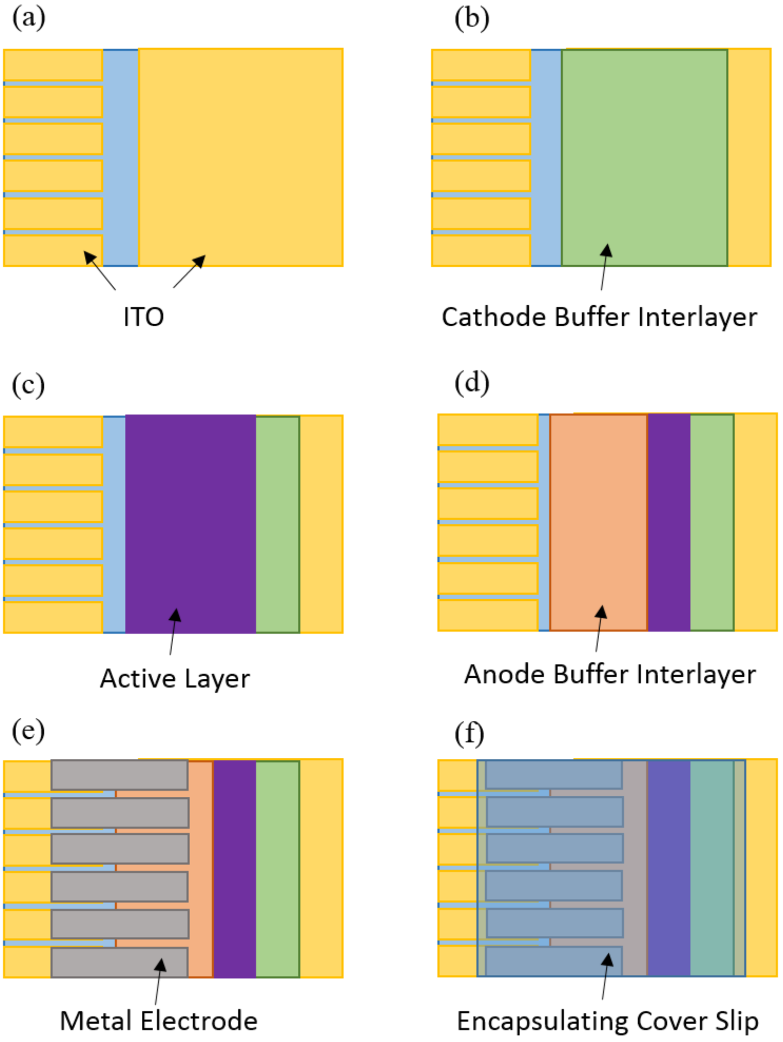

Figure 4.6 Summary of the process of fabricating inverted polymer cells

4.7 References

[1] R. A. Street, K. W. Song, and S. Cowan, "Influence of series resistance on the photocurrent analysis of organic solar cells," *Org. Electron.*, vol. 12, p. 244–248, 2011.

[2] R. A. Street, M. Schoendorf, A. Roy, and J. H. Lee, "Interface state recombination in organic solar cells," *Phys. Rev. B*, vol. 81, p. 205307, 2010.

[3] W. Shockley and H. J. Queisser, "Detailed Balance Limit of Efficiency of p-n Junction Solar Cells," *J. Appl. Phys.*, vol. 32, p. 510, 1961.

[4] C. G. Shuttle, B. O'Regan, A. M. Ballantyne, J. Nelson, D. D. C. Bradley, and J. R. Durrant, "Bimolecular recombination losses in polythiophene: Fullerene solar cells," *Phys. Rev. B - Condens. Matter Mater. Phys.*, vol. 78, p. 1–4, 2008.

[5] L. J. a Koster, V. D. Mihailetchi, R. Ramaker, and P. W. M. Blom, "Light intensity dependence of open-circuit voltage of polymer:fullerene solar cells," *Appl. Phys. Lett.*, vol. 86, p. 1–3, 2005.

[6] J.-L. Brédas, J. E. Norton, J. Cornil, and V. Coropceanu, "Molecular understanding of organic solar cells: the challenges.," *Acc. Chem. Res.*, vol. 42, p. 1691–1699, 2009.

[7] S. A. Hawks, G. Li, Y. Yang, and R. A. Street, "Band tail recombination in polymer:fullerene organic solar cells," *J. Appl. Phys.*, vol. 116, p. 113301–243502, 2014.

[8] A. Foertig, J. Kniepert, M. Gluecker, T. Brenner, V. Dyakonov, D. Neher, and C. Deibel, "Nongeminate and geminate recombination in PTB7:PCBM Solar Cells," *Adv. Funct. Mater.*, vol. 24, p. 1306–1311, 2014.

[9] G. Li, C.-W. Chu, V. Shrotriya, J. Huang, and Y. Yang, "Efficient inverted polymer solar cells," *Appl. Phys. Lett.*, vol. 88, p. 253503, 2006.

[10] Y. Sun, J. H. Seo, C. J. Takacs, J. Seifter, and A. J. Heeger, "Inverted polymer solar cells integrated with a low-temperature-annealed sol-gel-derived ZnO Film as an electron transport layer.," *Adv. Mater.*, vol. 23, p. 1679–83, 2011.

[11] Y.-M. Chang and C.-Y. Leu, "Conjugated polyelectrolyte and zinc oxide stacked structure as an interlayer in highly efficient and stable organic photovoltaic cells," *J. Mater. Chem. A*, vol. 1, p. 6446, 2013.

[12] C.-Z. Li, C.-Y. Chang, Y. Zang, H.-X. Ju, C.-C. Chueh, P.-W. Liang, N. Cho, D. S. Ginger, and A. K.-Y. Jen, “Suppressed Charge Recombination in Inverted Organic Photovoltaics via Enhanced Charge Extraction by Using a Conductive Fullerene Electron Transport Layer,” *Adv. Mater.*, vol. 26, p. 6262–6267, 2014.

[13] A. K. Thakur, G. Wantz, G. Garcia-Belmonte, J. Bisquert, and L. Hirsch, “Temperature dependence of open-circuit voltage and recombination processes in polymer-fullerene based solar cells,” *Sol. Energy Mater. Sol. Cells*, vol. 95, p. 2131–2135, 2011.

[14] L. Zhao, S. Zhao, Z. Xu, W. Gong, Q. Yang, X. Fan, and X. Xu, “Influence of morphology of PCDTBT:PC71BM on the performance of solar cells,” *Appl. Phys. A*, vol. 114, p. 1361–1368, 2013.

[15] C. J. Brabec, A. Cravino, D. Meissner, N. S. Sariciftci, T. Fromherz, M. T. Rispens, L. Sanchez, and J. C. Hummelen, “Origin of the Open Circuit Voltage of Plastic Solar Cells,” *Adv. Funct. Mater.*, vol. 11, p. 374–380, 2001.

[16] A. Gadisa, M. Svensson, M. R. Andersson, and O. Inganäs, “Correlation between oxidation potential and open-circuit voltage of composite solar cells based on blends of polythiophenes/ fullerene derivative,” *Appl. Phys. Lett.*, vol. 84, p. 1609, 2004.

[17] M. C. Scharber, D. Mühlbacher, M. Koppe, P. Denk, C. Waldauf, a. J. Heeger, and C. J. Brabec, “Design Rules for Donors in Bulk-Heterojunction Solar Cells—Towards 10 % Energy-Conversion Efficiency,” *Adv. Mater.*, vol. 18, p. 789–794, 2006.

[18] B. P. Rand, D. P. Burk, and S. R. Forrest, “Offset energies at organic semiconductor heterojunctions and their influence on the open-circuit voltage of thin-film solar cells,” *Phys. Rev. B*, vol. 75, p. 115327, 2007.

[19] K. Vandewal, K. Tvingstedt, A. Gadisa, O. Inganäs, and J. V Manca, “Relating the open-circuit voltage to interface molecular properties of donor:acceptor bulk heterojunction solar cells,” *Phys. Rev. B*, vol. 81, p. 2452041, 2010.

[20] T. M. Clarke and J. R. Durrant, “Charge photogeneration in organic solar cells,” *Chem. Rev.*, vol. 110, p. 6736–6767, 2010.

[21] V. D. Mihailetchi, P. W. M. Blom, J. C. Hummelen, and M. T. Rispens, “Cathode dependence of the open-circuit voltage of polymer:fullerene bulk heterojunction solar cells,” *J. Appl. Phys.*, vol. 94, p. 6849, 2003.

[22] G. F. a. Dibb, F. C. Jamieson, A. Maurano, J. Nelson, and J. R. Durrant, “Limits on the Fill Factor in Organic Photovoltaics: Distinguishing

Nongeminate and Geminate Recombination Mechanisms," *J. Phys. Chem. Lett.*, vol. 4, p. 803–808, 2013.

Chapter 5

Surface Characterization

5.1 Introduction

The techniques used to characterize the surface of thin films were ultraviolet photoelectron spectroscopy (UPS), X-ray photoelectron spectroscopy (XPS), absorbance spectroscopy and atomic force microscopy (AFM). These were essential to extract information on the electronic structure, chemical states, optical properties and surface topography of the relevant materials. The background to these techniques and the procedures followed to analyse the obtained data are highlighted in this chapter.

5.2 Ultraviolet Photoelectron Spectroscopy (UPS)

Ultraviolet photoelectron spectroscopy is the measurement of the kinetic energy spectrum of electrons emitted from a surface upon the absorption of ultraviolet photons. **Figure 5.1** shows a simplified layout of a Kratos AXIS Ultra Photoelectron Spectrometer. The spectrometer includes six parts: the sample loading chamber, transfer chamber, photon source chamber, analysis chamber, hemispherical analyser, and electron multiplier. Having multiple chambers within the spectrometer is crucial to maintain an ultra-high vacuum throughout the whole process. The photon flux is sourced from a helium discharge lamp that is separated from the analysis chamber by a highly transparent window. The energy of the photon flux is therefore dependent on the degree of ionised helium; 21.20 eV for a natural He (I), or 40.80 eV for a singly-ionized He (II) [1]. The sample is loaded onto a bar attached to a mobile arm that is able to be moved horizontally and rotated, allowing for angle resolved studies. It is then transferred to the analysis chamber where it is irradiated with UV photons. The emitted electrons are directed through the hemispherical analyser to enter a multiplier tube where the signal is amplified and then detected. The signal amplification is useful to detect small fluctuations in the number of emitted electrons at a specific kinetic energy.

The emitted electron passing through the hemispherical analyser experiences a Lorentz force as a result of an applied magnetic field, as given in **Equation 5.1**:

$$\bar{F} = q\ \bar{v}\ X\ \bar{B}$$ **Equation 5.1**

where F is the force, q is the elementary charge of an electron, v is the electron velocity, and B is the magnetic field [2]. As the analyser has a fixed radius R, the electron undergoes a centripetal force (**Equation 5.2**). The kinetic energy of an electron with a mass m is given in **Equation 5.3**. It is possible to determine the kinetic energy of the emitted electron (KE) as a function of the applied magnetic field, as **Equation 5.4** below indicates.

$$F = \frac{m\ v^2}{R}$$ **Equation 5.2**

$$KE = \frac{m\ v^2}{2}$$ **Equation 5.3**

$$KE = \frac{(q\ R)^2}{2\ m}\ B^2$$ **Equation 5.4**

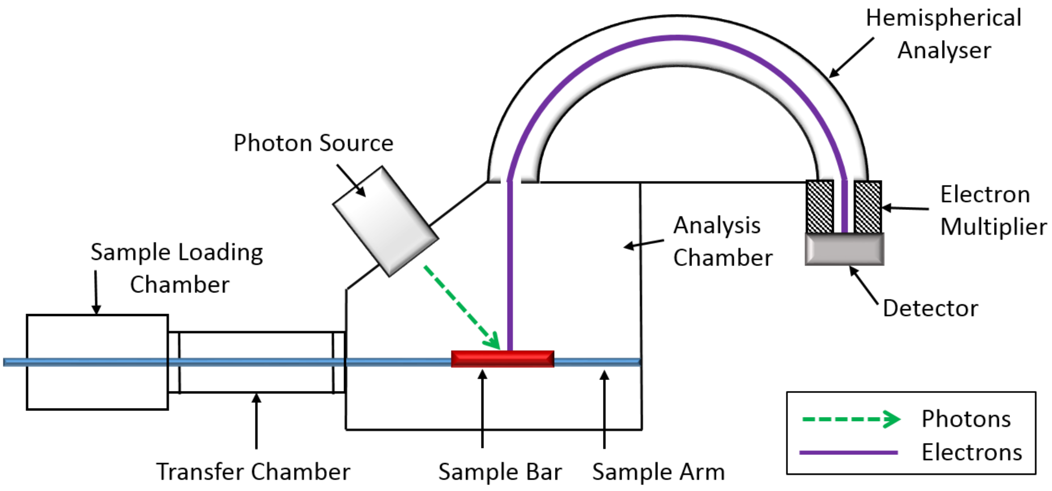

Figure 5.1 Simplified layout of a Kratos AXIS Ultra Photoelectron Spectrometer. Based on the type of ionized gas used within the discharge lamp housed in the photon source chamber, the instrument can be used for either UPS or XPS analysis of a thin film surface.

The kinetic energy spectrum is typically converted into a binding energy (BE) spectrum as shown in **Figure 5.2**. This is done by knowing that the photon energy (hv) overcomes the binding energy of the electron in the molecular orbitals to increase the electron kinetic energy, as seen in **Equation 5.5** [1]**:**

$$hv = BE + KE$$
$$BE = hv - KE$$

Equation 5.5

where h is Plank's constant, and v is the frequency of light. The binding energy spectrum induces elastic and inelastic scattered photoelectrons. **Figure 5.3a** illustrates two possible scenarios upon the absorption of a photon [3]. A primary electron is photoexcited from its ground state into an excited state with an excess energy to overcome the work function of the material (ϕ) and escape to the vacuum level (E_V) without any inelastic collision events with neighbouring atoms because it was originally located near to the surface. While the majority of primary electrons escape from close to the surface, therefore, those that have been excited from deeper energetic states scatter inelastically but have enough energy remaining to be emitted. These are known as secondary electrons. The average distance the excited electron travels without being scattered is referred to as the inelastic mean free path (IMFP). This determines the maximum depth allowing for an electron to be emitted from the surface, which is less than 2-3 nm for UPS [4]. **Figure 5.3b** exemplifies the contribution of both types of emitted electrons to the binding energy spectrum; primary electrons have a high probability of occurring at low binding energies, and secondary electrons extend over the background of the spectrum.

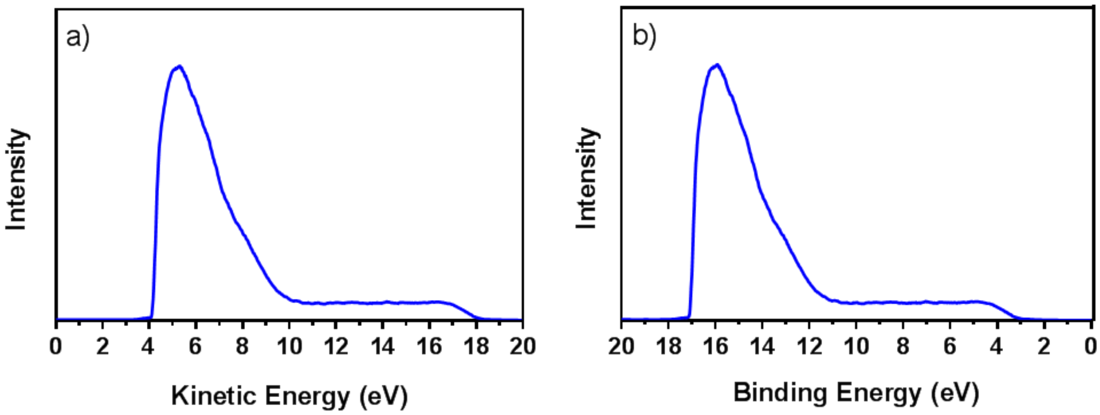

Figure 5.2 Examples of UPS spectra for a semiconductor sample presented by (a) the kinetic energy spectrum and (b) binding energy spectrum with the Fermi level calibrated to zero.

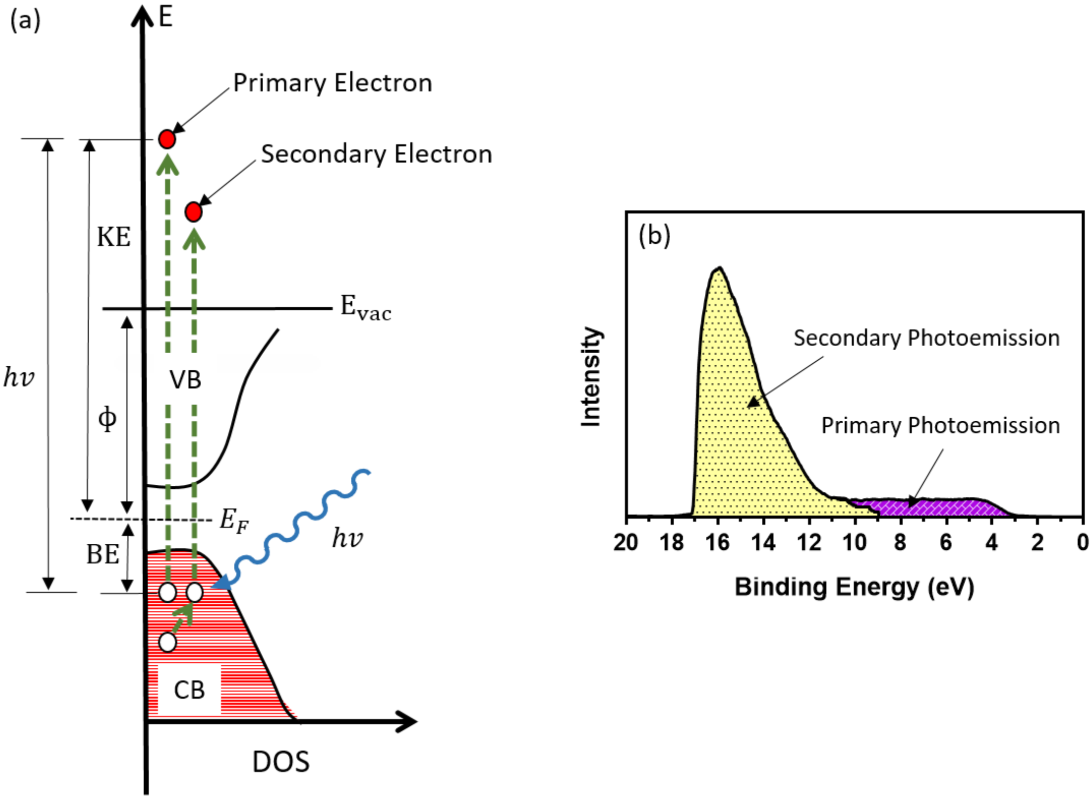

Figure 5.3 (a) Illustration of the UPS mechanism for a semiconducting material using an energetic diagram as a function of the density of states (DOS), showing that primary electrons are more likely to be photoemitted elastically from states close to the valence band (VB) edge whereas secondary electrons may be photoemitted inelastically from deeper states. The material conduction band (CB),he Fermi level energy (E_f), energy of incident UV photon (hv), material work function (ϕ), electron binding energy (BE), and kinetic energy of a photoemitted electron (KE) are shown with respect to the vacuum level energy (E_{vac}). (b) Illustration of the contribution of primary and secondary electrons to the UPS spectra.

UPS is a versatile and powerful technique to probe the valence electronic states of the thin film in detail. Parameters that can be measured include the work function, the position of the Fermi level, and the valence band/HOMO edge. These help to provide a better understanding of the transport of charge carriers across layer interfaces within PSC devices. Once the UPS spectrum is obtained, the work function (ϕ) can be determined using **Equation 5.6** below:

$$\phi = hv - (E_{Cutoff} - E_f) \qquad \textbf{Equation 5.6}$$

where hv is the energy of incident UV photon and E_{Cutoff} is the minimum kinetic energy of a photoelectron that can still escape the surface. Note that the minimum kinetic energy is typically plotted as the maximum binding energy. **Equation 5.6** holds true only if 0 eV BE = E_f, which can be valid for metals and semiconductors (albeit with some restrictions as will be discussed later on). This assumption is essentially made to ease the determination of the edge of the valence band.

The position of the valance band is determined practically from the primary photoemission region of the binding energy spectrum. The primary electrons are directly emitted from the occupied states within the valence band of metal oxides or the molecular states of organic polymers. A characteristic feature of primary photoemission is having multiple low intensity peaks at low binding energies, corresponding to the electronic distribution within the band. Since the peak with the lowest binding energy corresponds to the highest occupied state, it is possible to identify the valence band edge (which we refer to as the HOMO edge). This is done by fitting an intercept to the emission peak and the background. **Figure 5.4** shows an example of UPS spectra for an organic polymer, where both the cut-off binding energy used to calculate the work function, as seen in **Equation 5.6**, and the HOMO edge are annotated.

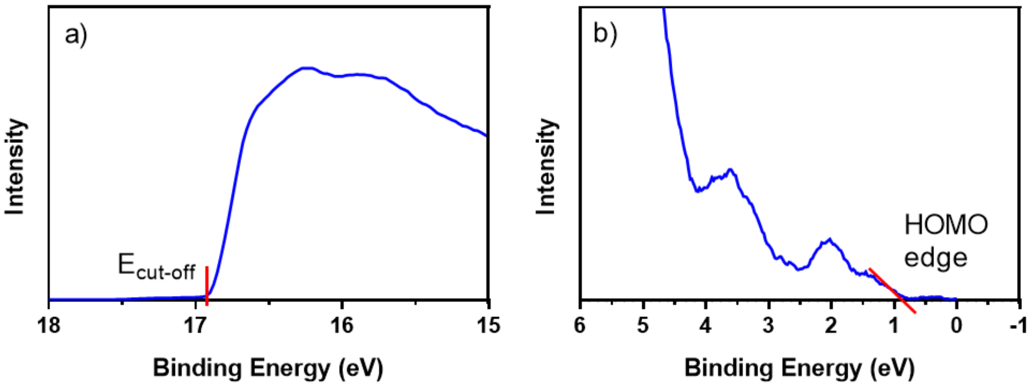

Figure 5.4 Use of UPS to determine (a) the work function using Equation 5.6, and (b) the edge of the HOMO level for a polymer thin film.

The identification of the Fermi level position within UPS spectrum varies in difficulty based on the measured material. A metal induces a spectrum in which it is easy to identify the Fermi level by eye. This is due to its unique electronic structure, where the valence and conduction bands overlap leading to high density states extending all the way to the Fermi level. As a result, a rapid drop in the photoemission spectrum to zero can be observed. This is not the case for semiconducting materials such as organic polymers and metal oxides, however. With these materials, the electronic structure of the semiconductor incorporates an energetic gap between the valence and conduction bands with a Fermi level lying in the middle. The density of states is very low between the valence band and Fermi level; hence it becomes more difficult to identify the position of the Fermi level from the spectrum, especially if there is a shift caused by charge accumulation onto the sample surface. More care is therefore usually taken when acquiring the UPS spectrum for a semiconducting sample. These include collecting the spectrum of a control sample (typically a metal gold), grounding the surface of the sample to avoid charge accumulation, and processing the acquired spectrum so as to be able to see the Fermi level position clearly. **Figure 5.5** shows the location of the Fermi level in the spectra of metallic and semiconducting samples. For the semiconductor sample, normalization and smoothing were done using an average adjacent filter in order to locate the Fermi level (**Figure 5.5c**).

UPS spectra were recorded using a Kratos AXIS Spectrometer with a He (I) emission line. For a full scan of the spectrum, the energy was varied from – 4 eV up to 21.20 eV at 0.025 intervals. The energy pass (10 eV) and normal emission angle were kept constant. Three samples were prepared to investigate each parameter with three different area detected per sample. All measurements were performed under a ultra-high vacuum and at room temperature. The CasaXPS software package was used for initial analysis and the data were then refined using Origin 6.0 graphing software.

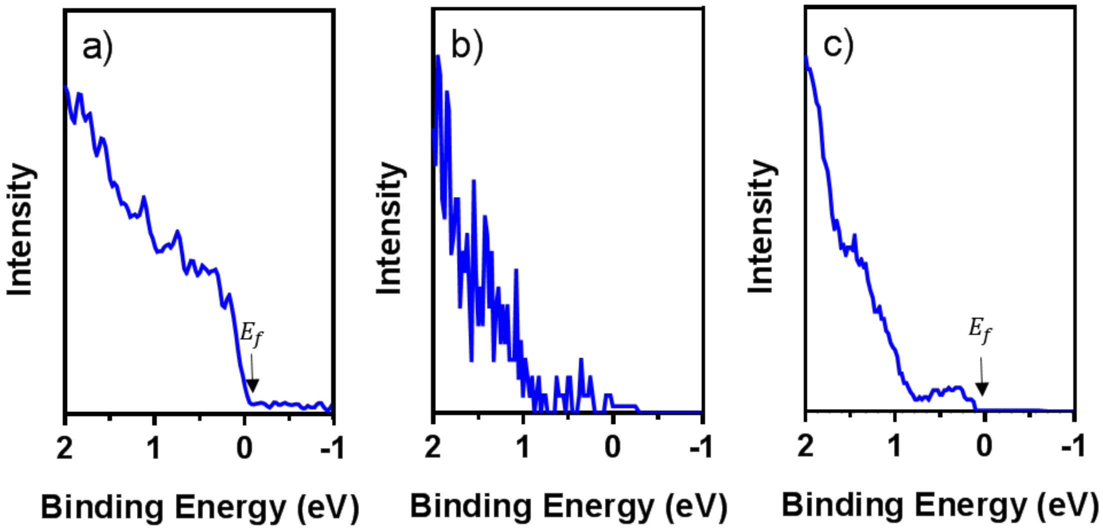

Figure 5.5 Locating the Fermi level position (E_f) within UPS spectra for different materials, including metal (gold foil) (a), and a semiconductor (polymer thin film) as-measured (b), and after being normalized and smoothed (c)

5.3 X-ray Photoelectron Spectroscopy (XPS)

Similar to UPS, XPS measures the kinetic energy of the photoemitted electrons from the surface of a thin film as a result of the absorption of X-ray photons. The Kratos AXIS Photoelectron Spectrometer shown previously in **Figure 5.1** is also used to perform XPS but with a different photon source. The source here generates monochromatic X-rays by the electron bombardment of a metallic target, most often aluminium. The energy of emitted X-rays is dependent on the line emission of the aluminium used, which is typically Al-Kα, which has a photon energy of 1486.90 eV. The emitted X-rays are then filtered through a quartz crystal in order to reduce signal noises arising from the Bremsstrahlung and Al Kβ emissions. Once the sample is loaded, it is irradiated with X-rays. The emitted electrons enter the hemispherical analyser and are then detected.

The photoemission in XPS leads to the ejection of electrons occupying core levels of the sample elements, as shown in **Figure 5.6**. When a core-level electron is emitted, the atom is left in a final state lacking one electron with respect to the initial state [5]. Consequently, an electron from an uppermost level fills into the vacancy level, emitting either an Auger electron or characteristic X-ray. The binding energies of both core-level and Auger electrons are characteristic of the element from which they were emitted [6]. XPS spectra provide information on the chemical composition and abundance of elements within the material. The photoemission of Auger electrons, however, can be characterized using an Auger Electron Spectrometer (AES) [7], but this is not the focus of the current work.

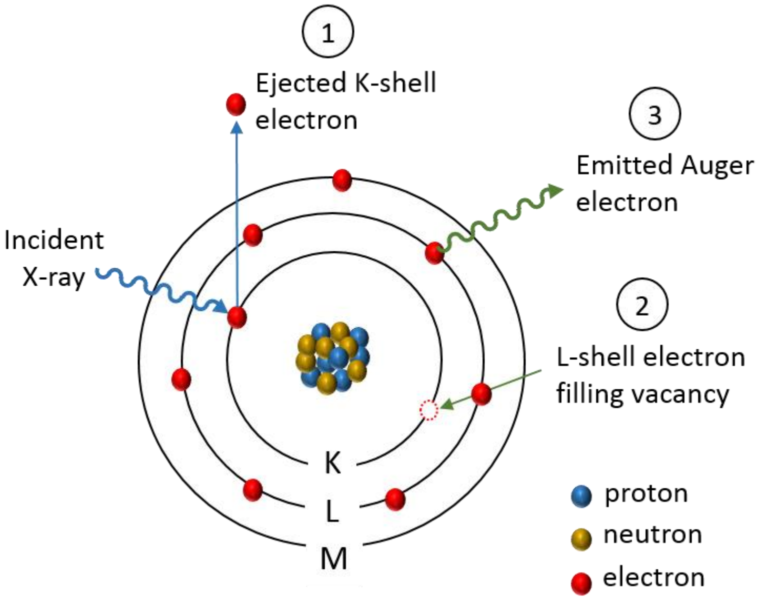

Figure 5.6 Atomic view illustrating the photoemission process in XPS.

A XPS spectrum is generated by counting the number of primary electrons emitted as a function of their binding energies. It can be presented in two different ways depending on the energy resolution used. A wide-scan spectrum with low energy resolution shows multiple peaks characterizing the elements existing within the material surface. A narrow-scan spectrum with a higher energy resolution shows a single/doublet peak structure. The precise position and shape of the peaks indicate the chemical states of the elements, while the area under the peak points out the relative amount of the element. To extract information on the chemical states of the element, several data post-processing steps need to be performed on the high-resolution spectrum.

The interpretation of the high-resolution spectrum involves correcting the background intensity, dividing the area under the peak into several individual peaks, and then recovering chemical shifts. The correction of the peak background is essential for the direct analysis of emitted core-level electrons and is done using mathematical approximation. The most commonly used method is the Shirley function [8], which uses an algorithm to relate the area of the measured spectrum against itself. This is done by removing the background from the spectrum between peak edges, leaving the peak area. The peak edges correspond to E_{max} and E_{min}, where E_{max} is the maximum binding energy of electrons emitted above the emission peak, and E_{min} is the minimum binding energy of electrons emitted below the emission peak. The area for electrons with kinetic energies higher and lower than the peak energy is calculated using an iterative process and has to match a specified ratio in order to calculate the correct background intensity. **Figure 5.7** shows the determination of background intensity using the Shirley approximation for a high-resolution spectrum of the In 3d for a cleaned ITO sample.

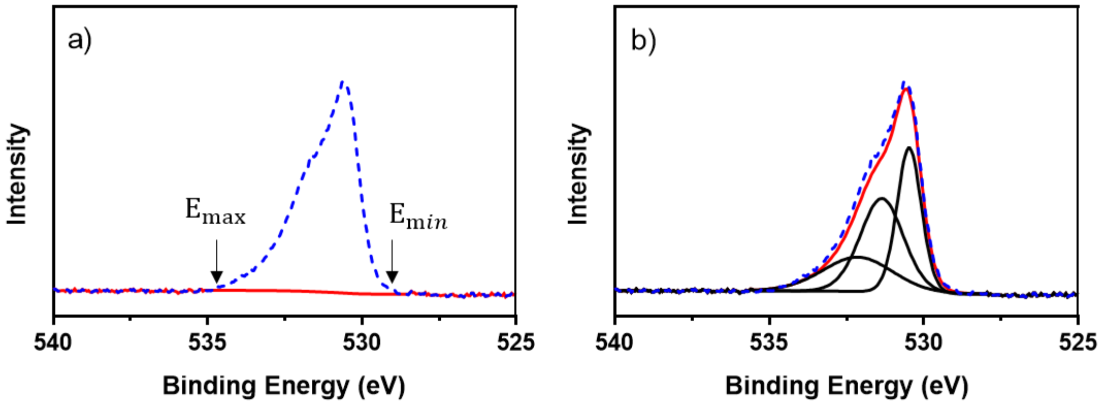

Figure 5.7 High resolution spectrum of 1s orbital showing (a) the measured spectrum with Shirley background, and (b) the corrected spectrum for background emission with fitted Gaussian peaks.

Once the background is corrected, the emission peak is divided into several individual Gaussian peaks, each with a unique binding energy that corresponds to a specific chemical state. By comparing the measured Gaussian binding energy with the binding energy expected for an elemental state or oxidation state (0), a chemical shift can be observed. This chemical shift refers to the difference in the binding energy between atom environments. It arises from the orbital relaxation of the atom (intra-atomic effect) due to Coulomb attraction, and the influence of surrounding elements (extra-atomic effect) due to their electronegativity [1]. A further implication of observing the chemical shift is to monitor surface contamination due to air exposure. Elements such as carbon, nitrogen, and oxygen, with electrons occupying 1s, 2s, and 2p orbitals, can be adsorbed onto the material surface. In practice, the most intense peaks for these elements using the narrow-scan mode arise from the 1s orbital. This is due to the overlap of the uppermost orbitals (2s, and 2p) with other existing elements, lowering the intensity of the photoemitted electrons until they cannot be seen above the background.

XPS spectra were measured using a Kratos AXIS Spectrometer with a Al-Kα emission line at 0.1 eV intervals and 300 seconds per scan over an appropriate energy range for the element under consideration. The measurements were performed at room temperature. The CasaXPS software package was used for initial analysis and the data were then refined using Origin 6.0 graphing software.

5.4 UV/Vis Absorbance Spectroscopy

UV/Vis Absorbance spectroscopy refers to the measurement of light transmission through a sample at different wavelengths, typically ranging from 300 nm to 800 nm. The transmittance can be experimentally determined using a Horiba Fluoromax-4 as shown in **Figure 5.8**. The light is sourced from a xenon arc lamp with an emission starting at 250 nm. An elliptical mirror focuses the light onto an entry slit that controls the resolution of the measurement. Once light enters the monochromator, it is collimated by a second mirror onto a blazed diffraction grating. Diffracted light is then reflected by a third mirror, directing the beam through a second slit to exit the monochromator. The angle of the blazed grating with respect to the mirror controls the wavelength of diffracted light. The slit width, therefore, tunes the resolution of the output spectra; the narrower slit width the higher resolution. The reflected light is next incident onto the sample, passing a beam splitter. The split beam is detected in the reference chamber to determine the intensity of the incident light. The incident light is transmitted by the sample and measured by a transmission detector.

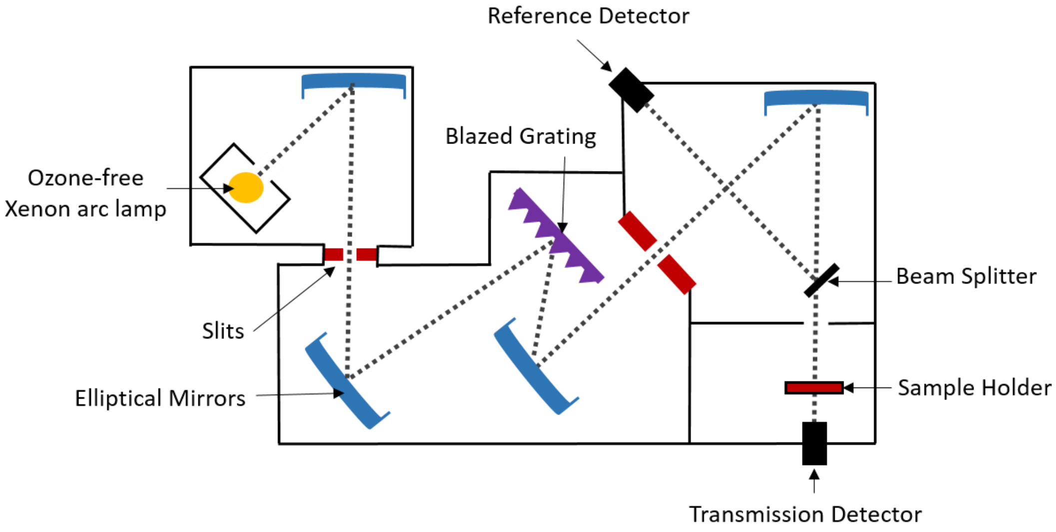

Figure 5.8 Simplified layout of a Horiba Floromax-4, displaying four discrete chambers: the light source, monochromator, reference beam detection, and transmission beam detection.

The ratio of the amount of light transmitted measured by the transmission detector $I(\lambda)$ to the amount of incident light measured by the reference detector $I_o(\lambda)$ defines the sample transmittance $T(\lambda)$ that is calculated using **Equation 5.7**, where λ is the wavelength of the light. Losses arising from reflections and dispersion of light at interfaces are typically included within the calculated transmittance. When the transmittance of thin films deposited onto glass substrate (either blank or ITO-coated) is measured, therefore, transmission spectra of the substrate are taken into account for the determination of losses caused by the substrate, assuming losses are the same at each side. Once transmittance of the sample is measured, its absorption spectrum $A(\lambda)$ can be then determined using Beer’s law [9] as shown in **Equations 5.8 and 5.9**, where l is the sample thickness and α is the sample absorption coefficient.

$$T(\lambda) = \frac{I(\lambda)}{I_o(\lambda)}$$ **Equation 5.7**

$$A(\lambda) = -log_{10}[T(\lambda)]$$ **Equation 5.8**

$$I(\lambda) = I_0(\lambda)e^{-\alpha(\lambda)d}$$ **Equation 5.9**

5.5 Atomic Force Microscopy (AFM)

Atomic force microscopy (AFM) is a kind of scanning probe microscopy that images the topography of a sample surface at a nanometre scale. It consists of three main components; a piezoelectric probe, a laser beam and a quadrant photodetector, as illustrated in **Figure 5.9**. The piezoelectric probe includes a piezoelectric cantilever integrated with a very sharp tip (a few nm sized). In principle, the cantilever deflects while the tip scans across the sample surface. As the distance between the reflected laser beam and photodetector is relatively large, any change in the cantilever position can be easily detected by measuring the position of the laser spot on the quadrant detector. It is therefore essential that, before starting AFM measurement, the laser beam is precisely aligned onto the cantilever surface and the presence of the laser spot is confirmed.

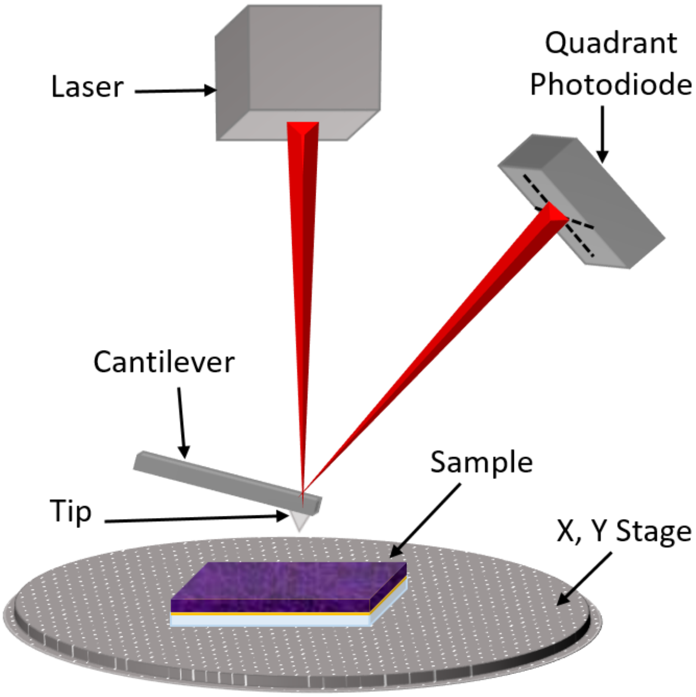

Figure 5.9 Simplified layout of atomic force microscopy (AFM).

There are three modes describing the interaction between the sharp tip and sample surface [10], [11]. The contact mode is where the tip is in continuous contact with the surface and changes in the cantilever deflection, which is controlled by applying voltages, relate directly to the sample topographic map. In the non-contact mode, when the tip is at a fixed distance from the surface corresponding to the distance of the Van der Waals attraction, the cantilever oscillates at low amplitude and changes in the amplitude or frequency of this oscillation are used to determine the topography. The third mode is the tapping mode, where the cantilever oscillates with high amplitude and the tip intermittently contacts the surface. A piezoelectric motor is used to oscillate the cantilever near to its resonant frequency once the tip is away from the surface. Getting closer to the surface, the oscillating amplitude is reduced due to the loss of energy and the tip quickly lifts away from the surface. A feedback loop keeps both the oscillating amplitude and force constant during the scan by adjusting the tip-surface distance. Hence topographical features can be identified and measured via the detection of reduced oscillating amplitude [12].

A Veeco dimension 3100 AFM instrument was used to perform a tapping mode scan to all samples in order to avoid any surface damage introduced by the tip. The AFM tips secured from Bruker Innovation (TESPA-V2) have a resonant frequency of 320 kHz and a 42 N/m spring constant. The data obtained was analysed using Gwydion software.

5.6 References

[1] S. Hufner, *Photoelectron Spectroscopy: Principles and Aplication*, 2nd ed. New York: Springer-Verlag, 1995.

[2] K. Siegbahn, “Electron spectroscopy for atoms, molecules, and condensed matter,” *Rev. Mod. Phys.*, vol. 52, p. 709, 1982.

[3] C. N. Berglund and W. E. Spicer, “Photoemission Studies of Copper and Silver: Theory,” *Phys. Rev. A*, vol. 136, p. 1030, 1964.

[4] D. R. Penn, “Quantitative Chemical Analysis by ESCA,” *J. Electron Spectros. Relat. Phenomena*, vol. 9, p. 29–40, 1976.

[5] J. C. Riviere and S. Myhra, *Handbook of Surface and Interface Analysis: Methods for problem-solving*, 2nd ed. Boca Raton, Fla. : CRC Press, 2009.

[6] G. Moretti, “Auger parameter and Wagner plot in the characterization of chemical states by X-ray photoelectron spectroscopy: a review,” *J. Electron Spectros. Relat. Phenomena*, vol. 95, p. 95–144, 1998.

[7] C. C. Chang, “Auger Electron Spectroscopy,” *Surf. Sci.*, vol. 25, pp. 53–79, 1971.

[8] D. A. Shirley, “High-Resolution X-Ray Photoemission Spectrum of the Valence Bands of Gold,” *Phys. Rev. B*, vol. 5, p. 4709–4714, 1972.

[9] M. Fox and A. Mark, *Optical Properties of Solids*, 2nd ed. Oxford: Oxford University Press, 2010.

[10] P. Eaton, *Atomic Force Microscopy*, 2nd ed. Oxford: Oxford University Press, 2010.

[11] G. Binning, C. F. Quate, and C. Greber, “Atomic Force Microscopy,” *Phys. Rev. Lett.*, vol. 56, p. 930, 1986.

[12] S. N. Magonov, V. Elings, and M. H. Whangbo, “Phase imaging and stiffness in tapping-mode atomic force microscopy,” *Surf. Sci.*, vol. 375, p. L385–L391, 1997.

[13] K.-Y. Law, *Surface Wetting: Characterization, Contact Angle, and Fundamentals*. Cambridge: Springer, 2016.

Chapter 6

Benchmark Inverted BHJ Devices

Abstract. This chapter reports the results of the procedures used to develop benchmark ITO only inverted devices (with no buffer layer inserted), as well as of the investigation of the electronic structure of ITO following different cleaning procedures. Inverted devices based on PCDTBT: PCBM BHJ are studied as an example. A maximum Voc of 0.89 V, Jsc of 10.55 mA.cm^{-2}, FF of 59 %, and PCE of 5.35 % are realized at optimal conditions. These conditions include ultrasonic cleaning in a sequence of Hellmanex, deionized water and isopropanol alcohol. A $90 - 95$ nm thick BHJ layer is then thermally annealed at 80 ℃ for 15 min, and capped with 20 nm of MoOx and 100 nm of Al, respectively. XPS studies confirm the surface's insensitivity to the chemical structures of cleaning solvents, whereas UPS studies confirm a significant reduction in the work function of non-cleaned ITO by 0.4 eV (from 4.69 eV to 4.29 eV) compared to cleaning with acetone.

6.1 Introduction

Indium tin oxide (ITO) has been widely used in optoelectronic devices because of its high optical transparency and electrical conductivity [1], [2]. ITO electrodes are typically fabricated by the deposition of a thin layer of tin-doped indium oxide onto a glass substrate. Various techniques have been employed to produce ITO films with optimum optical and electrical properties [3]–[7]. Sputtering is considered to be the most widely applicable technique [8]–[11]. Depending on the deposition conditions, commercially available ITO thin-film substrates often have traces of surface contaminations sourced from either the fabricating process or packaging and delivery processing. It has been found that surface contaminations, and hence the cleaning process applied, can be crucial for device performance [12]. This is because the adhesion of the following layer (e.g. an electron extraction layer or self-assembled monolayer) depends on the degree of cleanness of the ITO surface so as to provide a suitable surface chemistry [13]. With a cleaner surface, a better alignment of energy levels across the interface can be achieved, and this enhances electron extraction [14]–[17].

In the literature, when a new electron extraction layer is examined, the performances of devices are compared with and without the new layer in order to elucidate the effect of this layer [18]–[20]. Similar comparisons are conducted if an ITO surface is modified with a SAM [21]. Notably, ITO-only devices show very low efficiencies as seen in **Table 6.1**. This chapter reports the fabrication and optimization of benchmark ITO-only inverted devices based on PCDTBT BHJ. The performance of these devices are characterized in terms of the pre-treatments of the ITO surface, the active layer processing conditions, and the thickness of the top anode layers. The results of ITO surface pre-treatments, including ultrasonic cleaning, ultraviolet ozone plasma, and argon sputtering are presented here, while the effect of thermal annealing will be discussed in the following **Chapter 7**.

Table 6.1 Examples of ITO only inverted solar cell devices with various BHJ donor polymers, as reported in the literature.

BHJ Donor Polymer	**V_{OC} (V)**	**J_{SH} (mA.cm^{-2})**	**FF (%)**	**PCE (%)**	**R_S (Ω.cm^2)**	**R_{SH} (Ω.cm^2)**	**Ref**
PBDTTT-C-T	0.49	14.54	52.7	3.72	N/A	N/A	[18]
P3HT	0.3	8.5	25	0.63	26	36.1	[19]
PCDTBT	0.57	10.25	30	1.82	104.7	37.7	[20]
PTB7	0.38	16.29	51.3	3.18	6.4	N/A	[21]

6.2 Surface Treatment Dependence

Ultrasonic cleaning is an initial process that is typically conducted to clean commercially available ITO substrates. It involves the application of sound waves through a detergent solution (containing ITO substrates), whereby density waves of compression and expansion are created. The compression and expansion of the liquid happens rapidly in cycles, creating millions of tiny cavities (bubbles filled with a partial vacuum). These cavities last for a very short time before collapsing due to the high pressure of surrounding solution. When the cavity collapses, thermal energy is released, assisting the solvent molecules to break down the chemical bonds of contaminated species adsorbed onto the ITO surface. The degree of cleanliness therefore depends on several parameters, including the ultrasonic output frequency, the duration of cleaning, the solution temperature and the properties of the cleaning solvent.

One of the important properties is the functional group within the solvent backbone chain that determines the solvent polarity. This is because its functional group can react with certain species of contaminants existing on the ITO surface. The dipole moment, which measures the separation between the two terminal functional groups, can be used as an indicator of solvent reactivity. **Figure 6.1** shows the chemical structures of four organic cleaning solvents used to clean ITO substrates: isopropyl alcohol (IPA), methanol (MeOH), deionized water (DIW) and acetone (Ace), which have dipole moments of 1.66 D, 1.70 D, 1.85 D, and 2.61 D, respectively. Changing only the solvent used at the final cleaning step (prior to nitrogen drying) and keeping all other parameters constant, the ultimate chemical state of the ITO surface is determined by the physically adsorbed solvent molecules inducing changes to the local bond environment. Details of the cleaning conditions were previously described in **Chapter 4**.

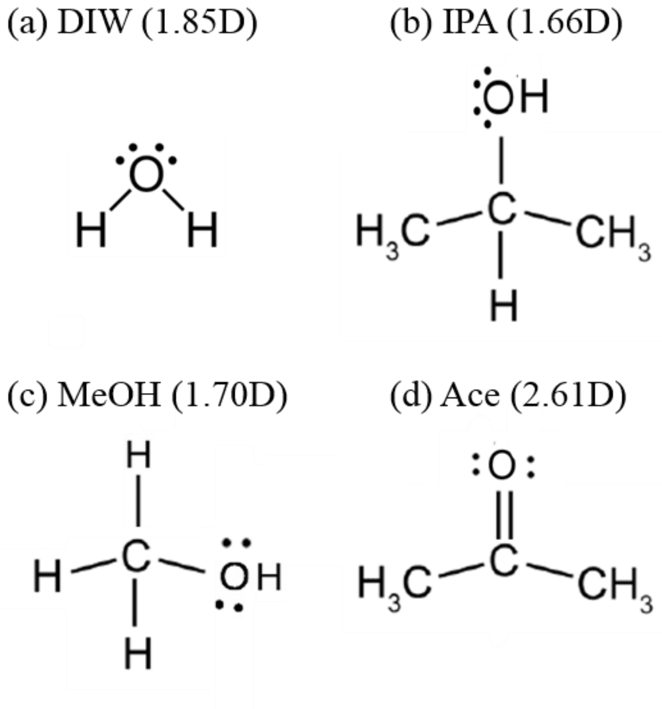
(a) DIW (1.85D)
(b) IPA (1.66D)
(c) MeOH (1.70D)
(d) Ace (2.61D)

Figure 6.1 Chemical structures of four detergents used to clean ITO at the second ultrasonic bath and their dipole moment values in Debye; (a) deionized water (DIW), (b) isopropyl alcohol (IPA), (c) methanol (MeOH), and (d) acetone (Ace).

6.2.1 Effect on Device Performance

The current density-voltage (JV) characteristics of inverted devices fabricated on cleaned blank ITO substrates are shown in **Figure 6.2**, along with the device structure. The reference device here is fabricated on an as-received non-cleaned ITO substrate, which was annotated with a zero dipole moment (0 D). This is to show how surface contamination could affect device performance in comparison to cleaned substrates. It can see that cleaning with different detergents significantly affects the device fill factor (FF) since the as-received device showed the worst JV characteristics, with the lowest FF of 33.76 % and hence efficiency PCE of 2.23 %. This was expected since surface contamination can provide paths for current leakage and charge recombination [22], [23], which is evident by the low shunt resistance (R_{SH}) as well as high series resistance (R_S), obtained to be in the order of 40 $\Omega.\mathrm{cm}^2$and 151 $\Omega.\mathrm{cm}^2$, respectively.

In comparison with the as-received devices, meanwhile, the shape of the JV curves improve significantly with cleaning, as seen in **Figure 6.3**. Maximum fill factors of 51.79 %, 52.57 %, and 53.22 % are r obtained for DIW (1.85 D), Ace (2.61 D), and MeOH (1.70 D) devices, respectively. The best FF is shown for the IPA-cleaned device, with a value of 59.45 % (1.66 D) and the highest PCE of 4.09 %. Although the Ace-cleaned device shows a lower FF than the MeOH-cleaned device, it exhibits a better PCE (3.93 % vis 3.73 %) due to a higher open-circuit voltage (Voc) and short circuit current (Jsc) (0.87 V, and 8.63 $\mathrm{mA.cm}^{-2}$) compared to that of the MeOH-cleaned device (0.85 V, and 8.23 $\mathrm{mA.cm}^{-2}$). Although, the Voc of the IPA-cleaned device (0.82 V) is higher than that of the As-cleaned device, it is the lowest of the tested devices. Meanwhile, the Jsc of this device (8.40 $\mathrm{mA.cm}^{-2}$) is in between those obtained for the MeOH-cleaned and Ace-cleaned devices. In comparison with the IPA-cleaned device, Zhu et al. [24] fabricated PCDTBT:PCBM inverted devices on bare ITO that had been subsequently cleaned in ultrasonic baths using deionized water, acetone and then isopropanol. These devices exhibited Voc of 0.48 V, J_{SC} of 7.34 $\mathrm{mA.cm}^{-2}$, FF of 36.9 %, and PCE of 1.63 %. The R_S and R_{SH} were 5.64 Ω.cm^2 and 113 Ω.cm^2, respectively. Compared to the devices reported by Zhu et al. [24], the slight enhancements seen for our IPA devices prove the validity of our cleaning approach, as well as the sensitivity of the ITO surface to pre-treatment conditioning. The unsystematic variations in the device parameters with varying solvent dipole moments, as shown in **Figure 6.3**, imply two main conclusions, however. First, the solvent dipole moment is not the only factor affecting device performance. Second, there are other sources that contribute to the chemical reactions undergone on ITO surfaces. UPS and XPS studies may identify these sources, as will be seen in the following sections.

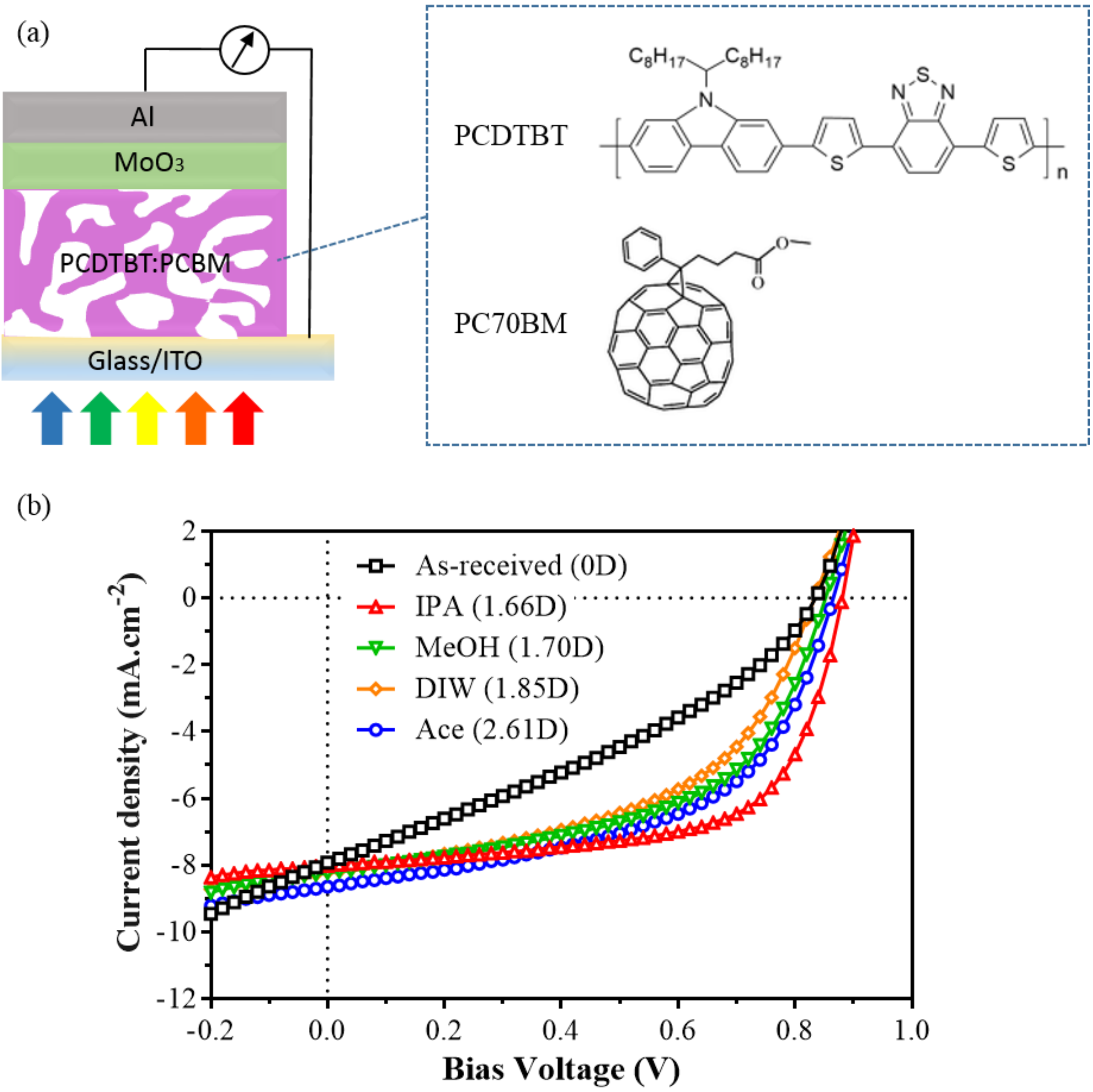

Figure 6.2 (a) Device architecture and chemical structures of active layer materials. (b) Current density-voltage characteristics of inverted devices fabricated onto modified blank ITO substrates.

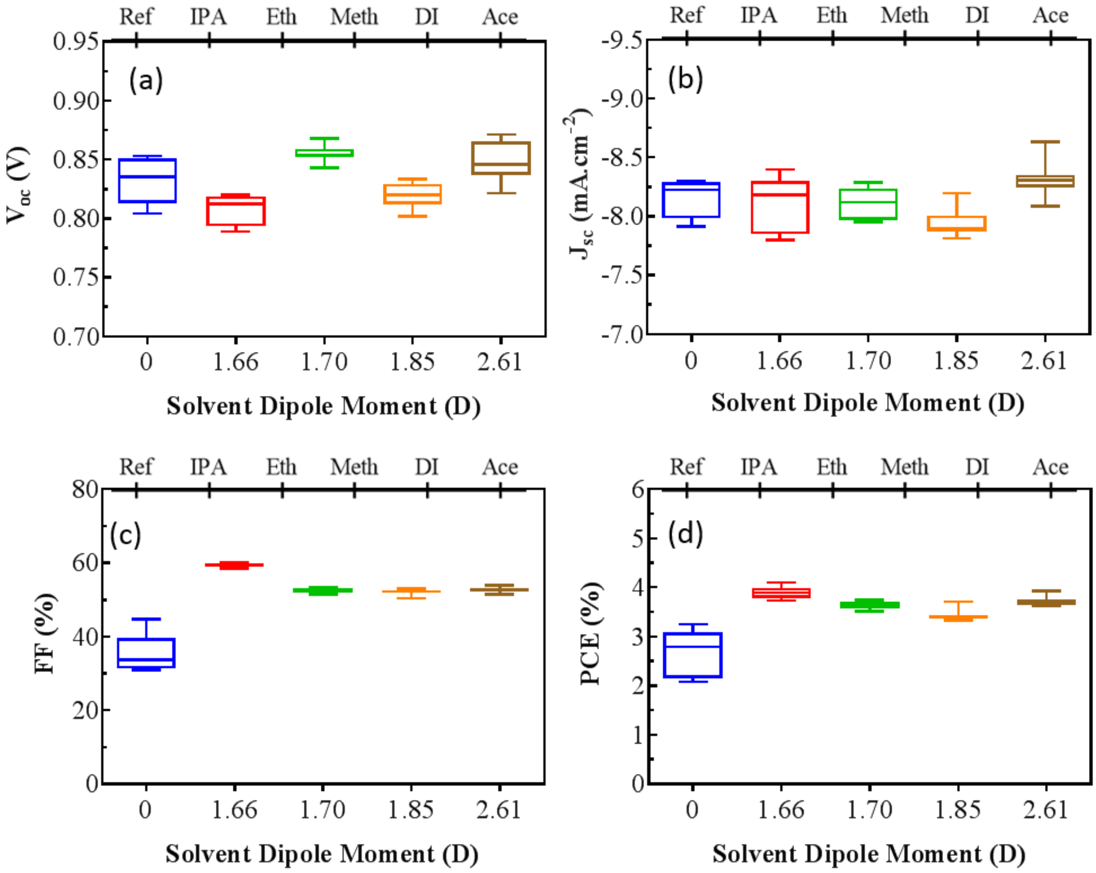

Figure 6.3 Device parameters for inverted devices fabricated onto blank ITO cleaned with different solvents, showing (a) open circuit voltage (Voc), (b) short circuit current (Jsc), (c) fill factor (FF), and (d) power conversion efficiency (PCE), as a function of solvent dipole moment. The Ref-device was fabricated onto an as-received ITO substrate. The boxes represent the average values of three devices (12 pixels in total) with an indication as to the median position per dipole moment. The vertical error bars represent the calculated standard deviation.

6.2.2 Effect of Ions

The surface composition of bare ITO treated with different cleaning solvents was investigated using X-ray photoemission spectroscopy. Details of the processing of XPS peaks were described earlier in **Chapter 5**. Wide scans of the ITO surface showed the existence of carbon, oxygen, indium and tin atoms, with no trace of physio-adsorbed ambient gasses, thus confirming the cleanness of the ITO surface.

Due to the asymmetry line-shape of high resolution scans for In and Sn core level spectra, two individual peaks are best fitted to show the possible oxidation states existing for each component. **Figure 6.4** shows the deconvolution of (a) In $3d_{5/2}$ spectra and (b) Sn $3d_{5/2}$ spectra as a function of the detergent dipole moment. The line shape of the In peak is often seen to be symmetrical [25], [26] but in some cases asymmetry associated with hydroxide is seen [27], [28]. The first fitted peak of In $3d_{5/2}$, located at 444.29 ± 0.18 eV, is assigned to In^{3+} bonding in a lattice as In_2O_3 [29]–[33]. The second peak located at 445.62 ± 0.19 eV is assigned to a different In oxidation state known as indium hydroxide ($In(OH)_3$). The $In(OH)_3$ peak originates typically from the presence of intermediated oxidation states like In^+ or In^{2+} [33]. The error values here consider the shifts in peak position due to detergent polarity.

Considering the Sn $3d_{5/2}$ spectra seen in **Figure 6.4 (b)**, the resolved peaks with binding energies of 486.40 ± 0.14 eV and 487.36 ± 0.21 eV are assigned to the well-known Sn^{4+} and Sn^{2+} oxidation states, respectively. The Sn^{4+} peak originates from the bonding in SnO_2 while the Sn^{2+} arises from the bonding in SnO [33]–[35]. The Sn^{4+} ion is considered to be an electron donor centre within ITO films due to the thermodynamic stability of SnO_2 [36]. Similar to the In 3d peaks, no significant shifts in Sn^{4+} peak positons were observed, implying that the cleaning procedure followed induces no chemical instability to the Sn atom. Compared to the as-received ITO, the lowest Sn^{4+} peak intensity was recorded for isopropyl alcohol (1.66 D), while the highest intensity was shown for deionized water (1.85 D). Changes in Sn^{4+} intensity indicate the changes in dopant concentration [36].

Figure 6.5 shows details of the peak position and relative strengths of the resolved peaks for both In $3\mathrm{d}_{5/2}$ and Sn $3\mathrm{d}_{5/2}$ core levels. For an IPA-cleaned ITO substrate and the as-received substrate, the In and Sn peak positions are constant, while for dipole moments higher than 1.66 D, they shift slightly to higher binding energies. Since three samples were measured for each cleaning condition, however, an avoidable error in the order of 0.2 eV was encountered within the acquired row data when the measurement was repeated on another day. This is called the ‘run-to-run’ error. The changes in peak positions seem to be statistically insignificant, therefore, because the calculated standard deviation errors fall within the run-to-run errors (i.e. they do not exceed 0.2 eV). It can be concluded that varying the cleaning solvent does not induce the effect on In and Sn core levels. A similar conclusion can be drawn for the relative strength of the peak intensities.

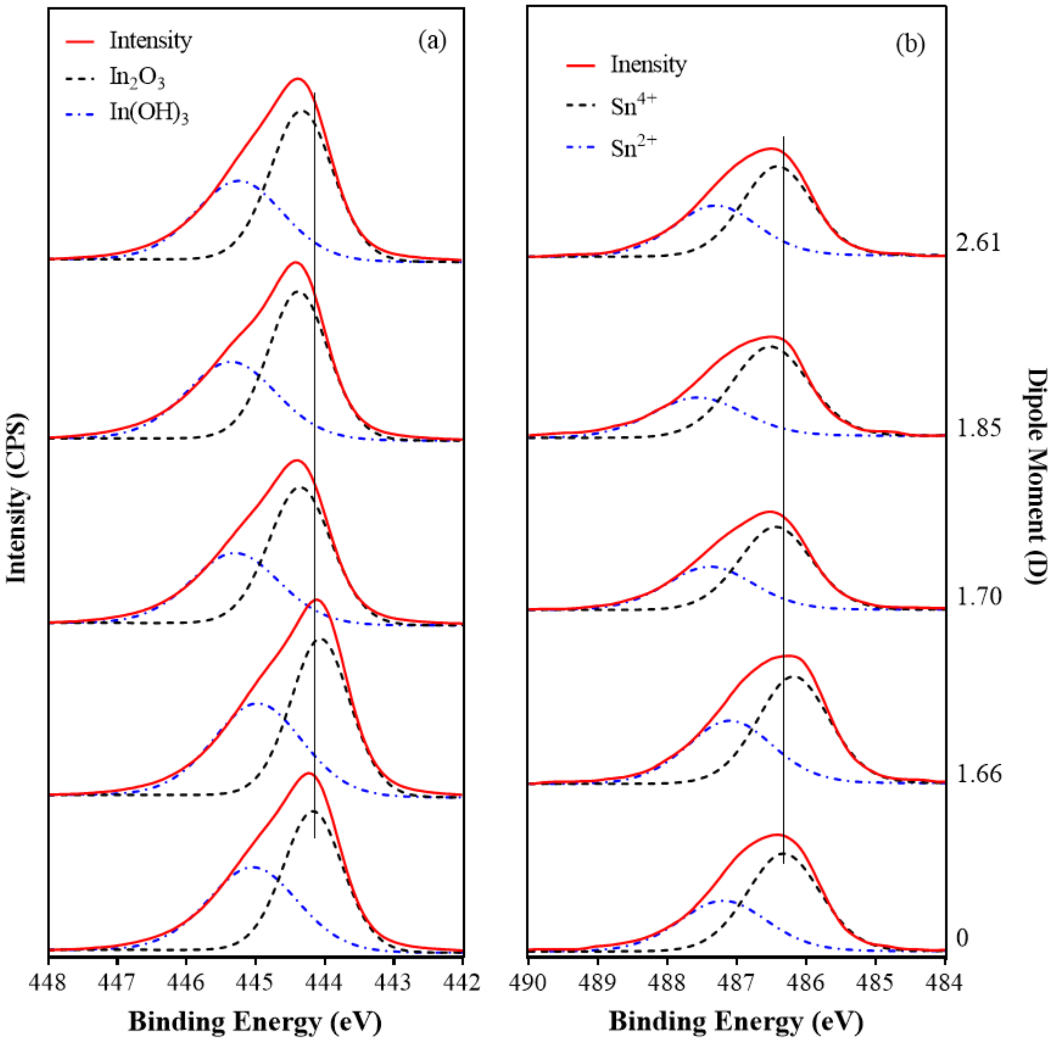

Figure 6.4 Deconvolution of high-resolution spectra of (a) In $3d_{5/2}$ and (b) Sn $3d_{5/2}$ core levels detected by XPS for bare ITO cleaned with different detergents at the final wash step. The dipole moment of the detergent is presented for as-received non-cleaned substrate (0 D), isopropyl alcohol cleaning (1.66 D), methanol cleaning (1.70 D), deionized water cleaning (1.85 D), and finally acetone cleaning (2.61 D).

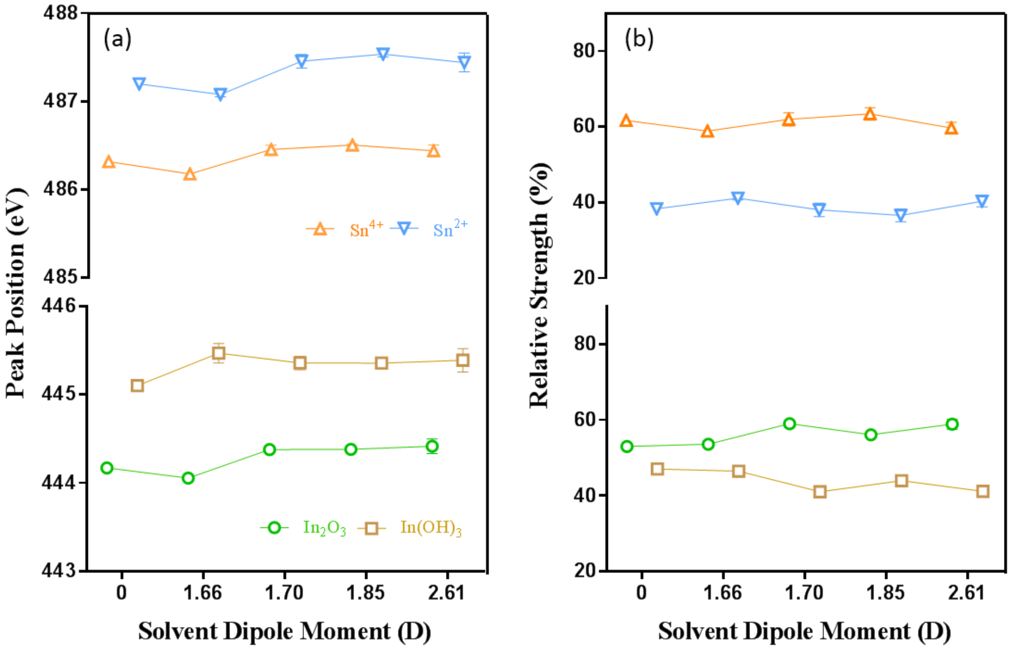

Figure 6.5 (a) Positions and (b) relative strengths of fitted peaks to the quantified spectra of In $3d_{5/2}$ and Sn $3d_{5/2}$ core-levels as a function of solvent dipole moments, showing average values with standard deviation errors of three samples per solvent, plotted vertically.

.

The O 1s core-level spectra were fitted with three adjacent component samples, as seen in **Figure 6.6 (c)**. These are assigned to the oxygen lattice in $\mathrm{In_2O_3}$, referenced as 'O-In', with a binding energy of 529.92 ± 0.15 eV, the $\mathrm{O^{2-}}$ ions in the oxygen deficient $\mathrm{In_2O_{3-x}}$ matrix located at 531.02 ± 0.17 eV, and the oxygen in $\mathrm{In(OH)_3}$ referenced as 'O-OH', at 532.40 ± 0.19 eV. The position of these three peaks are in agreement with those reported by Chuang et al. [37], [38]. An additional peak was fitted particularly to ITO samples cleaned by deionized water and positioned at 534.59 eV. Ishida et al. [30] attributed the O 1s peak at 534.1 eV to oxygen atoms in In-O-H species that are formed due to the adsorption of hydrogen atoms onto the ITO surface during ion-beam deposition. The high binding energy of the In-O-H peak was explained as being due to the difference in electronegativity between hydrogen

(2.20) and indium (1.78), which results in a raised work function for the obtained film. Although evidence shows that the work function of the DIW-ITO substrate is higher than those treated with other detergents (see **Figure 6.9**), the additional peak reported here is at a binding energy that is 0.49 eV higher than that reported by Ishida et al. This difference in peak position is understandable due to the different origin of the peak (i.e. it occurs as a result of the physio-absorbance of a water molecule). We therefore assign the additional O 1s peak at 534.59 eV to the H_2O species rather than In-O-H.

The position of all resolved O 1s peaks are shifted to high binding energy in comparison with the as-received sample, with slightly low intensities, except for the IPA sample, as shown in **Figure 6.7**. These shifts do not exceed the run-to-run error of 0.2 eV, however, indicating the insignificant effect of the solvent dipole moment on the O 1s core level. Furthermore, the amount of O^{2-} ions represented by the relative strengths can determine the contribution of these ions to the short circuit current. The IPA sample shows the highest amount of oxygen vacancy (O^{2-} ions), with a relative strength of 45.14 % compared to the as-received sample. IPA-devices showed a Jsc of 8.40 $\mathrm{mA.cm^{-2}}$, while 7.92 $\mathrm{mA.cm^{-2}}$ was achieved for the as-received devices. Having a high amount of oxygen vacancy does not guarantee a high Jsc, however. This is because oxygen vacancy is known to act as trapping centre for charge carriers, hence increasing the probability of charge carrier recombination. The Ace-cleaned sample showed a slightly lower level of O^{2-} ions, of 44.43 %, resulting in the highest Jsc of 8.63 $\mathrm{mA.cm^{-2}}$, which may also be attributed to the high Sn^{4+} (61.14 %) compared to 58.61 % for the IPA-cleaned sample. The results suggest no clear correlation between the solvent dipole moment and device parameters (since a high Jsc could be due to either O^{2-}or Sn^{4+}).

The analysis of the C 1s core level spectra gives an indication of the degree of surface contamination, which has been reported to affect the electronic structure of ITO [25], [39], [40]. Three clearly-distinguish peaks were fitted to the deconvoluted C 1s spectra, however, showing three chemically different carbon species. These are a carbon main-chain (C-C and C-H) at 285 eV, a carbon bonding to hydroxide (C-OH) at 286.32 ± 0.1 eV, and a carbon doubly bonded with oxygen (C=O) at 288.61 ± 0.15 eV. As seen in **Figure 6.6 (d)**, there were no observed shifts in peak position upon ITO treatment with different organic solvents. The sole change is in the amount of contamination present, which is represented by the relative strength of the peak. **Figure 6.8** shows the changes in the atomic ratio of surface elements to indium with the different cleaning solvents. The cleanest surface was following cleaning with IPA, with the lowest obtained carbon to indium (C/In) ratio (0.63%). This is evident with the significant reduction in the measured C 1s intensity. Cleaning with other solvents seemed to increase the surface contamination compared to the as-received sample (0.89 %). A maximum C/In of 1.41 % was obtained for methanol, while cleaning in water and acetone results in a carbon to indium ratio of 1.08 % and 1.06 % respectively. It is necessary, however, to establish a correlation between the amount of carbon contamination and the ITO work function and device efficiency, as will be discussed in the following sections.

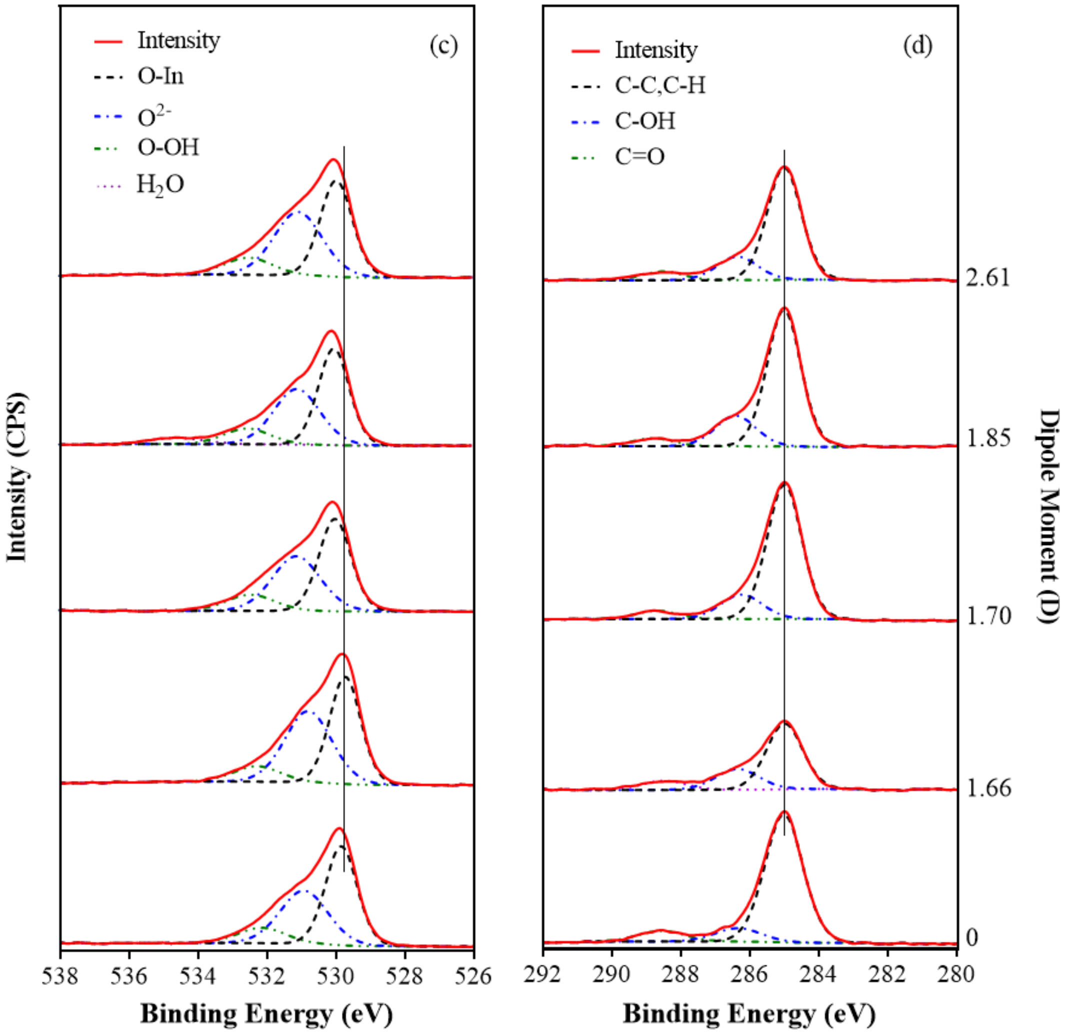

Figure 6.6 Deconvolution of high-resolution spectra of (c) O 1s and (d) C 1s core levels detected by XPS for bare ITO cleaned with different detergents at the final wash step. The dipole moments of detergents for as-received non-cleaned substrate (0 D), isopropyl alcohol cleaning (1.66 D), methanol cleaning (1.70 D), deionized water cleaning (1.85 D), and finally acetone cleaning (2.61 D)

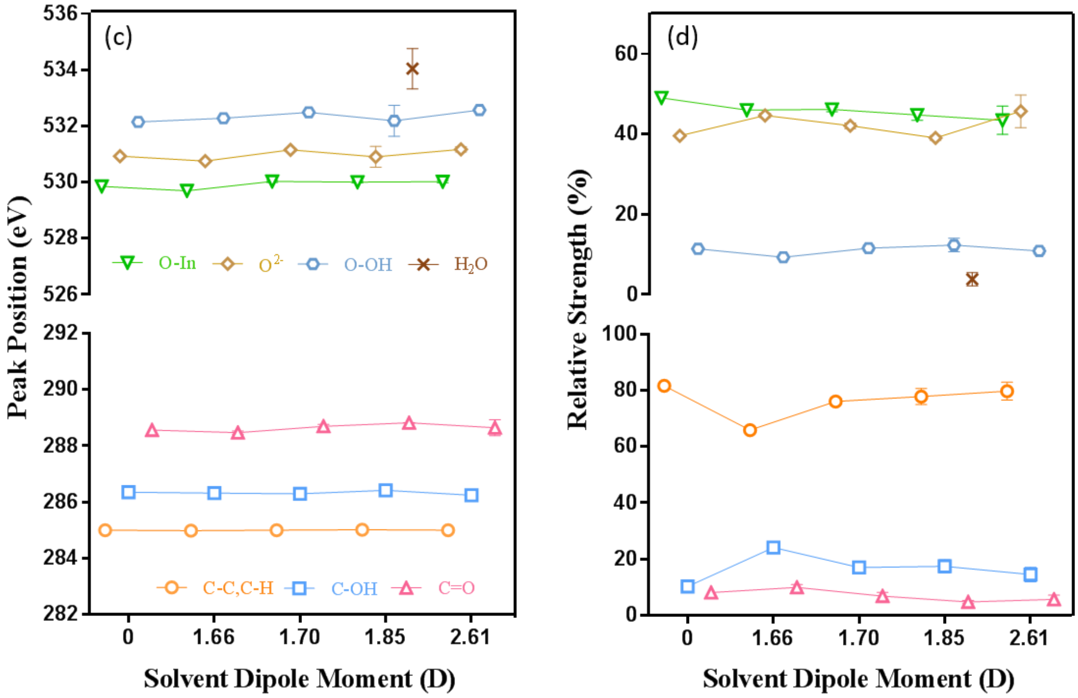

Figure 6.7 (c) Positions and (d) relative strengths of fitted peaks to the quantified spectra of O 1s and C 1s core-levels as a function of solvent dipole moments, showing the average values with standard deviation errors of three samples per solvent, plotted vertically.

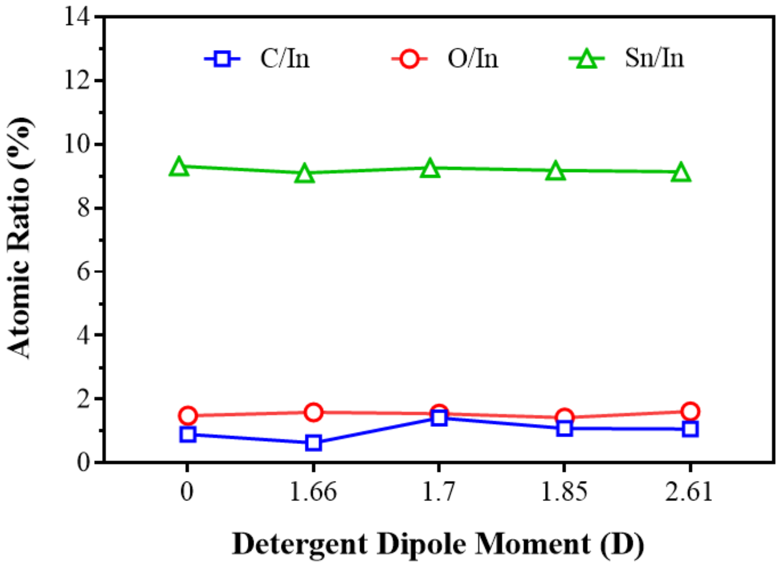

Figure 6.8 Changes in the atomic ratio of surface elements including carbon, oxygen, and tin with respect to indium for ITO samples cleaned ultrasonically with various detergents; isopropyl alcohol cleaning (1.66 D), methanol cleaning (1.70 D), deionized water cleaning (1.85 D), and finally acetone cleaning (2.61 D).

6.2.3 Effect of the Work Function

The UPS spectra of bare ITO cleaned with different detergents are shown in **Figure 6.9**. The work function was calculated by subtracting the secondary electron cut-off energy (**Figure 6.9 (a)**) from the incident photon energy as described previously in **Chapter 5**. Based on three samples with three different areas being measured per sample, the averaged work function for the as-received ITO was found to be 4.69 ± 0.02 eV. The errors here indicate the standard deviation of the measured values. Cleaning with detergents lowered the ITO work function as follows: 4.51 ± 0.02 eV (for DIW, 1.85 D), 4.49 ± 0.04 eV (for MeOH, 1.70 D), 4.40 ± 0.03 eV (for IPA, 1.66 D), and 4.29 ± 0.05 eV (for Ace, 2.61 D). A significant 0.4 eV reduction was therefore encountered after cleaning with acetone, but the changes in the work function between ITO samples cleaned by deionized water, isopropanol and methanol do not exceed 0.1 eV, as seen in **Figure 6.9 (c)**. In addition, the valence band edges of all cleaned samples remained constant at 2.87 ± 0.03 eV (**Figure 6.9 (b)**), although this was a 0.2 eV higher binding energy compared to that of the as-received non-cleaned sample (2.66 ± 0.02 eV). It can be concluded that solvent significantly reduces significantly the work function by a maximum of 0.4 eV compared to non-cleaned ITO.

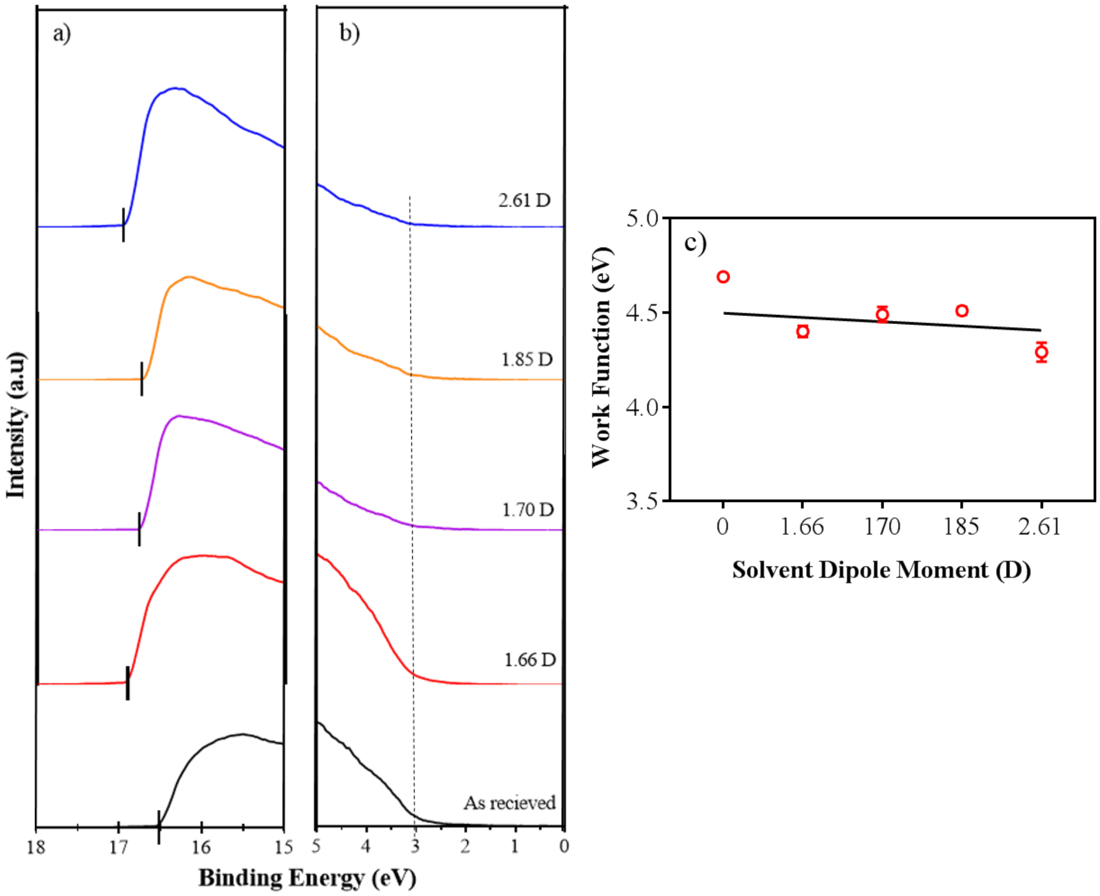

Figure 6.9 UV Photoelectron spectra of blank ITO samples cleaned ultrasonically with different solvents showing (a) the cut-off energy of the high binding energy region and (b) the valence band edge within the low binding energy region. (c) Plot showing the average work function of three samples per cleaning solvent and its corresponding standard deviation errors. Dipole moments of 0 D, 1.66 D, 1.70 D, 1.85 D, and 2.61 D are assigned to the non-cleaned as-received sample, isopropanol, methanol, deionized water, and acetone-cleaned samples, respectively.

6.2.4 Effect of Energetic Mismatch at Cathode Interface

The energetic mismatch at the ITO/PCBM interface was calculated for each cleaning solvent in order to investigate how far it would affect the device parameters. This was done by subtracting the value of the LUMO level for PCBM from the ITO work function. It was found that cleaning the ITO surface with acetone provides the lowest energetic mismatch at the interface (0.01 eV) compared to the non-cleaned as-received sample (0.39 eV). Meanwhile, energy mismatches of 0.10 eV, 0.15 eV and 0.21 eV were found for cleaning with IPA, methanol and deionized water, respectively. The correlation between the energetic mismatch and device parameters is shown in **Figure 6.10**. It can see that the bigger the energetic mismatch is, the lower the device efficiency achieved. This is because a large energetic mismatch significantly reduces Jsc rather than Voc, as proved by the fitted lines with slope gradients of 1.8 and 0.16, respectively. A slope gradient of less than 1 indicates the statistical insignificance of detected changes (as seen in Voc). With an energy mismatch of 0.39 eV, the as-received devices showed a PCE of 2.23 % (Jsc of 7.92 mA.cm^{-2}, Voc of 0.80 eV), whereas the acetone-cleaned devices, with a mismatch of 0.01 eV, showed a PCE of 3.93 % (Jsc of 8.63 mA.cm^{-2}, Voc of 0.82 eV). Since the enhancements in the Jsc of those devices originates from lowering the series resistance (40 Ω.cm verse 21 Ω.cm), it can be concluded that an energetic mismatch at the cathode interface can affect device efficiency by tuning the series resistance.

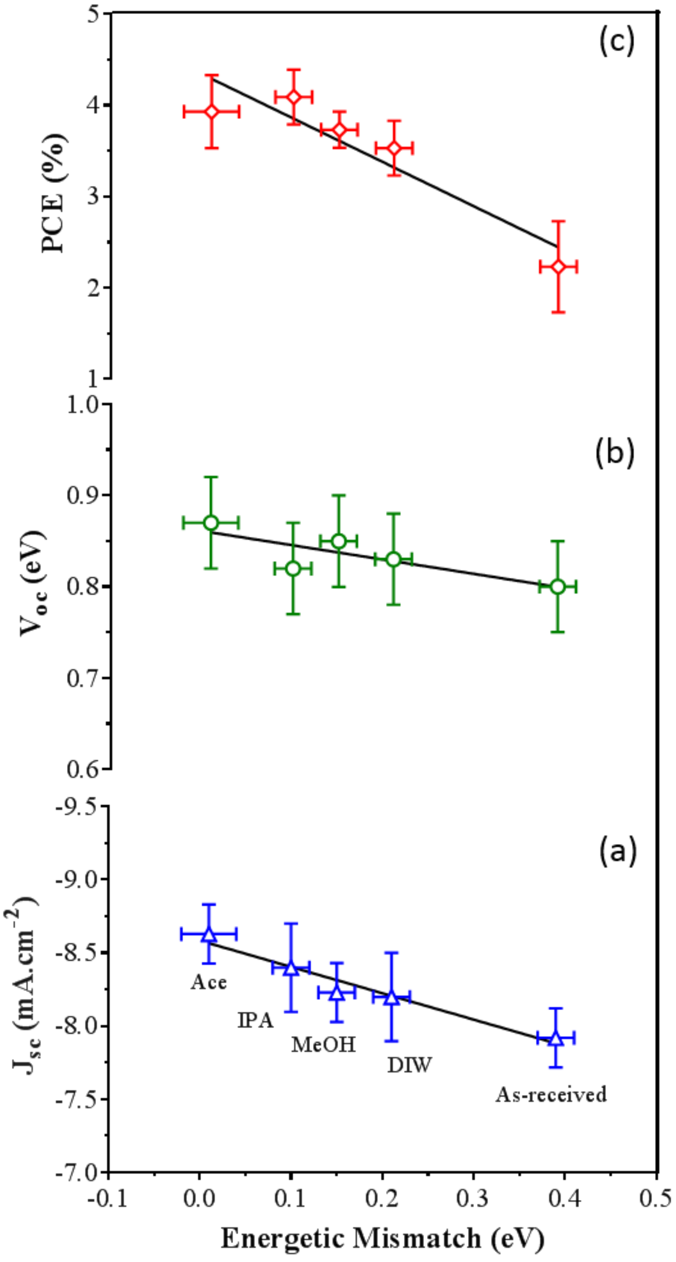

Figure 6.10 Plot showing the effect of the energetic mismatch at ITO/PCBM interfaces induced by different cleaning solvents on (a) short circuit current, Jsc, (b) open circuit voltage, Voc, and (c) device efficiency, PCE. The energetic mismatch is calculated by subtracting the value of the PCBM LUMO energy level from the ITO work function for each solvent. The average values with standard deviation errors (vertical) are calculated for each device parameter out of 12 pixels, whereas the standard errors (horizontal) are calculated from three samples per cleaning condition. The black lines show the best fit to the data presented.

6.2.5 Effect of Surface Contaminations

Surface contamination refers to the amount of different carbon species existing on the thin-film surface and so-called ‘carbon contamination’. Carbon contamination has been reported to affect the ITO work function and hence device performance [23], [41], [40]. Sugiyama et al. [42] showed that the ultrasonic cleaning of a commercial ITO substrate in respective organic solvents of acetone and isopropyl alone lowers the ITO work function to 4.5 eV compared to 4.75 eV for the UV ozone treatment. This was attributed to the considerable carbon contamination obtained (19 % for ultrasonic cleaning, 8 % for UV cleaning). Sharma et al. [40] reported that cleaning the ITO surface with organic detergents followed by O_2 plasma lowers the series resistance and hence enhances the performance of a standard polymer solar cell. To investigate the claim reported by Sharma et al. [40], therefore, a correlation between the work function of ITO samples cleaned by different techniques and the atomic concentration of carbon species detected by XPS was established, as seen in **Figure 6.11.** Cleaning techniques include sputtering with argon (Ar), ultraviolet (UV) plasma ozone, and a standard cleaning procedure with organic solvents. UV ozone was shown to provide the highest work function; up to 4.98 ± 0.06 eV with a low carbon contamination of 0.1 %. This procedure is reported to be suited to standard BHJ devices where a high ITO work function is required in order to facilitate the extraction of positive mobile charges [43]. It can also be used to enhance the adhesion and coverage of metal oxide cathode buffer layers which can result in highly efficient inverted devices [44], [45]. Details on the surface composition of UV ozone-treated ITO substrate will be discussed in **Chapter 8**. In addition, Ar sputtering cleans the ITO surface better, providing the lowest contaminated carbon amount of 0.02 %, as well as the lowest ITO work function of 4.20 ± 0.05 eV. PCDTBT: PCBM inverted devices fabricated onto bare ITO sputtered by Ar ions showed very poor performance, however. When comparing with a standard cleaning procedure, it can be seen that having a slightly contaminated surface does not really affect the work function of ITO samples. Samples cleaned by IPA, DIW, MeOH and Ace showed carbon concentrations of 0.19 %, 0.29 %, 0.34 %, and 0.39 %, respectively, and respective work functions of 4.40 eV, 4.51 eV, 4.49 eV, and 4.29 eV. In support of this, the fitted line in **Figure 6.11** has a slope in the order of – 0.15, showing the statistical insignificance of carbon contamination in respect to the ITO work function. It can be concluded that carbon contamination does not really tune ITO work function as had been claimed by Sharma et al. [40].

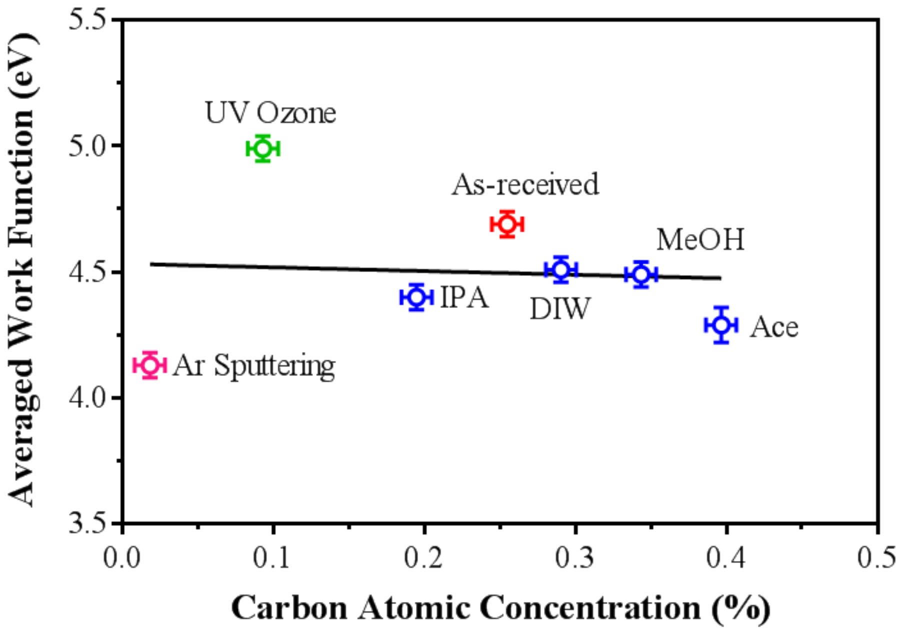

Figure 6.11 Plot showing the correlation between the atomic concentrations of carbon contaminants existing on the ITO surface, measured by XPS, and averaged ITO work function measured by UPS. The black line indicates a line of best fit to the data presented. The standard deviation errors are calculated for three samples per cleaning condition and plotted for both work function (vertical) and contaminant concentrations (horizontal).

6.3 BHJ Layer Properties

The bulk heterojunction (BHJ) layer is where the whole process of sunlight absorption, charge carrier generation and dissociation occurs. The properties of this layer are therefore of vital importance to determine device performance. These include layer thickness, roughness, post-deposition annealing and the properties of its component materials. Here results on layer thickness and post-deposition annealing are presented in order to investigate whether further enhancements in device performance will be obtained.

6.3.1 *Thickness Dependence*

One of the benefits of blending a conjugated polymer with fullerene molecules is to enhance light absorption within the visible light range by enabling fast charge transfer [46]. **Figure 6.12** shows UV-vis absorption spectra of thin films of PCDTBT: PC70BM blended as a function of their thickness and compared to pristine PCDTBT thin films. Films were spun from a chlorobenzene solution with a 1:4 stoichiometry. The pristine PCDTBT film shows a broadened absorption band with two unique peaks located at 394 nm and 572 nm. The onset of absorption of this polymer occurs at 660 nm, corresponding to an optical band gap of 1.88 eV. This result is in agreement with ref [47]. Note that the position of the absorption bands for pristine PCDTBT is slightly affected by the solvent used to prepare the film; 380 nm, 545 nm for TCB [46], and 398 nm, 576 nm for ODCB [48]. A thin film of PCDTBT: PC70BM BHJ shows a 20 % better absorption compared to the thin film of pristine PCDTBT. The unique double peaks are blue shifted due to the existence of fullerene molecules (378 nm compared to 397 nm for PCDTBT) as seen for the 70 nm thick film. Increasing the film thickness up to 120 nm results in a 26 % increase in the light absorption compared to that obtained for 70 nm. Rather than the 20 % absorption at the longer wavelength (>660 nm) not being real, however, it is likely to be a result of scattering events due to the measured organic film being deposited onto ITO samples.

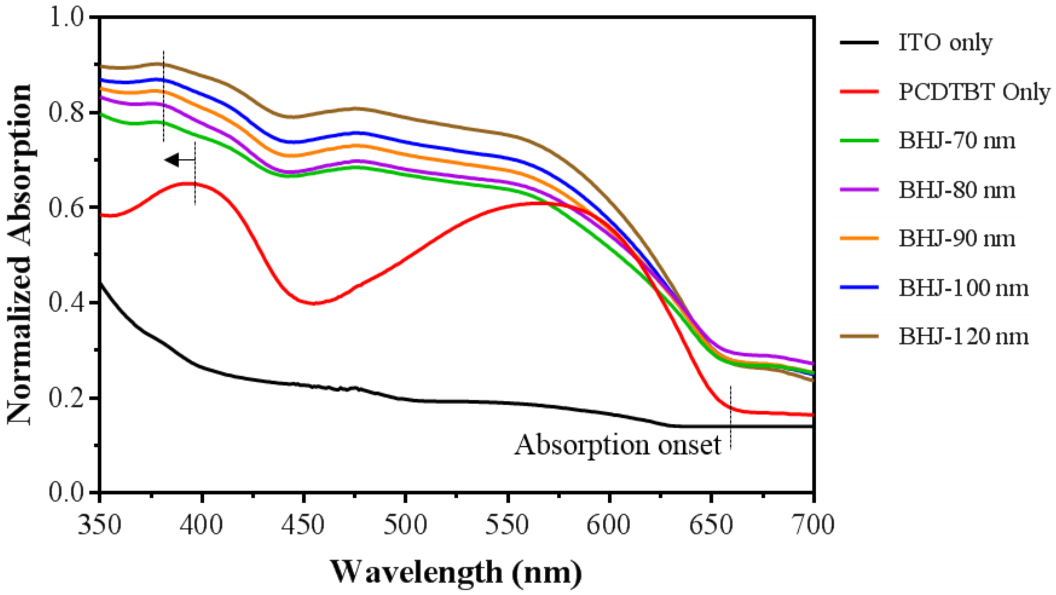

Figure 6.12 UV-vis absorption spectra for (1:4 blend ratio by weight) PCDTBT: $PC_{70}BM$ BHJ thin films with various thicknesses. The spectra of pristine PCDTBT thin film and bare ITO substrate are included for comparison.

The enhanced absorption for thicker films (≥ 100 nm) does result in deteriorating device performance, however, as shown in **Figure 6.13 (a-d)**. The power conversion efficiency of inverted devices prepared with various PCDTBT: PCBM active layer thickness was shown to gradually increase from $3.66 \pm 0.48\ \%$ for 75 nm to a maximum of $4.65 \pm 0.25\ \%$ for 95 nm. When the active layer thickness increases to 100 nm, the efficiency dropped to $4.50 \pm 0.36\ \%$. A further increase in thickness by 20 nm resulted in the efficiency being reduced to $3.85 \pm 0.23\ \%$. The open circuit voltage and fill factor follow a similar trend to the device efficiency. Slight fluctuations in the averaged short circuit current in a magnitude of

$\pm 0.5\,\mathrm{mA.cm^{-2}}$ were seen when the thickness was increased up to 95 nm. For $100\,\mathrm{nm}$ to 120 nm, however, the current dropped significantly from $9.92 \pm 0.28\,\mathrm{mA.cm^{-2}}$ to $9.24 \pm 0.12\,\mathrm{mA.cm^{-2}}$. The reduction in device performance for thick layers ($\geq 100\,\mathrm{nm}$) is in agreement with the changes observed for both series shunt resistances, see **Figure 6.13 (e, f)**. The high series resistance and low shunt resistance obtained for devices with thicker layers confirm the fact that having more PCBM can induce defects whose density is linearly dependent on the blend film thickness [49]–[51]. These defects provide different paths for charge recombination, such as coupled trap- assisted (bimolecular) recombination [52]. The optimal efficiency for PCDTBT:PCBM based solar cells has therefore been reported to be limited to active layer thickness of 70 – 90 nm [53]. We realized, however, that inverted devices with active layers 90 – 95 nm thick exhibit the best performance. This may be attributed to the absence of a cathode buffer layer assisting in the redistribution of the electromagnetic field within the device [54].

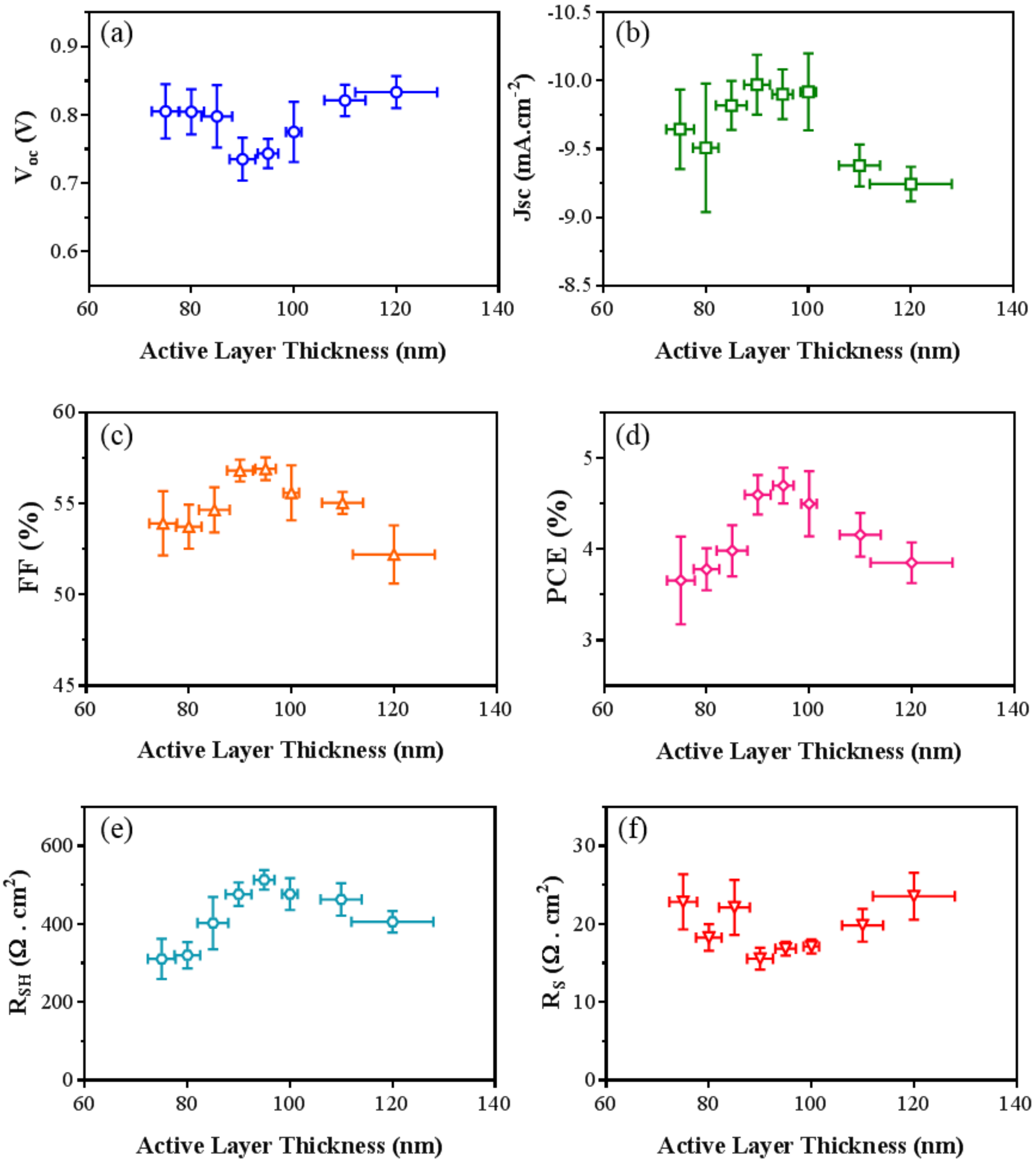

Figure 6.13 Effect of varying the thickness of the active layer on the parameter matrix of inverted PCDTBT: PCBM devices showing (a) open circuit voltage (Voc), (b) short circuit current (Jsc), (c) fill factor (FF), (d) power conversion efficiency (PCE), (e) sheet resistance (Rsh), and (f) series resistance (Rs). The average values of the parameters are plotted. Vertical error bars indicate the standard deviations of 12 pixels per thickness. Horizontal error bars indicate the standard deviation of eight readings from different areas across the surface of two samples per thickness, using a Dektak surface profile.

6.3.2 Temperature Dependence

The post-deposition annealing of the BHJ layer has been seen to effect device parameters. A common example is the benchmark P3HT: PCBM BHJ based standard devices. The power conversion efficiency of pristine devices has been shown to be limited to 1 – 2 % [55]. Annealing the active layer at a temperature (150 ℃) that fits between the glass transition and melting temperatures of P3HT, improves the PCE of the devices significantly, up to 4 – 5 % [56]. Thermal annealing drives the crystallinity of film constituents forming optimal phase-separated domains [57], [58], as well as modifying the vertical structure of the P3HT: PCBM thin film [59]. This is not the case for PCDTBT: PCBM based standard devices, however. Annealing PCDTBT at temperatures above 100 ℃ induces structural disorder, where the coherence length of π-π staking is reduced as a result of the better arrangement of side chains [60]. The coherence length refers to the length over which the crystalline packing remains ordered [60]. A consequence of this disorder is the energetic spread of HOMO level states [61], and hence the broadening of the sub-band gap tail state [62]. The deep HOMO states act then as a trapping centre for holes in the PCDTBT. As the temperature raises, the distribution of these trap states increases and the Jsc is evidently reduced, as reported for hole-only devices [60].

Mild temperature annealing appears, however, to be sufficient for enhancing PCDTBT: PCBM device efficiency. A 6.1 % efficient PCDTBT: PCBM (1:4 blend ratio) standard device annealed at 70 ℃ is reported by Park et al. [63]. A neutron reflectivity study of a freshly spin-coated PCDTBT: PCBM film conducted by Staniec et al. [64] illustrates the formation of a thin layer of PCBM at the surface where the negative gradient of PCBM exists normal to the film surface. Upon annealing at 70 ℃, no significant morphological changes were induced, except a further motion of PCBM molecules towards the anode interface and a slight broadening of the interface with the underlying layer [65]. Staniec et al. claimed that the observed vertical separation of the PCBM surface layer is suitable for standard based devices to facilitate electron transport through the top cathode. Hence, annealing at a low temperature is proposed to remove trapped casting solvent. To investigate this claim regarding the inverted structure, PCDTBT: PCBM devices were here fabricated with various annealing temperatures of the active layer. The temperature was systematically varied from 40 – 120 ℃ with 20 ℃ intervals while the annealing time kept constant for 15 min in an inert atmosphere. The reference device was a PCDTBT: PCBM inverted device fabricated without annealing and referred to as ‘non-annealed’ or ‘25 ℃’.

The current density–voltage characteristics under illumination are shown in **Figure 6.15**. Despite the good shape of the JV curves, minor enhancements in the fill factor are observed with annealing compared to the non-annealed device. The non-annealed device exhibits a Voc of 0.78 eV, Jsc of 10.03 mA.cm^{-2}, FF of 54.62 %, and PCE of 4.28 %. This is attributed to the very slight enhancement in the short circuit current, while the open circuit voltage shows neglectable changes, with a 0.08 eV maximum improvement observed at 80 ℃. **Figure 6.16** shows the changes induced on both Jsc and PCE by thermal annealing. It can be seen that annealing at 80 ℃ for 15 min produces the best device performance with 0.86 eV, 10.78 mA.cm^{-2}, 54.27 %, and 5.03 % obtained for Voc, Jsc, FF and PCE, respectively. This is due to the enhancement in light absorption, as confirmed by the UV-vis absorption measurement shown in **Figure 6.17**. Annealing at 80 ℃ seems to enhance absorption by 15 % compared to a non-annealed active layer. Rather than the 20 % absorption at the longer wavelength (>660 nm) not being real, however, it is likely to be a result of scattering events due to the measured organic film being deposited onto ITO samples.

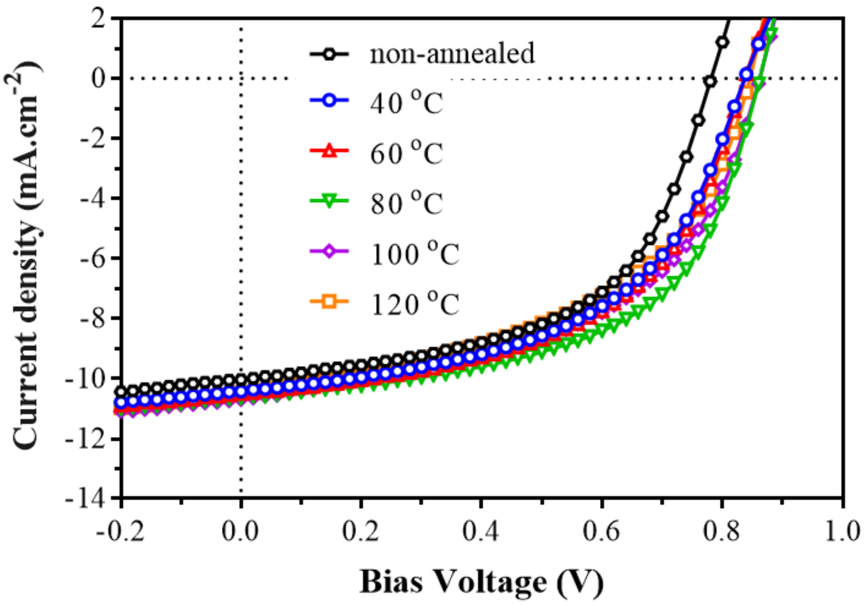

Figure 6.14 JV curves under illumination for inverted PCDTBT: PCBM devices having no electron transport layers as a function of active layer annealing.

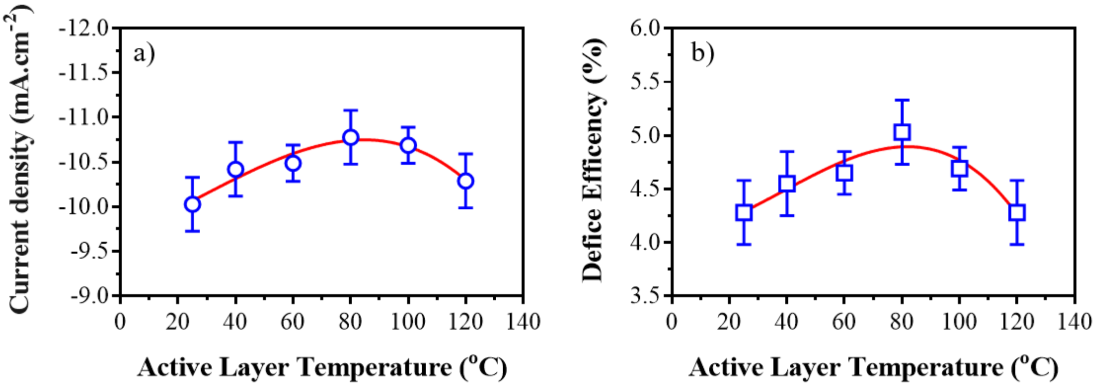

Figure 6.15 Effect of thermal annealing of the active layer of inverted PCDTBT: PCBM devices fabricated onto blank ITO, showing changes in (a) current density and (b) device efficiency. The plotted points represent the mean values of each parameter with error bars accounting for the standard deviations of the measured devices.

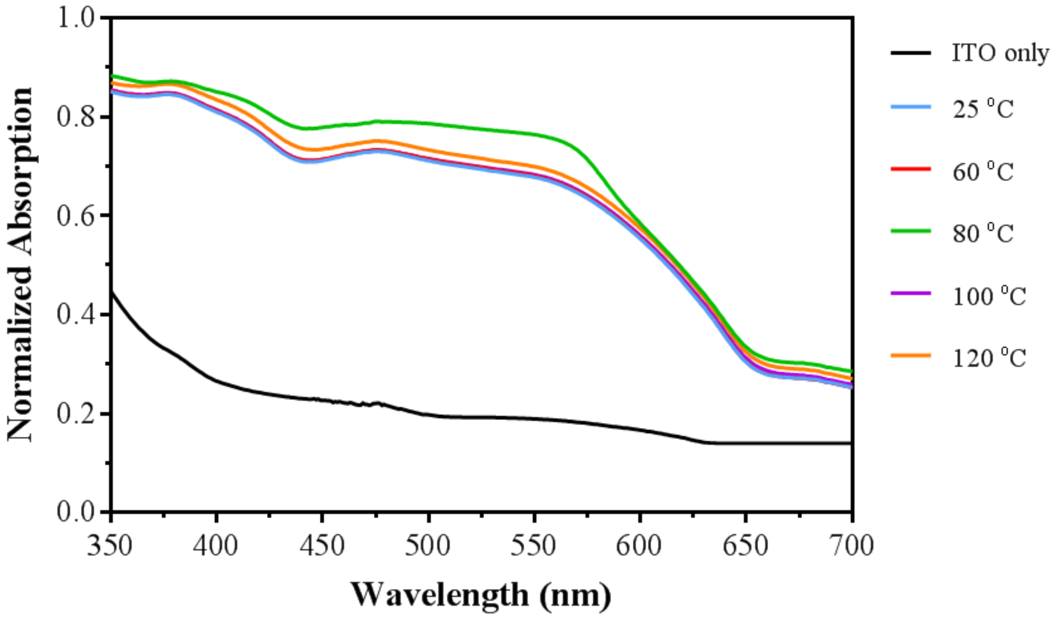

Figure 6.16 Absorbance spectra for PCDTBT:PCBM BHJ thin-films annealed at various temperatures while their thickness was kept constant at 90 nm. The reference sample is a BHJ thin film prepared at room temperature (25 ℃).

To encounter the effect of buffer layer, PCDTBT: PCBM inverted cells were also fabricated onto two different buffer layers, including sol-gel derived zinc oxide (ZnO) and conjugated polyelectrolyte (poly[(9,9-bis(3′-(N,N-dimethylamino)propyl)-2,7-fluorene)-alt-2,7-(9,9-dioctylfluorene) (PFN). Changes in device efficiency upon active layer annealing at 80 ℃ compared to non-annealed devices (25 ℃) are shown in **Figure 6.18**. Similar to devices fabricated onto blank ITO, an 18-28 % improvement in device efficiency is encountered for annealed devices. This implies the requirement of mild annealing to achieve the necessary nanoscale morphology of the active layer. It should note that the performance of our devices based on ZnO modification is unexpectedly lower than those reported in literature [66], showing maximum efficiency of 7.1 %. Our ZnO modified devices showed a maximum efficiency of 4.35 % due to low fill factor.

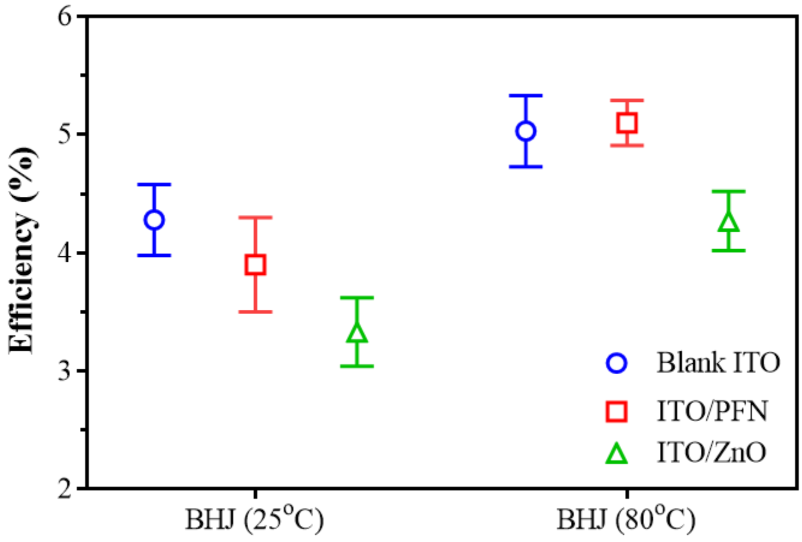

Figure 6.17 Plot showing changes in device efficiency of inverted PCDTBT: PCBM solar cells fabricated onto various substrates upon active layer annealing temperature. BHJ (25 ℃) represents devices fabricated without non-annealed active layer of 90 nm, while BHJ (80 ℃) represents devices with active layer annealed at 80 ℃.

6.4 Anode Thickness Dependence

In an inverted structure, the active layer is often capped with two layers; a hole selective layer and a metallic layer. The buffer layer used for this work is molybdenum oxide (MoO_x), capped with either aluminium (Al) or silver (Ag). Molybdenum oxide has been chosen in order to overcome the stability issue of the benchmark hole selective layer PEDOT:PSS [67], [68]. Its deep valance band (5.30 eV) [69] is suitable for extracting positive charge current from the active layer, see **Figure 6.19**. The thickness of the MoO_x layer has been reported to be critical for device performance, however [70], [71]. This is because some of the light is partly absorbed by the layer when it is deposited directly onto ITO [43]. A absorption of 3 % of the total light by the PCDTBT:PCBM active layer has been reported to be lost due to a 10 nm thick MoO_x layer [72]. In addition, a thicker layer redistributes the electromagnetic field within the device in a non-linear way whereby both active layer absorbance and hence photocurrent are both reduced [73]. Standard BHJ solar cells are therefore limited to MoO_x thin films ($\leq$ 10 nm) if devices are to be highly efficient. This is not the case for our fabricated inverted devices, however.

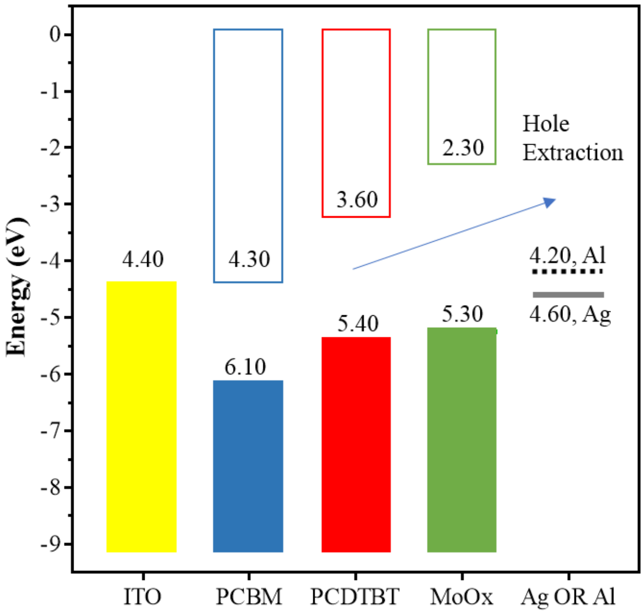

Figure 6.18 Energy level diagram for component materials used in inverted devices. Energy level of MoO_x is taken from the data sheet provided by Ossila Ltd.

Figure 6.20 summarizes the effect of molybdenum oxide layer thickness on the device parameters. Two sets of devices were identically fabricated with MoO_x/Al and MoO_x/Ag top anodes. The thicknesses of both Al and Ag layers were kept constant at 100 nm. For the MoO_x/Al anode, both Voc and Jsc are shown to be insensitive to MoO_x thickness. This agrees with a similar study reporting the insensitivity of the Voc of P3HT:PCBM based devices to the top anode metal [75]. Interestingly, gradual increases in both fill factor and device efficiency are obtained as the thickness increases. A maximum FF of 59 ± 0.2 % and PCE of 5.35 ± 0.25 % are seen for a 20 nm MoOx thick layer capped with a 100 nm Al layer. When it is capped with the 100 nm Ag layer, all parameters become sensitive to the MoO_x thickness. The Voc drops when the MoO_x thickness increases from 8 nm to 12 nm, and then returns to its initial value (at 8 nm) when the MoO_x thickness is further increased up to 18 nm. Voc becomes independent of MoO_x thickness and remains constant for layers thicker than 18 nm. This may be attributed to the high reflectivity of silver compared to aluminium. Watters et al. [54] argued that standard PCDTBT: PCBM devices capped with Ca/Al cathode layers are more efficient than those capped with Ca/Ag, which was attributed to the low optical density of the Ag. Modelling the distribution of the electromagnetic field within the layers showed the significantly large penetration of the field within the Ag compared to with Al, leading to high optical loss; a relative absorption of the optical field was predicted to be (21 %) 4 % for (Ca) Ag and (7 %) 10 % for (Ca) Al, respectively [54]. This claim is supported here by the gradual reduction in Jsc for inverted devices capped with MoO_x/Ag when the MoO_x thickness is increased from 8 nm to 18 nm. Similarly, both FF and PCE are seen to be reduced by 7.3 % and 5.8 %, respectively. Although a thick MoO_x layer ($\geq$ 18 nm) is shown to be sufficient to overcome the optical loss induced by Ag, device performance is still unsatisfactory. For the 20 nm device, a 15 % reduction in efficiency was observed compared to those fabricated with Al capping. Further investigation is needed to clarify the unexpected behaviour of the open circuit voltage observed for MoO_x/Ag capped devices.

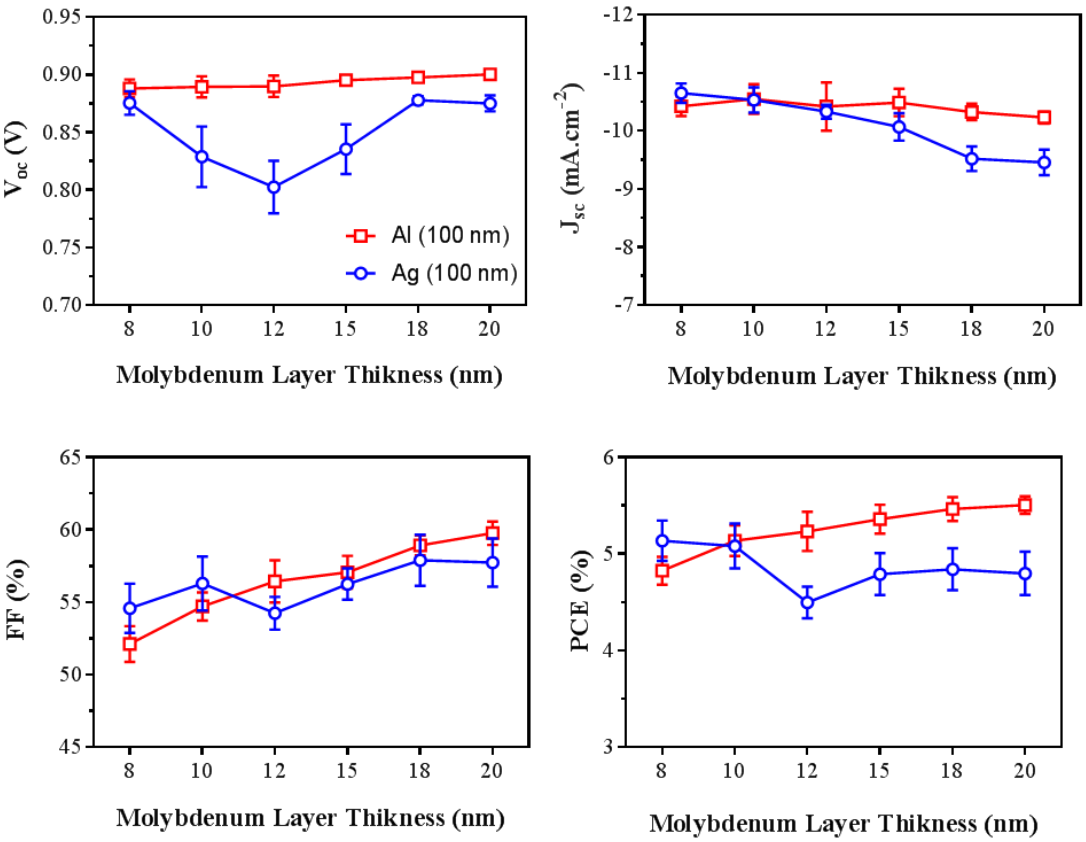

Figure 6.19 Device parameters as a function of molybdenum layer thickness. Data presents the mean values and standard deviation of 12 pixels with a structure of ITO/PCDTBT: PCBM (90 nm, 80 ℃ for 15 min)/MoO_x(varied)/Al (100 nm).

6.5 Conclusions

The development of benchmark ITO-only inverted devices along with the effects of cleaning techniques on the ITO electronic structure are investigated. XPS studies confirm the statistically insignificant effect of the dipole moment of the cleaning solvents on the ITO surface composition despite the local changes induced to bond environments. UPS studies, meanwhile, showed a significant effect on the ITO work function, which is reduced by a maximum of 0.4 eV upon cleaning with acetone (from 4.69 eV to 4.29 eV). This reduction has been proved to be not caused by surface contamination, as had been claimed by Sharma et al. [40]. Measurements of the energetic mismatch at ITO/PC70BM interfaces, however, showed the influence of ITO work function on the series resistance, affecting in turn the short circuit current and hence device efficiency.

Controlling the active layer thickness, annealing temperature and top anode materials was shown to enhance device performance. A mild annealing temperature for the thick active layer is shown to be necessary for realizing efficient devices. Compared to standard devices, a doubly thick layer of molybdenum oxide (18-20 nm) seems to be optimal for efficient devices capped with either aluminium or silver. The high optical reflectivity of the top metallic layer is seen to negatively affect the device parameters. The independence of the open circuit voltage is only seen for devices fabricated with thick molybdenum oxide layer capped with silver. Further investigation is required to elucidate the changes in device parameters for thin layers of MoO_3/Ag capped devices.

6.6 References

[1] H. Kim, C. M. G. Piqué, J. S. Horwitz, H. Mattoussi, H. Murata, Z. H. Kafafi, and D. B. Chrisey, "Electrical , optical , and structural properties of indium – tin – oxide thin films for organic light-emitting devices," *J. Appl. Phys.*, vol. 6451, no. 1999, 2000.

[2] R. Steim, F. R. Kogler, and C. J. Brabec, "Interface materials for organic solar cells," *J. Mater. Chem.*, vol. 20, no. 13, pp. 2499–2512, 2010.

[3] C. Su, T. K. Sheu, Y. T. Chang, M. A. Wan, M. C. Feng, and W. C. Hung, "Preparation of ITO thin films by sol-gel process and their characterizations," *Synth. Met.*, vol. 153, no. 1–3, pp. 9–12, 2005.

[4] T. Maruyama and K. Fukui, "Indium tin oxide thin films prepared by chemical vapour deposition," *Thin Solid Films*, vol. 203, no. 2, pp. 297–302, 1991.

[5] C. A. Pan and T. P. Ma, "High-quality transparent conductive indium oxide films prepared by thermal evaporation," *Appl. Phys. Lett.*, vol. 37, no. 2, pp. 163–165, 1980.

[6] H. Kim, J. S. Horwitz, G. P. Kushto, Z. H. Kafafi, and D. B. Chrisey, "Indium tin oxide thin films grown on flexible plastic substrates by pulsed-laser deposition for organic light-emitting diodes," *Appl. Phys. Lett.*, vol. 79, no. 3, pp. 284–286, 2001.

[7] M. Chuang, "ITO Films Prepared by Long-throw Magnetron Sputtering without Oxygen Partial Pressure," *J. Mater. Sci. Technol.*, vol. 26, no. 7, pp. 577–583, 2010.

[8] M. Huang, Z. Hameiri, A. G. Aberle, and T. Mueller, "Comparative study of amorphous indium tin oxide prepared by pulsed-DC and unbalanced RF magnetron sputtering at low power and low temperature conditions for heterojunction silicon wafer solar cell applications," *Vacuum*, vol. 119, pp. 68–76, 2015.

[9] S. Ishibashi, Y. Higuchi, Y. Ota, and K. Nakamura, "Low resistivity indium–tin oxide transparent conductive films. II. Effect of sputtering voltage on electrical property of films," *J. Vac. Sci. Technol. A Vacuum, Surfaces, Film.*, vol. 8, no. 3, pp. 1403–1406, 1990.

[10] T. Karasawa and Y. Miyata, "Electrical and optical properties of indium tin oxide thin films deposited on unheated substrates by d . c . reactive sputtering,"

Technology, vol. 223, pp. 135–139, 1993.

[11] L. Meng and M. . dos Santos, “Properties of indium tin oxide films prepared by rf reactive magnetron sputtering at different substrate temperature,” *Thin Solid Films*, vol. 322, no. 1–2, pp. 56–62, 1998.

[12] Y. T. Cheng, J. J. Ho, C. K. Wang, W. Lee, C. C. Lu, B. S. Yau, J. L. Nain, S. H. Chang, C. C. Chang, and K. L. Wang, “Improvement of organic solar cells by flexible substrate and ITO surface treatments,” *Appl. Surf. Sci.*, vol. 256, no. 24, pp. 7606–7611, 2010.

[13] H. Y. Yu, X. D. Feng, D. Grozea, Z. H. Lu, R. N. S. Sodhi, A.-M. Hor, and H. and Aziz, “Surface electronic structure of plasma-treated indium tin oxides,” *Appl. Phys. Lett.*, vol. 78, no. 17, pp. 2595–2597, 2001.

[14] R. Po, C. Carbonera, A. Bernardi, and N. Camaioni, “The role of buffer layers in polymer solar cells,” *Energy Environ. Sci.*, vol. 4, no. 2, p. 285, 2011.

[15] B. J. Worfolk, T. C. Hauger, K. D. Harris, D. A. Rider, J. A. M. Fordyce, S. Beaupré, M. Leclerc, and J. M. Buriak, “Work Function Control of Interfacial Buffer Layers for Efficient and Air-Stable Inverted Low-Bandgap Organic Photovoltaics,” *Adv. Energy Mater.*, vol. 2, no. 3, pp. 361–368, Mar. 2012.

[16] R. Kang, S.-H. Oh, S.-I. Na, T.-S. Kim, and D.-Y. Kim, “Investigation into the effect of post-annealing on inverted polymer solar cells,” *Sol. Energy Mater. Sol. Cells*, vol. 120, pp. 131–135, 2014.

[17] A. Sharma, A. Haldi, P. J. Hotchkiss, S. R. Marder, and B. Kippelen, “Effect of phosphonic acid surface modifiers on the work function of indium tin oxide and on the charge injection barrier into organic single-layer diodes,” *J. Appl. Phys.*, 2009.

[18] Y. Yan and Y. Song, “Effect of PEI cathode interlayer on work function and interface resistance of ITO electrode in the inverted polymer solar cells,” *Org. Electron.*, vol. 17, pp. 94–101, 2015.

[19] R. Xia, D.-S. Leem, T. Kirchartz, S. Spencer, C. Murphy, Z. He, H. Wu, S. Su, Y. Cao, J. S. Kim, J. C. DeMello, D. D. C. Bradley, and J. Nelson, “Investigation of a Conjugated Polyelectrolyte Interlayer for Inverted Polymer:Fullerene Solar Cells,” *Adv. Energy Mater.*, vol. 3, no. 6, pp. 718–723, Jun. 2013.

[20] Z. He, C. Zhong, S. Su, M. Xu, H. Wu, and Y. Cao, “Enhanced power-conversion efficiency in polymer solar cells using an inverted device structure,” vol. 6, no. September, pp. 591–595, 2012.

[21] A. Li, R. Nie, X. Deng, H. Wei, S. Zheng, Y. Li, J. Tang, and K. Y. Wong, "Highly efficient inverted organic solar cells using amino acid modified indium tin oxide as cathode," *Appl. Phys. Lett.*, vol. 104, no. 12, 2014.

[22] A. W. Hains, J. Liu, A. B. F. Martinson, M. D. Irwin, and T. J. Marks, "Anode interfacial tuning via electron-blocking/hole-transport layers and indium tin oxide surface treatment in bulk-heterojunction organic photovoltaic cells," *Adv. Funct. Mater.*, vol. 20, no. 4, pp. 595–606, 2010.

[23] Y. T. Cheng, J. J. Ho, C. K. Wang, W. Lee, C. C. Lu, B. S. Yau, J. L. Nain, S. H. Chang, C. C. Chang, and K. L. Wang, "Improvement of organic solar cells by flexible substrate and ITO surface treatments," *Appl. Surf. Sci.*, vol. 256, no. 24, pp. 7606–7611, 2010.

[24] Y. Zhu, X. Xu, L. Zhang, J. Chen, and Y. Cao, "High efficiency inverted polymeric bulk-heterojunction solar cells with hydrophilic conjugated polymers as cathode interlayer on ITO," *Sol. Energy Mater. Sol. Cells*, vol. 97, pp. 83–88, Feb. 2012.

[25] C. Donley, D. Dunphy, D. Paine, C. Carter, K. Nebesny, P. Lee, D. Alloway, and N. R. Armstrong, "Characterization of Indium−Tin Oxide Interfaces Using X-ray Photoelectron Spectroscopy and Redox Processes of a Chemisorbed Probe Molecule: Effect of Surface Pretreatment Conditions," *Langmuir*, vol. 18, no. 2, pp. 450–457, Jan. 2002.

[26] A. Sharma, G. Andersson, and D. A. Lewis, "Role of humidity on indium and tin migration in organic photovoltaic devices," *Phys. Chem. Chem. Phys.*, vol. 13, no. 10, p. 4381, 2011.

[27] H. Zhou and J. W. Park, "Effect of the crystallinity of indium tin oxide on the charge transfer at the interfaces and the performances of flexible organic light emitting diodes," *Phys. Status Solidi Appl. Mater. Sci.*, vol. 212, no. 2, pp. 414–424, 2015.

[28] M. Huang, Z. Hameiri, A. G. Aberle, and T. Mueller, "Influence of discharge power and annealing temperature on the properties of indium tin oxide thin films prepared by pulsed-DC magnetron sputtering," *Vacuum*, vol. 121, pp. 187–193, 2015.

[29] J. C. C. Fan and J. B. Goodenough, "X-ray photoemission spectroscopy studies of Sn-doped indium-oxide films," *J. Appl. Phys.*, vol. 48, no. 8, pp. 3524–3531, 1977.

[30] T. Ishida, H. Kobayashi, and Y. Nakato, "Structures and properties of electron-beam-evaporated indium tin oxide films as studied by x-ray photoelectron

spectroscopy and work-function measurements," *J. Appl. Phys.*, vol. 73, no. 9, pp. 4344–4350, 1993.

[31] M. T. Bhatti, A. M. Rana, and A. F. Khan, "Characterization of rf-sputtered indium tin oxide thin films," *Mater. Chem. Phys.*, vol. 84, no. 1, pp. 126–130, Mar. 2004.

[32] M. Thirumoorthi and J. T. J. Prakash, "Structure, optical and electrical properties of indium tin oxide ultra thin films prepared by jet nebulizer spray pyrolysis technique," *Superlattices Microstruct.*, vol. 4, pp. 124–132, 2016.

[33] M. Huang, Z. Hameiri, A. G. Aberle, and T. Mueller, "Comparative study of amorphous indium tin oxide prepared by pulsed-DC and unbalanced RF magnetron sputtering at low power and low temperature conditions for heterojunction silicon wafer solar cell applications," *Vacuum*, vol. 119, pp. 68–76, 2015.

[34] D. B. Fraser and H. D. Cook, "Highly Conductive, Transparent Films of Sputtered In[sub 2−x]Sn[sub x]O[sub 3−y]," *J. Electrochem. Soc.*, vol. 119, no. 10, p. 1368, 1972.

[35] J. C. C. Fan and J. B. Goodenough, "X-ray photoemission spectroscopy studies of Sn-doped indium-oxide films," *J. Appl. Phys.*, vol. 48, no. 8, pp. 3524–3531, 1977.

[36] W.-F. W. and B.-S. Chiou, "Effect of oxygen concentration in the sputtering ambient on the microstructure, electrical and optical properties of radio-frequency magnetron-sputtered indium tin oxide films," *Semicond. Sci. Technol.*, vol. 11, no. 2, p. 196, 1996.

[37] M. J. Chuang, H. F. Huang, C. H. Wen, and A. K. Chu, "On the structure and surface chemical composition of indium–tin oxide films prepared by long-throw magnetron sputtering," *Thin Solid Films*, vol. 518, no. 8, pp. 2290–2294, 2010.

[38] M. Chuang, "ITO Films Prepared by Long-throw Magnetron Sputtering without Oxygen Partial Pressure," *J. Mater. Sci. Technol.*, vol. 26, no. 7, pp. 577–583, 2010.

[39] K. Sugiyama, H. Ishii, Y. O. Seki, K. Sugiyama, H. Ishii, and Y. Ouchi, "Dependence of indium – tin – oxide work function on surface cleaning method as studied by ultraviolet and x-ray photoemission spectroscopies," vol. 87, no. 1, pp. 295–298, 2000.

[40] A. Sharma, S. E. Watkins, D. A. Lewis, and G. Andersson, "Effect of indium

and tin contamination on the efficiency and electronic properties of organic bulk hetero-junction solar cells,” *Sol. Energy Mater. Sol. Cells*, vol. 95, pp. 3251–3255, 2011.

[41] K. Sugiyama, H. Ishii, Y. Ouchi, and K. Seki, “Dependence of indium--tin--oxide work function on surface cleaning method as studied by ultraviolet and x-ray photoemission spectroscopies,” *J. Appl. Phys.*, vol. 87, no. 2000, p. 295, 2000.

[42] K. Sugiyama, H. Ishii, Y. Ouchi, and K. Seki, “Dependence of indium--tin--oxide work function on surface cleaning method as studied by ultraviolet and x-ray photoemission spectroscopies,” *J. Appl. Phys.*, vol. 87, no. 2000, p. 295, 2000.

[43] a. Godoy, L. Cattin, L. Toumi, F. R. Díaz, M. a. del Valle, G. M. Soto, B. Kouskoussa, M. Morsli, K. Benchouk, and a. Khelil, “Effects of the buffer layer inserted between the transparent conductive oxide anode and the organic electron donor,” *Sol. Energy Mater. Sol. Cells*, vol. 94, no. 4, pp. 648–654, Apr. 2010.

[44] X. Liu, X. Li, Y. Li, C. Song, L. Zhu, W. Zhang, H. Q. Wang, and J. Fang, “High-Performance Polymer Solar Cells with PCE of 10.42% via Al-Doped ZnO Cathode Interlayer,” *Adv. Mater.*, pp. 7405–7412, 2016.

[45] M. Thambidurai, J. Y. Kim, J. Song, Y. Ko, H. Song, C. Kang, N. Muthukumarasamy, D. Velauthapillai, and C. Lee, “High performance inverted organic solar cells with solution processed Ga-doped ZnO as an interfacial electron transport layer,” *J. Mater. Chem. C*, vol. 1, no. 48, p. 8161, Nov. 2013.

[46] N. Blouin, A. Michaud, D. Gendron, S. Wakim, E. Blair, R. Neagu-plesu, M. Bellete, G. Durocher, Y. Tao, and M. Leclerc, “Toward a Rational Design of Poly (2,7-Carbazole) Derivatives for Solar Cells,” *J. Am. Chem. Soc.*, no. 130, pp. 732–742, 2008.

[47] N. Banerji, S. Cowan, M. Leclerc, E. Vauthey, and A. J. Heeger, “Exciton formation, relaxation, and decay in PCDTBT.,” *J. Am. Chem. Soc.*, vol. 132, no. 49, pp. 17459–70, Dec. 2010.

[48] N. Blouin, a. Michaud, and M. Leclerc, “A Low-Bandgap Poly(2,7-Carbazole) Derivative for Use in High-Performance Solar Cells,” *Adv. Mater.*, vol. 19, no. 17, pp. 2295–2300, Sep. 2007.

[49] G. Namkoong, J. Kong, M. Samson, I.-W. Hwang, and K. Lee, “Active layer thickness effect on the recombination process of PCDTBT:PC71BM organic solar cells,” *Org. Electron.*, vol. 14, no. 1, pp. 74–79, Jan. 2013.

[50] O. S. Cells, “Analytical Model for Voltage-Dependent Photo and Dark Currents in Bulk Heterojunction,” 2016.

[51] F. Etzold, I. a Howard, R. Mauer, M. Meister, T.-D. Kim, K.-S. Lee, N. S. Baek, and F. Laquai, “Ultrafast exciton dissociation followed by nongeminate charge recombination in PCDTBT:PCBM photovoltaic blends.,” *J. Am. Chem. Soc.*, vol. 133, no. 24, pp. 9469–79, Jun. 2011.

[52] G. Namkoong, J. Kong, M. Samson, I.-W. Hwang, and K. Lee, “Active layer thickness effect on the recombination process of PCDTBT:PC71BM organic solar cells,” *Org. Electron.*, vol. 14, no. 1, pp. 74–79, Jan. 2013.

[53] S. Beaupré and M. Leclerc, “PCDTBT: en route for low cost plastic solar cells,” *J. Mater. Chem. A*, vol. 1, no. 37, p. 11097, 2013.

[54] D. C. Watters, J. Kingsley, H. Yi, T. Wang, A. Iraqi, and D. Lidzey, “Optimising the efficiency of carbazole co-polymer solar-cells by control over the metal cathode electrode,” *Org. Electron.*, vol. 13, no. 8, pp. 1401–1408, Aug. 2012.

[55] F. Padinger, R. S. Rittberger, N. S. Sariciftci, F. Padinger, R. S. Rittberger, R. S. Rittberger, N. S. Sariciftci, and N. S. Sariciftci, “Effects of postproduction treatment om plastic solar cells,” *Adv. Funct. Mater.*, vol. 13, no. 1, p. 85, 2003.

[56] W. Ma, C. Yang, X. Gong, K. Lee, and A. J. Heeger, “Thermally stable, efficient polymer solar cells with nanoscale control of the interpenetrating network morphology,” *Adv. Funct. Mater.*, vol. 15, no. 10, pp. 1617–1622, 2005.

[57] J. S. Moon, J. K. Lee, S. Cho, J. Byun, and A. J. Heeger, “‘Columnlike’ structure of the cross-sectional morphology of bulk heterojunction materials,” *Nano Lett.*, vol. 9, no. 1, pp. 230–234, 2009.

[58] B. A. Collins, E. Gann, L. Guignard, X. He, C. R. McNeill, and H. Ade, “Molecular miscibility of polymer-fullerene blends,” *J. Phys. Chem. Lett.*, vol. 1, no. 21, pp. 3160–3166, 2010.

[59] A. J. Parnell, A. D. F. Dunbar, A. J. Pearson, P. A. Staniec, A. J. C. Dennison, H. Hamamatsu, M. W. A. Skoda, D. C. Lidzey, and R. A. L. Jones, “Depletion of PCBM at the cathode interface in P3HT/ PCBM thin films as quantified via neutron reflectivity measurements,” *Adv. Mater.*, vol. 22, no. 22, pp. 2444–2447, 2010.

[60] Z. M. Beiley, E. T. Hoke, R. Noriega, J. Dacuña, G. F. Burkhard, J. A. Bartelt,

A. Salleo, M. F. Toney, and M. D. McGehee, “Morphology-dependent trap formation in high performance polymer bulk heterojunction solar cells,” *Adv. Energy Mater.*, vol. 1, no. 5, pp. 954–962, 2011.

[61] R. Noriega, J. Rivnay, K. Vandewal, F. P. V Koch, N. Stingelin, P. Smith, M. F. Toney, and A. Salleo, “A general relationship between disorder, aggregation and charge transport in conjugated polymers,” *Nat. Mater.*, vol. 12, no. 11, pp. 1038–1044, 2013.

[62] H. Bassler, “Localized states and electronic transport in single component organic solids with diagonal disorder,” *Phys. Status Solidi*, vol. 107, no. 1, pp. 9–54, 1981.

[63] & A. J. H. Sung Heum Park, Anshuman Roy, Serge Beaupré, Shinuk Cho, Nelson Coates, Ji Sun Moon, Daniel Moses, Mario Leclerc, Kwanghee Lee, “Bulk heterojunction solar cells with internal quantum efficiency approaching 100%,” *Nat. Photonics*, vol. 3, pp. 297–302, 2009.

[64] P. a. Staniec, A. J. Parnell, A. D. F. Dunbar, H. Yi, A. J. Pearson, T. Wang, P. E. Hopkinson, C. Kinane, R. M. Dalgliesh, A. M. Donald, A. J. Ryan, A. Iraqi, R. a. L. Jones, and D. G. Lidzey, “The Nanoscale Morphology of a PCDTBT:PCBM Photovoltaic Blend,” *Adv. Energy Mater.*, vol. 1, no. 4, pp. 499–504, Jul. 2011.

[65] P. a. Staniec, A. J. Parnell, A. D. F. Dunbar, H. Yi, A. J. Pearson, T. Wang, P. E. Hopkinson, C. Kinane, R. M. Dalgliesh, A. M. Donald, A. J. Ryan, A. Iraqi, R. a. L. Jones, and D. G. Lidzey, “The Nanoscale Morphology of a PCDTBT:PCBM Photovoltaic Blend,” *Adv. Energy Mater.*, vol. 1, no. 4, pp. 499–504, Jul. 2011.

[66] K. D. G. I. Jayawardena, S. Li, L. F. Sam, C. T. G. Smith, M. J. Beliatis, K. K. Gandhi, M. R. R. Prabhath, T. R. Pozegic, S. Chen, X. Xu, G. D. M. R. Dabera, L. J. Rozanski, R. A. Sporea, C. A. Mills, X. Guo, and S. R. P. Silva, “High efficiency air stable organic photovoltaics with an aqueous inorganic contact,” *Nanoscale*, vol. 7, p. 14241, 2015.

[67] M. Girtan and M. Rusu, “Role of ITO and PEDOT:PSS in stability/degradation of polymer:fullerene bulk heterojunctions solar cells,” *Sol. Energy Mater. Sol. Cells*, vol. 94, no. 3, pp. 446–450, Mar. 2010.

[68] Y. Sun, C. J. Takacs, S. R. Cowan, J. H. Seo, X. Gong, A. Roy, and A. J. Heeger, “Efficient, air-stable bulk heterojunction polymer solar cells using MoO(x) as the anode interfacial layer.,” *Adv. Mater.*, vol. 23, no. 19, pp. 2226–30, May 2011.

[69] S. Chen, J. R. Manders, S.-W. Tsang, and F. So, “Metal oxides for interface engineering in polymer solar cells,” *Journal of Materials Chemistry*. p. 24202, 2012.

[70] S. Chambon, L. Derue, M. Lahaye, B. Pavageau, L. Hirsch, and G. Wantz, “MoO3 thickness, thermal annealing and solvent annealing effects on inverted and direct polymer photovoltaic solar cells,” *Materials (Basel).*, vol. 5, no. 12, pp. 2521–2536, 2012.

[71] V. Shrotriya, G. Li, Y. Yao, C.-W. Chu, and Y. Yang, “Transition metal oxides as the buffer layer for polymer photovoltaic cells,” *Appl. Phys. Lett.*, vol. 88, no. 7, p. 73508, 2006.

[72] D. C. Watters, J. Kingsley, H. Yi, T. Wang, A. Iraqi, and D. Lidzey, “Optimising the efficiency of carbazole co-polymer solar-cells by control over the metal cathode electrode,” *Org. Electron.*, vol. 13, no. 8, pp. 1401–1408, Aug. 2012.

[73] A. Roy, S. H. Park, S. Cowan, M. H. Tong, S. Cho, K. Lee, and A. J. Heeger, “Titanium suboxide as an optical spacer in polymer solar cells,” *Appl. Phys. Lett.*, vol. 95, no. 1, pp. 1–4, 2009.

[74] A. R. B. Jonathan Griffin, Andrew J. Pearson, Nicholas W. Scarratt, Tao Wang, David G. Lidzey, “Organic photovoltaic devices incorporating a molybdenum oxide hole-extraction layer deposited by spray-coating from an ammonium molybdate tetrahydrate precursor,” *Org. Electron.*, vol. 15, pp. 692–700, 2014.

[75] C. Tao, S. Ruan, X. Zhang, G. Xie, L. Shen, X. Kong, W. Dong, C. Liu, and W. Chen, “Performance improvement of inverted polymer solar cells with different top electrodes by introducing a MoO3 buffer layer,” *Appl. Phys. Lett.*, vol. 93, no. 19, pp. 2006–2009, 2008.

Chapter 7

Open Circuit Voltage in Polycarbazole: Fullerene Inverted Devices

Abstract. An analysis was conducted of open circuit voltage (V_{oc}) in polycarbazole: fullerene (PCDTBT: PCBM) inverted devices with reference to experimental variations in cathode materials and work function. The work function of ITO electrodes was tuned by thermal annealing up to 400 ^{o}C. The best device performance was found to be for those fabricated at room temperature; with an ITO work function of 4.2 eV, V_{oc} of 0.89 eV, J_{sc} of 8.06 mA.cm^{-2}, FF of 64.70 % and PCE of 4.62 %. By combining the experimental results from this study with devices incorporating additional electron transport layers (ETL) reported previously by other researchers, two regimes of cathode work function dependency were extracted: a linear V_{oc} regime for work functions exceeding the LUMO level of PCBM, and a constant V_{oc} regime for work functions lower than the LUMO level.

7.1 Introduction

Most of the polymer: fullerene solar cells with efficiencies exceeding the theoretical limit of 10% that have been reported up to now have been fabricated using an inverted structure [1]–[4]. As discussed earlier in **Chapter 2**, **Section 2.6**, using ITO as a bottom cathode electrode within the inverted structure can be beneficial as well as detrimental to cell performance. Despite the benefits of the longer lifetime and better air stability and durability seen for these devices, multi-step chemical treatments are required to prepare the ITO surface for the deposition of the organic photoactive layer. These treatments (i.e. the use of buffer layers) are aimed to minimize the energetic mismatch by lowering the height barrier for charge transport across the interface and enhancing the coverage of the organic layer. The buffer layer inserted between the ITO layer and the organic layer also needs excessive chemical processing to realize highly efficient inverted cells. For example, 10.31 % and 10.42 % cells are achieved by the doping of zinc oxide (ZnO) buffer layers [2], [4]. The dual doping with indium and fullerene derivative resulted in a PCE of 10.31% whereas doping with aluminium resulted in a further slight increase in PCE to 10.42%. In both cases, the high efficiencies achieved were due to the enhancements in both surface conductivity and electron mobility of the ZnO layer.

An alternative approach to realize highly efficient inverted devices is to replace the thin BHJ layer (<100 nm) with a thicker layer (up to 300 nm) of highly crystallized polymer blended with fullerene [5]. Although the ZnO layer was not doped with any element, the reported device broke the efficiency limit as a result of the charge recombination being reduced. The polymer crystallinity helped to enhance the vertical segregation across the device, where favourable crystallite was distributed edge-on at the organic/ZnO interface and face-on at the organic/anode interface, hence improving charge transport.

The major improvements in efficiencies for devices fabricated by these approaches mainly result from the significant enhancements in the short circuit current. The open circuit voltage of these devices, however, were either constant [2] or slightly reduced [5]. As the efficiency is a product of both short circuit current (Jsc) and open circuit voltage (Voc), a model study is needed to understand the correlation between the electronic structure of ITO and Voc, which is of importance regarding device engineering and contact design. For this purpose, inverted BHJ devices based on a poly (N-9’-heptadecanyl-2-7-carbazole-alt-5,5-(4’,7’-di-2-thienyl-2’-1’-3’-benzothiadiazole) (PCDTBT) and [6,6]-phenyl-C71 butyric acid methyl ester (PC70BM) blend were fabricated on blank ITO electrodes. The device structure is ITO/PCDTBT: PCBM (90 nm)/MoO_x (20 nm)/Al (100 nm) with the ITO surface tuned by thermal annealing. This chapter reports on the device performance and surface characteristics, and compares the result with the existing literature. Some of these results have already been published in Ref [6].

7.2 Thermal Annealing Dependence

7.2.1 J-V Characteristics Under illumination

Device structure and J-V characteristics under illumination are shown as a function of ITO annealing temperature in **Figure 7.1**. The increase in annealing temperature has no direct effect on the shape of the JV curves obtained. This is evident by the balanced changes in both series resistance ($\mathrm{R_s}$) and shunt resistance ($\mathrm{R_{sh}}$). For example, un-annealed devices show $\mathrm{R_s} = 28\ \Omega.\mathrm{cm}^2$ and $\mathrm{R_{sh}} = 737\ \Omega.\mathrm{cm}^2$. For ‘100 °C’ devices , $\mathrm{R_s}$ and $\mathrm{R_{sh}}$ are both reduced to $16\ \Omega.\mathrm{cm}^2$ and $672\ \Omega.\mathrm{cm}^2$, respectively. Further annealing at 200 °C results in reduced $\mathrm{R_s}$ to $15\ \Omega.\mathrm{cm}^2$, while the $\mathrm{R_{sh}}$ is slightly increased up to $698\ \Omega.\mathrm{cm}^2$ compared to those fabricated at 100 °C. The exponential current response that is typically expected when increasing the voltage applied to a diode was observed despite the absence of the cathode buffer layer, and is reported here for the first time [6]. Indeed, the JV characteristic of ITO-only devices reported in literature has been very poor, with an S-shaped deformation evident [7]–[10]. The S-shaped deformation describes an unusual current response where the current increases sharply after being locally saturated around certain values of the applied voltage. This typically happens for multilayer organic solar cells when one or more layer is not optimized. For example, the existence of an energy barrier with a critical height at the organic-electrode interface can cause misalignment of the Fermi level of the organic layer with the charge quasi Fermi level under illumination [11]. The consequence is charge accumulation at the electrode interface, leading to a reduction in surface recombination velocity, and hence a deformed JV curve [12]. Other possible sources for this S-shaped deformation include the degradation of the organic layer at electrode interfaces [13] and the formation of interfacial dipoles [14]. The disappearance of these deformations, as seen in **Figure 7.1(b)**, therefore confirms the excellent diode characteristics of the fabricated devices, as well as the sensitivity of the ITO electrodes to the pre-treatment conditioning. Shifts to lower open circuit voltages with high temperatures are incorporated with slight changes around the short circuit currents, however. This indicates the negative effect of thermal annealing on the device parameters.

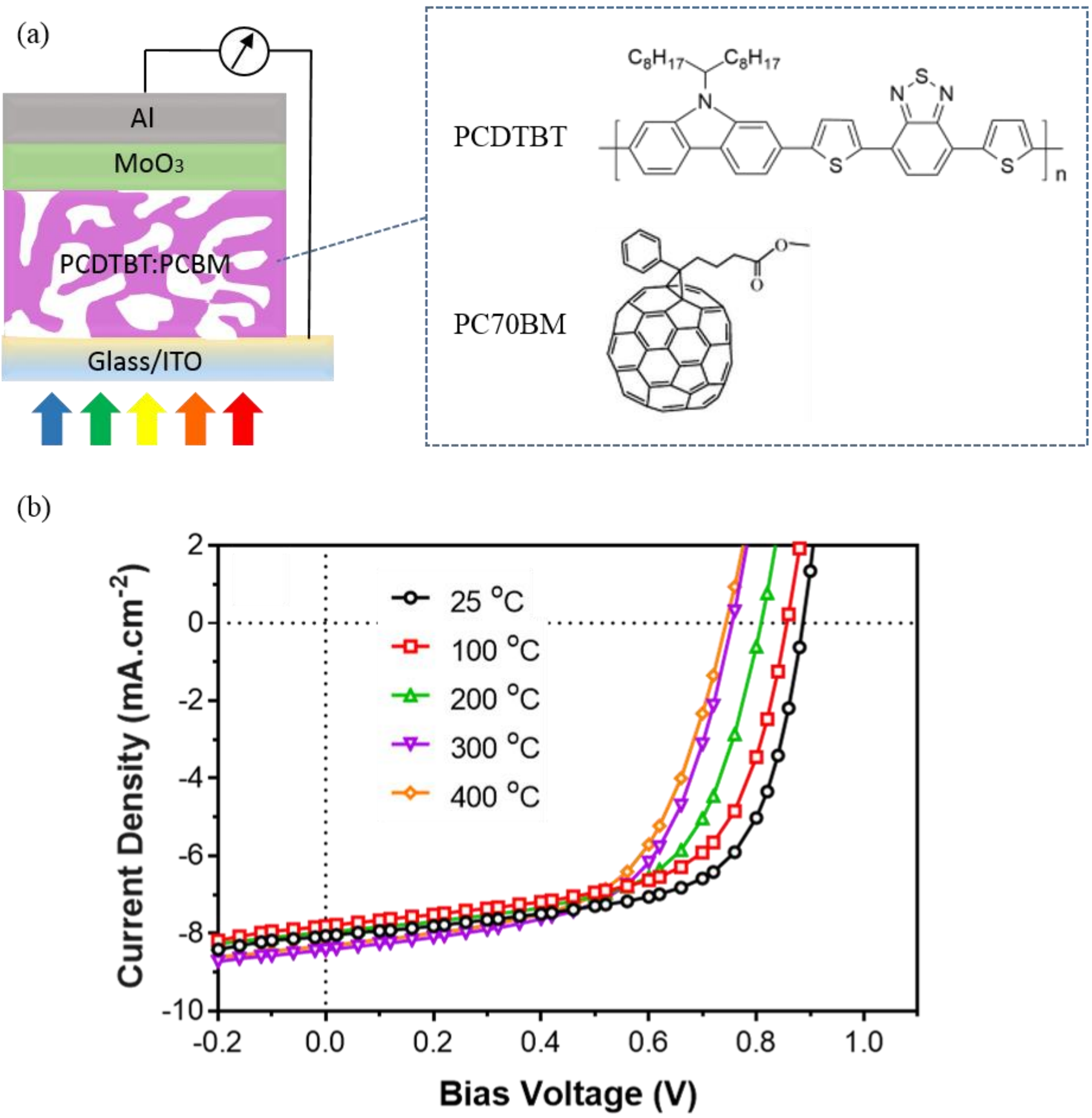

Figure 7.1 (a) Configuration of inverted BHJ devices based on a PCDTBT: PCBM blend, and their chemical structures. (b) JV characteristics of fabricated devices showing the effect of ITO annealing temperature.

7.2.2 Device Parameters

Figure 7.2 shows the changes in device parameters, including open-circuit voltage (Voc), short-circuit current (Jsc), fill factor (FF), and power conversion efficiency

(PCE), with ITO temperature. Reference devices were fabricated at room temperature with non-annealed ITO electrodes, and the so-called $25\ ℃$ sample. Gradual reductions in the values of all parameters, except for Jsc, were observed as the temperature was increased. **Table 7.1** summarizes the average and best performance for both our fabricated devices and the devices reported in the literature. The Jsc was reduced by $\sim 4.00\ \%$ when the temperature increased to $200\ ℃$, while it improved by $\sim 5.00\ \%$ and $2.50\ \%$ at $300\ ℃$ and $400\ ℃$, respectively. The variation in the short circuit current with temperature can be correlated to the series resistance ($\mathrm{R_s}$), as will be discussed later in **Section 7.3.3**. Despite the slight enhancement in the short circuit current at high temperatures, the device efficiency was not improved due to the notable reduction in the fill factor; an FF of $58.5\ \%$ and PCE of $3.65\ \%$ were found at $300\ ℃$. Defining the reasons for the reduced FF is crucial due to the absence of the S-shaped deformation. The charge carrier transport across the device layers is known to regulate the fill factor, given by $FF = P_{out}/V_{oc}J_{sc}$, where P_{out} is the maximum power the solar cell can deliver to an external load. Reductions of $19.10\ \%$, $9.42\ \%$, and $21.46\ \%$ were seen, respectively, for Voc, FF and PCE compared to their initial values at $25\ ℃$. It can be concluded that the best device performance was achieved at $25\ ℃$ with $0.89\ \mathrm{eV}$ ($\mathrm{V_{oc}}$), $8.04\ \mathrm{mA.cm^{-2}}$ ($\mathrm{J_{sc}}$), $63.68\ \%$ (FF), and $4.52\ \%$ (PCE).

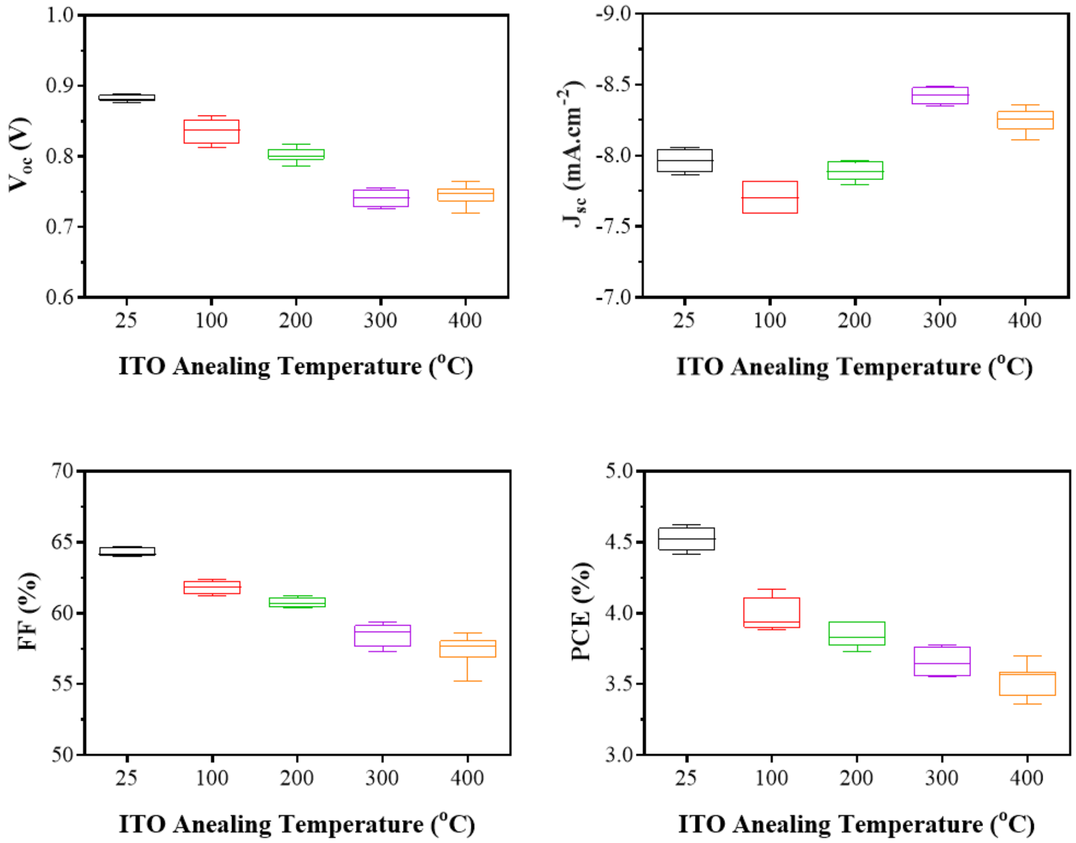

Figure 7.2 Comparison of performance for inverted PCDTBT: PCBM devices fabricated on blank ITO electrodes with various annealing temperatures. Performance parameters are (a) open circuit voltage, Voc, (b) short circuit current, Jsc, (c) fill factor, FF, and (d) power conversion efficiency, PCE.

Table 7.1 Summary of average parameters for inverted solar cells based on PCDTBT: PCBM bulk heterojunction fabricated on blank ITO annealed at various temperatures; open circuit voltage (Voc), short circuit current (Jsc), fill factor (FF), power conversion efficiency (PCE), series resistance (R_S), and shunt resistance (R_{SH}). (a) The maximum deviation error of ten devices with four working pixels for every annealing temperature. (b) Reference devices fabricated in our lab. (c) Devices with a structure of ITO/MoO_3-Al/PCDTBT:PCBM/MoO_3/Al reported in Ref [15]. (d) Devices with a structure of ITO/PFN/PCDTBT: PCBM/MoO_3/Ag reported in Ref [16]. (e) Devices with a structure of ITO/PCP-EP/PCDTBT: PCDBM/MoO_3/Al reported in Ref [10].

ITO Treatment	**V_{OC} (V) (±0.05)[a)]**		**J_{SC} (mA.cm^{-2})**	**FF (%)**	**PCE (%)**	**R_S (Ω.cm^2)**	**R_{SH} (Ω.cm^2)**
	Average	Max					
[b)]25° C	0.85	0.89	8.04	63.7	4.52	28.0	737
100° C	0.81	0.86	7.73	61.7	3.99	16.0	672
200° C	0.80	0.83	7.89	60.8	3.84	15.0	698
300° C	0.71	0.76	8.43	58.5	3.65	12.0	568
400° C	0.70	0.72	8.24	57.7	3.55	14.0	576
[c)]MoO_3-Al	----	0.89	10.70	66.0	6.28	----	----
[d)]PFN	----	0.91	11.71	57.0	5.94	2.7	474
[e)]PCP-EP	----	0.88	08.76	56.9	5.48	6.7	597

7.2.3 Contribution of ITO Sheet Resistance

To understand the variation in the short circuit current of the fabricated devices in respect to the annealing temperatures, a correlation to the series resistance is established, as shown in **Figure 7.3**. The series resistance here is equivalent to the sum of the ITO sheet resistance and internal resistances at both electrode interfaces. The experimental data showed no changes in ITO sheet resistance with low annealing temperatures (< 300 ℃). At high temperatures (≥ 300 ℃), a $20\,\%$ increase in the initial resistance was obtained. This result is in agreement with the work of Bhatti et al. [17], who measured the sheet resistance of annealed ITO thin film using a four-point probe. They attributed the increased sheet resistance at high temperatures to the filling up of oxygen vacancies with ambient atmosphere molecules. XPS data from our devices also shows evidence of such introduced defects, as will be seen in **Section 8.3.4**. Overall, however, the device series resistance was found to reduce Jsc dramatically at $100\ ^\circ\mathrm{C}\ (16\ \Omega.\mathrm{cm}^2)$, $200\ ^\circ\mathrm{C}\ (15\ \Omega.\mathrm{cm}^2)$, $300\ ^\circ\mathrm{C}\ (12\ \Omega.\mathrm{cm}^2)$ before rising slightly to $14\ \Omega.\mathrm{cm}^2$ at $400\ ^\circ\mathrm{C}$. We can conclude that the device parameters are not significantly affected by the sheet resistance of the ITO electrode.

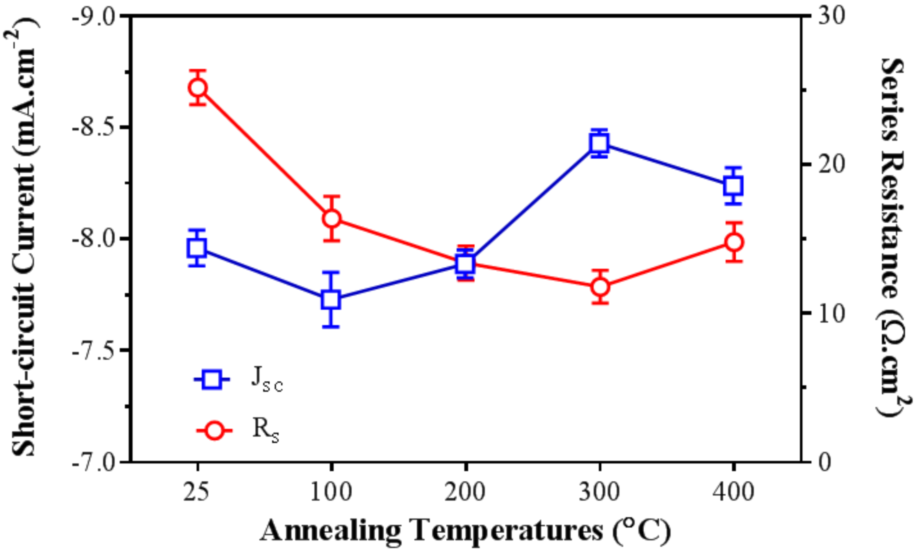

Figure 7.3 Dependence of the short circuit current (Jsc, squares) on the series resistance (Rs, circles) of inverted PCDTBT: PCBM devices fabricated on annealed-blank ITO electrodes. The data shows average values with error bars and linked lines.

7.2.4 *ITO Work Function*

The changes in ITO work function with varying annealing temperatures were investigated to elucidate the reduction in the open circuit voltage. **Figure 7.4 (a)** shows the UPS spectra for blank ITO substrates annealed at different temperatures. The cut off at the low energy region of the spectrum is directly related to the sample's work function, as shown previously in **Chapter 5**. In comparison with the non-annealed substrate, referenced as '$25\ ℃$', the work function is systematically elevated as the annealing temperature increases, see **Figure 7.5**. With a WF of 4.20 ± 0.03 eV at $25\ ℃$, work functions of 4.28 ± 0.03 eV, 4.35 ± 0.03 eV, 4.47 ± 0.04 eV and 4.44 ± 0.05 eV were observed at $100\ ℃$, $200\ ℃$, $300\ ℃$, and $400\ ℃$, respectively. The slight reduction in the WF at $400\ ℃$ compared to the one obtained at $300\ ℃$ suggests the induction of discrete sources of chemical reaction on the ITO surface, as will be seen in **Section 7.3.4**.

Since the ITO substrate serves as a cathode in the fabricated devices, the electronic structure of the ITO/PCBM interface has also been investigated. Thin layers of PCBM with average thicknesses of 20 ± 2.5 nm (errors showing the standard deviations of five different area per sample and a total of two samples per annealing temperature) were spun onto cleaned ITO substrates that were pre-annealed at different temperatures. The photoelectron spectra of ITO/PCBM, showing the low kinetic energy region as a function of annealing temperature are shown in **Figure 7.4 (b)**. At $25\ ℃$, the work function of the ITO/PCBM sample was reduced to 4.19 eV, compared to the non-annealed blank ITO. When the temperature was raised, however, the work function of the non-annealed sample was further reduced by $0.03-0.06$ eV at 100 ℃ (4.13 eV) and 200℃ (4.16 eV), until it returned to its initial value at 300 ℃ (4.19 eV). At higher a temperature (400 ℃), a further increase of 0.03 eV was observed compared to the initial value. The reduction in the ITO/PCBM work function compared to the blank ITO at different temperatures implies the pinning of the Fermi level across interfaces. The Fermi level of ITO pins to the LUMO level of PCBM once the PCBM layer is deposited onto the ITO surface. The exchange of charges needed at the interface to reach equilibrium at room temperature results in the vacuum level shifting downwards, and hence a reduction in the work function of ITO/PCBM films. The downward shift represents the difference between the ITO work function with and without a PCBM layer, and so-called 'interfacial potential energy', based on the assumption of the exchanged charges forming a dipole layer at the interface.

Considering the low-binding energy region seen in **Figure 7.4 (c)**, the position of the HOMO level of the ITO/PCBM sample was identified with respect to the Fermi level by calculating the valance band onset ($\mathrm{VB_{onset}}$). For the non-annealed substrate, the HOMO edge of the fullerene layer was positioned at 1.74 ± 0.02 eV near to the Fermi level. This position seems to be 0.12 eV shallower than the one reported in the literature [18]. Although the spin-coated fullerene similarly here was also PC70BM, this discrepancy can perhaps be attributed to the different fullerene batch used. Once the layer is deposited onto the annealed substrates, the HOMO edge was slightly elevated, with a new location of 1.72 ± 0.02 eV at 100 ˚C. Deposition onto a "higher anneal temperature" substrate does not affect the new position of the HOMO edge, however: it remains constant at 1.72 ± 0.02 for 200 ˚C, 300 ˚C and 400 ˚C, suggesting a negligible amount of charge transfer across the ITO/PCBM interface [19].

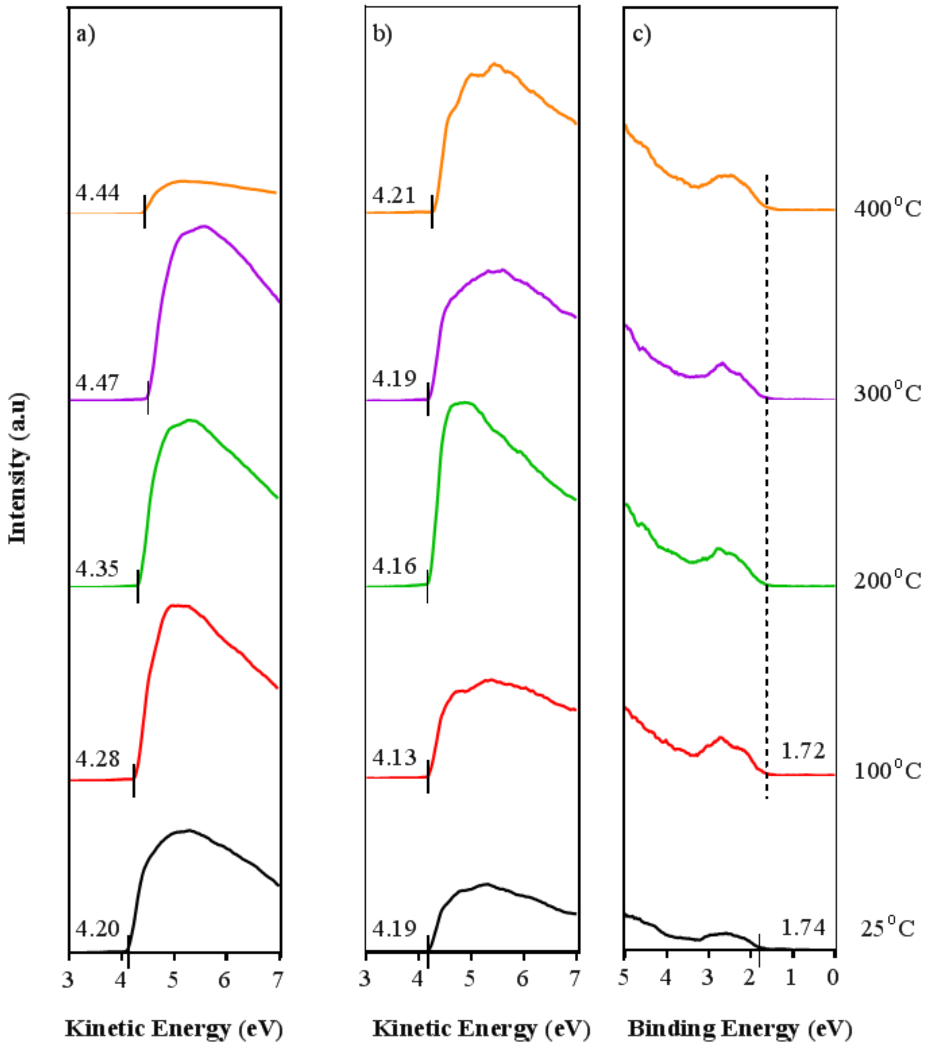

Figure 7.4 Ultraviolet photoelectron spectrum as a function of ITO temperature showing the kinetic energy of electrons emitted from (a) blank ITO and (b) ITO/PCBM substrates. (c) low binding energy region of ITO/PCBM substrates.

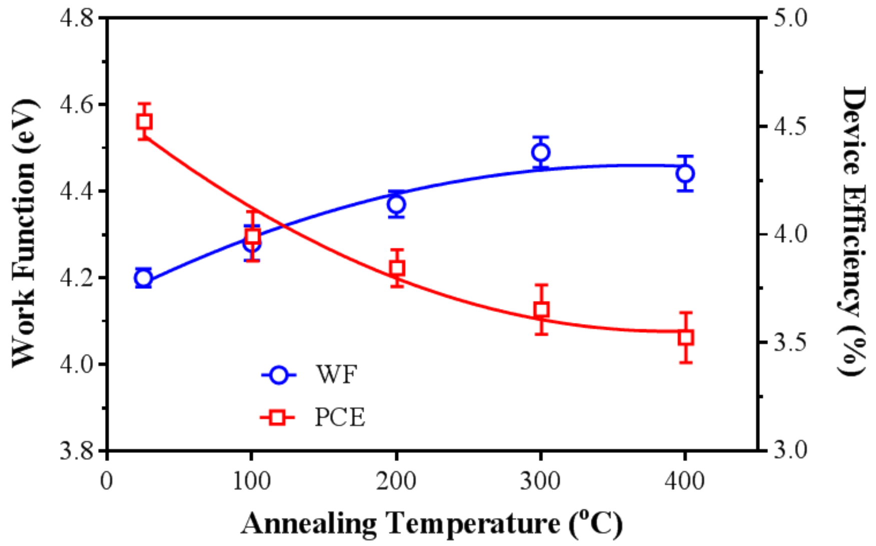

Figure 7.5 Relation between the blank ITO work function (WF, circle) and the device efficiency (PCE, square) according to the annealing temperature. The data shows average values with error bars and fitted curves.

In order to identify how well the Fermi level is pinned at the ITO/PCBM interface, the potential energy (Δ) of the interfacial dipoles that were formed was calculated. This was done by subtracting the ITO/PCBM work functions from those of the blank ITO at each temperature ($\Delta = \phi_{\mathrm{ITO/PCBM}} - \phi_{\mathrm{ITO}}$). The sign of this potential determines the direction of the vacuum level alignment at the interface, as discussed before in **Chapter 2, Section 5.4**. As seen in **Table 7.2,** the negative sign of Δ indicates Fermi level pinning to the LUMO energy level of fullerene. The value of this potential is generally increased in respect to temperature, with the highest value (Δ= 0.29 eV) obtained at 300 °C. **Figure 7.6** illustrates the correlation between the interfacial potential energy and open circuit voltage. It can see that the highest Voc obtained for devices fabricated at room temperature is due to better alignment of the Fermi level at the interface with the lowest potential (Δ= 0.01 eV) formed.

Table 7.2 Tabulated data extracted from the UPS measurement of ITO/PCBM substrates as a function of the ITO temperature, showing valence band offset (VB_{offset}), the cut-off of the high-binding energy region (E_{cutoff}), the ITO/PCBM work function (ϕ), the ionization potential (IP), and the potential energy of the interfacial dipoles (Δ).

Temperature **(°C)**	**VB_{onset}** **(eV)**	**E_{cutoff}** **(eV)**	**ϕ** **(eV)**	**IP** **(eV)**	**Δ** **(eV)**
25	1.74	17.02	4.19	5.93	- 0.01
100	1.72	17.08	4.13	5.85	- 0.15
200	1.72	17.05	4.16	5.88	- 0.17
300	1.72	17.02	4.19	5.91	- 0.29
400	1.72	16.99	4.21	5.93	- 0.23

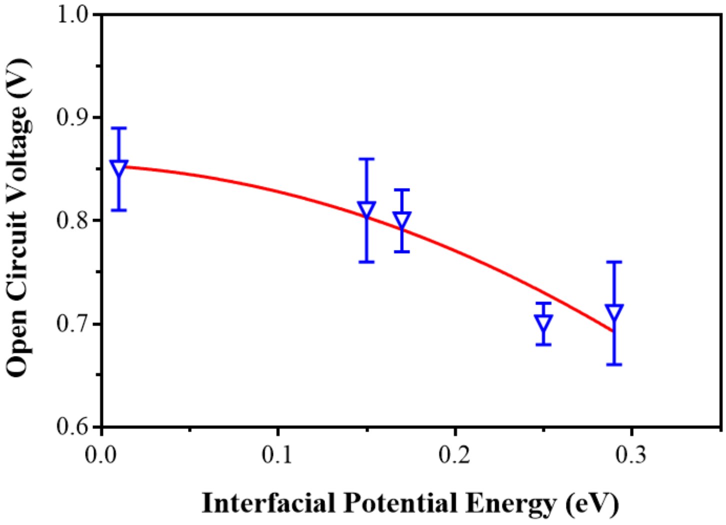

Figure 7.6 Dependence of the open circuit voltage on the potential energy at the ITO/PCBM interfaces. The potential energy per temperature is determined by the difference in the work functions of the ITO/PCBM and the blank ITO substrates.

7.2.5 ITO Surface Chemical Composition

The core level spectra of the elements located on the surface of blank ITO samples were measured using XPS. All peaks were calibrated to carbon binding energy (C 1s) at 285.0 eV in order to eliminate any charge-induced shifts. A Shirley background subtraction and a Gaussian-Laurentzian line-shape were used to calculate the background intensity and to deconvolute the area under high resolution peaks. For all samples, however, wide scans show various amounts of oxygen, indium, tin and carbon, with a trace of potassium.

The appearance of potassium peaks in all the samples reported here, including the non-annealed one is unexpected. This is because we followed the optimum cleaning process, as reported earlier in **Chapter 6**, before the samples were annealed, and the XPS of the IPA-cleaned sample (**Chapter 6**) showed no trace for potassium. The existence of potassium could be sourced from the glass itself. To investigate the origin of this contamination, therefore, a wide and high resolution (For C 1s) scan of the glass surface on the reverse of the clean and non-annealed ITO sample was conducted, and the results are presented in **Figure 7.7**. Note that the K 2p level core spectrum typically overlaps with the carbon high resolution spectrum and extends from 292 eV up to 297 eV. The fitted peaks will be discussed later. This wide scan spectrum shows the presence of 0.1 % of potassium.

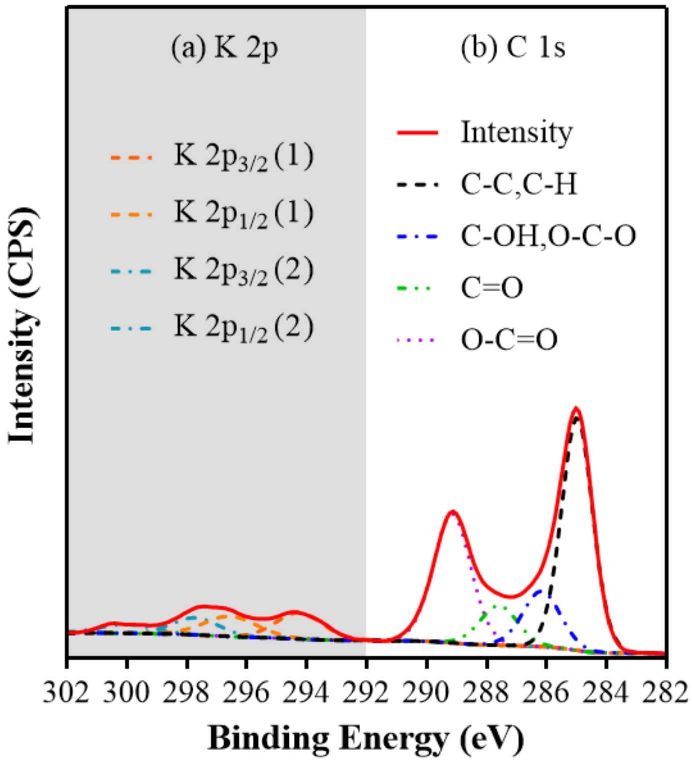

Figure 7.7 High resolution scan of C 1s core level on the reverse (glass) side of the cleaned, non-annealed, ITO substrate, showing the overlap K 2p core level with fitted peaks.

The effect of thermal annealing on the atomic concentrations of the detected elements is shown in **Figure 7.8**. The intensity of potassium peak can be seen to increase with as the annealing temperatures increase. Potassium concentrations of 0.30 %, 0.86 %, 1.05 %, 1.10 %, and 1.13 % were observed for the non-annealed sample (25 °C) at 100 °C, 200 °C, 300 °C and 400 °C, respectively. The increased potassium content is associated with reductions in both tin and oxygen content and a slight increase in indium. This suggests that the potassium is being diffused from the glass towards the ITO surface upon thermal annealing, which may explain the relatively high concentrations at high temperatures..

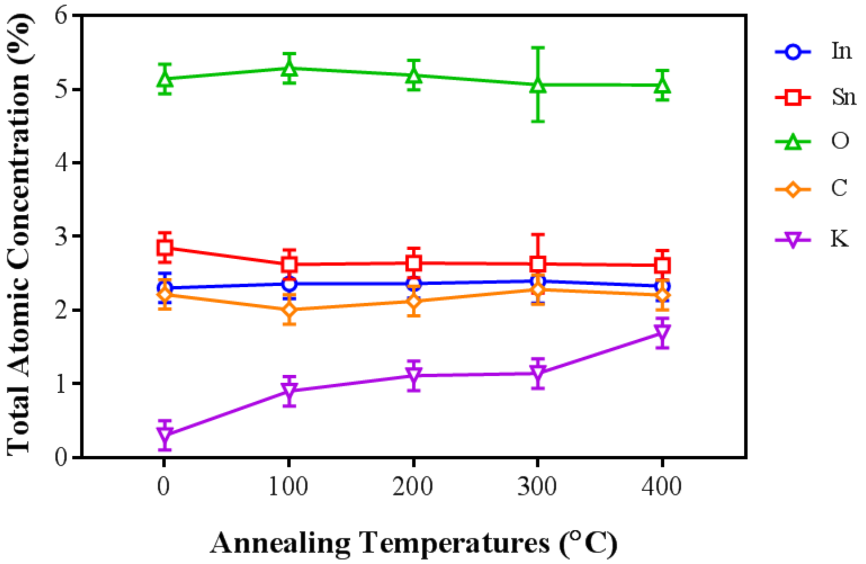

Figure 7.8 The effect of thermal annealing on the total atomic concentration for detected elements; In, Sn, O, C and K. Note that the concentration of C, In and O were divided by 10 to illustrate changes in K concentrations upon annealing. Vertical bars represent standard deviation errors of run-to-run measurements calculated for three samples per temperature, plotted vertically. Offset lines are fitted horizontally for clarity.

Figure 7.9 illustrates the deconvolution of (a) In $3d_{5/2}$ and (b) Sn $3d_{5/2}$, showing changes in peak shape and intensity upon annealing. The asymmetric shapes of both spectral lines indicate the existence of In and Sn in different chemical environments. The In $3d_{5/2}$ and Sn $3d_{5/2}$ peaks are typically shown to be insensitive to the changes in valance states [20], [21]. This can be attributed to ITO being an n-type semiconductor with conductivity originating from both the oxygen vacancies and the presence of tin dopants with a higher valance than indium. The In $3d_{5/2}$ and Sn $3d_{5/2}$ peaks reported here are best fitted by resolving into two adjacent peaks. The line shape of the In peak is often seen to be symmetrical [22], [23] but in some cases asymmetry associated with hydroxide is seen [24], [25]. The In peak at 444.21 ± 0.05 eV is therefore assigned to the In^{3+} bonding within the $\mathrm{In_2O_3}$ lattice, while the one at 445.18 ± 0.04 eV is assigned to indium hydroxide $\mathrm{In(OH)_3}$ (**Figure 7.9 (a)**). The $\mathrm{In(OH)_3}$ peak typically originates from the presence of intermediated oxidation states like In^{+} or In^{2+} [26]. The error values here consider the shifts in peak position upon annealing. It should be noted that the position of the In 3d peaks of the non-annealed sample are at slightly lower binding energies (with a difference of 0.1-0.3 eV) compared to what has been reported in literature. This sits within the error range due to the variation in the processing conditions, however [25]–[27]. For Sn $3\mathrm{d}_{5/2}$, meanwhile, the Sn peaks at 486.22 ± 0.12 eV and 487.15 ± 0.17 eV are assigned to the well-documented tin oxidation states Sn^{4+} and Sn^{2+}(**Figure 7.9 (b)**). The Sn^{4+} peak originates from the bonding in $\mathrm{SnO_2}$, while the Sn^{2+} arises from the bonding in SnO [20], [26], [28]. Since $\mathrm{SnO_2}$ is shown to be thermodynamically more stable than SnO, Sn^{4+} is considered to be electron donor centre within ITO films [29].

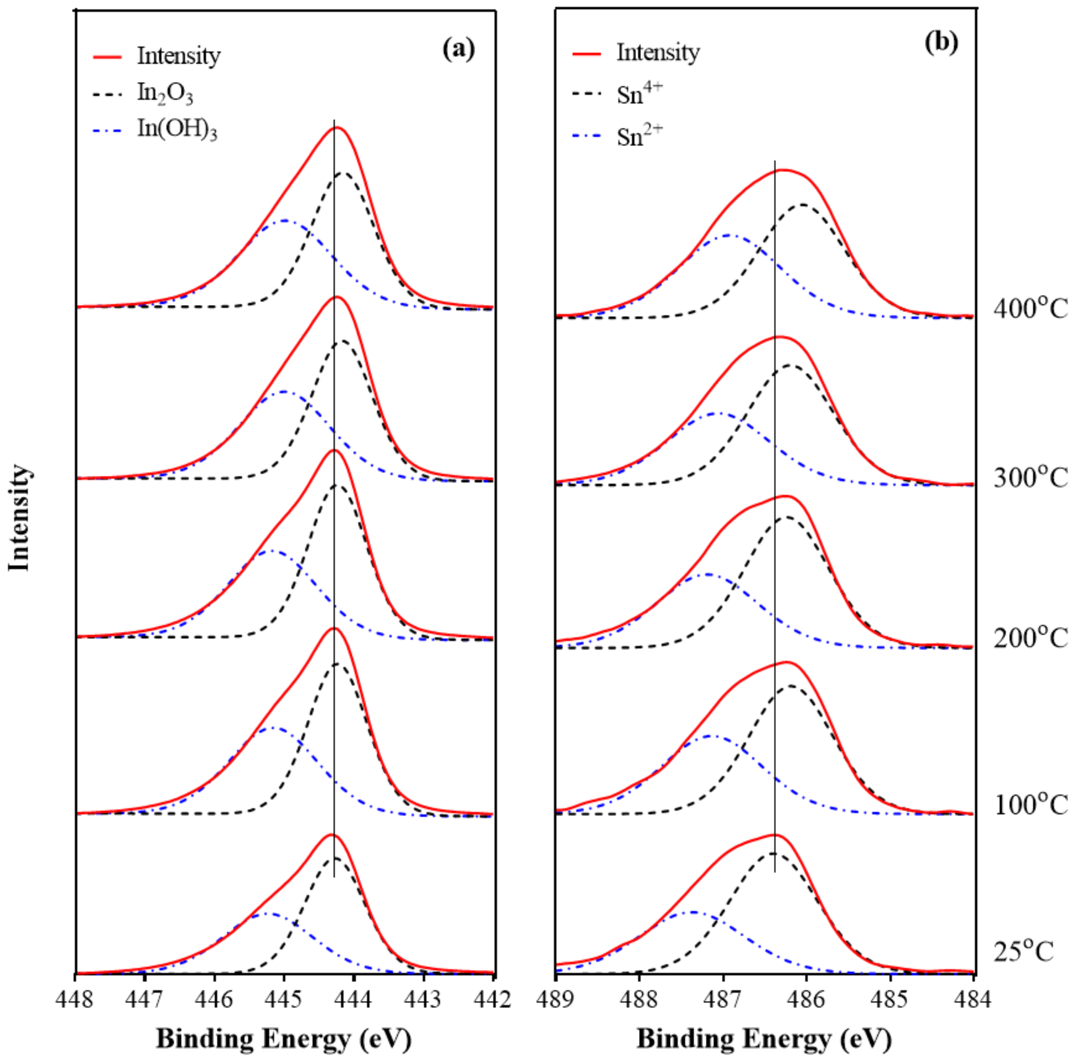

Figure 7.9 Core level spectra for blank ITO samples annealed at different temperatures showing deconvolution of (a) In 3d5/2 and (b) Sn 3d5/2 peaks.

Three distinguished peaks are resolved from the deconvolution of the O 1s core level spectra, as seen in **Figure 7.10 (c)**. These have binding energies of 529.74 ± 0.12 eV, 530.79 ± 0.11 eV and 532.15 ± 0.08 eV. The literature reports up to five peaks in XPS results for O 1s in ITO, indicating different oxidation states for oxygen, the exact locations of which could vary depending upon the deposition conditions and film properties [30] [31], [32]. Chuang et al. [31], [33] attributed their best fitted five peaks to lattice oxygen in the amorphous ITO region (at 529.98 eV), lattice oxygen in the crystalline ITO region (at 530.41 eV), oxygen deficiency in the $\mathrm{In_2O_3}$ matrix (at 531.42 eV), oxygen in $\mathrm{In(OH)_3}$ or InOOH species (at 532.56 eV), and oxygen binding to organic impurities (for 533.64 eV). Huang et al. [25], [30] reported only three individual peaks and assigned these to the oxygen lattice in $\mathrm{In_2O_3}$, with six $\mathrm{O^{2-}}$ fully surrounded by In atoms or Sn substitutional (at 529.9 eV), $\mathrm{O^{2-}}$ ions in the oxygen deficient $\mathrm{In_2O_{3-x}}$ matrix (at 531.4 eV), and chemisorbed oxygen like $\mathrm{O-OH}$ or $\mathrm{H_2O}$ (at 532.22 eV). The O peaks presented here, therefore, and located at 529.74 ± 0.12 eV, are assigned to the oxygen lattice in $\mathrm{In_2O_3}$, and referred to as ‘O-In’, while the one at 532.15 ± 0.08 eV is identified as chemisorbed hydroxide (O-OH). The observed peak at 530.79 ± 0.11 eV sits between the binding energies of the second peaks reported by both Chuang et al. [31], [33] and Huang et al. [25], [30]. We assign this peak to the $\mathrm{O^{2-}}$ ions in the oxygen deficient $\mathrm{In_2O_{3-x}}$ matrix.

The high resolution scan of the C 1s core level shows the presence of five chemically different carbon species, as shown in **Figure 7.10 (d) and (e)**. These are a superimposed peak of C-C and C-H at 285.0 eV, C-OH at 286.34 ± 0.06 eV, and C=O at 288.51 ± 0.08 eV. The fourth and fifth peaks at 293.01 ± 0.04 eV and 295.79 ± 0.06 eV are assigned to the weak peaks of K $2\mathrm{p}_{3/2}$ and K $2\mathrm{p}_{1/2}$, respectively. Note that the K 2p level core spectrum typically overlaps with the carbon high resolution spectrum and extends from 292 eV up to 297 eV, as shown in **Figure 7.10 (d)**. Evidence of the existence of K 2p is the unique 2.8 eV separation observed between the two peaks.

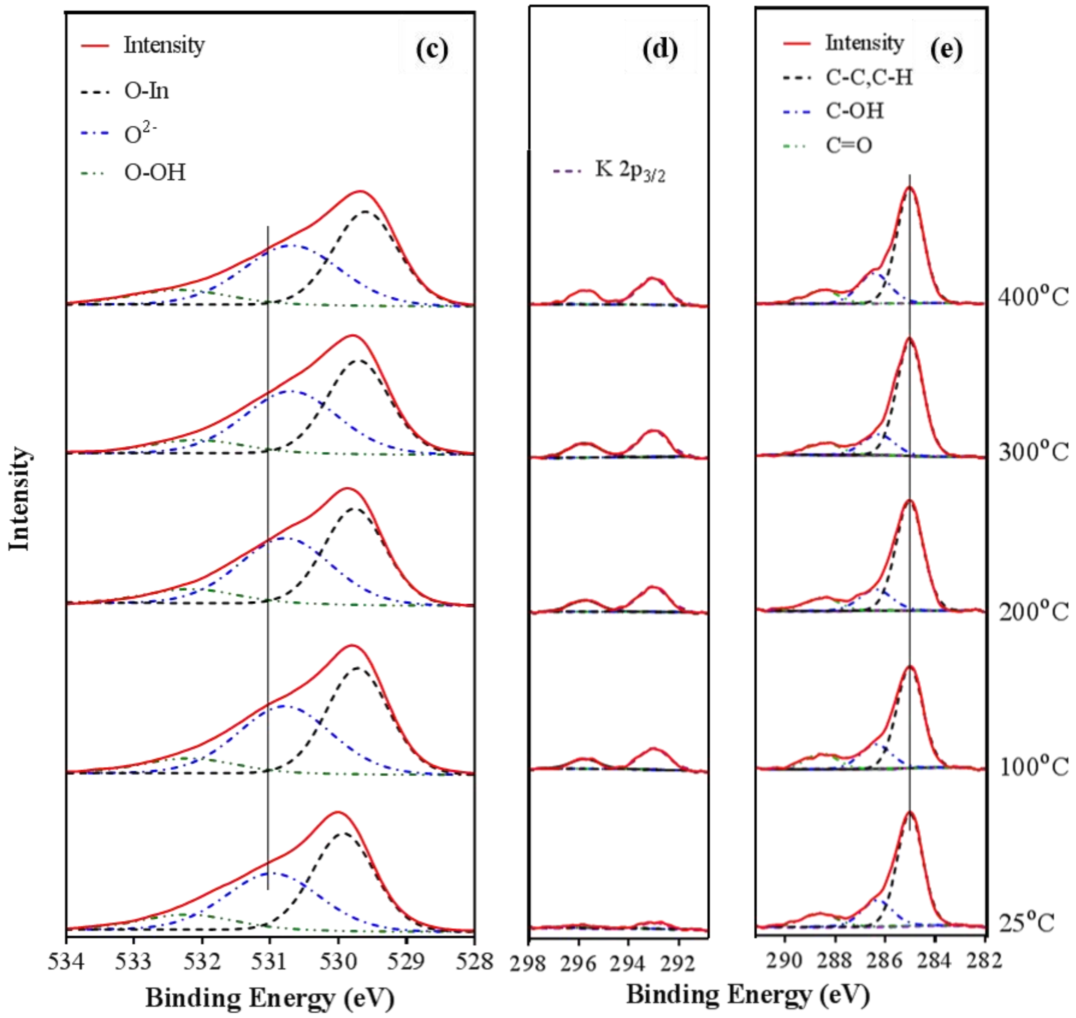

Figure 7.10 Core level spectra for blank ITO samples annealed at different temperatures showing the deconvolution of (c) O 1s, (d) K 2p and (e) C 1s peaks.

Tracking the shifts in peak positions, or changes in the relative strength of the peak intensity, can be used as an indicator of effects induced by ITO annealing. **Figure 7.11** shows changes in both peak position and strength for all fitted peaks into In 3d5/2, Sn 3d5/2, and O 1s core level spectra. It can see that, compared to the non-annealed sample, the slight shifts in peak positions for all peaks are towards low high binding energies with lowered intensities (except at 300 ℃). This is expected due to the diffusion of both potassium and indium atoms towards the surface with annealing. Having more potassium atoms makes the surface positively charged, and hence reduces the amount of electron withdrawing atoms that cause shifts towards high binding energies. At 300 ℃, the peaks are shifted towards high binding energies, and associated with increases in the intensities of both O^{2-} and Sn^{4+} peaks. This may be correlated with the increase seen in Jsc for devices made at ITO substrates annealed at 300 ℃ (see **Figure 7.2**). Since the errors plotted for both peak positions and relative strengths do not exceed 0.2 eV, however, which corresponds to the run-to-run measuring errors (as discussed in **Chapter 6**, **Section 6.2.2**), it can be concluded that the effect of thermal annealing is statistically insignificant, despite the slight changes in peak positions and strengths observed.

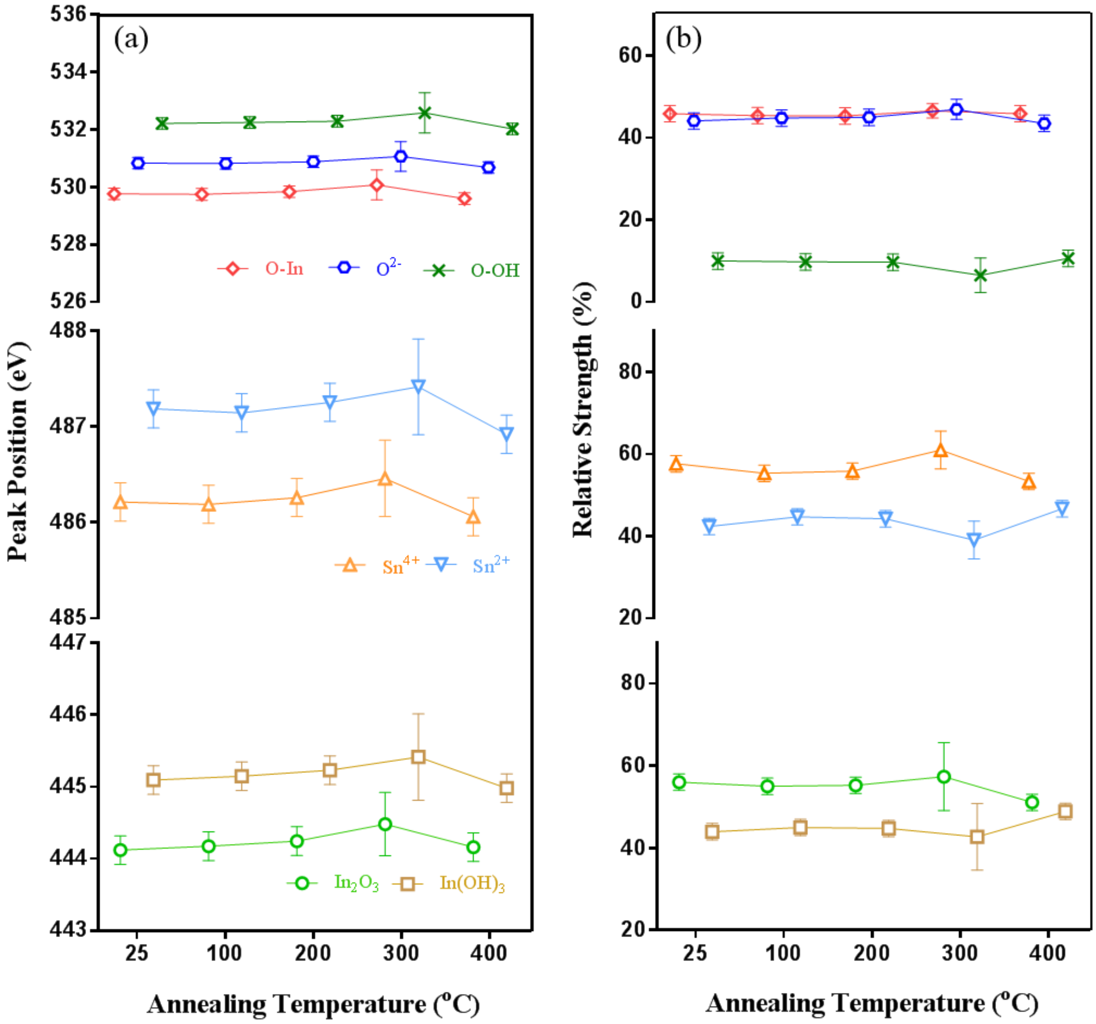

Figure 7.11 (a) Positions and (b) relative strengths of the fitted peaks to the quantified spectra of In $3d_{5/2}$, Sn $3d_{5/2}$ and O 1s core-levels as a function of ITO annealing temperatures. Vertical bars represent standard deviation errors of run-to-run measurements calculated for three samples per temperature, plotted vertically. Offset lines are fitted horizontally for clarity.

7.2.6 *ITO Surface Roughness*

The AFM images of blank ITO samples annealed at different temperatures are shown in **Figure 7.12 (a-e)**, showing their topography before and after the deposition of the bulk heterojunction thin film. The RMS roughness of non-annealed blank ITO is 2.48 nm. Thermal annealing of ITO samples does not significantly change its surface roughness; 2.40 nm, 2.41 nm, and 2.49 nm for 100 ℃, 200 ℃ and 300 ℃, respectively. An increase by 0.8 nm as observed for 400 ℃, however, which results in smoother coverage of the organic BHJ layer, as seen in **Figure 7.12 (f-m)**. The RMS roughness of annealed ITO/BHJ thin film shows a change of about 1 nm compared to the non-annealed ITO/BHJ sample. Changes of 1.2 nm (for 25 ℃), 1.17 nm (for 100 - 300 ℃), and 1.10 nm (for 400 ℃) are also realized.

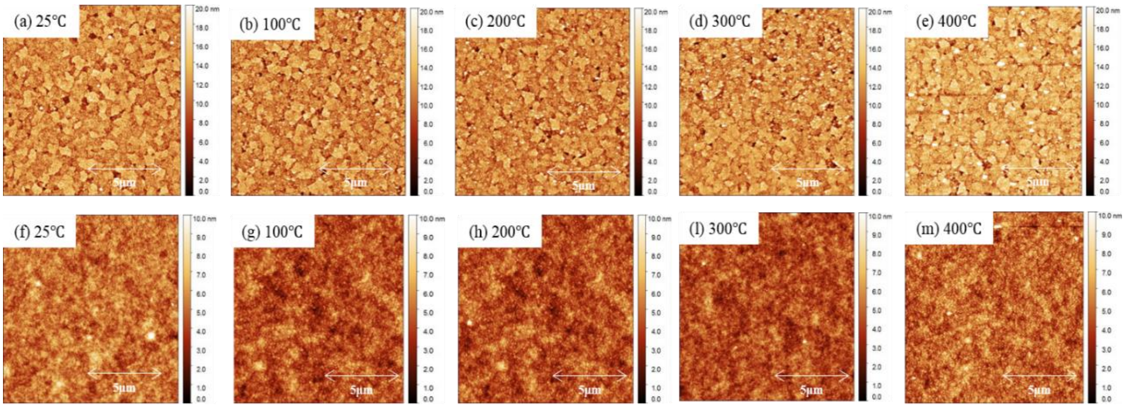

Figure 7.12 AFM images of blank ITO substrates (from (a) to (e)) annealed at various temperatures and PCDETBT: PCBM thin film deposited onto annealed ITO substrates (from (f) to (m)).

7.3 Comparison to Existing Cathode Buffer Layers

The dependence of open circuit voltage on cathode work function is shown in **Figure 7.13**. The data plotted presents only voltages of PCDTBT: PCBM inverted devices with various modified ITO cathodes. Work functions of modified surfaces with interfacial buffer layers, including aluminium doped molybdenum oxide (MoO_3-Al) [15], conjugated polyelectrolyte (PFN) [16], and hydrophilic conjugated polymers (PCP-EP) [10] were extracted from the literature and compared to our results. Details of these devices were shown earlier in **Table 7.1**. Work functions of our devices fabricated onto bare ITO cleaned with different techniques, as reported previously in **Chapter 6**, are also included along with those made onto annealed substrates reported here.

Two distinct behaviours of Voc are evident when a guided line is fitted. The first of these is their independence from the work function, in that voltages nearly plateau for low work functions (≤ 4.30 eV). As seen earlier, non-annealed ITO devices (at $25\ ℃$) exhibited an average Voc of 0.85 ± 0.05 eV (WF; 4.20 ± 0.03 eV). Meanwhile, a maximum Voc of 0.88 eV (WF; 4.30 eV), 0.89 eV (WF; 4.10 eV) and 0.90 eV (WF; 4.00 eV) were reported, respectively for modified ITO with PCP-EP, MoO_3-Al and PFN thin layers. Regarding the high efficiencies acquired by these devices, their best voltages fall within the range of errors calculated for our devices. This is true even for the least well-modified ITO devices.

The second distinct behaviour, meanwhile, is an inverse proportionality to the cathode work function, where the open circuit voltage decreases as the work function increases. This is realized for work functions higher than 4.30 eV. Although the work function is modified with different cleaning techniques, the voltage seems to be not really affected, showing variations that fall within the error range of the annealed devices (except for UV-cleaning with a change of 0.2 eV at 5.0 eV). This, therefore, does not influence the general Voc dependence observed. Knowing that the LUMO level of PCBM lies at 4.30 eV, it can be concluded that the threshold work function is, within the range of error, the same as the fullerene LUMO level.

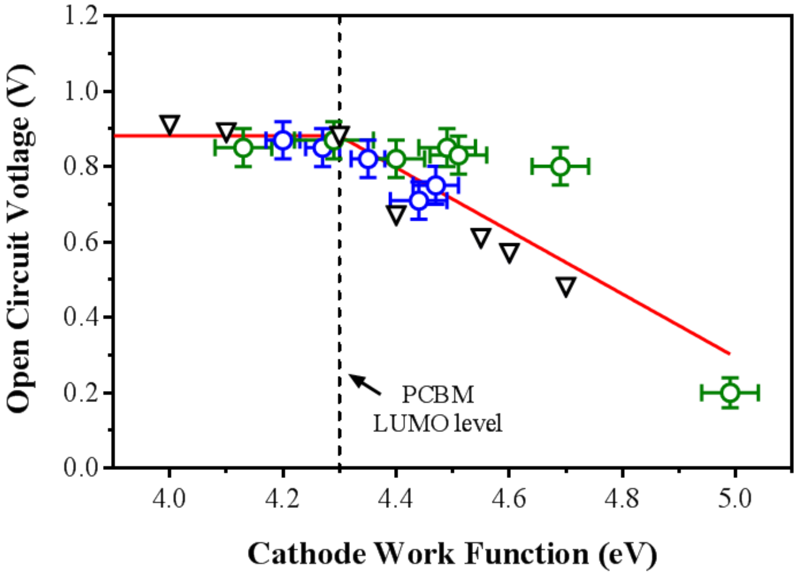

Figure 7.13 Dependence of the open-circuit voltage on the substrate work function for inverted PCDTBT: PCBM solar cells. Black triangles represent devices fabricated on modified ITO electrodes with buffer interlayers taken from Ref [10], [15], [16]. Blue circles represent our devices fabricated onto thermally annealed ITO electrodes without an interfacial layer. Green circles represent our devices fabricated onto non-annealed ITO that were cleaned by different cleaning techniques, as reported previously in Chapter 6. The error bars indicate the standard deviations for 12 pixels (vertical) and three UPS samples (horizontal). The solid-red line is a guide for the eye. The dotted-vertical line indicates the value of the LUMO energy level of PCBM.

7.4 Conclusions

This chapter has studied the open circuit voltage of inverted solar cells based on polycarbazole: fullerene bulk heterojunction. Devices were fabricated on blank ITO with various annealing temperatures. Although the devices exhibit good current-voltage characteristics, and there was no effect from ITO sheet resistance, indicating the desired rectifying property, their voltages show inverse proportionality to ITO temperature. UPS and XPS measurements confirm the correlation between reduced voltage and high potential energy of interfacial dipoles induced by physical adsorption of ambient gasses. A comparison with previously reported devices incorporating cathode buffer layers reveals the existence of a threshold work function equalizing the LUMO level of the fullerene material used. This needs to be overcome for the realization of high voltage. It is still unknown, however, whether a further reduction in the substrate work function is necessary to realize the very highest open-circuit voltage.

7.5 References

[1] M. C. Scharber, D. Mühlbacher, M. Koppe, P. Denk, C. Waldauf, a. J. Heeger, and C. J. Brabec, "Design Rules for Donors in Bulk-Heterojunction Solar Cells—Towards 10 % Energy-Conversion Efficiency," *Adv. Mater.*, vol. 18, p. 789–794, 2006.

[2] S.-H. Liao, H.-J. Jhuo, P.-N. Yeh, Y.-S. Cheng, Y.-L. Li, Y.-H. Lee, S. Sharma, and S.-A. Chen, "Single Junction Inverted Polymer Solar Cell Reaching Power Conversion Efficiency 10.31% by Employing Dual-Doped Zinc Oxide Nano-Film as Cathode Interlayer," *Sci. Rep.*, vol. 4, p. 6813, 2014.

[3] S. Nam, J. Seo, S. Woo, W. H. Kim, H. Kim, D. D. C. Bradley, and Y. Kim, "Inverted polymer fullerene solar cells exceeding 10% efficiency with poly(2-ethyl-2-oxazoline) nanodots on electron-collecting buffer layers," *Nat Commun*, vol. 6, pp. 1–9, 2015.

[4] X. Liu, X. Li, Y. Li, C. Song, L. Zhu, W. Zhang, H. Q. Wang, and J. Fang, "High-Performance Polymer Solar Cells with PCE of 10.42% via Al-Doped ZnO Cathode Interlayer," *Adv. Mater.*, p. 7405–7412, 2016.

[5] V. Vohra, K. Kawashima, T. Kakara, T. Koganezawa, I. Osaka, K. Takimiya, and H. Murata, "Efficient inverted polymer solar cells employing favourable molecular orientation," *Nat. Photonics*, vol. 9, p. 403, 2015.

[6] R. Alqurashi, J. Griffin, A. Alsulami, and A. Buckley, "Open-Circuit Voltage in Inverted Polycarbazole:Fullerene Bulk Heterojunction Solar Cells," *IEEE J. Photovoltaics*, vol. 6, p. 918–923, 2016.

[7] Y. Yan and Y. Song, "Effect of PEI cathode interlayer on work function and interface resistance of ITO electrode in the inverted polymer solar cells," *Org. Electron.*, vol. 17, p. 94–101, 2015.

[8] and K.-Y. Aiyuan Li, Riming Nie, Xianyu Deng, HuaixinWei, Shizhao Zheng, Yanqing Li, Jianxin Tang, "Highly efficient inverted organic solar cells using amino acid modified indium tin oxide as cathode," *Appl. Phys. Lett.*, vol. 104, p. 123303, 2014.

[9] T. Yang, M. Wang, C. Duan, X. Hu, L. Huang, J. Peng, F. Huang, and X. Gong, "Inverted polymer solar cells with 8.4% efficiency by conjugated polyelectrolyte," *Energy Environ. Sci.*, vol. 5, p. 8208, 2012.

[10] Y. Zhu, X. Xu, L. Zhang, J. Chen, and Y. Cao, "High efficiency inverted

polymeric bulk-heterojunction solar cells with hydrophilic conjugated polymers as cathode interlayer on ITO," *Sol. Energy Mater. Sol. Cells*, vol. 97, p. 83–88, 2012.

[11] K. Schulze, C. Uhrich, R. Schüppel, K. Leo, M. Pfeiffer, E. Brier, E. Reinold, and P. Bäuerle, "Efficient Vacuum-Deposited Organic Solar Cells Based on a New Low-Bandgap Oligothiophene and Fullerene C60," *Adv. Mater.*, vol. 18, no. 21, pp. 2872–2875, 2006.

[12] A. Wagenpfahl, D. Rauh, M. Binder, C. Deibel, and V. Dyakonov, "S-shaped current-voltage characteristics of organic solar devices," *Phys. Rev. B*, vol. 82, p. 115306, 2010.

[13] H. Jin, M. Tuomikoski, J. Hiltunen, P. Kopola, A. Maaninen, and F. Pino, "Polymer−Electrode Interfacial Effect on Photovoltaic Performances in Poly(3-hexylthiophene):Phenyl-C61-butyric Acid Methyl Ester Based Solar Cells," *J. Phys. Chem. C*, vol. 113, p. 16807–16810, 2009.

[14] A. Kumar, S. Sista, and Y. Yang, "Dipole induced anomalous S-shape I-V curves in polymer solar cells," *J. Appl. Phys.*, vol. 105, p. 1–6, 2009.

[15] J. Liu, S. Shao, G. Fang, B. Meng, Z. Xie, and L. Wang, "High-Efficiency Inverted Polymer Solar Cells with Transparent and Work-Function Tunable MoO3-Al Composite Film as Cathode Buffer Layer," *Adv. Mater.*, vol. 24, p. 2774–2779, 2012.

[16] R. Xia, D.-S. Leem, T. Kirchartz, S. Spencer, C. Murphy, Z. He, H. Wu, S. Su, Y. Cao, J. S. Kim, J. C. DeMello, D. D. C. Bradley, and J. Nelson, "Investigation of a Conjugated Polyelectrolyte Interlayer for Inverted Polymer:Fullerene Solar Cells," *Adv. Energy Mater.*, vol. 3, p. 718–723, 2013.

[17] M. T. Bhatti, A. M. Rana, and A. F. Khan, "Characterization of rf-sputtered indium tin oxide thin films," *Mater. Chem. Phys.*, vol. 84, pp. 126–130, 2004.

[18] R. Nakanishi, A. Nogimura, R. Eguchi, and K. Kanai, "Electronic structure of fullerene derivatives in organic photovoltaics," *Org. Electron.*, vol. 15, p. 2912–2921, 2014.

[19] S. Zhong, R. Wang, H. Ying Mao, Z. He, H. Wu, W. Chen, and Y. Cao, "Interface investigation of the alcohol-/water-soluble conjugated polymer PFN as cathode interfacial layer in organic solar cells," *J. Appl. Phys.*, vol. 114, p. 113709, 2013.

[20] J. C. C. Fan and J. B. Goodenough, "X-ray photoemission spectroscopy studies

of Sn-doped indium-oxide films,” *J. Appl. Phys.*, vol. 48, p. 3524–3531, 1977.

[21] W.-F. W. and B.-S. Chiou, “Effect of oxygen concentration in the sputtering ambient on the microstructure, electrical and optical properties of radio-frequency magnetron-sputtered indium tin oxide films,” *Semicond. Sci. Technol.*, vol. 11, p. 196, 1996.

[22] C. Donley, D. Dunphy, D. Paine, C. Carter, K. Nebesny, P. Lee, D. Alloway, and N. R. Armstrong, “Characterization of Indium−Tin Oxide Interfaces Using X-ray Photoelectron Spectroscopy and Redox Processes of a Chemisorbed Probe Molecule: Effect of Surface Pretreatment Conditions,” *Langmuir*, vol. 18, p. 450–457, 2002.

[23] A. Sharma, G. Andersson, and D. A. Lewis, “Role of humidity on indium and tin migration in organic photovoltaic devices,” *Phys. Chem. Chem. Phys.*, vol. 13, p. 4381, 2011.

[24] H. Zhou and J. W. Park, “Effect of the crystallinity of indium tin oxide on the charge transfer at the interfaces and the performances of flexible organic light emitting diodes,” *Phys. Status Solidi Appl. Mater. Sci.*, vol. 212, p. 414–424, 2015.

[25] M. Huang, Z. Hameiri, A. G. Aberle, and T. Mueller, “Influence of discharge power and annealing temperature on the properties of indium tin oxide thin films prepared by pulsed-DC magnetron sputtering,” *Vacuum*, vol. 121, p. 187–193, 2015.

[26] M. Huang, Z. Hameiri, A. G. Aberle, and T. Mueller, “Comparative study of amorphous indium tin oxide prepared by pulsed-DC and unbalanced RF magnetron sputtering at low power and low temperature conditions for heterojunction silicon wafer solar cell applications,” *Vacuum*, vol. 119, p. 68–76, 2015.

[27] M. Thirumoorthi and J. T. J. Prakash, “Structure, optical and electrical properties of indium tin oxide ultra thin films prepared by jet nebulizer spray pyrolysis technique,” *Superlattices Microstruct.*, vol. 4, p. 124–132, 2016.

[28] D. B. Fraser and H. D. Cook, “Highly Conductive, Transparent Films of Sputtered In[sub 2−x]Sn[sub x]O[sub 3−y],” *J. Electrochem. Soc.*, vol. 119, p. 1368, 1972.

[29] W.-F. W. and B.-S. Chiou, “Effect of oxygen concentration in the sputtering ambient on the microstructure, electrical and optical properties of radio-frequency magnetron-sputtered indium tin oxide films,” *Semicond. Sci. Technol.*, vol. 11, p. 196, 1996.

[30] T. Ishida, H. Kobayashi, and Y. Nakato, “Structures and properties of electron-beam-evaporated indium tin oxide films as studied by x-ray photoelectron spectroscopy and work-function measurements,” *J. Appl. Phys.*, vol. 73, p. 4344–4350, 1993.

[31] M. J. Chuang, H. F. Huang, C. H. Wen, and A. K. Chu, “On the structure and surface chemical composition of indium–tin oxide films prepared by long-throw magnetron sputtering,” *Thin Solid Films*, vol. 518, p. 2290–2294, 2010.

[32] M. Chuang, “ITO Films Prepared by Long-throw Magnetron Sputtering without Oxygen Partial Pressure,” *J. Mater. Sci. Technol.*, vol. 26, p. 577–583, 2010.

[33] M. Chuang, “ITO Films Prepared by Long-throw Magnetron Sputtering without Oxygen Partial Pressure,” *J. Mater. Sci. Technol.*, vol. 26, p. 577–583, 2010.

[34] K. Sugiyama, H. Ishii, Y. Ouchi, and K. Seki, “Dependence of indium--tin--oxide work function on surface cleaning method as studied by ultraviolet and x-ray photoemission spectroscopies,” *J. Appl. Phys.*, vol. 87, p. 295, 2000.

[35] Y. Gao, “Surface analytical studies of interfaces in organic semiconductor devices,” *Mater. Sci. Eng. R Reports*, vol. 68, p. 39–87, 2010.

[36] A. Sharma, S. E. Watkins, D. A. Lewis, and G. Andersson, “Effect of indium and tin contamination on the efficiency and electronic properties of organic bulk hetero-junction solar cells,” *Sol. Energy Mater. Sol. Cells*, vol. 95, p. 3251–3255, 2011.

[37] M. T. Greiner and Z.-H. Lu, “Thin-film metal oxides in organic semiconductor devices: their electronic structures, work functions and interfaces,” *NPG Asia Mater.*, vol. 5, p. 55, 2013.

Chapter 8

Biomaterial Based Self-Assembled Monolayers as Alternative Cathode Modifiers

Abstract. This chapter investigates the electronic and chemical structures of ITO surfaces modified with self-assembled monolayers (SAMs) based on naturally occurring materials. Five different biomaterials were studied, with some being newly utilized within polymer solar cells (namely Glutamic acid and Glycyl-L-phenylalanine). Inverted devices with various BHJ layers employing different donor polymers were fabricated onto SAM modified ITO electrodes. BHJ cell performance was shown to depend on the SAM backbone polarity and tail group charge, as well as the post-annealing temperature. Surface characterizations of exemplary peptide SAMs prove the successful formation of the monolayer.

8.1 Introduction

In organic solar cells, particularly inverted BHJ cells, the modification of the lower cathode electrode has been critical for the realization of highly efficient cells. Many approaches have been applied to overcome the poor electron extraction of ITO electrodes. The leading approach to date has been the insertion of a 30 – 50 nm thick-layer of n-type metal oxides, or alkali metal salts, at the ITO/active layer interface [1]–[4]. Alternatively, a thin layer (in the order of 5 – 10 nm) of solution-deposited conjugated polyelectrolyte, neutral insulating polymers, or zwitterions can be used [5], [6]. These layers can form ohmic contacts by adjusting the height of the energetic barrier at the interface, which results in large enhancements in both the electron collection efficiency and the open circuit voltage. Their intrinsic properties, however, have been shown to affect ITO bulk properties such as conductivity, transparency and surface roughness [7]. Alternatively, an ultra-thin layer (of no more than 2 nm) can be used to modify ITO surfaces with a negligible influence on bulk electrical properties. This has been achieved by using the technique of self-assembled monolayers (SAMs).

SAMs require very little material in order to modify the work function of the ITO significantly. The increase or decrease in the work function that can be achieved through this technique is dependent on the orientation of the SAM dipole molecules. Several materials have been reported as being able successfully to form adhesive SAMs. These typically consist of organic molecules with terminal groups of carboxyl acid, phosphoric acid, or saline compounds [8]–[11]. Changes in the ITO work function up to a maximum of 1.0 eV have already been seen using these materials, with resultant work functions varying from 4.4 eV to 5.5 eV. These materials are usually processed from toxic-organic solvents, however, and require the ITO surface to be pre-treated with a strong acid solution.

This chapter reports the results of an attempt to modify an ITO using biomaterial peptides to obtain a desired low work function (3.77 eV). These materials are environmentally friendly, inexpensive, water soluble, and do not require chemically aggressive pre-treatment of the ITO surface. They are composed of three functional groups, allowing two-dimensionally-arranged dipoles to be formed via chemical adsorption. The head group is typically a carboxyl group to assist adhesion onto an inorganic surface, while the backbone chain is made out of carbon atoms whose length can significantly affect the packing density of the SAM. Finally, the tail group regulates the direction of the arranged dipoles and hence the interfacial properties of the SAM. **Figure 8.1** shows the adhesion mechanism of peptide molecules onto an ITO surface. Once the carboxyl group is covalently attached to the oxygen or hydroxide sites on the surface, hydrogen bonds are formed across the molecules to co-ordinate dipole arrangement [12].

Although a few types of peptide have already been applied to modify inverted devices, showing remarkable improvements [12]–[14], unfortunately, the studies reporting these do not give sufficient detail to allow repetition and validation of the experimental results, in particular in terms of characterisations of the chemical composition of the as-modified surface. Here, therefore, the performance dependence of inverted devices are studied for five different types of peptide molecules in respect to the effect of different peptide backbones, different post-annealing temperatures, and different types of BHJ donor polymer. It should be noted that among the studied biomaterial SAMs, Glutamic acid (Glut) and Glycyl-L-phenylalanine (Gly-Phe) are yet to be reported in literature and hence the data for modified inverted devices with Glut and Gly-Phe shown here are novel. The surfaces of the modified ITO have also been characterized using XPS, UPS and AFM with detailed discussions provided.

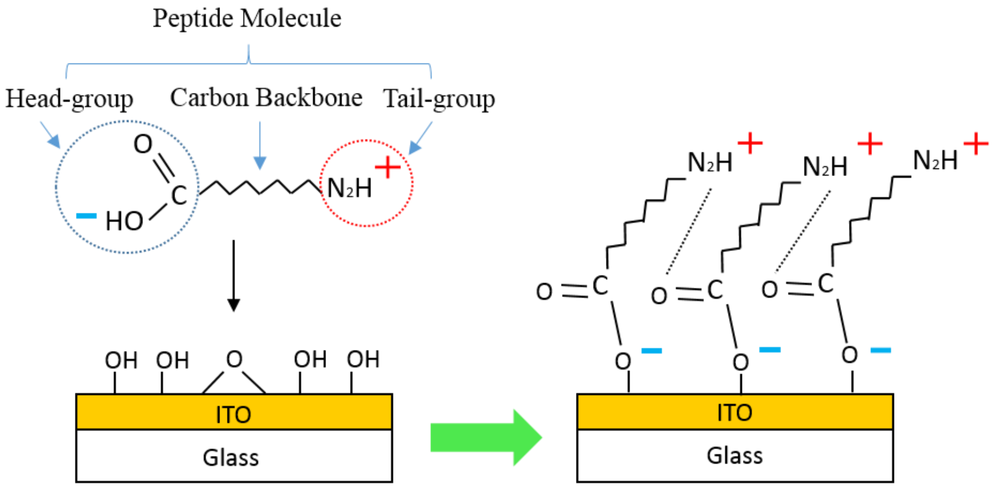

Figure 8.1 Adhesion mechanism of a peptide molecule onto an ITO surface to form thin layer of arranged dipoles. Covalent bonds are formed with the ITO surface whereas hydrogen bonds are formed across the dipole layer.

8.2 Device Performance

8.2.1 Backbone polarity and tail-group charge

ITO surfaces were therefore modified with five different types of amino acid-based materials. These are divided into two groups depending on the polarity of the amide backbone (polar or non-polar). **Figure 8.2** shows the chemical structure of polar and non-polar peptide molecules.

Polar amino acids have a primary amide backbone with two functional groups (**Figure 8.2a**). The head group is carboxyl which is terminal in order to react with the inorganic surface. The second functional group defines the tail charge and hence controls the direction of the formed dipole layer. When a hydroxyl (-OH) is attached at the tail, the amino acid molecule becomes neutrally uncharged and is known as Serine (Ser). Having a second carboxyl group (-COOH) instead of the hydroxyl group makes the molecule tail negatively charged, which is known as Glutamic acid (Glut). If a primary amine (-NH_2) is added as the terminal group, the molecule end becomes positive and the resultant molecule is known as L-Lysine (Lys).

In contrast, non-polar molecules consist of a secondary amide backbone terminated with both a negative head having (-COOH) and a positive tail having (-NH_2) (**Figure 8.2b**). The non-polarity arises from the existence of a second carbonyl group (-C=O). A well-known example is Glycyl-glycine (Gly-Gly), which is the simplest peptide made out from a dipeptide of glycine. A dipeptide of glycine and phenylalanine forms Glycyl-L-phenylalanine (Gly-Phe) with a benzene ring attached.

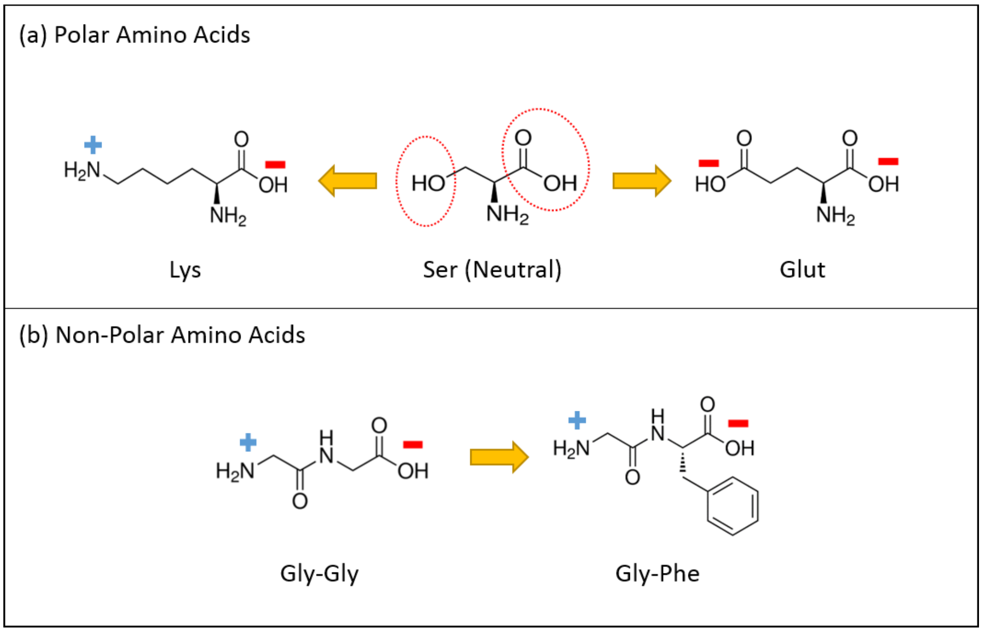

Figure 8.2 Chemical structures of peptide materials used to modify ITO surface.

The influence of tail-group charge and chain polarity on inverted PBDTT-FTTE: PCBM BHJ solar cells with modified ITO substrates were subsequently analysed. **Figure 8.3** shows both the device configuration and the current density/voltage characteristics of the tested devices. The reference device is prepared onto a blank ITO with no monolayer inserted. Generally, all the devices exhibit good diode rectification with free S-shaped deformation observed within the JV curves. The best JV response is recorded for the Lys modified device. Noticeable shifts towards low voltages were observed sequentially as follows, however; Lys, Blank ITO, Glut, Ser, Gly-phe and Gly-Gly. This is due to the gradual reduction in shunt resistance, as seen in **Table 8.1**. There were very small changes in current densities, suggesting the significant effect of the monolayer formed onto Voc rather than Jsc. Surprisingly, no significant change is seen for the series resistance. These observations have been confirmed by the analysis of 24 devices per SAM material, see **Figure 8.4**, where the standard deviation errors are calculated and vertically plotted.

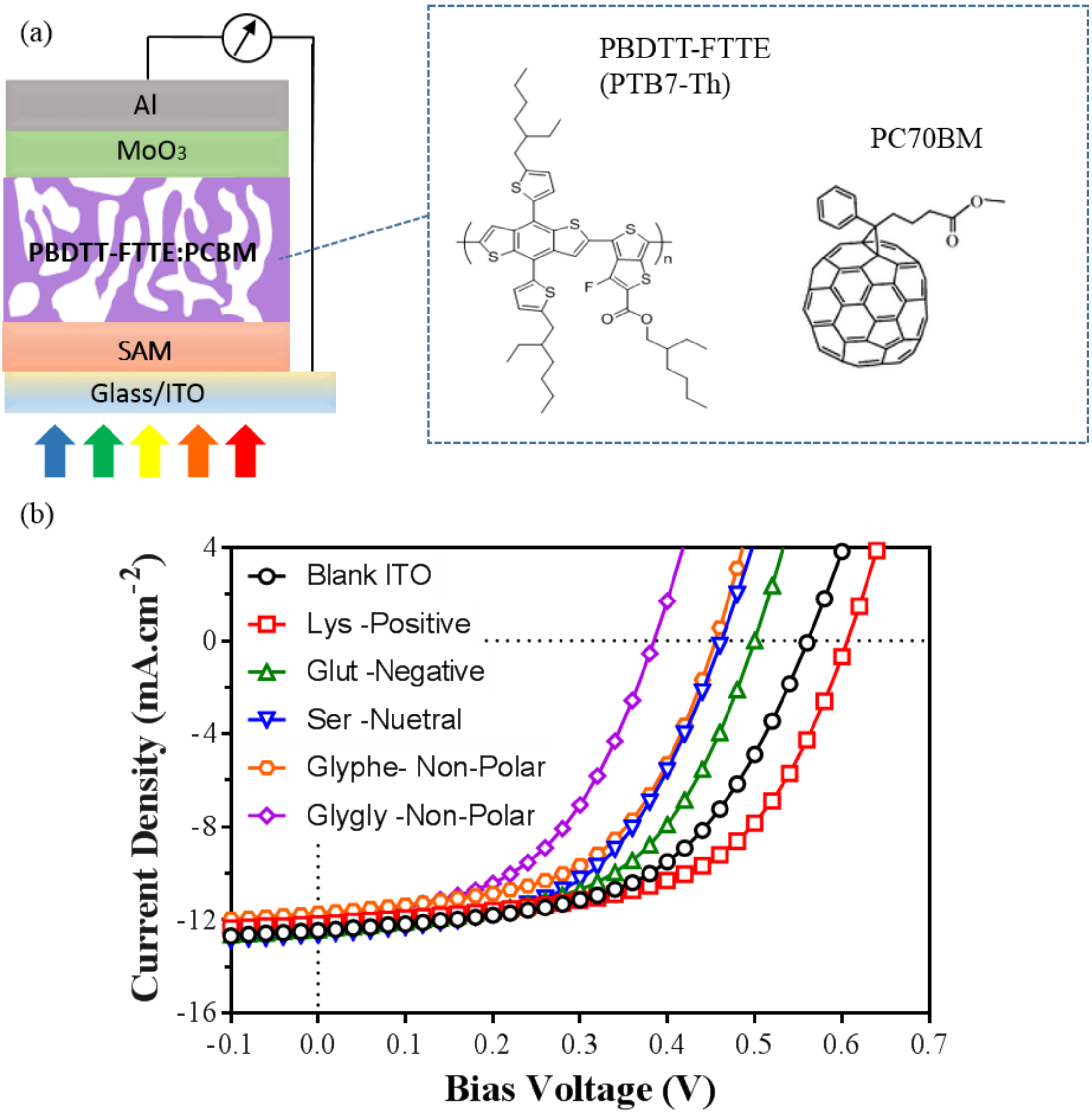

Figure 8.3 (a) Configuration of PBDTT-FTTE: PCBM inverted devices, including the chemical structures of the active layer components. (b) JV Characteristics of the inverted devices modified with various peptide self-assembled monolayers.

Table 8.1 Parameters matrix for the best inverted PBDTT-FTTE: PCBM devices fabricated onto SAM modified ITO.

SAM	V_{OC} (V)	J_{SH} ($mA.cm^{-2}$)	FF (%)	PCE (%)	R_{SH} ($\Omega.cm^2$)	R_S ($\Omega.cm^2$)
Blank ITO	0.61	11.74	57.69	4.18	229	7
Lys	0.64	12.19	58.17	4.41	294	6
Glut	0.60	12.54	56.98	4.13	175	7
Ser	0.58	12.14	55.04	3.65	126	6
Gly-Phe	0.50	12.25	54.89	3.45	120	6
Gly-Gly	0.46	11.81	54.56	2.97	62	6

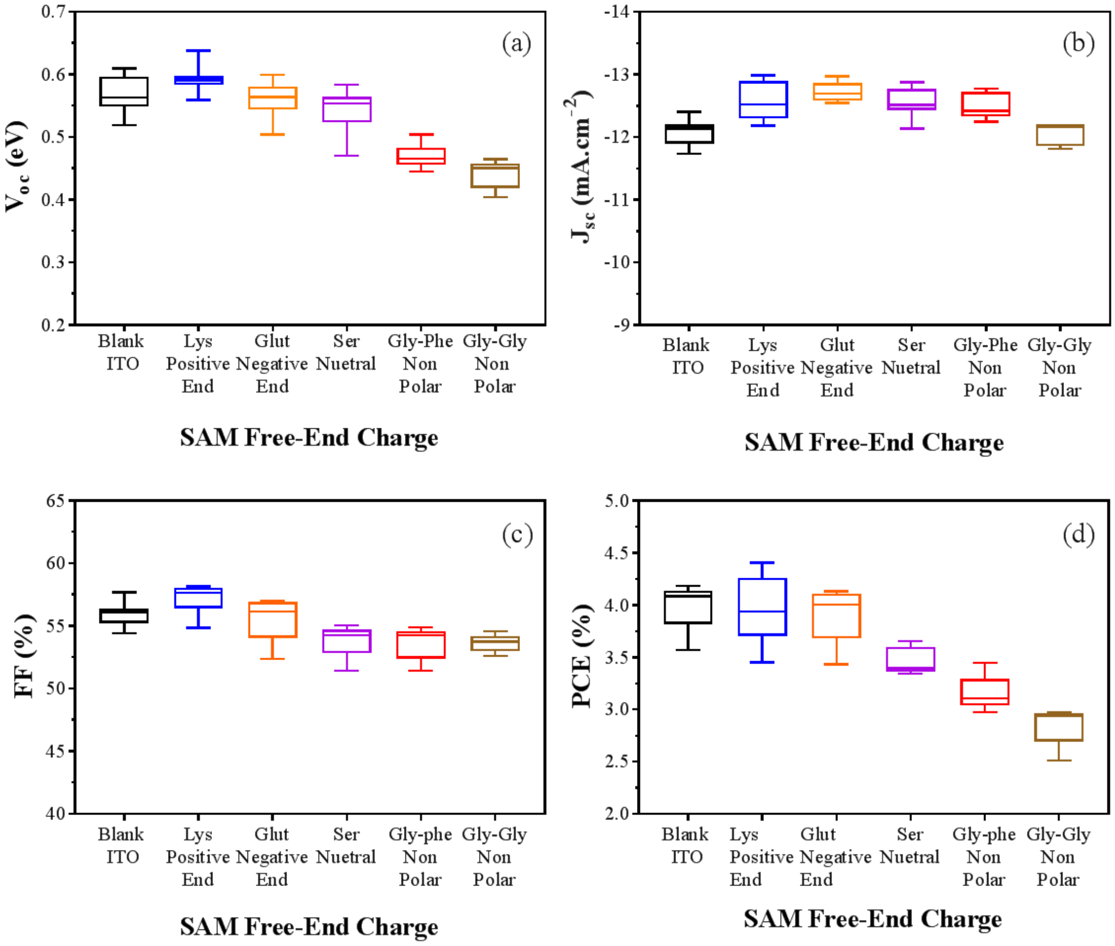

Figure 8.4 Performances of inverted PBDTT-FTTE: PCBM solar cells fabricated onto modified ITO with various amino acids. A reference device fabricated without SAM modification is annotated as 'Blank ITO'.

8.2.2 Post-deposition Annealing

The effect of thermal annealing on the dipole layer formed by peptide SAM modified ITO has been studied. Inverted devices based on PTB7: PCBM were fabricated on dried ITO/Gly-Gly substrates that were annealed at different temperatures (60 – 150 ℃) before the spin-coating of the active layers. **Figure 8.5** shows the configuration of the fabricated devices and the performance of these devices as a function of Gly-Gly SAM annealing temperatures. Note, these are primary results intended to show the effect of annealing on the monolayer and hence there is room for further enhancements. The reference devices here are inverted PTB7: PCBM devices without Gly-Gly and with non-annealed Gly-Gly monolayers, annotated as 'Ref' and '25 ℃', respectively. It can be seen that devices without Gly-Gly modification show better performance than those having non-annealed Gly-Gly monolayer. The best Ref-device exhibits $0.57\,\mathrm{V}$, $11.51\ \mathrm{mA.cm^{-2}}$, 58.71 %, and 4.1 %, whereas the best 25 ℃ - device has $0.47\ \mathrm{V}$, $10.37\ \mathrm{mA.cm^{-2}}$, 53.69 % and 2.84 %.

When annealed at 60 ℃, device performance was reduced, with total reductions of 8.5 %, 2.3 %, 14.4 %, and 2.8 % observed for Voc, Jsc, FF and PCE, respectively, compared to non-annealed devices. A 20 ℃ rise in temperature (to 80 ℃) results in general improvements in device parameters (maximum PCE of 3.0 %), although these are still less efficient than those of the Ref-device. Compared to the Ref-device, an 8.11 % enhancement in efficiency was realized for annealing at 150 ℃. These are attributed to the gradual increase in shunt resistance with increasing temperature; $122\ \Omega.\mathrm{cm^2}$ (60 ℃), $125\ \Omega.\mathrm{cm^2}$ (80 ℃), $193\ \Omega.\mathrm{cm^2}$ (100 ℃) and $462\ \Omega.\mathrm{cm^2}$ (150 ℃), compared to 152 $\Omega.\mathrm{cm}^2$ (25 ℃) and 436 $\Omega.\mathrm{cm}^2$ (Ref device). Surprisingly, the series resistance increased by only 1 $\Omega.\mathrm{cm}^2$ as the temperature changes from 60 ℃ to 80 ℃, and is constant at high temperatures (100-150 ℃).

Ghandhi et al. [15] showed that the thermal annealing of organosilane SAM enhances layer strength. When the layer was annealed at temperatures (400 – 700 ℃) higher than the boiling point of the solvent used to dissolve the organosilane molecules (110 ℃), the interfacial fracture toughness was measured and found to increase with increasing temperature. This was attributed to thermal activation reinforcing the bonds of the head and tail groups to both interfaces, since the SAM layer was sandwiched between copper and silicon layers. Since the thermal annealing was conducted on Gly-Gly modified ITO substrates in air, and before the active layer was deposited, however, the former argument seems to be invalid in our case. Despite the very slight enhancement in PCE observed at 150 ℃, redeeming device performance at 150 ℃ to be similar to those made without Gly-Gly SAM (Ref-device) suggests the desorption of Gly-Gly layer upon annealing. Further work is needed to investigate whether the Gly-Gly layer is fully or partially desorbed after annealing.

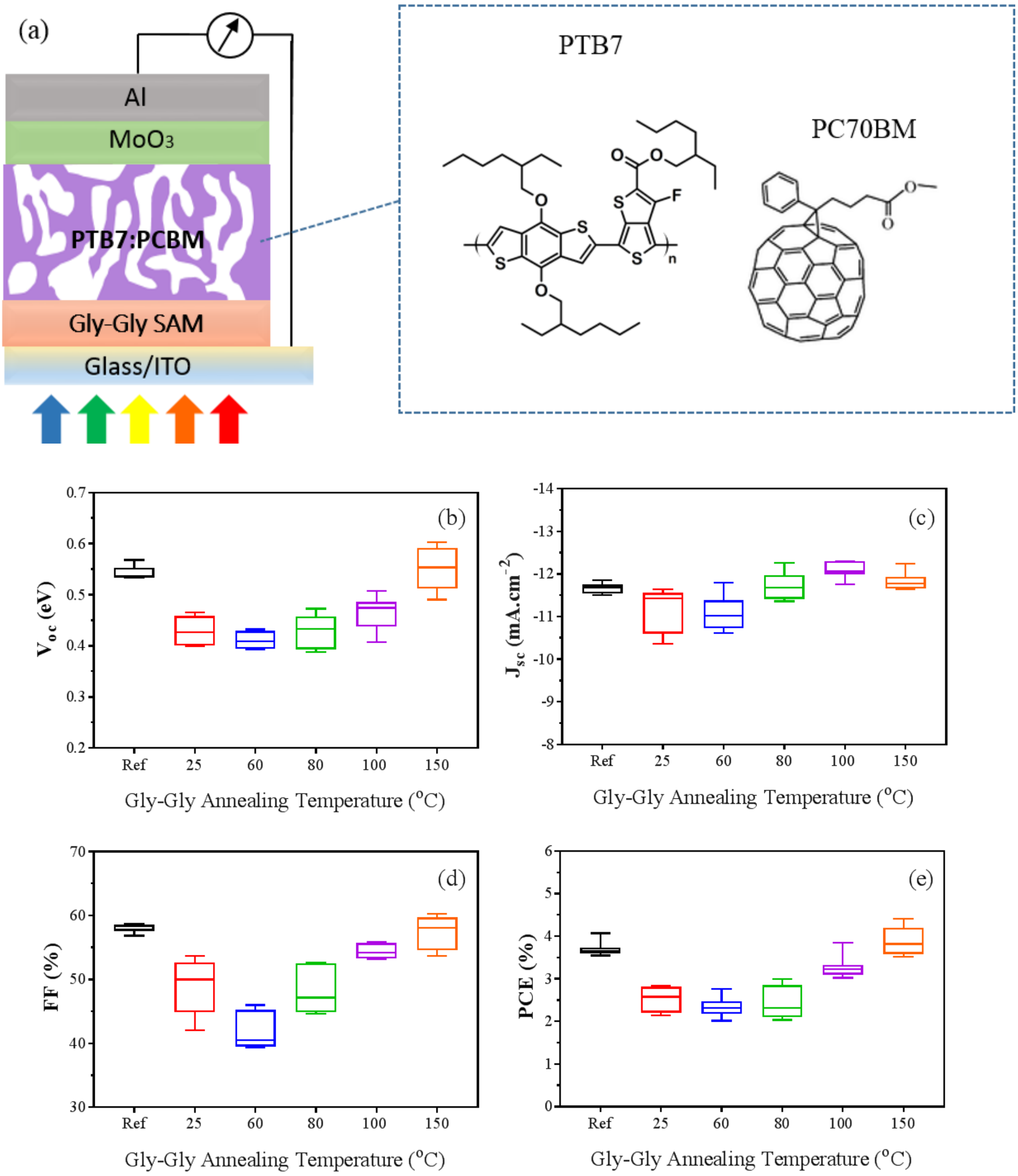

Figure 8.5 (a) Configuration of modified PTB7: PCBM inverted devices modified with Gly-Gly SAM. (b) – (e) Performances of these devices as a function of the Gly-Gly/ITO annealing temperatures. The ‘Ref’ device has the same structure as the other devices but without the ITO being modified with Gly-Gly SAM. The ‘25 °C’ shows results for non-annealed Gly-Gly treated ITO devices.

8.2.3 BHJ System Dependence

To investigate the dependence of device performance on BHJ layer components, Gly-Gly modified inverted solar cells employing different donor polymers blended with PC70BM were fabricated and analysed, as seen in **Figure 8.6**. The Gly-Gly/ITO substrates were thermally annealed at 150 ℃ for 15 min prior to depositing the active layer, in order to establish a valid comparison to existing literature [12] The donor polymers studied were PCDTBT, PTB7, and PBDTT-FTTE (see **Chapter 4** for more details).

The performance of the devices with and without Gly-Gly treatment in comparison to those reported in Ref [12] is showed in **Figure 8.6 (b-e)**. PCDTBT-based devices with a Gly-Gly layer show unexpectedly inferior performance, while noticeable enhancements were seen for both PTB7 and PBDTT-FTTE devices. A 23 % reduction in device efficiency was observed for PCDTBT modified devices, compared to non-modified ITO. This reduction is mainly due to reduced Voc and FF, which results from the reduced shunt resistances (from 591 $\Omega.\mathrm{cm}^2$ to 490 $\Omega.\mathrm{cm}^2$). Although the Jsc shows no significant change upon Gly-Gly modification, an increase up to 6 % in efficiency upon Gly-Gly modification is identified for PTB7 and PBDTT-FTTE devices, as a result of improved Voc and FF. Similar to PCDTBT devices with Gly-Gly, the Jsc of these devices is kept nearly constant. Nie et al. [12], however, reported significant improvements in efficiency of up to 7 % and 17 % for P3HT and PBDTT-CF devices fabricated onto annealed ITO/Gly-Gly substrates, respectively, when compared to ITO only devices. This was attributed to significant enhancements in all device parameters including Jsc. The variety seen in the response of device parameters to the same peptide material suggests the sensitivity of SAM to the BHJ system employed. Further investigations are required to understand the unexpected response of PCDTBT based inverted devices.

We have shown, however, that annealing Gly-Gly at high temperatures can cause desorbing of the monolayer, as can be concluded from **Figure 8.5**, above. In addition, the difference in our device efficiencies between ITO only devices (or Gly-Gly non-annealed devices) and Gly-Gly annealed devices does not exceed a 9 % enhancement. Therefore, the claims raised by Nie et al. [12] must be questioned, especially the results reported for PBDTT-CF based devices.

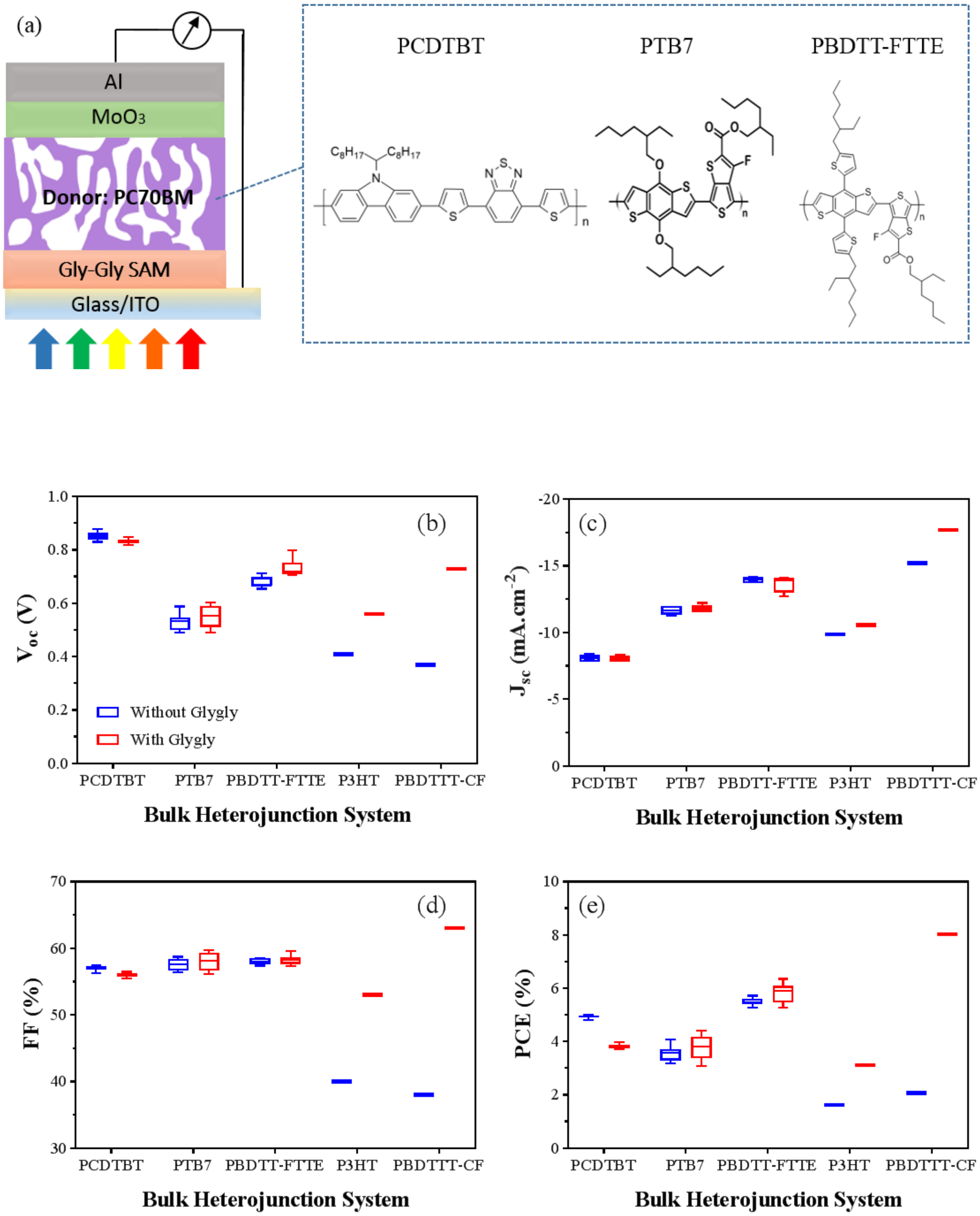

Figure 8.6 Performances of inverted BHJ devices employing different donor polymer materials without and with Gly-Gly SAM modification. Data showed for P3HT: PCBM and PBDTTT-CF: PCBM based solar cells were taken from ref [12].

8.3 Surface Characterization

The treatment of the ITO surface with peptide molecules is assumed to lead to the formation of a very thin layer of arranged dipoles. The thickness of this layer is expected to be no more than 2 nm, which exceeds the resolution limit of standard techniques used to measure layer thicknesses (i.e. Dektak profiling). Alternative techniques are therefore necessary to prove the existence of the self-assembled monolayer. Here, we report evidence on layer formation using highly sensitive methods including XPS, UPS and AFM. It should be noted that because an identical procedure has been used to modify the ITO surface with different amino acids, the results presented for Gly-Gly treatment exemplify the expected influences of other forms of SAM modification onto ITO chemical and electronic structures. In addition, the results that will be discussed in the following sections were obtained for non-annealed Gly-Gly/ITO substrates only.

8.3.1 Chemical composition

The chemical structure of the ITO surface without and with Gly-Gly modification was studied by XPS. To correct shifts within the binding energy scale, possibly induced by surface charging, the binding energy of the C 1s core level (285 eV) was used to calibrate the measured peaks. A Shirley background subtraction and a Gaussian-Laurentzian line-shaped distribution were applied for the calculation of the background intensity and deconvolution of the area under high resolution peaks.

Wide scans of the ITO surface without and with Gly-Gly SAM are shown in **Figure 8.7**. Considering first the blank ITO (without Gly-Gly), traces of carbon, oxygen, indium, tin, potassium and chlorine elements were detected. In comparison to the survey scans of the blank ITO samples acquired for the purpose of **Chapter 7**, the presence of potassium atoms is evident as a result of an unknown source of contamination, although only 0.3 % of the total atomic concentration is detected in the non-annealed sample. Since the non-annealed sample is free from chlorine contamination, the appearance of a chlorine peak (Cl 2p) within the spectra of blank ITO (with 1.56 At. %) reported here may indicate a similar source of contamination. Note that the ITO samples were cleaned in detergents followed by UV ozone plasma for 60 min prior to Gly-Gly treatment (see **Chapter 4**). Principally, UV ozone cleaning removes organic contaminants by photo-oxidation processes, forming products of volatile organic compounds (i.e. $CO_2, H_2O,$ and N_2) [16]. Thus, it is unlikely to form chlorinated hydrocarbon products.

Elemental traces of carbon, oxygen, indium, tin and nitrogen were identified on the ITO/Gly-Gly sample, however. The appearance of a nitrogen (N 1s) peak confirms the formation of the Gly-Gly monolayer. The N 1s peak is positioned at 399.1 eV, which is a 0.8 eV lower binding energy than those reported by Nie et al. [12]. This could be attributed to different exposure times to UV-ozone with a longer time (60 min verses 15 min) applied for our samples. It should be noted that the XPS peaks of peptide-treated ITO that have been reported in the literature [12]–[14] have been shown to prove the presence of a peptide layer, with no attempt to deconvolute the area under the peak. Here, we report for the first time details of resolved peaks for all measured spectra. As seen in the inset in **Figure 8.7**, the high resolution scan of the N 1s core level spectrum is fitted with two adjacent peaks. The resolved peaks at 398.8 eV and 400.5 eV are assigned, respectively, to the primary (-NH_2) and secondary (-NH) amine functional groups that exist within the Gly-Gly structure (see **Figure 8.2**). Another proof of the formation of Gly-Gly is the disappearance of Cl 2p and K 2p peaks from the survey scan when it is compared to the one for the blank ITO, indicating that the chemical reaction has taken place successfully.

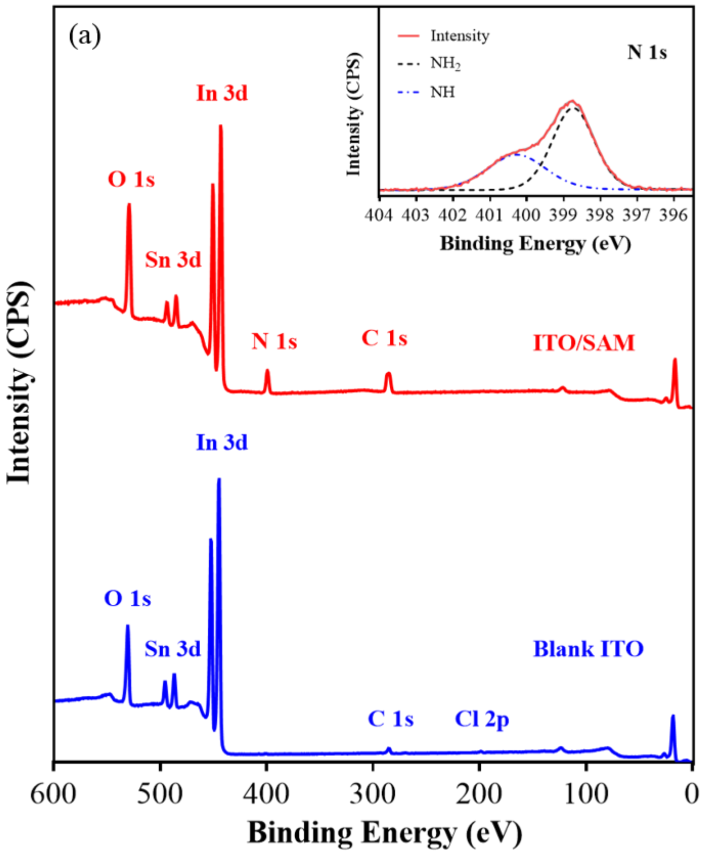

(b)

	Blank ITO	ITO/SAM
In 3d	35.42	19.48
Sn 3d	3.70	1.97
O 1s	47.09	38.49
C 1s	11.95	29.41
N 1s	0	10.65
K 2p	0.27	0
Cl 2p	1.59	0

Figure 8.7 XPS wide scans for the ITO surface without and with Gly-Gly modification. The inset shows a high resolution scan of the nitrogen core level (N 1s) for the modified sample, proving the existence of the self-assembled layer. (b) Table of atomic concentration (At. %) of detected elements.

High resolution scans of In 3d5/2 and Sn 3d5/2 core levels are shown in **Figure 8.8** with fitted peaks. The In 3d5/2 spectra for both samples are fitted with three adjacent peaks: In 1, In 2 and In 3 (**Figure 8.8a**). For the blank ITO, the three peaks correspond to $\mathrm{In_2O_3}$ lattice, indium hydroxide $\mathrm{In(OH)_3}$, and chlorinated indium $\mathrm{InCl_3}$, respectively [17]–[21]. Details of the peak positions and relative strengths are shown in **Table 8.2**. The reaction between contaminated Cl (detected in the survey spectrum) and Indium generates the $\mathrm{InCl_3}$ peak located at 446.65 eV, which is at a slightly higher binding energy (by 0.55 Ev) than the one reported very recently [21]. In comparison with the non-annealed sample (**Chapter 7**), the $\mathrm{In_2O_3}$ and $\mathrm{In(OH)_3}$ peaks reported here are at higher binding energies, by 0.35 eV and 0.32 eV respectively. This is understandable and is expected to have been caused by the high electronegativity of Cl (3.16). Nonetheless, remarkable shifts in all peak positions, by 1.75 - 2.31 eV towards low binding energies, were observed when the ITO surface was treated with Gly-Gly. As expected, these shifts are caused by the formation of a thin-layer of arranged dipoles. In addition, since there is no trace of Cl contamination on the ITO/Gly-Gly sample. The In 3 (444.93 eV) is assigned to indium oxy-hydroxide indium InOOH [17], arising probably from In bonding to the -OOH group. The In 1 (442.92 eV) and In 2 (443.86 eV) are allocated to indium metal $\mathrm{In_2O_3}$ and $\mathrm{In(OH)_3}$, respectively.

Two adjacent peaks (Sn 1 and Sn 2) are best fitted to all Sn 3d5/2 spectra, see **Figure 8.8b**. For the blank ITO and ITO/Gly-Gly samples, the Sn 1 and Sn 2 peaks are assigned to $\mathrm{SnO_2}$ and SnO, respectively [22]–[24]. Besides the significant shifts (by 1.72 – 1.93 eV) towards low binding energies upon Gly-Gly treatment, the total intensity of the Sn spectra is reduced, indicating the existence of Gly-Gly. Considering the relative strengths of the resolved Sn peaks for ITO/Gly-Gly, the increase in Sn 2 strength (56.89 %) compared to the one for bare ITO (34.63 %) confirms the covalent bonds formed between the carboxyl group and Sn atoms, as described earlier in **Section 8.2**.

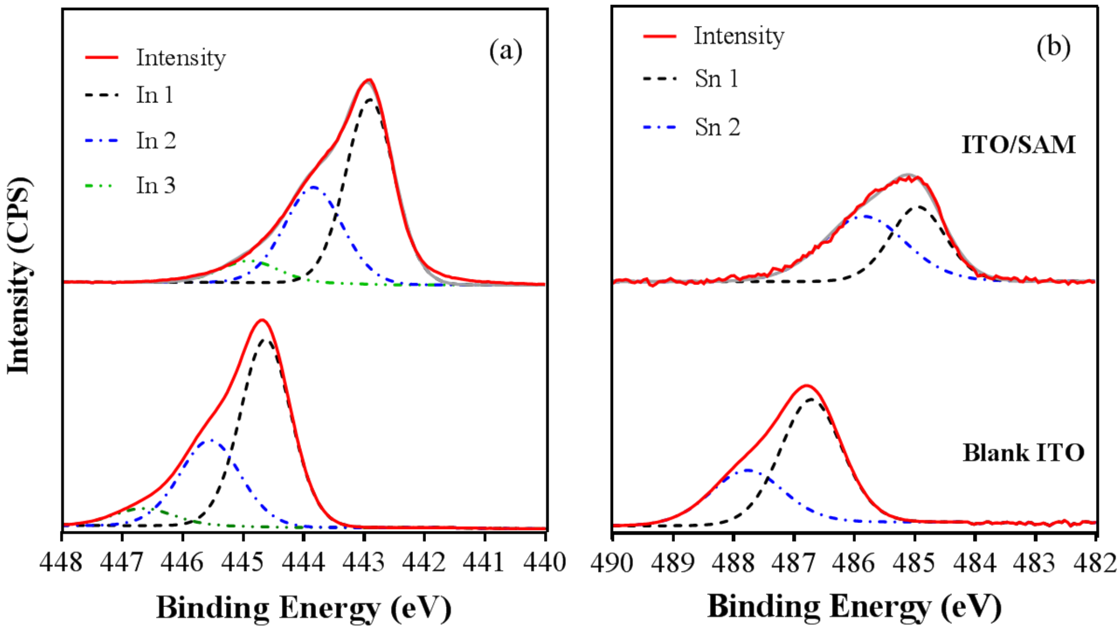

Figure 8.8 High resolution scans of (a) In 3d5/2 and (b) Sn 3d5/2 core levels and fitted peaks for untreated and treated ITO samples with Gly-gly amino acid.

Table 8.2 Detailed peak position and relative strength of resolved peaks from the high resolution scans of In 3d5/2 and Sn 3d5/2 core level spectra.

Treatment	Position/ Relative Strength	In 1	In 2	In 3	Sn 1	Sn 2
Blank ITO	eV	444.63	445.55	446.65	486.72	487.78
	%	60.40	33.02	6.58	65.37	34.63
ITO/SAM	eV	442.92	443.86	444.93	484.97	485.85
	%	57.04	35.19	7.77	43.11	56.89

Figure 8.9 shows the core level spectra of O 1s and C 1s with best fitted peaks. Three distinct peaks are resolved in the O 1s spectra of bare ITO, namely O 1, O 2, and O 3, with respective energies of 530.29 eV, 531.34 eV and 532.79 eV. These are respectively assigned to the oxygen lattice in In_2O_3 (O-In), the oxygen vacancy in the oxygen deficient In_2O_{3-x} matrix (O^{2-}), and chemisorbed hydroxide (-OH), which is in agreement with what has been reported by other scholars [18], [25]–[27]. The –OH peak here arises from the adsorption of a volatile hydroxide ion during the UV-ozone treatment. Interestingly, the ITO/Gly-Gly scan shows a significant change in the line-shape of the O 1s spectrum compared to the one for blank ITO indicating that it had undergone chemical reaction. In addition, a large shift across the whole spectrum towards lower binding energies is observed to be in order of 2.25 eV, as seen in **Table 8.3**. An extra peak, named O 4, with a binding energy of 531.81 eV (and 4.76 % strength) has been inserted to achieve the best fit to the spectrum, see **Figure 8.9c**. Taking into consideration the fact that Gly-Gly has two types of oxygen bonding; a double bond to carbon in the carbonyl group (C=O) and single bonds to hydrogen and carbon in the hydroxyl group (C-O-H). The four peaks are assigned as follows: O 1 to O-In, O 2 to O^{2-}, O 3 to C-O-H, and O 4 to C=O. Despite the different origins of the

O 3 peak, the increase in its strength from 9.32 % to 23.81 % upon Gly-Gly treatment proves the adhesion of Gly-Gly onto the ITO surface.

For C 1s, the spectra of both samples were deconvoluted into five adjacent peaks, as seen in **Figure 8.9d**. The C 1s of blank ITO has a similar shape-line to those reported previously in **Chapter 7**. The first three carbon peaks are therefore assigned to superimposed C-C and C-H (for C 1), C-OH (for C 2), and C=O (for C 3), with respective binding energies of 285 eV, 286.41 eV, and 287.70 eV. The new C 4 at 289.30 eV is attributed to a carbonate species (O-C=O) that was possibly adsorbed onto the surface during the UV-ozone treatment. The C 5 at 293.41 eV is actually allocated as a weak signal of potassium chloride KCl with a total atomic concentration of 0.62 %. Considering the Gly-Gly surface, similar to the O 1s, a totally different shape-line with a noticeable disappearance of the K 2p peaks is observed. Surprisingly, the whole spectrum is shifted toward higher binding energies by 1.29 eV, as revealed by the change in position of the main carbon peak C 1. **Table 8.3** shows details of the positions and relative strengths of the resolved peaks for the ITO surface with and without Gly-Gly modification. This shift may be attributed to the contribution of amine and carboxyl groups to the Gly-Gly backbone. Thus, the C4 and C 5 peaks are re-assigned to the C-N, and COOH groups, respectively, while the first three peaks are the same ones allocated previously for the blank ITO; i.e. superimposed C-C and C-H (C 1), C-OH (C 2), and C=O (C 3).

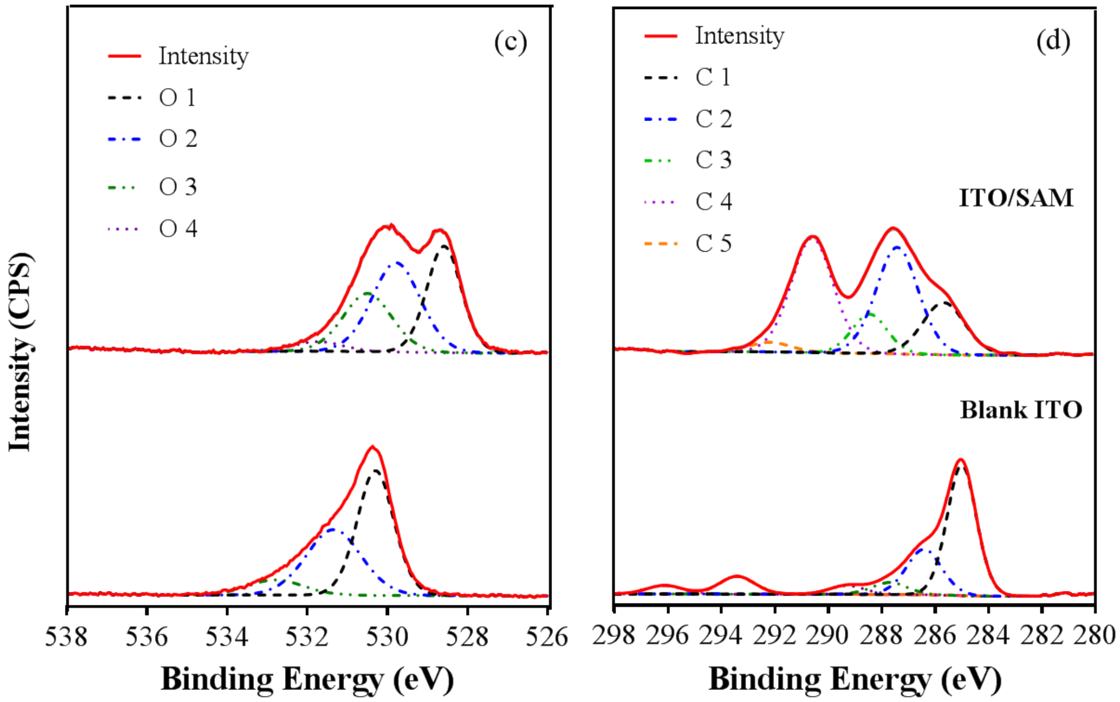

Figure 8.9 High resolution scans for (c) O 1s and (d) C 1s core levels and fitted peaks for untreated and treated ITO samples with a self-assembled monolayer of Gly-gly amino acid.

Table 8.3 Detailed positions and relative strengths of the resolved peaks from the high resolution scans of O 1s and C 1s core level spectra.

Treatment	**Position/ Relative Strength**	**O 1**	**O 2**	**O 3**	**O 4**
Blank ITO	eV	530.29	531.34	532.79	--
	%	50.69	39.99	9.32	--
ITO/SAM	eV	528.60	529.73	530.54	531.81
	%	34.20	37.24	23.81	4.76

		C 1	**C 2**	**C 3**	**C 4**	**C 5**
Blank ITO	eV	285	286.41	287.70	289.30	293.41
	%	54.06	22.61	5.93	4.31	8.84
ITO/SAM	eV	283.71	284.83	285.54	287.02	288.13
	%	19.47	29.86	13.25	33.48	3.98

8.3.2 Surface Work Function

The influence of peptide modification on the ITO work function was studied using UPS. **Figure 8.10** shows the photoelectron spectra for ITO samples without and with Gly-Gly SAM. The cut-off edge of kinetic energy for the unmodified surface gives a work function of 4.75 eV, which is similar to the one reported in **Chapter 6** and in the literature [28], [29]. The valance band edge (VBE) is at a binding energy of 2.98 eV. When treated with Gly-Gly, the whole spectrum shifts towards high energies, indicating the reduction in the work function. Indeed, 3.77 eV and 3.46 eV are determined for the work function and valance band edge of the modified ITO, respectively. These are similar to the results for the formation of the dipole layer. It should be noted that the ITO/Gly-Gly work function is slightly larger than the one reported by Nie et al. [12]. The electronic structure of ITO before and after Gly-Gly treatment is shown in **Figure 8.11a**, however. Assuming that the Fermi level is continued across the ITO/Gly-Gly interface, the deeper VBE leads the vacuum level shifting (Evac) downwards by 0.98 eV, hence lowering the energetic barrier and reducing the effective charge transport.

The energetic mismatch at the PCBM/Gly-Gly interface was calculated to elucidate the unexpected performance of PCDTBT modified devices (**Section 8.2.3**). PC70BM was used as an acceptor with a LUMO energy level of 4.15 eV. Hence, the difference between the work function of the ITO/Gly-Gly substrate and that of PC70BM LUMO is 0.38 eV. Taking into account that all three polymers, PCDTBT, PTB7 and PBDTT-FTTE, were blended with the same fullerene molecules and have an identical device structure, the reduction seen in the efficiency of PCDTBT modified devices cannot be attributed to the interface sourced. It could be due to other sources like incomplete morphology of active layer. A topography of the active layer morphology taken by a scanning electron microscope (SEM) and a 3D image of the dipole layer constructed by scanning tunnelling microscopy (STM) can clarify whether the SAM's sensitivity to donor polymer is induced by either the BHJ morphology or the electronic interface, or whether it is a combined effect. A detailed study of the J-V measurement in the dark for SAM devices is also recommended. These suggested experiments were not conducted as part of this study, however, due to time constraints.

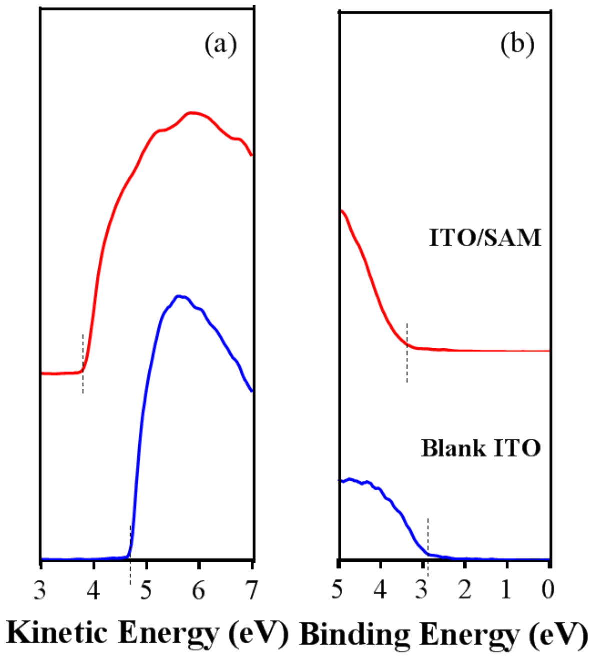

Figure 8.10 Ultraviolet photoelectron spectra showing (a) the ITO work function and (b) the valance band edge changes before and after treatment with Gly-Gly SAM.

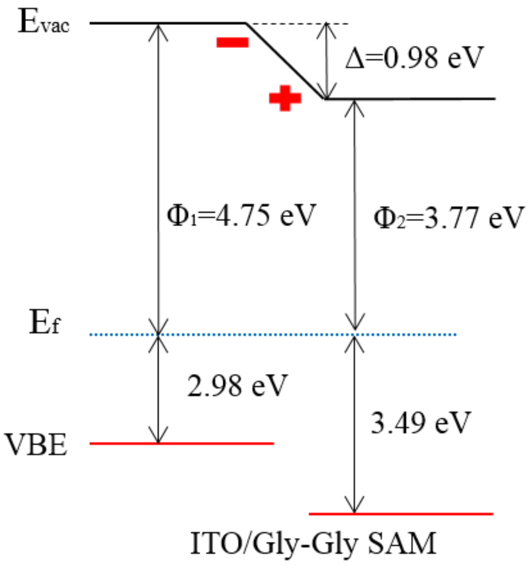

Figure 8.11 Vacuum level shift for the ITO surface before and after being treated with Gly-Gly SAM.

8.3.3 *Surface Coverage*

The coverage of the dipole layer onto the ITO surface was examined in order to understand the reasons behind the variation in pixel performance per device. This was done by measuring the work function of the ITO/Gly-Gly at three different areas per sample. These were located at the far left-edge (A1), middle (A2), and far right-edge (A3). Similarly, the XPS data were taken also for these areas for each prepared sample. Because the appearance of the N 1s peak is considered to be a strong indication of the existence of the monolayer, the atomic concentrations of the N 1s peak for each area were estimated. A correlation between the nitrogen concentration, surface work function, and pixel efficiency is shown in **Figure 8.12**. The pixel (P) efficiency is assigned for each area based on pixel location. For example, the average of P1 and P2 efficiencies is allocated to A1, whilst P3 and P4 averaged PCE is calculated for A2. The A3 is correlated to the average of P5 and P6 PCE. The results are compared to the unmodified bare ITO, where the nitrogen concentration is zero (A0). The pixel efficiency is therefore equal to the sum of all six pixels. The standard error represents the variation in PCE and work function values.

It can clearly be seen, however, that the nitrogen concentration varies between different positions by 1 %. It increases when moving from the left-edge towards the right-edge sides; 10.65 % for A1, 12.80 % for A 2, and 13.79 % for A3. This is accompanied by a gradual reduction in both the work function and pixel efficiency, with the highest values being obtained for bare ITO. (4.08 eV, 4.75 %), (3.0 eV, 4.35 %), (2.85 eV, 4.1 %), and (2.50 eV, 3.84 %) are realized for A0, A1, A2 and A3, respectively. This result has two implications: first, although the assembled peptide molecules cover the ITO surface uniformly, in some areas the arrangement of the dipoles seems to be denser. Second, the thickness of the dipole layer controls the surface work function. A high nitrogen concentration indicates a more condensed layer and hence a lowering of the surface work function.

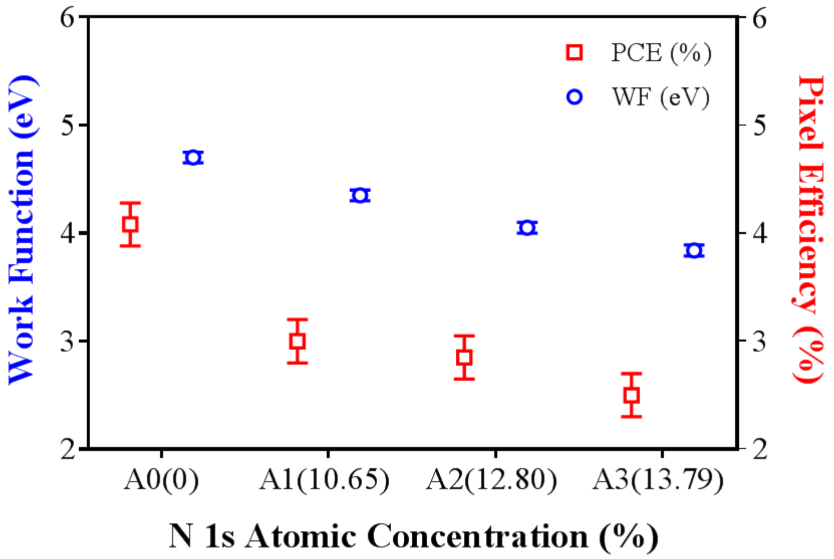

Figure 8.12 Plot showing the correlation between the atomic concentration of the N 1s core level, ITO work function, and the efficiency of PBDTT-FTTE:PCBM BHJ inverted devices upon treating ITO surface with Gly-Gly SAM. Atomic concentrations and work functions were measured from three different areas per sample; A1 (far left-edge), A2 (middle), and A3 (far right-edge). A percentage of zero is assigned to the reference sample and devices that were fabricated onto non-treated ITO. Averaged PCE values are shown depending on pixel location; P1 and P2 for A1, P3 and P4 for A2, and P5 and P6 for A3.

8.3.4 RMS Roughness

Investigations were also conducted into the effect of peptide modification on the surface morphology of ITO and bulk heterojunction. **Figure 8.13 (a, b)** shows the AFM images for ITO samples before and after being modified with Gly-Gly SAM. The RMS roughness of the unmodified surface was 2.00 nm, which is lower than either non-annealed sample (**Chapter 7**) or reported by Nie et al. [12]. This is because UV-ozone cleaning has effectively removed carbon contamination and hence smoothed the ITO surface [16], [30]. When ITO is modified with Gly-Gly SAM, an increase in its surface roughness of less than 1 nm was observed, indicating the existence of the monolayer. This disagrees with what is reported in literature, however [12]. Nie et al. [12] found that Gly-Gly SAM reduces the RMS of bare ITO from 3.46 nm to 3.28 nm, which was attributed to the insignificant change in surface energy.

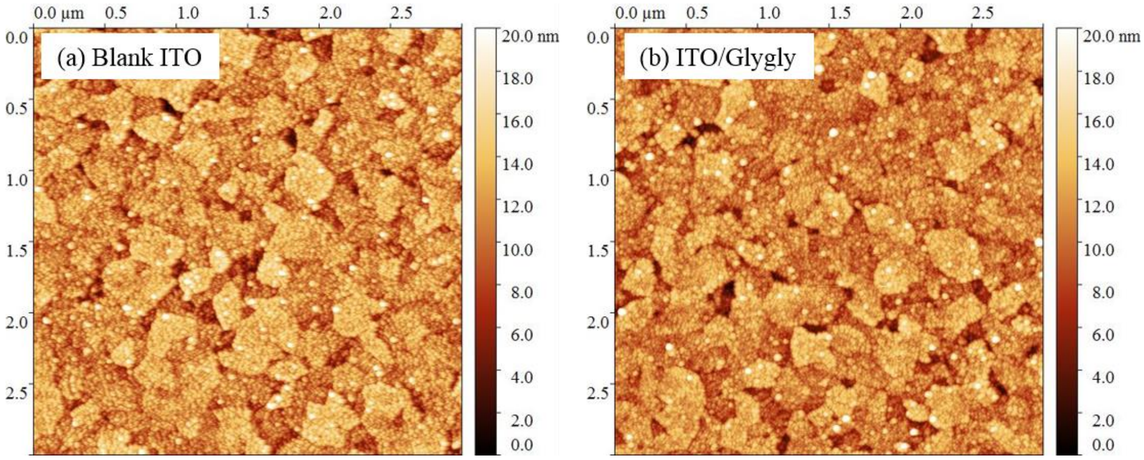

Figure 8.13 AFM images for ITO surface (a) before and (b) after treating with Gly-Gly SAM. Scan sizes are 3 µm X 3 µm.

8.4 Conclusions

The ITO surface has been modified with many novel biomaterials used to form self-assembled monolayers. These biomaterials are non-toxic and water soluble, and hence provide a green alternative to standard modifying methods with no need for aggressive chemical treatments. Inverted devices with different donor polymers were fabricated onto a peptide SAM modified substrate. The existence of the peptide layer was demonstrated by a study of the chemical composition and roughness of the ITO surface, with and without SAM. The appearance of the nitrogen N 1s peak with various concentrations across the ITO surface confirms the inhomogeneous coverage of the monolayer. Since they have an amide backbone with a carboxyl head group and various tail groups, the polarity and tail group charge of the peptide molecules have been seen to affect PBDTT-FTTE based inverted devices, with the best performance obtained for a polar peptide having a positive tail group (Lysine).

Thermal annealing of a Glycyl-Glycine (Gly-Gly) modified substrate has been shown to have a negative effect on the performance of PTB7 inverted devices. This is attributed to Gly-Gly desorption as Gly-Gly devices annealed at high temperature performed like those having no Gly-Gly. In comparison with the existing literature, peptide modification proves to very slightly improve device efficiency by enhancing the open-circuit voltage, fill factor and shunt resistance. This observation holds true for all tested BHJ materials except for polycarbazole devices, where inferior performance is seen for all parameters. The large difference in efficiency reported for PBDTTT-CF modified devices by Nie et al. [12] therefore seems to be questionable based on the systematic study presented in this thesis. Since all the tested SAM devices had identical structures, and all donor polymers blended with PC70BM, detailed SEM studies of the topography of the active layer topography, 3D STM imaging of the dipole layer, and dark current measurements are all recommended so as to elucidate the effects of BHJ morphology and the electronic interface.

8.5 References

[1] B. J. Richardson, X. Wang, A. Almutairi, and Q. Yu, “High efficiency PTB7-based inverted organic photovoltaics on nano-ridged and planar zinc oxide electron transport layers,” *J. Mater. Chem. A*, vol. 3, no. 10, pp. 5563–5571, 2015.

[2] Z. He, C. Zhong, S. Su, M. Xu, H. Wu, and Y. Cao, “Enhanced power-conversion efficiency in polymer solar cells using an inverted device structure,” vol. 6, no. September, pp. 591–595, 2012.

[3] M. T. Greiner and Z.-H. Lu, “Thin-film metal oxides in organic semiconductor devices: their electronic structures, work functions and interfaces,” *NPG Asia Mater.*, vol. 5, no. 7, p. e55, Jul. 2013.

[4] G. Li, C. W. Chu, V. Shrotriya, J. Huang, and Y. Yang, “Efficient inverted polymer solar cells,” *Appl. Phys. Lett.*, vol. 88, no. 25, pp. 3–6, 2006.

[5] T. Yang, M. Wang, C. Duan, X. Hu, L. Huang, J. Peng, F. Huang, and X. Gong, “Inverted polymer solar cells with 8.4% efficiency by conjugated polyelectrolyte,” *Energy Environ. Sci.*, vol. 5, no. 8, p. 8208, Jul. 2012.

[6] I. Etxebarria, J. Ajuria, and R. Pacios, “Solution-processable polymeric solar cells: A review on materials, strategies and cell architectures to overcome 10%,” *Org. Electron.*, vol. 19, pp. 34–60, Jan. 2015.

[7] B. A. E. Courtright and S. A. Jenekhe, “Polyethylenimine Interfacial Layers in Inverted Organic Photovoltaic Devices : Effects of Ethoxylation and Molecular Weight on Efficiency and Temporal Stability,” 2015.

[8] P. J. Hotchkiss, S. C. Jones, S. A. Paniagua, A. Sharma, B. Kippelen, N. R. Armstrong, and S. R. Marder, “The modification of indium tin oxide with phosphonic acids: Mechanism of binding, tuning of surface properties, and potential for use in organic electronic applications,” *Acc. Chem. Res.*, 2012.

[9] H. Li, E. L. Ratcliff, A. K. Sigdel, A. J. Giordano, S. R. Marder, J. J. Berry, and J.-L. Brédas, “Modification of the Gallium-Doped Zinc Oxide Surface with Self-Assembled Monolayers of Phosphonic Acids: A Joint Theoretical and Experimental Study,” *Adv. Funct. Mater.*, vol. 24, no. 23, pp. 3593–3603, Jun. 2014.

[10] Y. Zhao, L. Duan, D. Zhang, G. Dong, J. Qiao, L. Wang, and Y. Qiu, “Systematic investigation of surface modification by organosiloxane self-assembled on indium-tin oxide for improved hole injection in organic light-emitting diodes.,” *ACS Appl. Mater. Interfaces*, vol. 6, no. 6, pp. 4570–7, Mar. 2014.

[11] J. Luo, H. Wu, C. He, A. Li, W. Yang, and Y. Cao, “Enhanced open-circuit

voltage in polymer solar cells," *Appl. Phys. Lett.*, vol. 95, no. 4, p. 43301, 2009.

[12] A. L. and X. D. Riming Nie, "Environmentally friendly biomaterials as an interfacial layer for highly efficient and air-stable inverted organic solar cells," *J. Mater. Chem. A*, vol. 2, pp. 6734–6739, 2014.

[13] X. Deng, R. Nie, A. Li, H. Wei, S. Zheng, W. Huang, Y. Mo, Y. Su, Q. Wang, Y. Li, J. Tang, J. Xu, and K. Wong, "Ultra-Low Work Function Transparent Electrodes Achieved by Naturally Occurring Biomaterials for Organic Optoelectronic Devices," *Adv. Mater. Interfaces*, vol. 1, no. 7, pp. 1400215–1400221, Oct. 2014.

[14] A. Li, R. Nie, X. Deng, H. Wei, S. Zheng, Y. Li, J. Tang, and K. Y. Wong, "Highly efficient inverted organic solar cells using amino acid modified indium tin oxide as cathode," *Appl. Phys. Lett.*, vol. 104, no. 12, 2014.

[15] D. D. Gandhi, M. Lane, Y. Zhou, A. P. Singh, S. Nayak, U. Tisch, M. Eizenberg, and G. Ramanath, "Annealing-induced interfacial toughening using a molecular nanolayer," *Nature*, vol. 447, no. 7142, pp. 299–302, 2007.

[16] J. R. Vig, "UV/ozone cleaning of surface," *J. Vac. Sci. Technol. A*, vol. 3, pp. 1027–1034, 1985.

[17] H. Zhou and J. W. Park, "Effect of the crystallinity of indium tin oxide on the charge transfer at the interfaces and the performances of flexible organic light emitting diodes," *Phys. Status Solidi Appl. Mater. Sci.*, vol. 212, no. 2, pp. 414–424, 2015.

[18] M. Huang, Z. Hameiri, A. G. Aberle, and T. Mueller, "Influence of discharge power and annealing temperature on the properties of indium tin oxide thin films prepared by pulsed-DC magnetron sputtering," *Vacuum*, vol. 121, pp. 187–193, 2015.

[19] C. Donley, D. Dunphy, D. Paine, C. Carter, K. Nebesny, P. Lee, D. Alloway, and N. R. Armstrong, "Characterization of Indium−Tin Oxide Interfaces Using X-ray Photoelectron Spectroscopy and Redox Processes of a Chemisorbed Probe Molecule: Effect of Surface Pretreatment Conditions," *Langmuir*, vol. 18, no. 2, pp. 450–457, Jan. 2002.

[20] A. Sharma, G. Andersson, and D. A. Lewis, "Role of humidity on indium and tin migration in organic photovoltaic devices," *Phys. Chem. Chem. Phys.*, vol. 13, no. 10, p. 4381, 2011.

[21] Y. Hu, D.-Y. Zhou, B. Wang, Z.-K. Wang, and L.-S. Liao, "Chlorinated indium tin oxide electrode by InCl3 aqueous solution for high-performance organic light-emitting diodes," *Appl. Phys. Lett.*, vol. 108, no. 15, p. 153303, 2016.

[22] D. B. Fraser and H. D. Cook, "Highly Conductive, Transparent Films of

Sputtered In[sub 2−x]Sn[sub x]O[sub 3−y],” *J. Electrochem. Soc.*, vol. 119, no. 10, p. 1368, 1972.

[23] J. C. C. Fan and J. B. Goodenough, “X-ray photoemission spectroscopy studies of Sn-doped indium-oxide films,” *J. Appl. Phys.*, vol. 48, no. 8, pp. 3524–3531, 1977.

[24] M. Huang, Z. Hameiri, A. G. Aberle, and T. Mueller, “Comparative study of amorphous indium tin oxide prepared by pulsed-DC and unbalanced RF magnetron sputtering at low power and low temperature conditions for heterojunction silicon wafer solar cell applications,” *Vacuum*, vol. 119, pp. 68–76, 2015.

[25] T. Ishida, H. Kobayashi, and Y. Nakato, “Structures and properties of electron-beam-evaporated indium tin oxide films as studied by x-ray photoelectron spectroscopy and work-function measurements,” *J. Appl. Phys.*, vol. 73, no. 9, pp. 4344–4350, 1993.

[26] M. J. Chuang, H. F. Huang, C. H. Wen, and A. K. Chu, “On the structure and surface chemical composition of indium–tin oxide films prepared by long-throw magnetron sputtering,” *Thin Solid Films*, vol. 518, no. 8, pp. 2290–2294, 2010.

[27] M. Chuang, “ITO Films Prepared by Long-throw Magnetron Sputtering without Oxygen Partial Pressure,” *J. Mater. Sci. Technol.*, vol. 26, no. 7, pp. 577–583, 2010.

[28] K. Sugiyama, H. Ishii, Y. O. Seki, K. Sugiyama, H. Ishii, and Y. Ouchi, “Dependence of indium – tin – oxide work function on surface cleaning method as studied by ultraviolet and x-ray photoemission spectroscopies,” vol. 87, no. 1, pp. 295–298, 2000.

[29] J.-L. Leea, Soo Young Kim and Ki-Beom Kim and Yoon-Heung Tak, “Effect of ultraviolet–ozone treatment of indium–tin–oxide on electrical properties of organic light emitting diodes,” *J. Appl. Phys.*, vol. 95, p. 2560, 2004.

[30] Y. Zhou, J. W. Shim, C. Fuentes-Hernandez, A. Sharma, K. A. Knauer, A. J. Giordano, S. R. Marder, and B. Kippelen, “Direct correlation between work function of indium-tin-oxide electrodes and solar cell performance influenced by ultraviolet irradiation and air exposure,” *Physical Chemistry Chemical Physics*. pp. 12014–12021, 2012.

Chapter 9

Conclusions and Further Work

9.1 Conclusions in respect to the Work Undertaken

The overarching theme of the work undertaken in this thesis was the study of the electronic structure at the interface of inverted polymer solar cells with the aim to identify novel green alternative materials to form self-assembled monolayers (SAM) onto ITO surface. The systematic investigations of the ITO surface with and without these SAM revealed some interesting results, as follows.

Chapter 6 described initial work conducted to provide a background knowledge of the effect of surface cleaning procedures on the ITO electronic structure, as well as the development of benchmark inverted devices fabricated onto bare ITO. Investigations of XPS spectra revealed that the ITO surface is sensitive to the chemical structures of organic solvents used to clean ITO in the final ultrasonic bath. Although the effect of the dipole moments of these solvents onto the surface bond environments were found to be statistically insignificant, the dipole moments were shown to reduce the ITO work function by a maximum of 0.4 eV, with the lowest work function achieved by cleaning in isopropanol alcohol (IPA). When compared to other cleaning procedures, such as UV-ozone plasma and Ar sputtering, carbon surface contaminants were found not to control the ITO work function, which disapproves the claim reported by Sharma et al. [40]. These results were then used to fabricate PCDTBT: PCBM inverted devices and to further examine the effects of the active layer thickness and post-deposition annealing temperature, and the material and thickness of the top anode layer. Due to the absence of a buffer interlayer inserted at the ITO/BHJ interface, the optimum thickness was found to be 90 – 95 nm, which is at the far end range of PCDTBT optimal thickness for standard devices. Thermal annealing of the spin-coated active layer at 80 ℃ for 15 min in an inert atmosphere was shown to induce optimal vertical segregation. In addition, device parameters, especially open circuit voltage (Voc), were showed to be affected by the thickness of the hole extraction layer (MoOx) and the materials used in the capped metallic layer (Ag as opposed to Al). Interestingly, upon systematic changes to the MoOx thickness, Voc kept constant for devices capped with Al (100 nm), while it fluctuated, with a lowest value of 12 nm for devices with an Ag (100 nm) capping layer. Taking into account all these variables, benchmark ITO inverted devices based on PCDTBT: PCBM BHJ were fabricated with a maximum efficiency of 5.4 % being obtained. These results were used in later chapters to investigate the effects of thermal annealing and SAM formation on ITO based inverted devices.

Chapter 7 presented an exemplary study of the open circuit voltage of PCDTBT: PCBM inverted devices fabricated onto bar ITO substrates that were annealed in air at different temperatures. Despite the fact that the performance of these devices deteriorated with increasing annealing temperature, their current density-voltage responses showed good diode rectifying properties. The ITO sheet resistance was demonstrated to only negligibly affect the JV curves, and, based on UPS and XPS measurements, it was seen that Voc was affected by the high potential energy of the interfacial dipoles induced by physical adsorption of ambient gasses. A comparison with previously reported devices incorporating various buffer layers, however, illustrated the presence of a threshold work function. This threshold was equivalent to the LUMO level of the fullerene material used. It is necessary to overcome this threshold in order to realize a high voltage. This promising result poses the following question; whether a further reduction in the substrate work function is necessary to realize the very highest open-circuit voltage?

In **Chapter 8**, five novel biomaterials were used to study the effect of SAM modification on both the ITO surface and device performance. Lys, Glut, Ser, Gly-Phe and Gly-Gly were chosen because they are non-toxic, water soluble, and can be processed with no need for aggressive chemical pre-treatments of the ITO surface, as is otherwise typically required for phosphoric acid based SAM [1]–[3]. Although Glut and Gly-Phe have not yet been reported in the literature as modifying materials, the formation of these monolayers onto the ITO surface was successfully confirmed by careful investigations of the chemical composition and roughness of the ITO surface, with and without SAM. The appearance of nitrogen a N 1s peak with various concentrations across the ITO surface proved the inhomogeneous coverage of the monolayer, as seen by XPS. Inverted devices based on three BHJ donor polymers, PBDTT-FTTE, PTB7, and PCDTBT were fabricated on ITO, with and without SAM, in order to illustrate the effect of SAM backbone polarity, post-deposition annealing temperature and dependency on the BHJ system employed. For PBDTT-FTTE based devices, their efficiencies were shown to be improved by 6 % when Glut SAM is formed while a 18 % reduction compared to the initial PCE was obtained for Gly-Phe SAM. The lowest reduced PCE, by 29 %, was obtained for Gly-Gly SAM. These results were achieved with no thermal annealing conducted prior to the spin-coating of the active layer. Upon thermal annealing of Gly-Gly SAM modified devices, overall enhancements (by 6 % in PCE) were obtained for both PTB7 and PBDTT-

FTTE devices, but not for PCDTBT devices. A comparison to previously reported Gly-Gly modified devices showed further improvements in PCE for P3HT (by 7 %) and PBDTT-CF (by 17 %). Due to the systematic investigations presented throughout this thesis, it can be stated that the reported enhancements for PBDTT-CF by Nie et al. [12] are not real. This is because the Gly-Gly layer was suspected to be evaporated upon annealing due to the similarity in device performance to those devices that deliberately do not have any SAM layer (ITO-only devices). Another conclusion is that having ultra-low work function (3.77 eV as measured by UPS) does not guarantee an efficient inverted device, which supports observations extracted regarding Voc, as seen in **Chapter 7**.

9.2 Suggestions for Further Work

The work presented within this thesis provides some insights into the suitability of biomaterials with amide backbones to modify the surface of ITO cathodes by forming SAM and hence improving the performance of inverted BHJ solar cells. Additional work is required, however, to further understand the mechanisms of some of the effects observed.

It was seen that inverted devices are sensitive to the dipole layer formed onto the ITO surface, with this layer having various effects on the device parameters depending on the choice of the BHJ donor polymer. Further investigations are needed to elucidate whether this sensitivity is induced by the influences of either BHJ morphology or the electronic structure at the interface, or as a combined effect. An example would be studying the surface topography of the modified ITO substrate using scanning tunnelling microscopy (STM) [4]. STM will be beneficial in terms of drawing a 3D image of the SAM by detecting the length of the dipole hanging out of ITO surface. It can also be used to estimate the thickness of the dipole layer, as proposed by Ahmed et al. [5]. The topography of blend layers can also be imaged using scanning electron microscopy (SEM). SEM has been reported to be able to identify morphological changes at a nanoscale for various types of surface within organic solar cells [6], [7]. By imaging the organic layer surface before and after ITO treatments, it would be possible to investigate the changes induced by thermal-annealed SAM.

Furthermore, a detailed study on the dark current of modified devices would illustrate the recombination mechanism at the contact interface and thus enable a better understanding of the dependence of the open circuit voltage on the SAM backbone polarity.

One of the purposes of developing inverted BHJ solar cells is the potential gain in operating life-time compared to standard cells [8], [9]. Considering the fact that peptide materials are naturally occurring, non-toxic and water soluble, and can be processed in air, a study on device stability and life time is required. Other work would be the fabrication of inverted devices with a ZnO interlayer modified with peptide SAM. This is one of the recent approaches that results in improved lifetime, as well as operating efficiency [10]–[13]. If these devices show enhanced performance, the next step would be fabricating an all-solution device, where the

MoOx layer will be deposited from a solution following the procedure reported by Griffin et al. [14].

A final suggested piece of research in this area would be the transfer of the lessons learnt throughout this thesis to new BHJ solar cells that employ a Florine doped tin oxide (FTO) substrate. FTO has been developed in recent years and appears to be a strong candidate to replace ITO, given the latter’s scarcity and toxicity, and the high cost of the Indium source [15], [16].

9.3 References

[1] H. Li, E. L. Ratcliff, A. K. Sigdel, A. J. Giordano, S. R. Marder, J. J. Berry, and J.-L. Brédas, "Modification of the Gallium-Doped Zinc Oxide Surface with Self-Assembled Monolayers of Phosphonic Acids: A Joint Theoretical and Experimental Study," *Adv. Funct. Mater.*, vol. 24, no. 23, pp. 3593–3603, 2014.

[2] S. a Paniagua, P. J. Hotchkiss, S. C. Jones, S. R. Marder, A. Mudalige, F. S. Marrikar, J. E. Pemberton, and N. R. Armstrong, "Phosphonic Acid Modification of ITO Electrodes - Combined XPS - UPS - Contact Angle Studies," *J. Phys. Chem. C*, vol. 112, no. 21, pp. 7809–7817, 2008.

[3] A. Sharma, A. Haldi, P. J. Hotchkiss, S. R. Marder, and B. Kippelen, "Effect of phosphonic acid surface modifiers on the work function of indium tin oxide and on the charge injection barrier into organic single-layer diodes," *J. Appl. Phys.*, 2009.

[4] J. Tersoff and D. R. Hamann, "Theory of the scanning tunneling microscope," *Phys. Rev. B*, vol. 31, no. 2, pp. 805–813, 1985.

[5] J. U. Ahamed, S. Katano, and Y. Uehara, "Capacitance Behavior of Alkanethiol Self-Assembled Monolayer Studied by Scanning Tunneling Microscope Light Emission Spectroscopy," *Trans. Indian Inst. Met.*, vol. 69, no. 8, pp. 1579–1585, 2016.

[6] K. C. Choi, E. J. Lee, Y. K. Baek, D. C. Lim, Y. C. Kang, Y. Do Kim, K. H. Kim, J. P. Kim, and Y. K. Kim, "Morphologically controlled ZnO nanostructures as electron transport materials in polymer-based organic solar cells," *Electrochim. Acta*, vol. 180, pp. 435–441, 2015.

[7] R. C. Masters, Q. Wan, Y. Zhang, M. Dapor, A. M. Sandu, C. Jiao, Y. Zhou, H. Zhang, D. G. Lidzey, and C. Rodenburg, "Novel organic photovoltaic polymer blends: A rapid, 3-dimensional morphology analysis using backscattered electron imaging in the scanning electron microscope," *Sol. Energy Mater. Sol. Cells*, vol. 160, no. October 2016, pp. 182–192, 2017.

[8] P. Cheng and X. Zhan, "Stability of organic solar cells: challenges and strategies," *Chem. Soc. Rev.*, vol. 45, pp. 2544–2582, 2016.

[9] Y. T. Ta-Ya Chu, T.-Y. Chu, S.-W. Tsang, J. Zhou, P. G. Verly, J. Lu, S. Beaupré, M. Leclerc, and Y. Tao, "High-efficiency inverted solar cells based on a low bandgap polymer with excellent air stability," *Sol. Energy Mater. Sol.*

Cells, vol. 96, pp. 155–159, 2012.

[10] Y. E. Ha, M. Y. Jo, J. Park, Y.-C. Kang, S.-J. Moon, J. H. Kim, Y.-C. K. Ye Eun Haa, Mi Young Joa, Juyun Parkb, J. H. K. Sang-Jin Mooncc, Y. E. Ha, M. Y. Jo, J. Park, Y.-C. Kang, S.-J. Moon, and J. H. Kim, "Effect of self-assembled monolayer treated ZnO as an electron transporting layer on the photovoltaic properties of inverted type polymer solar cells," *Synth. Met.*, vol. 187, pp. 113–117, Jan. 2014.

[11] L. Nian, W. Zhang, S. Wu, L. Qin, L. Liu, Z. Xie, H. Wu, and Y. Ma, "Perylene Bisimide as a Promising Zinc Oxide Surface Modifier: Enhanced Interfacial Combination for Highly Efficient Inverted Polymer Solar Cells," *ACS Appl. Mater. Interfaces*, vol. 7, no. 46, pp. 25821–25827, 2015.

[12] X. Liu, X. Li, Y. Li, C. Song, L. Zhu, W. Zhang, H. Q. Wang, and J. Fang, "High-Performance Polymer Solar Cells with PCE of 10.42% via Al-Doped ZnO Cathode Interlayer," *Adv. Mater.*, pp. 7405–7412, 2016.

[13] O. Mahesh, P. H. Lin, and Y. Tai, "Impact of self-assembled monolayer assisted surface dipole modulation of PET substrate on the quality of RF-sputtered AZO film," *Appl. Surf. Sci.*, vol. 403, pp. 356–361, 2017.

[14] J. Griffin, A. J. Pearson, N. W. Scarratt, T. Wang, and D. G. Lidzey, "Organic photovoltaic devices incorporating a molybdenum oxide hole-extraction layer deposited by spray-coating from an ammonium molybdate tetrahydrate precursor," *Org. Electron.*, vol. 15, pp. 692–700, 2014.

[15] S. Optik, F. Nipis, T. Oksida, and T. Florin, "Structural , Optical and Electrical Properties of Fluorine Doped Tin Oxide Thin Films Deposited Using Inkjet Printing Technique," *Sains Malaysiana*, vol. 40, pp. 251–257, 2011.

[16] F. Li, C. Chen, F. Tan, C. Li, G. Yue, L. Shen, and W. Zhang, "Semitransparent inverted polymer solar cells employing a sol-gel-derived TiO2 electron-selective layer on FTO and MoO3/Ag/MoO3 transparent electrode," *Nanoscale Res. Lett.*, vol. 9, no. 1, pp. 579, 2014.